

Cover Page



Universiteit Leiden



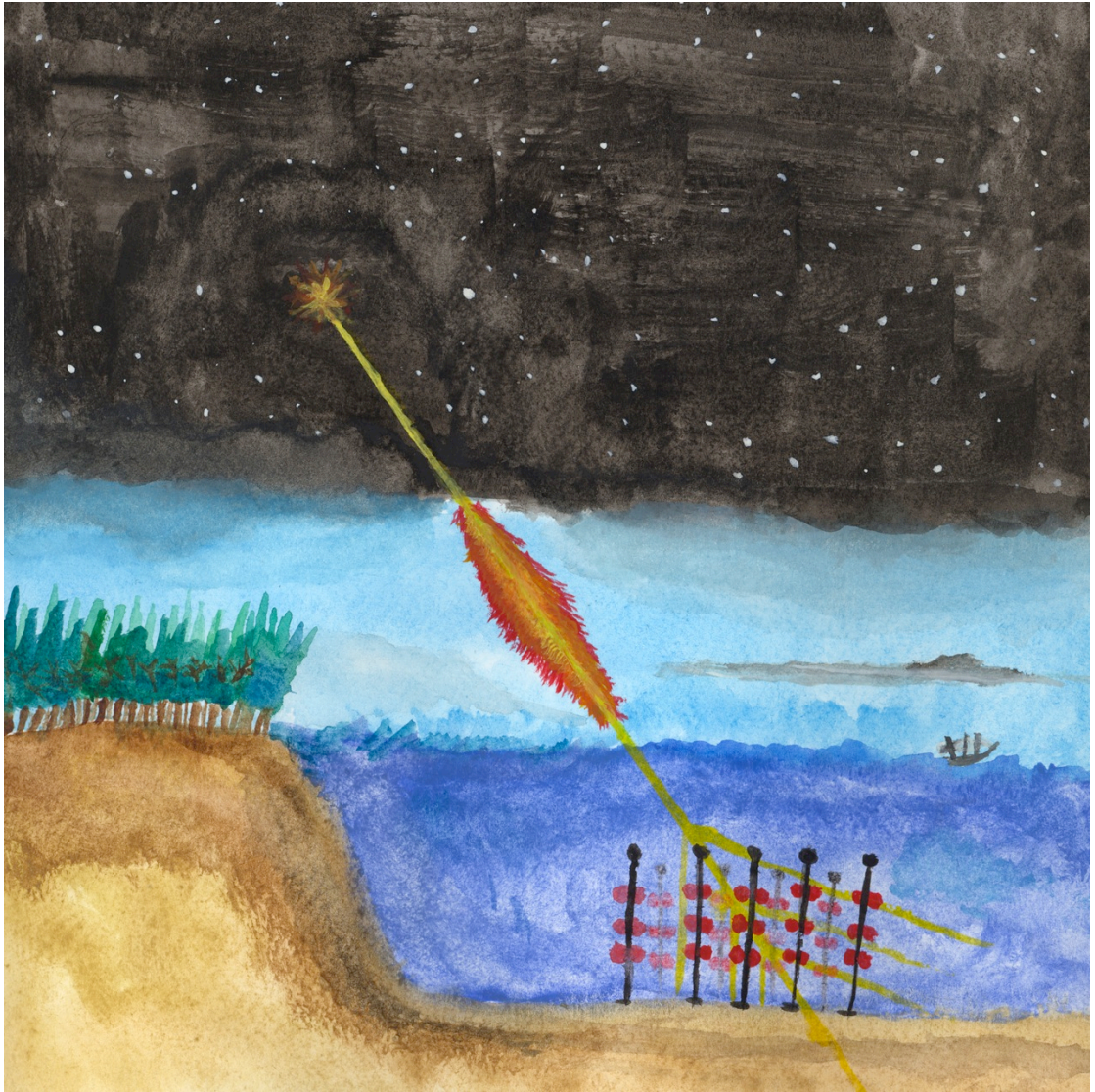
The handle <http://hdl.handle.net/1887/20680> holds various files of this Leiden University dissertation.

**Author:** Astraatmadja, Tri Laksmana

**Title:** Starlight beneath the waves : in search of TeV photon emission from Gamma-Ray Bursts with the ANTARES Neutrino Telescope

**Issue Date:** 2013-03-26

Starlight beneath the waves



Frontispiece: An illustration of the physical processes described in this dissertation. A Gamma-Ray Burst (GRB) emits high-energy  $\gamma$ -rays towards the Earth. Depending on the distance to the GRB and the energy of the  $\gamma$ -ray, some of them will get annihilated by the cosmic infrared background. Those that survive will initiate electromagnetic showers in the atmosphere, producing some amount of muons. The muons then penetrate the sea, losing their energy along the way. As the muons traverse the sea, electromagnetic shock-waves will be generated in the form of Čerenkov photons. These photons will then be detected as signals by the array of photomultiplier tubes that comprise ANTARES. Illustration by the author.

# Starlight beneath the waves

In search of TeV photon emission from Gamma-Ray Bursts  
with the ANTARES Neutrino Telescope

Proefschrift

ter verkrijging van  
de graad van Doctor aan de Universiteit Leiden,  
op gezag van Rector Magnificus prof. mr. C. J. J. M. Stolker,  
volgens besluit van het College voor Promoties  
te verdedigen op dinsdag 26 maart 2013  
klokke 11.15 uur

door

Tri Laksmana Astraatmadja

geboren te Djakarta, Indonesië  
in 1981



# Promotiecommissie

Promotor: Prof. dr. M. de Jong

Overige leden: Prof. dr. A. Achúcarro  
Prof. dr. ing. J. F. J. van den Brand (Vrije Universiteit Amsterdam)  
Prof. dr. E. R. Eliel  
Prof. dr. P. M. Kooijman (Universiteit van Amsterdam)  
Dr. A. Kouchner (Université Paris Diderot – Paris VII, Parijs)  
Prof. dr. K. H. Kuijken  
Dr. K. E. Schalm  
Prof. dr. R. A. M. J. Wijers (Universiteit van Amsterdam)

Casimir PhD series, Delft-Leiden 2012-33

ISBN 978-90-8593-146-1

First published in print format 2013

© Tri L. Astraatmadja 2012

This work is licensed under Creative Commons Attribution-NonCommercial 3.0. The licence permits the copy, distribution, transmission, and adaption of this work for non-commercial use, so long as attribution is given. For more information, see <http://creativecommons.org/licenses/by-nc/3.0>

Cover image: An artist's impression of a Gamma-Ray Burst (GRB), by A. Roquette (ESO)  
Cover design by Fitorio Leksono

Typeset by the author using the Tufte- $\LaTeX$  class developed by Kevin Godby  
<http://tufte-latex.googlecode.com>

Printed in The Netherlands by Ipskamp Drukkers B.V., Enschede

The author has no responsibility for the persistence or accuracy of urls for external or third-party internet websites referred to in this publication, and does not guarantee that any content on such websites is, or will remain, accurate or appropriate

Dit is zeker echt niets nieuws  
dit smalle pad is al vaak betreden  
alleen deze keer  
is het om de weg uit te stippelen.

*Aarde der Mensen*  
Pramoedya Ananta Toer

Dedicated to the next generation  
Putri Mahalia  
and  
Aria Widiadana Astraatmadja



# Contents

	<i>Preface</i>	9
1	<i>Introduction</i>	11
1.1	<i>Photon, cosmic ray, and neutrino astronomy</i>	12
1.2	<i>Gamma-ray burst astronomy</i>	18
1.3	<i>Teraelectronvolt astronomy: tools of the trade</i>	36
1.4	<i>The rise of neutrino telescopes</i>	45
1.5	<i>This thesis: Neutrino telescopes as <math>\gamma</math>-ray observatories</i>	52

## PART I THEORY

2	<i>The creation and propagation of TeV photons</i>	57
2.1	<i>VHE <math>\gamma</math>-ray productions and the photon spectrum of a GRB</i>	57
2.2	<i>Normalising the observed photon spectrum</i>	73
2.3	<i>Photon absorption by ambient infrared photons</i>	75
3	<i>Muon production in the atmosphere</i>	80
3.1	<i>The cascade equation: Approximation A</i>	81
3.2	<i>Pion decay</i>	82
3.3	<i>Direct muon-pair production</i>	84
3.4	<i>Other channels of muon production</i>	89
3.5	<i>Cosmic ray-induced muon background</i>	89
3.6	<i>Passage of muons through seawater</i>	90
3.7	<i>On the multiplicity of downgoing muons</i>	93
4	<i>Muon event rate from single GRBs</i>	98
4.1	<i>Muon flux from a fictive test source</i>	98

4.2	<i>Muon flux from single GRB</i>	99
4.3	<i>Conclusions</i>	105
5	<i>Muon event rate and discovery potential from stacked GRB events</i>	108
5.1	<i>GRB world model</i>	108
5.2	<i>GRB event generation and muon flux calculations</i>	116
5.3	<i>Result and conclusions</i>	117

## PART II DETECTOR & SIMULATIONS

6	<i>The ANTARES neutrino telescope</i>	121
6.1	<i>Čerenkov photons</i>	121
6.2	<i>Detection principle of a neutrino telescope</i>	122
6.3	<i>The ANTARES detector</i>	123
6.4	<i>Data acquisition (DAQ) system</i>	127
6.5	<i>Calibrations</i>	130
6.6	<i>Triggering and track reconstruction</i>	132
7	<i>Simulation of the detector response to downgoing muons</i>	140
7.1	<i>Simulation chains</i>	140
7.2	<i>Detector performance</i>	143
8	<i>The point spread function and the optimization of quality cuts</i>	157
8.1	<i>Background data</i>	157
8.2	<i>Weighting scheme and the point spread function</i>	159
8.3	<i>Optimization for discovery: The model discovery potential</i>	164

8.4 *Optimization for sensitivity: The model rejection factor* 168

9 *Hypothesis testing* 171

### PART III DATA ANALYSIS

10 *Prospective GRB sources* 181

10.1 *Selection Procedure* 181

10.2 *GRB 090907A* 186

10.3 *GRB 070220* 187

11 *Analysis of ANTARES data coinciding with two GRB events* 190

11.1 *Muon production* 190

11.2 *Muon duplication* 192

11.3 *Further simulation chains* 196

11.4 *Results of the reconstruction* 197

11.5 *Optimization* 201

11.6 *Summary* 205

11.7 *The result of data unblinding* 206

### PART IV EPILOGUE

12 *Conclusions and outlook* 211

*Summary* 216

*Samenvatting* 224

*Ringkasan* 232

*Bibliography* 240

*Curriculum vitae* 249

# Preface

THIS booklet is a doctoral dissertation which came out as a result of four years of research conducted at the National Institute for Subatomic Physics (Nikhef) in Amsterdam, The Netherlands. Some of the text written in this dissertation is based on the following material:

- Astraatmadja T. L. 2011. *On the detection of TeV  $\gamma$ -rays from GRB with  $\text{km}^3$  neutrino telescopes — I. Muon event rate from single GRBs.* *MNRAS*, **418**: 1774–1786 (Sections 1.5, 2.2–2.3, 3.1–3.6, Chapter 4)
- Astraatmadja T. L., 2012a, *On the detection of TeV  $\gamma$ -rays from GRB with  $\text{km}^3$  neutrino telescopes: ANTARES's responses to down-going muons.* Technical Report ANTARES-PHYS-2012-005 (Section 3.7, Chapters 7–10)
- Astraatmadja T. L., 2012b, *On the detection of TeV  $\gamma$ -rays from GRB with  $\text{km}^3$  neutrino telescopes: Simulation and optimization of three selected GRBs.* Technical Report ANTARES-PHYS-2012-006 (Chapter 11)

THE OFFER to do this research project came from Maarten de Jong. I attended his class on astroparticle astrophysics in 2007, during my master studies at the Leiden Observatory. He was later appointed as a professor at Leiden University and offered me a PhD position. I was interested and quite enthusiastic, but was unsure to undertake a project in such an unfamiliar topic. During my visit to Nikhef for the job interview, the then leader of the ANTARES group at Nikhef (to which I was later attached), Gerard van der Steenhoven, assured me that somebody with my background and capabilities could be a useful addition to the group. I was convinced. I would like to thank Gerard for his confidence and for telling me that there is a place for an astronomer like me in astroparticle physics.

The ANTARES group at Nikhef is akin to a close-knit family. The bond that developed over the years helped me ease the



stress of doing research. Claudio Bogazzi, Giada Carminati, Akis Gkaitatzis, Claudio Kopper, Gordon Lim, Tino Michael, Dimitris Palioselitis, Jelena Petrovic, Eleonora Presani, Corey Reed, Stephan Schulte, Erwin Visser, Guus Wijnker, thank you all for your suggestions and comments, for giving me the most awesome time at Nikhef, and for showing me how to survive at ANTARES. Thank you Ana Carolina Assis Jesus, Ching-Cheng Hsu, and Jeroen Snijdwint for your patience in sharing an office with me. Special thanks to Erwin for all those Dutch translations, and thank you Maria Tselengidou for making working in Nikhef at weekends much less dreary. You guys are a constant reminder that I was never alone in working on this project.

My research is greatly aided by Mieke Bouwhuis, Aart Heijboer, and Dorothea Samtleben. Thank you for helping me in matters of the GCN alert messages, track reconstruction, and L0 data analysis. The dissertation would not be the same without your help. I want to thank also Antoine Kouchner and Clancy James for their suggestions and for refereeing my work towards data unblinding. Additional thanks should also be given to Aart and Clancy for presenting my results on my behalf respectively in Moscow and Bologna. I thank also Yuri Cavecchi, Samia Drappeau, and Peter Polko from the Anton Pannekoek Astronomical Institute for sharing their knowledge of high-energy astrophysics.

Thank you Ralph Wijers for reading the manuscript of my first paper. Without your suggestions and constant assurance that the paper is worth publishing, it would never have ended up the way it is.

Finally, I would like to thank Maarten de Jong for supervising my research and for his support and belief in this work. Without his constant push in the right direction and encouragement, this dissertation would have run out of steam and would never have been completed.

Tri L. Astraatmadja

# 1 Introduction

THE IDEA on which this dissertation is based is a very old one, but today can become a reality with the recent advent of very large volume neutrino telescopes.

When a downgoing high-energy  $\gamma$ -ray passes through the atmosphere of the Earth, it will interact with the particles in the atmosphere and initiate an electromagnetic shower of particles (not unlike what is shown in Figure 1.1). This shower could produce, among others, a small number of muons that can penetrate deep into the Earth, losing their energy along the way. If a muon moves with a speed exceeding the speed of light in its surrounding medium, the medium will radiate so-called Čerenkov photons at a characteristic angle relative to the direction of the muon. An undersea or under-ice large-volume neutrino telescope can detect the surviving muons by detecting these Čerenkov photons. The Čerenkov photons are recorded by the light-sensitive photomultiplier tubes that comprise the neutrino telescope. By finding signals causally connected in space and time, the track of a muon can be reconstructed to obtain the energy of the muon and its direction of arrival. A neutrino telescope primarily intended to observe upgoing neutrino-induced muons could then have a secondary function as a  $\gamma$ -ray telescope.

With the completed construction of the ANTARES<sup>1</sup> neutrino telescope in the Mediterranean Sea (Ageron et al., 2011) and Ice-Cube<sup>2</sup> at the South Pole (Halzen & Klein, 2010), it is now possible to revisit this old idea of using a neutrino detector as a  $\gamma$ -ray telescope. The goal of this dissertation is to find out whether this is actually possible, to study the response of the detector to downgoing muons if that is the case, and also to perform an analysis of the now-available data from ANTARES.

This method of  $\gamma$ -ray detection can in principle be applied to any astrophysical source that emits high-energy  $\gamma$ -rays. However for reasons that will be discussed later on, in this dissertation gamma-ray bursts (GRB) will be the sole target of the attempt to detect high-energy  $\gamma$ -rays using an underwater large-volume neutrino telescope.

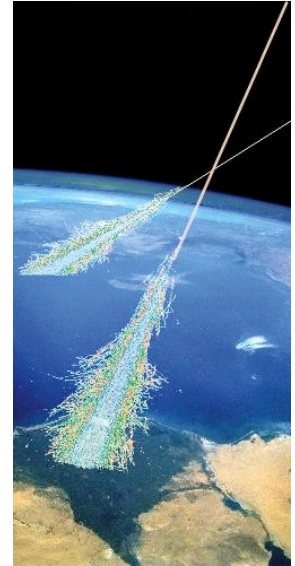


Figure 1.1: An illustration of a particle shower initiated by cosmic rays. Credit: Simon Swordy (University of Chicago, NASA).

<sup>1</sup> Astronomy with a Neutrino Telescope and Abyss environmental REsearch project, <http://antares.in2p3.fr>

<sup>2</sup> <http://icecube.wisc.edu/>

Many things need to be outlined first before we venture deeper into this endeavour. In the following subsections I will outline the leitmotif that drives this particular line of research and elaborate upon the basic idea described above.

### 1.1 *Photon, cosmic ray, and neutrino astronomy*

ON ALL of its surface and at all times, the Earth is bathed with particles. They are emitted from various astronomical sources and produced by various physical processes. They carry information on the nature of the astronomical sources from which they are produced. In order to comprehend the workings of the universe, astronomers build various instruments to detect these particles and interpret the results.

AMONG these particles are the photons, carriers of the electromagnetic force. Starlight, i.e. photon emissions from astronomical sources, has inspired generations of natural philosophers since time immemorial. Gods were made, myths and religions were built, and musings concerning the nature of the sources were thought out (Krupp, 1994). It can be said that the traditional method of astronomical observation is carried out by observing photons emissions from celestial sources, hence in hindsight it can also be classified as *photon astronomy*.

Photon astronomy as a modern science began when Hans Lippershey, a Dutch-German lensmaker who lived in Middelburg, The Netherlands, developed the first known optical telescope in 1608 (van Helden, 1977). The development of photographic plates in the mid-19th century and their usage in astronomy as a mean to permanently record astronomical observations can only accelerate our progress in astronomical research (de Vaucouleurs, 1961), and the same could be said with the development of spectroscopy—pioneered by German optician Joseph Fraunhofer in 1814—as a method to decompose a beam of light into its constituent lights of different wavelengths. Nowadays the instruments of the photon astronomers are as varied as the energy regimes and sources of the photons. From radio waves to high-energy  $\gamma$ -rays, the electromagnetic spectrum has been thoroughly explored, and multiwave-

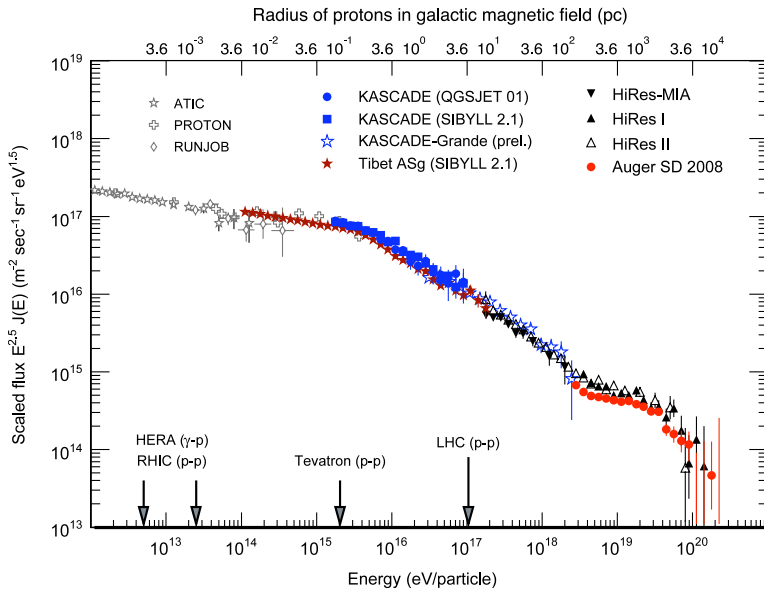


Figure 1.2: The energy spectrum of cosmic rays, reproduced from Hörandel (2010).

length astronomy has become the norm in photon astronomy.

ASIDE from photons, cosmic rays also constantly bombard the Earth. They are fully ionized atomic nuclei accelerated to relativistic velocities. Their interactions with the nuclei in the atmosphere produce showers of particles (Figure 1.1) that could be detected at the surface of the Earth. They were first discovered by Victor Hess through a series of balloon experiments (Figure 1.3) to measure the change of ionization level in the Earth's atmosphere. The prevailing view at that time was that the Earth is the source of ionizing radiation and thus the rate should decrease as we ascend to higher altitude. Hess however measured instead an increasing rate of ionization with increasing altitude, and concluded that the radiation that penetrates the atmosphere comes from outer space (Hess, 1912).

The energy spectrum of cosmic rays (Figure 1.2) stretch from below 100 Megaelectronvolt (MeV) up to  $10^{20}$  eV. At very high energy, the energy gained from their acceleration exceeds anything that could be performed in the largest manmade particle acceler-



Figure 1.3: Victor Hess preparing for his balloon ascent to measure cosmic rays, Austria, 1912. Credit: American Physical Society (APS), <http://www.aps.org>

ators on Earth. How these natural accelerators could accelerate particles to such enormous level of energy is a mystery that still puzzle scientists up to this day.

Efforts to pinpoint their sources and thus obtain a better understanding of the acceleration mechanism are however hampered by the fact that cosmic rays are charged particles and could thus get deflected to random directions by ambient magnetic fields. Only cosmic rays of the highest energies are minimally deflected by magnetic fields and could thus point back relatively close to their sources, but these events are very rare (approximately one  $10^{19}$  eV particle per  $\text{km}^2$  per year per steradian) and their observation would require a detector with a very large collecting area so that enough particles could be detected within reasonable observation time. The Pierre Auger Observatory<sup>3</sup> (Abraham et al., 2004) is currently the largest cosmic ray observatory in the world, operating at Malargüe in Argentina.

<sup>3</sup> <http://www.auger.org>

It is now generally accepted that cosmic rays with energies below 100 MeV come from the Sun. Cosmic rays with energies up to  $10^{15}$  eV (the so-called “knee” in the cosmic ray energy spectrum) are usually considered to be Galactic in nature. The most possible accelerators are the supernova remnants (SNRs). As the shock front of the supernova propagates through the interstellar medium, repeated scattering of the particles across the shock front enable them to gain energy (Blandford & Eichler, 1987).

Cosmic rays with energies above  $10^{18}$  eV are considered to be accelerated at extragalactic sites such as active galactic nuclei (AGN) or gamma-ray bursts (GRB) (Hörandel, 2010). These two sources are an attractive candidate because their total energy output is roughly equal to the total energy output of observed extragalactic cosmic rays (Gaisser, 1997; Halzen, 2007). If we integrate the energy spectrum of extragalactic cosmic rays to obtain their energy density  $\rho_E$ , we will arrive at roughly  $\rho_E = 10^{-19}$  TeV  $\text{cm}^{-3}$ . In order to generate an energy density with that magnitude over a period of  $10^{10}$  years, a population of sources would have to release  $\sim 3 \times 10^{37}$  erg  $\text{s}^{-2}$   $\text{Mpc}^{-3}$ . This required energy release corresponds roughly to  $\sim 2 \times 10^{44}$  erg per AGN or  $\sim 2 \times 10^{52}$  erg per GRBs, which is coincident with the the observed output in electromagnetic energy of these sources.

To confirm that GRBs or AGN are the primary sources of cosmic rays is difficult because of the aforementioned reason that they are deflected by ambient magnetic fields. However, the interaction of cosmic rays with the ambient matters produce secondary particles that does not interact with magnetic fields and points back to its source: very-high energy (VHE) photons—which is of particular interest to this dissertation—and ultra-high energy (UHE) neutrinos. Thus the motivation to understand the origin of cosmic rays at the highest energy is linked with the motivation of this dissertation and is also inextricably related to the search of high-energy neutrinos. Next we shall discuss on how by searching for VHE photons and UHE neutrinos could aid in pinpointing the exact location of cosmic rays.

NEUTRINOS are another kind of particle that have interest astronomers soon after their discovery in 1956 (Cowan et al., 1956), since they are also produced in the nuclear fusion reaction that powers the Sun (Fowler, 1958). Because of the high density at the core of the Sun, photons took hundreds of thousands of years ricocheting through the Sun before they finally escape and reach Earth. On the other hand, neutrinos interact very weakly with matter and could travel unimpeded throughout the Sun. Neutrinos are then an important carrier of information about what is going on at the core of the Sun, deep under the photosphere and is hidden from the observations of photon astronomers. Their weak interaction with matters, on the other hand, makes their detection difficult. Neutrino astronomy was born when the first detection of solar neutrinos was made (Davis, Harmer & Hoffman, 1968).

Up to the time of writing, the astrophysical neutrino sources thus far discovered are only the Sun and Supernova (SN) 1987A (Hirata et al., 1987; Bionta et al., 1987), which emits neutrinos with relatively low-energy, i.e. in the MeV regime. However, the neutrino energy spectrum (Figure 1.5) extends from the very low energies of 1.9 Kelvin cosmic neutrino background (CNB) radiation to the very high at the EeV regime. CNB might never be directly detected although it is possible to indirectly detect them by analysing the power spectrum of the CMB (De Bernardis et al., 2008). Aside from the Sun and SN 1987A, atmospheric neutri-

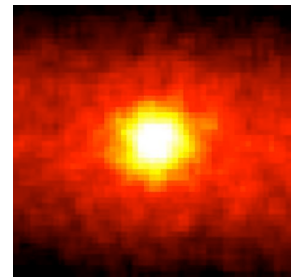


Figure 1.4: A Super-Kamiokande neutrino image of the Sun. The center of this image is the position of the Sun, and the size of the image is  $90^\circ \times 90^\circ$ . Brighter colors represent the higher flux of neutrinos. This image is made using 500 days of Super-K data. Credit: Robert Svoboda and K. Gordan, Louisiana State University. Retrieved from Astronomy Picture of the Day (APOD).

The cosmic neutrino background (CNB) is the neutrino counterpart to the cosmic microwave background (CMB). The CNB decoupling from matters occurred when the universe was a mere 2 second old.



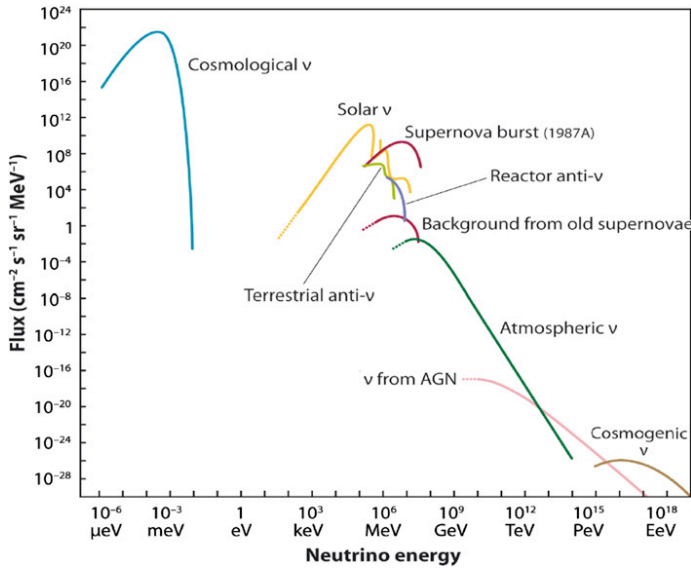


Figure 1.5: The energy spectrum of natural and reactor neutrinos, reproduced from Katz & Spiering (2012).

nos produced from cosmic-ray interactions with the Earth's atmosphere have also been regularly detected (Gaisser, 2011). Ultra high-energy (UHE) neutrinos from astrophysical sources are still awaiting detection and will probably be detected within the next decade by existing or future very large volume neutrino telescopes.

Observing UHE neutrinos is the tell-tale sign for the acceleration site of cosmic rays. The emission of high-energy neutrinos is expected as a consequence of the interaction between cosmic rays with ambient matter. A relativistically expanding matter will interact with its surrounding environment and create a shock wave. Shock-accelerated protons could escape and be observed on Earth as cosmic rays, but some will interact dominantly with photons to produce Delta resonances which will subsequently decay into charged pions (Waxman & Bahcall, 1997):

$$p\gamma \rightarrow \Delta^+ \rightarrow n\pi^+ \quad (1.1)$$

$$\pi^+ \rightarrow \nu_\mu + \mu^+ \quad (1.2)$$

$$\mu^+ \rightarrow \bar{\nu}_\mu + e^+ + \nu_e \quad (1.3)$$

$$n \rightarrow p + e^- \quad (1.4)$$

As we can see, the resulting neutrino flavour ratio at the source is approximately  $\nu_e : \nu_\mu : \nu_\tau = 1 : 2 : 0$ . If we assume that the secondary pions receive 20% of the proton energy for each interaction, and each secondary lepton shares  $1/4$  of the pion energy, each flavor of neutrino is then emitted with 5% of the proton energy which is dominantly in the PeV regime (Mészáros, 2006).

As has mentioned before, GRBs are an attractive candidate as the source of cosmic-rays because their total energetics “suspiciously” match the integrated energy of cosmic rays. It is possible then that this injected energy is converted into the production of cosmic rays. Observing UHE neutrinos could establish the corresponding source—be it AGN or GRBs—as the source of extragalactic cosmic rays. Since most GRBs are located at cosmological distances with a redshift  $z \sim 1$ , detecting neutrinos from each individual GRBs might not be possible. However, nearby GRBs do occur and it may be possible for a km-scale neutrino telescope to detect neutrinos from these objects. In addition, the detection of UHE neutrinos is also important in understanding the internal mechanism of the probed source, e.g. GRBs: particle acceleration, radiation mechanism, and the progenitor itself could be characterized.

VERY-HIGH energy photons could also be produced from the interaction of cosmic rays with ambient matters. The first channel that can be considered is through the production of Delta resonance:

$$p\gamma \rightarrow \Delta^+ \rightarrow \pi^0 + p, \quad (1.5)$$

$$\pi^0 \rightarrow \gamma\gamma, \quad (1.6)$$

here  $\pi^0$  will decay into VHE photons. Another way to produce VHE photons is through the Inverse Compton (IC) mechanism:

$$e^- + \gamma \rightarrow e^- + \gamma, \quad (1.7)$$

here low-energy photons  $\gamma$  are scattered by relativistic electrons and thus gain energy, becoming high-energy photons  $\gamma$ .

The first channel can be an important contribution to the total flux provided there are protons accelerated in significant number and that their energy exceeds that of the VHE photon by at least

one order of magnitude. The proton spectral index should be hard, e.g.  $dN/d\epsilon_p \propto \epsilon_p^{-2}$  rather than  $\epsilon_p^{-2.2}$ , otherwise there will not be enough protons to produce VHE photons and the  $p\gamma$  channel will be a less important channel than the IC component (Mészáros, 2006).

Another variation of the IC process is the synchrotron-self Compton (SSC) process in which the photons are provided by the synchrotron radiation from accelerated electrons. This model is leptonic in nature, i.e. pure electron acceleration model, and not hadronic. This means that they do not directly explain the origin of cosmic rays. In most realistic cases, however, both hadronic and leptonic models do take place. Observing VHE photons from GRBs could then provide not only hints on the origin of cosmic rays but also on the acceleration mechanisms of hadrons and leptons in the source. The production of VHE photons will be elaborated in Section 2.1.

The main problem that troubles observations of VHE photons is the fact that they interact very strongly with ambient infrared photons to produce pairs of electron-positron. The universe is transparent to photons up to  $\epsilon_\gamma \sim 10$  GeV, but at  $\epsilon_\gamma = 1$  TeV the mean free path is only a few hundred Mpc (Finke, Razzaque & Dermer, 2010). This limits our observational window only to nearby GRBs, which very rarely go off at such nearby distance. However, one can hope as such an event has happened in the past, e.g Galama et al. (1998); Mirabal et al. (2006); Starling et al. (2011).

## 1.2 *Gamma-ray burst astronomy*

GAMMA-RAY BURSTS are a brief flash of  $\gamma$ -rays occurring approximately once per day at random time and direction in space (Fishman & Meegan, 1995; van Paradijs, Kouveliotou & Wijers, 2000; Woosley & Bloom, 2006; Gehrels, Ramirez-Ruiz & Fox, 2009). In this brief moment, the  $\gamma$ -radiation lit up the otherwise dark  $\gamma$ -ray sky, outshining any other  $\gamma$ -ray sources. Their spatial directions are isotropically distributed and so far are found to be nonrepeating. The  $\gamma$ -ray production mechanism of GRBs are thought to involve particles accelerated to ultrarelativistic speeds and colli-

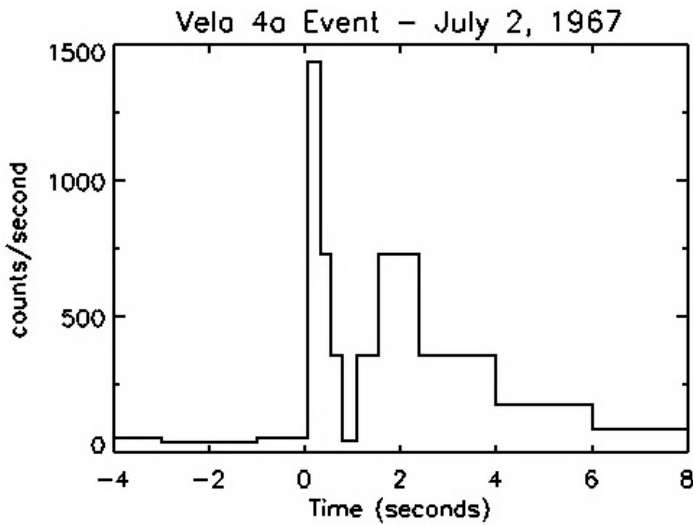


Figure 1.6: The first ever GRB signature detected by *Vela*. Credit: Goddard Space Flight Center.

mated into bipolar jets (e.g. Rees & Mészáros 1992, Mészáros & Rees 2001). The total energy output in  $\gamma$ -rays for a typical GRB, corrected for beaming effects, is  $\sim 10^{51}$  erg (Woosley & Bloom, 2006).

The discovery of GRBs is a quintessential example of serendipity in scientific endeavour. In the midst of the Cold War and the looming threat of an all-out nuclear war, the Nuclear Test Ban Treaty was signed in July 1963 by the governments of the Soviet Union, United Kingdom, and the United States. The treaty prohibits nuclear detonation test anywhere except underground. To assure compliance to this treaty, the United States government launched a series of satellites called *Vela* (Figure 1.7) to detect any nuclear test conducted in space or in the atmosphere.

In 1967, *Vela 4A* detected a flash of  $\gamma$ -radiation which time profile showed a double-peaked curve (Figure 1.6): a short intense peak followed by a softer but prolonged peak. Although this is a tell-tale signature of a nuclear explosion, it was later clear that this gamma-ray burst did not come from a nuclear explosion. The intense first peak shown in Figure 1.6 is much too long for an atmospheric nuclear test, which duration lasts typically in the order of milliseconds. Several bursts of this nature were later detected,



Figure 1.7: The *Vela 5B* satellite. Credit: NASA.

but the military nature of the *Vela* mission kept this discovery from going public until 1973, when it was finally declassified and published by Klebesadel, Strong & Olson (1973). This was confirmed shortly after by Soviet scientists who observed similar bursts detected by the satellite Kosmos 461 (Mazets, Golenetskij & Il'Inskij, 1974).

Serendipity is characterized by a “happy accident”, i.e. finding an unforeseeable event that turns out to be better than what could be foreseen by the original intent. What was meant to be a rather mundane task of detecting nuclear test in space—some sort of an anti-shoplifting mirror in space—turns out to be one of the greatest mysteries astronomers ever faced.

THE DIRECTION of  $\gamma$ -rays is notoriously difficult to pinpoint. This difficulty hampered early attempts to understand GRBs. A first attempt to determine their direction was performed by triangulation using the arrival time of the  $\gamma$ -rays at different satellites. This way, the Interplanetary Network (IPN) of six satellites managed to localize GRBs with uncertainty up to within arcminutes from their actual location (Vedrenne, 1981; Cline et al., 1981). No optical counterpart, however, was found within this error circle. There was no way to determine the distance to the GRBs either, and thus without any knowledge of their intrinsic brightness it was next to impossible to discern the true nature of GRBs.

In the face of this gross lack of observational data, controversies and wild speculations were rampant. Since the discovery of GRBs up to 1995, about 2000 papers have been published about GRBs (Fishman & Meegan, 1995). Theories abound on their nature, ranging from the exotic which involves cosmic strings (e.g. Paczyński, 1988) to the rather standard such as comets impacting a neutron star (e.g. Tremaine & Żytkow, 1986), or even simple local events such as the scattering of solar photons by relativistic dust grains (e.g. Grindlay & Fazio, 1974). Ideas kept popping out and at one point there were about 100 competing models that tried to explain GRBs (Nemiroff, 1994). One of the main issues of this debate is whether GRBs are local events or located at cosmological distances.

The anti-shoplifting-mirror-in-space analogy was described by Ralph Wijers in one of his lectures on GRB: “If you own a shop and you don’t trust your customers, you put mirrors at the corners to prevent shoplifters. In the Cold War you put satellites in space to make sure the other side keep their side of the bargain.”

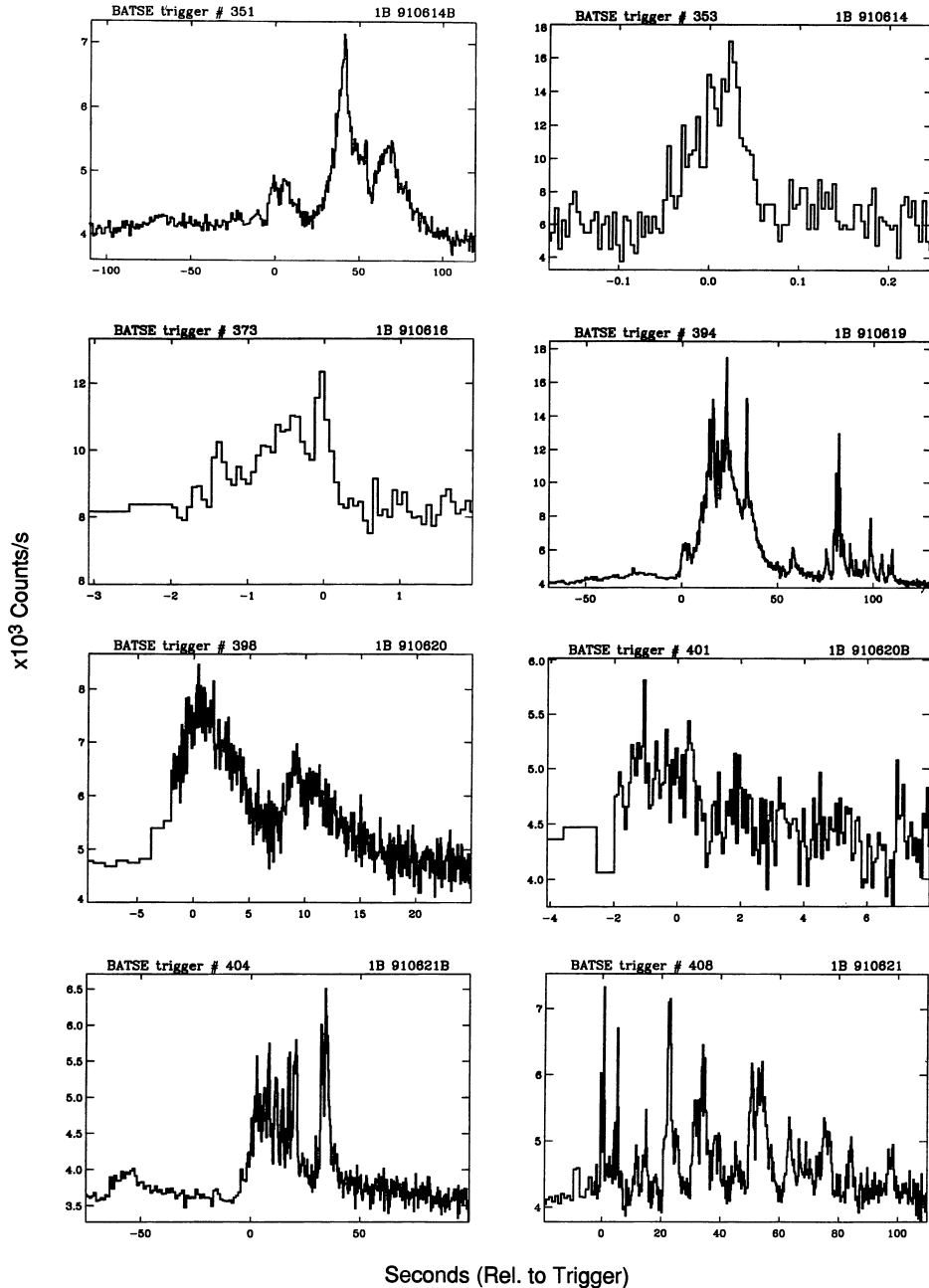


Figure 1.8: A sample of several GRB light curves from the First BATSE Gamma-Ray Burst Catalog (Fishman et al., 1994). The profile of the light curves exhibit a variety in their profiles, intensities, and duration.



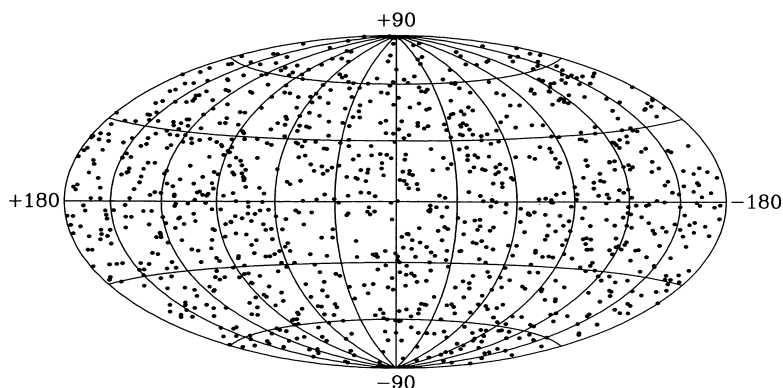


Figure 1.9: The sky distribution of the 1122 GRBs from the BATSE 3B catalog, mapped on Hammer-Aitoff projection in Galactic coordinates. The isotropic distribution of the GRB directions suggests that they are located at cosmological distances. The map is reproduced from Meegan et al. (1996).

PROGRESS in our observational knowledge of GRBs before 1997 was mostly obtained from the observations of the  $\gamma$ -ray detector BATSE<sup>4</sup> on board the *Compton Gamma-Ray Observatory* (CGRO)<sup>5</sup>. In BATSE, NaI crystals are used as a scintillator which is sensitive to  $\gamma$ -rays with energies from  $\sim 25$  to 2000 keV (Paciesas et al., 1999). This wide energy range makes BATSE very sensitive and thus enable it to detect 2 or 3 GRBs on a typical day. To complement BATSE, *Compton* also carried with it the EGRET<sup>6</sup> instrument, a multilevel thin-plate spark chamber that produces pairs of electron-positron upon impact with a  $\gamma$ -ray (Kanbach et al., 1988). EGRET is sensitive to  $\gamma$ -rays from 20 MeV to 40 GeV and is thus suitable to probe the high-energy component of a GRB.

Between 1991 and 2000 BATSE observed 2704 GRBs. Their spatial distribution indicates an isotropic angular distribution (Figure 1.9) which implies that GRBs must be located at cosmological distances (Meegan et al., 1992; Briggs et al., 1996), or at least located at the halo of our Galaxy (Podsiadlowski, Rees & Ruderman, 1995). If GRBs are located at cosmological distances, consequently their energy output should be extremely huge. This narrows down the possible theoretical explanations.

Two other BATSE results of note will be described here. The first is the realization that the time-averaged energy spectrum of a GRB emission can be well-described at low energy by a power-law function with an exponential cutoff (Band et al., 1993, Figure

<sup>4</sup>Burst And Transient Source Experiment, <http://www.batse.msfc.nasa.gov/batse/>

<sup>5</sup><http://heasarc.gsfc.nasa.gov/docs/cgro/>

<sup>6</sup>Energetic Gamma-Ray Experiment Telescope, <http://heasarc.gsfc.nasa.gov/docs/cgro/egret/>

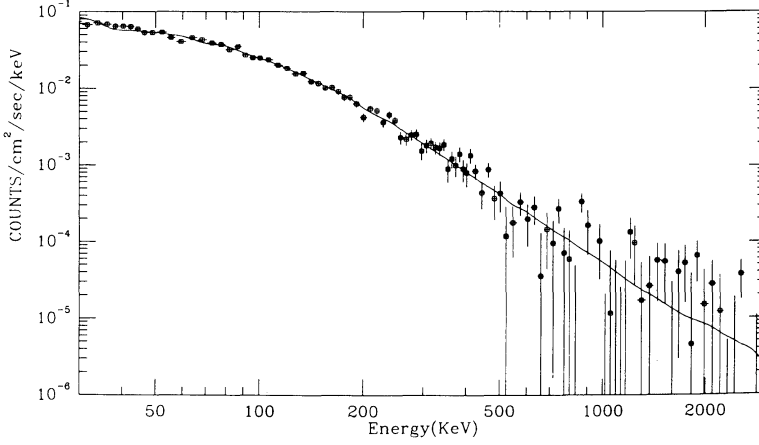


Figure 1.10: An example of a GRB photon spectral density and the spectral fitting of the Band function to the data, here reproduced from Band et al. (1993). The GRB shown here is GRB 1B 911127. The low-energy spectral index is  $\alpha = -0.968 \pm 0.022$ , the high-energy spectral index is  $\beta = -2.427 \pm 0.07$ , and the break energy is  $\epsilon_b = 149.5 \pm 2.1$ .

1.10),

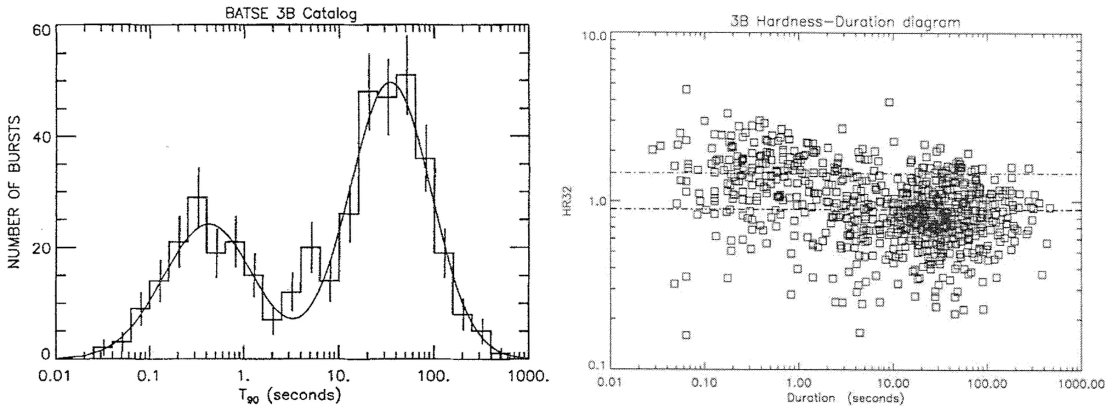
$$\frac{dN}{d\epsilon_\gamma} \propto \epsilon_\gamma^{-\alpha} \exp\left(-\frac{\epsilon_\gamma}{\epsilon_b}\right), \quad \epsilon_\gamma \leq (\beta - \alpha)\epsilon_b \quad (1.8)$$

and at high energy with a steeper power-law

$$\frac{dN}{d\epsilon_\gamma} \propto \epsilon_\gamma^{-\beta}, \quad \epsilon_\gamma \geq (\beta - \alpha)\epsilon_b, \quad (1.9)$$

in which  $\beta > \alpha$  and  $\epsilon_b$  is the break energy, i.e. the energy at which the spectrum breaks. This broken but smoothly-connected power-law is called the Band function, named after astronomer David Band who first-authored the paper discussing the energy spectra of BATSE GRBs (Band et al., 1993). It is necessary here to point out that the Band function is phenomenological in nature and is not physically motivated. Nevertheless it is without doubt very useful since it could fit well with a large number of GRB spectra and thus provide hints to the mechanisms of  $\gamma$ -ray emission.

The second notable BATSE result is the identification of two classes of GRBs based on their burst duration and hardness ratio. The now-standard method to determine the burst duration is to measure the time interval during which the integrated counts from the burst increase from 5% to 95% of the total counts (Kouveliotou et al., 1993). Such duration is called  $T_{90}$ . The distribution of  $T_{90}$  exhibits a bimodality suggesting two different classes of

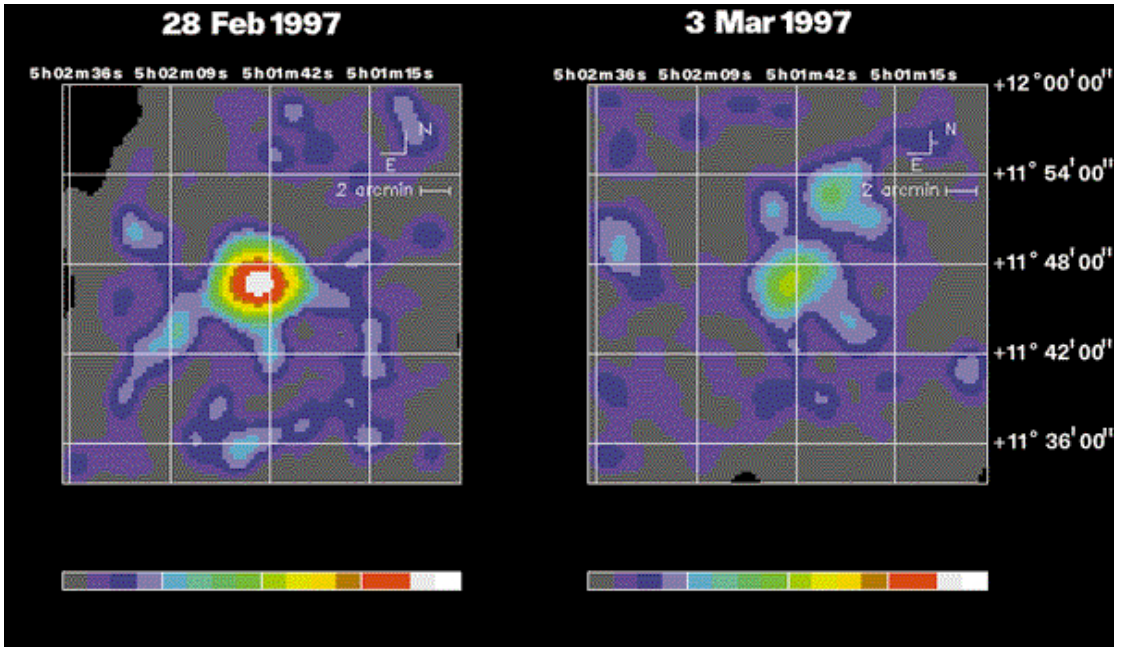


GRBs: short-duration GRBs which typically last less than 1 second and long-duration GRBs which typically last more than 10 second (Kouveliotou et al., 1996, Figure 1.11, left). The demarcation between short and long GRBs is usually taken to be 2 second. We can also correlate  $T_{90}$  with what is known as the hardness ratio. Denoted as  $HR_{32}$ , the hardness ratio is the ratio of the total count of a GRB during the  $T_{90}$  interval in the range of 100–300 keV with the total count between 50–100 keV. The correlation between  $HR_{32}$  and  $T_{90}$  shows that long GRBs are predominantly soft while short GRBs are predominantly hard (Kouveliotou et al., 1996, Figure 1.11, right).

Figure 1.11: *Left*: The  $T_{90}$  distribution for GRBs from the BATSE 3B Catalogue, here reproduced from Kouveliotou et al. (1996). The solid line is a fitting of two log-normal distribution to the data. *Right*: The hardness ratio –  $T_{90}$  diagram for GRBs from the BATSE 3B, also reproduced from Kouveliotou et al. (1996). The dashed-dotted lines are the average hardness for the short (top line) and long (bottom line) GRBs, which is separated at 2 second.

AN IMPORTANT event in GRB astronomy happened in 1997, when the first high-resolution X-ray images of a GRB were made for the first time by the Italian-Dutch satellite *BeppoSAX*<sup>7</sup> (Costa et al., 1997). Eight hours after the  $\gamma$ -ray detection of GRB 970228, a fading X-ray afterglow of the burst was discovered (Figure 1.12), which has been theoretically predicted (Mészáros & Rees, 1997). This leads to an arcminute-accuracy pinpointing of the GRB position, which allows us to perform follow-up observations in the longer wavelength. An optical observation of the afterglow would soon follow (van Paradijs et al., 1997) as well as the discovery of the first GRB afterglow in the radio band (Frail et al., 1997, GRB 970508). The discovery of the afterglow allows us to determine

<sup>7</sup> Satellite per Astronomia a raggi X. *Beppo* is the nickname of physicist Giuseppe Occhialini. <http://www.asdc.asi.it/bepposax/>



their redshift, to identify the host galaxies, and to confirm their cosmological origin (Metzger et al., 1997). GRB astronomy has gone multiwavelength.

A MODEL of GRB has appeared even before their actual detection, when Colgate (1968, 1974) proposed the very first model of a  $\gamma$ -ray burst. In this model, prompt  $\gamma$ -rays and X-rays could be emitted as the breakout of relativistic shocks from the photosphere of supernovae (SNe). The lack of GRB-supernova connection was however noted by Klebesadel, Strong & Olson (1973), who pointed out that there were no observed supernovae within several weeks around the time of the bursts. They did however aware that numerous supernovae could occur undetected if it is too faint in the optical regime.

The idea of GRB-SNe connection resurfaced time and again (e.g. Paczyński, 1986), but it was not firmly established until much later, in 1998, when GRB 980425 occurred in conjunction with SN 1998bw. The GRB was detected both by *BeppoSAX* (Soffitta et al.,

Figure 1.12: The discovery of the first X-ray afterglow of a GRB, 970228. These are false-colour images of the afterglow taken with the *BeppoSAX* Medium Energy Concentrator Spectrometer (2–10 keV). White corresponds to 31 counts per pixel<sup>2</sup>, green corresponds to 6 counts per pixel<sup>2</sup>, and grey to a background of 0–1 counts per pixel<sup>2</sup>. Images reproduced from Costa et al. (1997).

1998) and BATSE. Within the  $8'$ -radius error circle lies a late-type galaxy ESO184-G82 ( $z = 0.0085$ , Tinney et al. 1998), hosting in one of its spiral arm a luminous supernova designated 1998bw (Sadler et al., 1998). Initially the association of the GRB with the SN was controversial, but follow-up observations by *BeppoSAX* reveal a variable X-ray source at the location of the SN (Pian et al., 2000). Further *Chandra* observations of the location increase the confidence in the connection between the GRB and the SN (Kouveliotou et al., 2004).

On the surface, the GRB looks unremarkable. It has a smoothly-broken power law with break energy  $\epsilon_b = 148$  keV and a moderate burst duration that last  $T_{90} = 23.3$  s (Galama et al., 1998). However GRB 980425/SN 1998bw was quite unusual for a GRB because its redshift implies an underluminous  $\gamma$ -ray energy output, having an isotropic emission of  $L_\gamma = 8 \times 10^{47}$  erg (Galama et al., 1998). This is more than three orders of magnitude fainter than a typical long-duration GRB, which is at the order of  $10^{52}$  erg (Butler, Bloom & Poznanski, 2010), and any collimation into jets would make the energy output in  $\gamma$ -ray even smaller. This unusual property led to the consensus that GRB 980425/SN 1998bw is an example of one extreme end of a spectrum of events with the same underlying physical mechanism (Woosley & Bloom, 2006), and the notion that GRBs are associated with SNe is maintained. The first unambiguous association of a GRB with a Supernova came later when HETE<sup>8</sup> satellite (Ricker et al., 2003) detected GRB 030329/SN 2003dh (Hjorth et al., 2003).

The large redshifts of GRBs imply that the isotropic  $\gamma$ -ray fluences are of the order of one solar rest mass,  $M_\odot c^2 \sim 2 \times 10^{54}$  erg, which is  $\sim 1000$  times the total energy emitted by a typical SN (Mészáros, 2006). This huge energy requirement could be reduced significantly, however, if the emission is collimated into a jet. Observations of breaks in the optical and IR light curves of the GRB afterglows show that this is indeed the case (Kulkarni et al., 1999; Castro-Tirado et al., 1999). This collimation would then make the total energy output comparable to that of SNe, the difference being that the energy of GRBs is emitted mostly in  $\gamma$ -ray over a very short period of tens of seconds, while SNe emit their energy isotropically mostly in the optical wavelengths over longer period

GRBs are designated by the date of their detection. In this way, GRB 980425 is the burst that has been detected on April 25 1998. If more than one burst is detected during the day, a letter is appended to the name: GRB 980425A, for example, is the first GRB detected on April 25 1998, GRB 980425B is the second, and so on. The same naming convention also applies to supernovae, except that only the year is used to name the supernova, e.g. SN 1998, which means that the supernova is detected in 1998. Capital letters from A to Z are appended to indicate the order of detection in that year, followed by pairs of lower-case letters after all the letters of the alphabet has been used. Hence SN 2005nc is the 367th supernova discovered in 2005.

<sup>8</sup>High Energy Transient Explorer, <http://space.mit.edu/HETE/>

of several weeks.

The small time variability  $\delta t$  of GRBs, which is at the order of milliseconds, implies typical emitting regions of several thousand kilometers, i.e.  $c\delta t = 3000 \text{ km}(\delta t/10 \text{ ms})$ . Within this very small space, around  $10^{51}$ – $10^{53}$  erg of energy—which is more than the total emission of the Sun during its lifetime—must be injected within a few tens of seconds. The sudden release of this large amount of energy will result in the conversion of a fraction of this energy into neutrinos and gravitational waves, and a significantly smaller fraction ( $10^{-3}$ – $10^{-2}$ ) is converted into a fireball composed of baryons,  $e^\pm$ , and  $\gamma$ -rays. This fireball is transparent to gravitational waves as well as to neutrinos (Mészáros, 2006).

OBSERVATIONS suggest that the photon luminosity of the fireball is many orders of magnitude larger than the Eddington luminosity  $L_E = 4\pi GMm_p c / \sigma_T = 1.25 \times 10^{38} (M/M_\odot) \text{ erg s}^{-1}$ , which means that the radiation pressure of the fireball exceeds its self-gravity and thus should expand. However, the injection of so much energy into a very small space within a very short time implies that the fireball should be very opaque to high-energy photons. Photons with MeV energy and higher would annihilate to create electron-positron pair. Consequently we should not observe high-energy  $\gamma$ -rays, yet we do. The energy spectrum of GRBs extend to MeV (Matz et al., 1985; Schneid et al., 1992) and occasionally also observable to the GeV regime (Abdo et al., 2009). To solve this compactness problem, first the total mass of baryons in the central region of the progenitor must be below  $\sim 10^{-12} M_\odot$  so that the electrons do not produce a large opacity (Paczynski, 1990), and second the fireball must expand relativistically so that the baryon density decrease rapidly and thus the opacity to photon-photon collisions could be avoided.

The relativistic expansion of the fireball solves the compactness problem in three ways. Suppose the fireball expands relativistically with a bulk Lorentz factor  $\Gamma$ . The observed photons will then be blueshifted by a factor  $\Gamma$ , so that the observed  $\gamma$ -rays are actually X-rays in the fireball. This greatly reduces the number of photons at the fireball that is actually above the pair-production threshold. Secondly, for a typical observed timescale of  $\delta t$ , the

The energy threshold for two photons to annihilate and create a pair of electron-positron is  $\epsilon_{\text{th}} = m_e c^2 = 0.511 \text{ MeV}$



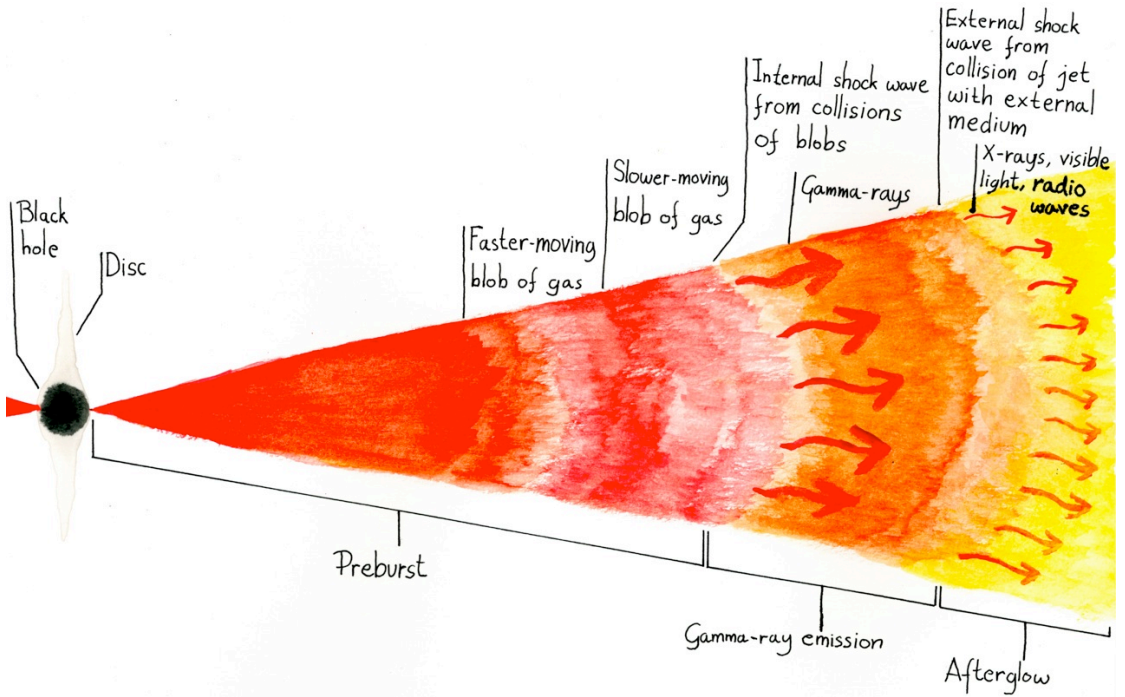


Figure 1.13: An illustration of the various phases in the GRB standard model, with the internal and external shocks and the radiations they emit. Illustration by the author, based on an illustration by Juan Velasco in Gehrels, Piro & Leonard (2002).

physical size of the emitting region is actually  $\Gamma c\delta t$  instead of  $c\delta t$  for a stationary source, which means that the density of photons is reduced considerably. Thirdly, relativistic beaming implies that only a small fraction  $1/\Gamma$  of the source is observable, regardless of the opening angle of the jet. This means that the relative angle of the photon-photon collisions must be less than the  $\Gamma^{-1}$ , which also reduces the effective rate of pair-production for a large  $\Gamma$ .

These three combined effects reduce the optical depth for pair creation by a factor  $\Gamma^{2+2\alpha}$ , where  $\alpha$  is the spectral index of the observed photon spectrum,  $dN_\gamma/d\epsilon_\gamma \propto \epsilon_\gamma^{-\alpha}$ . For  $\alpha \sim 2$  this would mean a drop of optical depth by a factor of  $\Gamma^6$  (Zhang & Mészáros, 2004). Considering these effects, for  $\alpha \sim 2$  it is found that  $\Gamma \geq 100$  is required in order that the pair-production optical depth is less than unity (Piran, 1999; Lithwick & Sari, 2001).

Evidence for the relativistic expansion of the fireball is provided by radio observations of the GRB afterglow, which shows a strong

irregular variations in the radio flux that dampened after about a month. These variations are caused by the interstellar scintillation in our Galaxy. The damping of the fluctuations afterwards reflects the increasing size of the source. By knowing the distance to the source and the properties of the interstellar medium along the line of sight, the size of the source by the time the fluctuations disappear could be determined. Frail et al. (1997) employed this method to GRB 970508 and found out that the radio afterglow expanded with velocity close to the speed of light.

It is inside and around this relativistically expanding fireball that the  $\gamma$ -ray emission we observe is produced, through internal shocks (Rees & Mészáros, 1994) and external shocks (Rees & Mészáros, 1992). Inside the fireball, time-varying outflow from the GRB central engine leads to successive shells of materials ejected with varying Lorentz factor (Figure 1.13). A fast blob ejected after a slower one will eventually overtake and collide with it. Due to the relativistic expansion of the fireball, the timescale that we observed is compressed by a factor  $\Gamma^{-1}$ . Thus the  $\gamma$ -ray burst that we observe in only a few seconds could actually take a day to produce. These shocks can thus explain the rapidly varying light-curves of the prompt  $\gamma$ -ray emission.

As the fireball expands and eventually slows down, it collides with the external medium surrounding the GRB, forming an external shock wave that will persist even as the fireball slows down. This type of shock explains quite well the GRB afterglow emission and its gradual degradation from  $\gamma$ -rays to X-rays to visible light and finally to radio waves. A reverse shock that propagates back into the fireball can also occur. As the reverse shock crosses the fireball, it will heat up the matter in the fireball and accelerates electrons, producing a strong optical flash and a radio flare (Mészáros & Rees, 1997).

THE PROGENITOR that becomes the central engine of a GRB is thought to involve compact objects at its heart. It is natural to think this way because of the small time variability which implies a progenitor possessing huge energy occupying a very small volume. The nonrepetition of a GRB means that the progenitor is catastrophically destroyed.

One family of progenitor models, called the hypernova or collapsar model, involves rotating massive stars with  $M_* \gtrsim 20M_\odot$ . In this model the iron core of such star will eventually collapse, forming a black hole encircled by a debris disk (Woosley, 1993; Popham, Woosley & Fryer, 1999; MacFadyen & Woosley, 1999). Within minutes following the collapse, the black hole accretes the residual matter into the center and funnels them into a powerful relativistic jet that will be observed as a GRB if the jet happens to point towards the Earth. The massive star must also have shed its hydrogen-rich envelope at the time of collapse, in order to not only avoid a significant amount of baryon-loading into the jet, but also to allow the jet, which is formed deep inside the star, to break through the body of the star and develops.

Numerical simulations of collapsars show that the progenitors can not produce bursts shorter than  $\sim 5$  s (MacFadyen & Woosley, 1999). We observe nevertheless short-hard bursts in Figure 1.11, so their existence require other kind of progenitors. The merger of a compact binary could explain this.

There are many variations within the merger of compact binary scenario: a neutron star merges with another neutron star (NS-NS), black hole + neutron star (BH-NS), black hole + white dwarf (BH-WD), or black hole + helium star (BH-He).

The merger of two neutron stars provide a huge supply of gravitational binding energy that can be channeled into the fireball, and a baryon-clean region along the rotation axis of the binary. The fireball is created from the enormous compressional heating and dissipation associated with the accretion. The relativistic expansion of the fireball is driven by  $\nu\bar{\nu} \rightarrow e^+e^-$  annihilation or strong magnetic fields in at the order of  $10^{14}$  G (Rosswog, Ramirez-Ruiz & Davies, 2003). A black hole will be formed from the NS-NS merger, while remnants of the merger form a neutron-rich high-density torus that will orbit the black hole. Neutrinos and antineutrinos from the torus then annihilate to produce an ultrarelativistic  $e^+e^-$  plasma outflow along the rotation axis, which becomes the fireball.

The torus is very dense and thus only neutrinos can extract its thermal energy present in the torus. The neutrino emission will be focused along the original binary rotation axis, as the pole regions

are covered with high-density walls of the thick disk and the steep density gradient in the radial direction prevents lateral expansion. In a particularly baryon-clean region, a relativistic outflow can be accelerated by  $\nu\bar{\nu}$  annihilation. While it is similar to the collapsar mechanism suggested by MacFadyen & Woosley (1999), in this case the jet does not have to burrow through the stellar envelope.

The typical isotropic energy provided by the  $\nu\bar{\nu}$  annihilation is  $E_{\text{iso}} \sim 10^{48}$  erg, emitted within 0.2 second after the merger (Ross-wog, Ramirez-Ruiz & Davies, 2003). This is comparable to the typical duration of a short-hard burst. Gravitational wave emission is also expected from short-hard bursts (Cutler & Thorne, 2002).

THE EXTENSION of the Band spectrum to the megaelectronvolt (MeV) regime has been observed even before the launch of *Compton*. The Solar Maximum Mission<sup>9</sup> (SMM) and the Franco-Soviet PHEBUS detector on the *Granat*<sup>10</sup> mission has detected GRBs with  $\gamma$ -ray energy up to 10 MeV (Matz et al., 1985; Barat et al., 1992). These authors showed that the spectra of GRBs very often extend to this high-energy regime, while on the other hand the observations of  $\gamma$ -ray emissions up to 100 MeV have only been reported for a small number of GRBs, mainly by the COMPTEL<sup>11</sup> and EGRET instruments on board the CGRO (Schneid et al., 1992; Hanlon et al., 1994; Winkler et al., 1995; Kippen et al., 1998). Between 1991 and 1995 COMPTEL observed 29 GRBs in the range 0.75–30 MeV and suggested that GRB spectra extend at least to hundreds of MeV.

Observations in the gigaelectronvolt (GeV) regime has been reported only for a handful of GRBs. EGRET observed seven GRBs with emissions in the MeV and GeV regime (Kwok et al., 1993; Hurley et al., 1994; Sommer et al., 1994; Dingus, 1995). Particularly interesting is GRB 940217 which lasted for 90 minutes and includes an emission of an 18 GeV photon emitted  $\sim 4500$  s after the low-energy emission has ended (Hurley et al., 1994). The launch of *Fermi*<sup>12</sup> in 2008 provides an opportunity to observe the GeV part of GRB spectra since one instrument on board *Fermi*, the Large Area Telescope<sup>13</sup> (LAT), is particularly sensitive to GeV  $\gamma$ -rays. The LAT is a pair-conversion telescope that measures the

<sup>9</sup> <http://heasarc.nasa.gov/docs/heasarc/missions/solarmax.html>

<sup>10</sup> <http://heasarc.gsfc.nasa.gov/docs/granat/granat.html>

<sup>11</sup> Imaging *Compton* Telescope, <http://heasarc.gsfc.nasa.gov/docs/cgro/comptel/>

<sup>12</sup> *Fermi* was formerly named GLAST (Gamma-ray Large Area Space Telescope) before NASA invited the general public to suggest a new name for it. <http://fermi.gsfc.nasa.gov/>

<sup>13</sup> <http://www-glast.stanford.edu/>

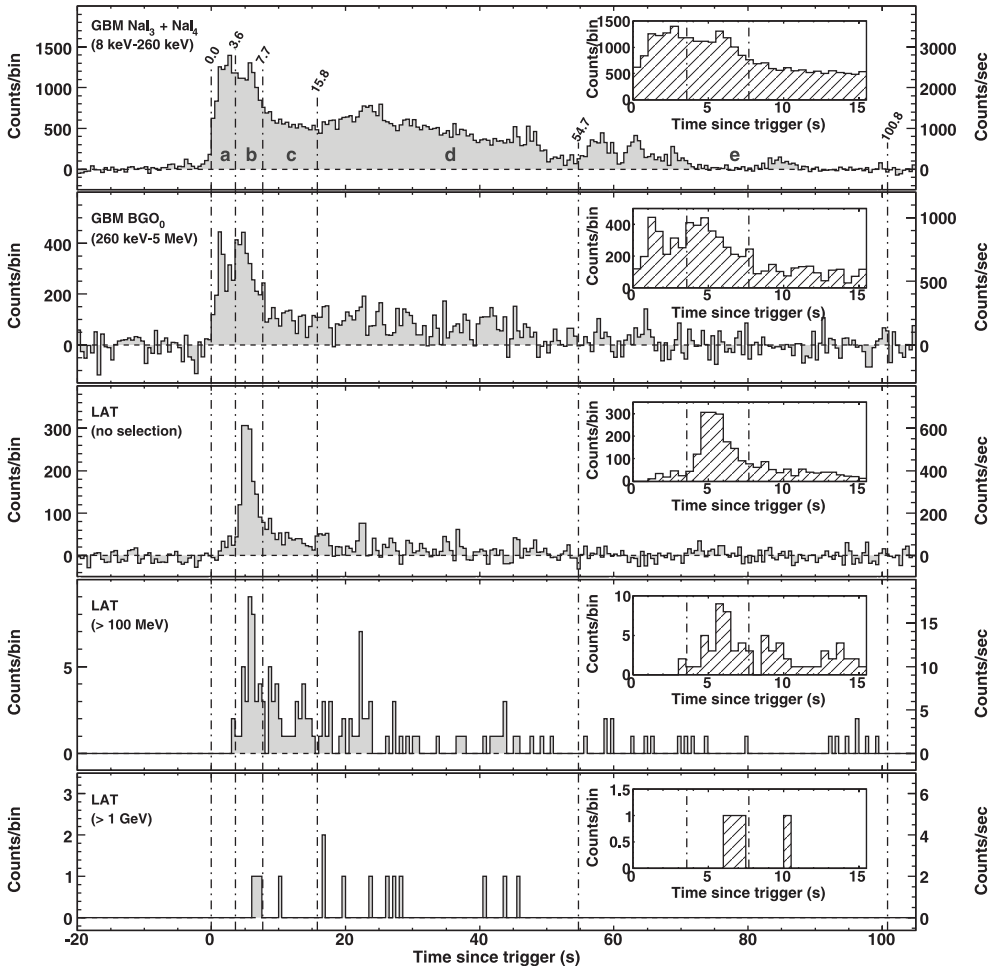


Figure 1.14: The light curves of GRB 080916C observed with the GBM and the LAT, from the lowest to the highest energies. The Figure is reproduced from Abdo et al. (2009).

tracks of the electron ( $e^+$ ) and positron ( $e^-$ ) that result when an incident  $\gamma$ -ray passes through the detector and undergoes pair-conversion. It is sensitive to  $\gamma$ -rays with energies between 20 MeV–300 GeV, and has an effective area of  $0.95 \text{ m}^2$  for  $\gamma$ -rays coming at normal incidence (Atwood et al., 2009). On September 16 2008, an exceptionally bright GRB triggered the Gamma-Ray Burst Monitor<sup>14</sup> (GBM) instrument onboard *Fermi*. Both GBM and LAT observed the GRB and extract the light curve of the GRB at various energy ranges (Abdo et al., 2009). Fourteen events were observed to have energies in excess of 1 GeV and the highest observed  $\gamma$ -ray

<sup>14</sup> <http://gamma-ray.msfc.nasa.gov/gbm/>

energy is  $\sim 13$  GeV. What is particularly interesting with the observation of this GRB is that the peak of the emission is shifted as we move to higher energy regime (Figure 1.14). One way to explain this shift to the higher energy is by invoking a hadronic model associated with ultra-high energy cosmic-ray (UHECR). The delay of the emission is simply the consequence of the time required to accelerate protons into higher energies where they can generate an electromagnetic cascade either by photopion or by proton synchrotron radiation (Abdo et al., 2009). This could be one of the major clues on the emission mechanism of GRBs.

Moving further to the teraelectronvolt (TeV) regime, up to the time of writing there is still no firm evidence of TeV  $\gamma$ -ray emission from GRBs, but not for the lack of trying. Attempts have been made to detect TeV components of GRBs. Using coordinates distributed by the BATSE Coordinates Distribution Network (BACODINE) and later on by the GRB Coordinates Network (GCN), the *Whipple*<sup>15</sup> collaboration has observed 9 BATSE GRBs and 7 other GRBs announced by GCN within minutes to hours after the burst time given by the alert (Connaughton et al., 1997; Horan et al., 2007). No evidence of TeV emission were found but upper limits were reported. The MAGIC<sup>16</sup> Telescope, using the same observation principle as *Whipple*, observed 9 GRBs announced by GCN and found no evidence of TeV emission as well (Albert et al., 2007).

So far the only indication of TeV emission were detections by the HEGRA<sup>17</sup> AIROBICC<sup>18</sup> detector who claimed  $\gtrsim 16$  TeV emission from GRB 920925c (Padilla et al., 1998), the *Milagrito*<sup>19</sup> collaboration (Atkins et al., 2000b, 2003, 2005) who reported detection of  $\gamma$ -rays at  $\sim 650$  GeV, and the GRAND<sup>20</sup> array (Poirier et al., 2003) at 0.01 TeV. The observations by *Milagrito* and GRAND will be described below.

*Milagrito* is a water Čerenkov array of size  $35 \times 44 \times 2$  m at an altitude of 2650 m near Los Alamos, New Mexico, United States. It comprise 228 photomultiplier tubes arranged in a  $2.8 \times 2.8$  m grid, submerged in a large pool of water with volume  $24 \times 10^6$  liter (Atkins et al., 2000a). *Milagrito* operated in 1997–1998 and was later replaced by *Milagro* which has better sensitivity. During the period of *Milagrito*'s activity, 54 BATSE GRBs were observed but

<sup>15</sup> <http://www.sao.arizona.edu/FLW0/whipple.html>

<sup>16</sup> Major Atmospheric Gamma-ray Imaging Čerenkov, <http://wwwmagic.mppmu.mpg.de/>

<sup>17</sup> High-Energy-Gamma-Ray Astronomy, <http://www.mpi-hd.mpg.de/hfm/HEGRA/HEGRA.html>

<sup>18</sup> AIRshower Observation By angle Integrating Čerenkov Counters

<sup>19</sup> A prototype of the *Milagro* Gamma-ray Observatory, <http://www.lanl.gov/milagro/index.shtml>

<sup>20</sup> Gamma Ray Astrophysics at Notre Dame, <http://www.nd.edu/~grand/>

*Milagro* is Spanish for *miracle*, while its aptly-named smaller predecessor *Milagrito* is the diminutive form of *milagro*.

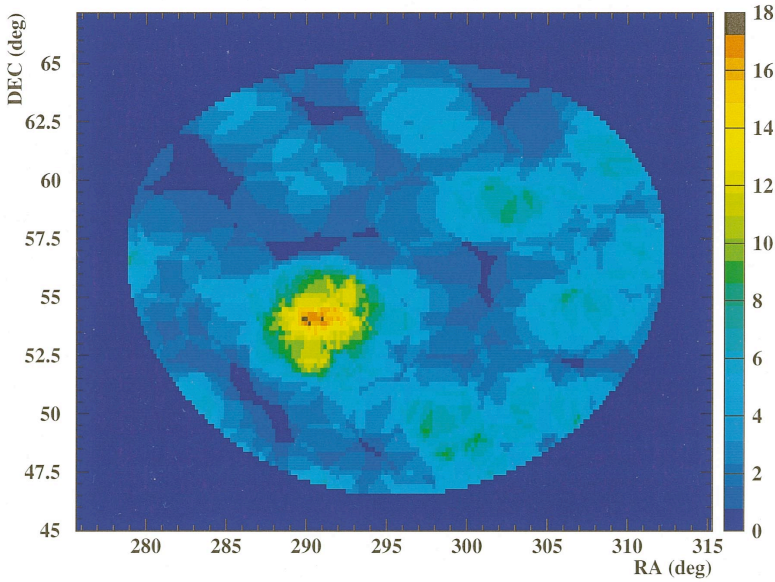


Figure 1.15: *Milagro* observation of TeV  $\gamma$ -ray emission from GRB 970417A, here reproduced from Atkins et al. (2000b). The plot shows the number of events recorded during the  $T_{90}$  duration in overlapping  $1.6^\circ$  radius bin within vicinity of the GRB.

only one, namely GRB 970417A, exhibits an excess of events over background (Atkins et al., 2000b). The probability that such an excess is caused by background fluctuation is  $2.8 \times 10^{-5}$  (Figure 1.15), however this increases to  $1.5 \times 10^{-3}$  if we take into account the fact that all 54 GRBs were observed. Further analysis indicate that this excess over background must be caused by  $\gamma$ -rays with energies of at least 650 GeV (Atkins et al., 2003). If this excess is true then it can be implied that the total isotropic energy of the GRB in the TeV range is  $\sim 10^3$  times than the total isotropic energy in the MeV (Totani, 2000). One interpretation of this phenomenon is through the proton-synchrotron model, in which only  $(m_e/m_p) \sim 10^{-3}$  of the kinetic energy of the fireball is carried by electrons and the rest is carried by protons. If this energy carried by the protons is then emitted as  $\gamma$ -rays, much more energy could be radiated in the TeV regime than the sub-MeV range by a factor of  $\sim 1000$  (Vietri, 1997; Totani, 1998a,b, 1999).

GRAND is a muon detector array located north of the University of Notre Dame campus, approximately 150 km east of Chicago, Illinois, United States. It detects  $\gamma$ -ray-induced muons

at ground level by employing 64 tracking stations of proportional wire chambers (PWC). GRAND has a collecting area of  $\sim 80 \text{ m}^2$ . Eight GRB candidates were observed by GRAND and one of them, GRB 971110, showed an excess of  $466 \pm 171$  muons during its BATSE  $T_{90}$  interval. The probability that this excess is caused by background fluctuation is  $3 \times 10^{-3}$ , or 0.025 probability to observe such background fluctuation in one of the eight bursts observed by GRAND. The detection significance of GRB 971110 is therefore marginal at  $2.7\sigma$  (Poirier et al., 2003).

Another attempt to detect TeV  $\gamma$ -ray was done by the Tibet AS $\gamma$  Experiment<sup>21</sup>. It is a Sino-Japanese experiment located in Yangbajing, Tibet, at 4300 m above sea level. Tibet AS $\gamma$  consists of 221 scintillation counters with area  $0.5 \text{ m}^2$  each and are placed on a  $15 \text{ m}^2$  grid. Using the scintillation detector array, Tibet is able to observe the extensive air shower induced by not only cosmic rays but also by  $\gamma$ -rays. With a duty cycle of 24 hours per day regardless of weather condition and a wide field of view of about 2 steradian, Tibet AS $\gamma$  provide an unbiased survey of TeV sources in the northern sky (Amenomori et al., 2010). They have successfully observed  $\gamma$ -ray sources in the TeV range, such as the Crab Nebula (Amenomori et al., 1999), Markarian 501 (Amenomori et al., 2000), and Markarian 421 (Amenomori et al., 2003). Between October 1995 and March 1996, data coincident with 69 BATSE GRBs were analysed, in search of multi-TeV signals. No significant TeV  $\gamma$ -rays were discovered (Amenomori et al., 2001).

We can see that there are very little results from the search of TeV  $\gamma$ -ray emission from GRBs, but nevertheless the question of whether GRBs emit TeV  $\gamma$ -rays is an important one, as the observations or the lack thereof TeV  $\gamma$ -rays from GRBs would provide important constrains on the acceleration mechanisms of cosmic rays. One of the more specific big questions in GRB astronomy is whether the jets of GRBs are dominated by ultrarelativistic protons or pairs of  $e^+e^-$ . We have seen that protons are an important component in producing TeV  $\gamma$ -rays, and thus the observation of TeV  $\gamma$ -ray emissions from GRBs is an important clue in answering these questions.

<sup>21</sup> AS stands for *air shower*.  
<http://www.icrr.u-tokyo.ac.jp/em/>



### 1.3 *Teraelectronvolt astronomy: tools of the trade*

IT CAN be said that TeV  $\gamma$ -ray astronomy is the “final frontier” in photon astronomy, as it is the last electromagnetic window to be opened (Aharonian, 2004). Whereas photons with energies lower than X-ray are mostly emitted by thermal processes and exhibit blackbody spectrum, photons with energies at the X-ray regime and above are emitted through nonthermal and relativistic processes. Their power-law spectrum also confirms their nonthermal origins.

To observe  $\gamma$ -ray photons is then to observe the most extreme part of the universe. These energetic phenomena are of particular interest to particle physicists as they involve natural accelerators and physical processes that are difficult, if not impossible, to emulate in laboratories. It is a small wonder then that the first  $\gamma$ -ray astronomers generally came from high-energy particle physics community interested in energetic phenomena in the universe (Weekes, 2003).  $\gamma$ -ray astronomy as a concept was first put forward by Morrison (1958). In his seminal 1958 paper, he not only described the physical process that could produce cosmic  $\gamma$ -rays but also outlined the methods to detect them and list a number of possible  $\gamma$ -ray sources.

The  $\gamma$ -ray regime covers at least 14 decades in energy. It spans from approximately the energy of an electron,  $E = m_e c^2 \approx 0.5 \times 10^6$  eV to  $\geq 10^{20}$  eV. This lower bound corresponds to the region of nuclear  $\gamma$ -ray lines as well as the electron-positron annihilation line, while the upper bound corresponds to the highest observed energy of cosmic rays (Aharonian, 2004). We can divide this wide energy band into several areas defined somewhat arbitrarily: the *low* energy (LE, below 30 MeV), *high* (HE, 30 MeV–100 GeV), *very high* (VHE, 100 GeV–100 TeV), and *ultra high* (UHE, beyond 100 TeV). This subdivision has little to do with the physical processes involved in their radiation but has more to do with the interaction phenomena of  $\gamma$ -rays with matter and the various techniques employed for their detection.

Observations in the low and high-energy band are carried out by space satellites or balloons in the upper atmosphere. In the LE regime the Compton process is the dominant interaction mode

used for the detection. Detection in the HE and VHE regime makes use of the pair-production interaction but in different ways: balloons or spaceborne HE telescopes employ spark chambers to identify the electron-positron pair produced as  $\gamma$ -rays interact within the spark chamber plates. On the other hand, ground-based VHE detectors detect the electromagnetic showers that develop in the Earth's atmosphere as  $\gamma$ -rays interact with the atmosphere.

It is readily apparent that there are certain peculiarities unique to  $\gamma$ -ray astronomy that are not present at lower energy regimes. In other regimes of the electromagnetic spectrum, astronomical telescopes take advantage of the fact that light passing through a large aperture can be concentrated to a much smaller area through reflection or refraction, making the size of the detector just a small fraction of the telescope aperture. Optical, infrared, radio, and even X-ray astronomers take advantage of this fact and design a suitable geometry to concentrate photons into a small detector element, so that the signals are detectable above a certain background.

The penetrating power of  $\gamma$ -rays at MeV energies and above prevents them to be efficiently reflected off a surface and thus nuclear physics detection methods must be employed to observe the interaction of  $\gamma$ -rays with matters. In general, the size of a  $\gamma$ -ray "telescope" is then effectively only as big as the size of the detector itself (however, as we shall see later on, this will not be the case for ground-based VHE  $\gamma$ -ray telescopes). It is also necessary to identify cosmic  $\gamma$ -ray events from the charged particle backgrounds. Payload constraints must also be taken into account for spaceborne telescopes. *Compton* was one of the largest and heaviest scientific instruments ever put into space and yet its LE telescope, COMPTEL, and its HE telescope, EGRET, had effective apertures of respectively  $5 \text{ cm}^2$  (Diehl, 1988) and  $2000 \text{ cm}^2$  (Kanbach et al., 1988).

The second peculiarity of cosmic  $\gamma$ -ray detection is that the Earth's atmosphere is opaque to all  $\gamma$ -rays. Even on top of the highest mountains it is still many radiation lengths below the top of the atmosphere, thus it is virtually impossible to directly detect

Even though spark chambers have been obsolete for high-energy physics experiments, they have long been the workhorse detector in HE  $\gamma$ -ray astronomy and has been employed to great success among others by EGRET.

$\gamma$ -rays without sending instruments to outer space. Balloons can lift  $\gamma$ -ray detectors to near the top of the atmosphere and much of the pioneering works in  $\gamma$ -ray astronomy was done this way. Later on as rocket technology improves, satellites operating high above the atmosphere can carry heavier  $\gamma$ -ray detectors. The absorption of  $\gamma$ -rays by the atmosphere, however is not without its own merit, as their interaction will produce a cascade of charged particles that could be detected by dedicated instruments.

Not long after the publication of Morrison's paper on  $\gamma$ -ray astronomy, Cocconi published an optimistic prediction for VHE  $\gamma$ -ray astronomy and suggested a design of a VHE  $\gamma$ -ray telescope consisting of arrays of particle detectors (Cocconi, 1960). This method has been successfully applied to detect cosmic ray showers, however other experimenters realized that for  $\gamma$ -ray-induced cascade a higher sensitivity could be gained by detecting instead the Čerenkov radiation. A group of Soviet physicists from the Lebedev Institute then build an array of 12 light detectors in the Crimea, and after four years of observing the sources suggested by Cocconi (radio galaxies and supernova remnants) no convincing detection was made (Chudakov et al., 1967).

THE EARTH'S atmosphere is opaque to all electromagnetic radiation with energy greater than 10 eV. The vertical thickness of the atmosphere above sea level is approximately  $1030 \text{ g cm}^{-2}$ . Since one radiation length in air is  $X_0 = 36.62 \text{ g cm}^{-2}$  (Nakamura & Particle Data Group, 2010), the thickness of the atmosphere is equal to more than 28 radiation lengths. While the  $\gamma$ -ray itself may be absorbed by the atmosphere, the secondary products of its interaction with the atmosphere do survive and are detectable.

The dominant interaction of a  $\gamma$ -ray with energy greater than 10 MeV is pair-production. Typically this will occur after one radiation length has been traversed. The resulting electron-positron pair will share the energy of the parent  $\gamma$ -ray and will be emitted in virtually the same direction as the original direction of the  $\gamma$ -ray. After this pair traverse another radiation length, they could interact with the atmosphere to emit secondary  $\gamma$ -rays through bremsstrahlung. A secondary  $\gamma$ -ray could also produce another electron-positron pair after another radiation length. This pro-

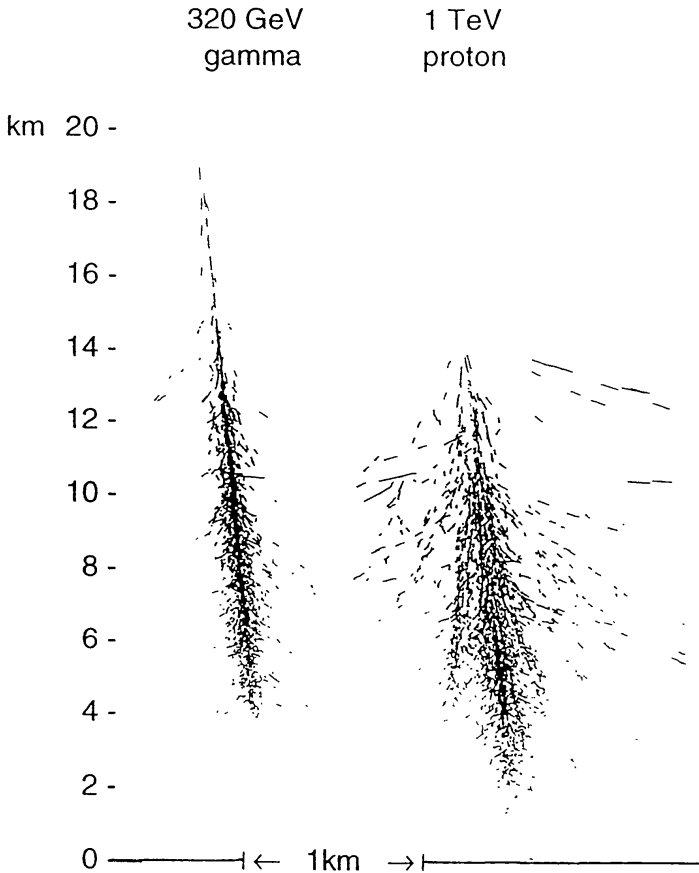


Figure 1.16: Monte Carlo simulations of a 320 GeV  $\gamma$ -ray shower and a 1 TeV proton shower. The horizontal scale is exaggerated by a factor of 5. Figure reproduced from Hillas (1996).

cess continues down through the atmosphere (Figure 1.16) until the average energy of the particles drops to a point where ionization energy losses and the radiation losses become equal (Rossi & Greisen, 1941). At this point the shower reaches a maximum and the number of particles gradually diminishes and the cascade dies away.

If the energies of the secondary electron-positron pairs are above the Čerenkov threshold, i.e. they travel with velocities above the velocity of light in the atmosphere, they will make the atmosphere radiate Čerenkov photons. Since many of the electron-positron pairs will be above the threshold, the cascade will also be accompanied by a shower of Čerenkov photons. As the refractive index

The Čerenkov threshold for the atmosphere is 21 MeV at sea level. The Čerenkov angle at sea level is  $\theta_c \sim 1.3^\circ$  where the refractive index is  $n = 1.00029$ .

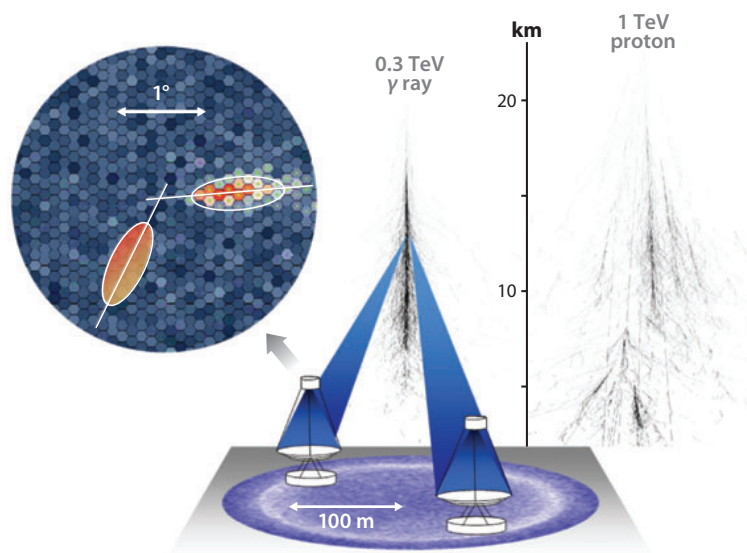


Figure 1.17: An illustration describing the method to detect VHE  $\gamma$ -rays using ground-based optical reflectors. As  $\gamma$ -rays interact with the Earth's atmosphere, they will produce pairs of electron-positron that will make the atmosphere radiate Čerenkov photons. With ground-based telescopes one could detect these photons and reconstruct the direction and energy of the  $\gamma$ -rays. Because the secondary radiation arrives at detector level as a broad but thin disk, the detector can have a large collecting area for the primary  $\gamma$ -ray detection. The formation of an image on the camera of a Čerenkov telescope is also shown. Illustration reproduced from Hinton & Hofmann (2009).

of air is close to unity, the shower will point in the forward direction. From an observer on the ground, the shower of Čerenkov photons will look similar to meteoric trails (Weekes, 2003). If the trails are extrapolated backward they will point back to their origin. A simple reflector equipped with photomultiplier tubes and a fast pulse-counting electronics could in principle detect the cascade (Figure 1.17) and determine the point of origin, energy, and the time of arrival of the  $\gamma$ -ray. Thus a map of VHE  $\gamma$ -rays could be produced, the energy spectrum be determined, and variability of the source could be measured.

The unique feature of atmospheric Čerenkov telescopes (ACT) is that the telescope can have a large collecting area for the detection of the primary  $\gamma$ -rays, beyond of the size of the mirror area itself. This is because the secondary radiation arrives at detector level as a broad but thin disk (Figure 1.17). Since the radius of the Čerenkov light pool on the ground could reach  $\sim 120$  m, the shower detection area is  $\sim 5 \times 10^4$  m<sup>2</sup> (Weekes, 2003), which is huge by astronomical standards. Since at high-energies the fluxes of cosmic  $\gamma$ -ray are low, this large collecting area is a key advan-

tage compared to spaceborne  $\gamma$ -ray detectors.

The main limitation of ACTs is that they can only operate with a low duty cycle, because the photomultiplier tubes are sensitive to stray background lights such as moonlight, starlights, airglow, lightning and meteoric trails, and manmade light sources such as satellite lights and airplanes. By building the telescope away from human habitations, manmade background lights could be avoided. By choosing the observing time, natural background lights such as the Sun, Moon, and lightning could be avoided. To minimize the natural background due to starlight and airglow, it is best to choose the photomultipliers with higher quantum efficiency in the blue light, which is the peak emission of the Čerenkov photons (Weekes, 2003). As a consequence of these limitations, ACTs can only operate  $\sim 1000$  hours per year (Hinton & Hofmann, 2009). This corresponds to a duty cycle of  $\sim 10\%$ . Other limitations of ACTs are their narrow field of view, which is typically  $\sim 5^\circ$  (Hinton & Hofmann, 2009), and their slow slewing capability toward an intended target. The shortest slewing time is  $\sim 80$  s for MAGIC (Albert et al., 2007).

Despite the huge collecting area and high sensitivity, the low duty cycle and the long slewing time make ACTs a limited instrument to observe GRBs. As we have discussed in the previous section, efforts were made by ACTs to observe GRBs but no significant signals were found. On the other hand, for the observations of steady sources such as supernova remnants and active galactic nuclei, ACTs have been proven to be the most powerful instrument to study these objects.

THE FIRST large optical reflector built to observe atmospheric Čerenkov radiation was the *Whipple* 10 m  $\gamma$ -ray telescope installed on Mount Hopkins in southern Arizona in 1968. It was not until 1989 that *Whipple* finally made the first robust detection of VHE  $\gamma$ -rays, the Crab Nebula (Weekes et al., 1989). Since then numerous other Čerenkov telescopes have been built and today  $\sim 80$  VHE  $\gamma$ -ray sources have been identified (Hinton & Hofmann, 2009).

The performance of ACTs can be significantly improved if multiple telescopes are employed so that the shower could be imaged

Over time, the Crab Nebula has become the “standard candle” of high-energy astrophysics. Fluxes of high-energy sources are customarily measured in units of the Crab’s flux.

Instrument	Lat. [°]	Long. [°]	Alt. [m]	Tels.	Area [m <sup>2</sup> ]	Pixels/ camera	FoV [°]	Thresh. [TeV]	Sens. [% Crab]
HESS	-23	16	1800	4	428	960	5	0.1	0.7
VERITAS	32	-111	1275	4	424	499	3.5	0.1	0.7
MAGIC	29	18	2225	2	468	1039	3.5	0.03	1.0
CANGAROO	-31	137	160	3	172	427	4	0.4	15
<i>Whipple</i>	32	-111	2300	1	75	379	2.3	0.3	15

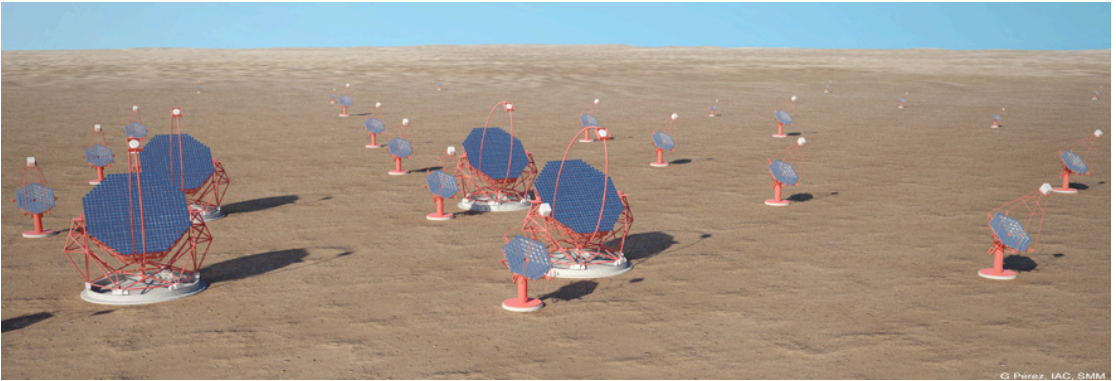
from different viewing angles. The telescope separation must be large enough so that the baseline is long enough for stereoscopic imaging, yet small enough that multiple telescopes can still fit within the Čerenkov light pool (Figure 1.17). This stereo detection could improve angular resolution as well as the rejection of backgrounds due to cosmic-ray induced showers. The availability of multiple images of the same shower allows for a reduction of the energy threshold by using a coincident trigger between telescopes, a determination of shower maximum, and better angular resolution. The advantages of this system is first demonstrated by HEGRA, an Armenian-German-Spanish collaboration and the precursor of the MAGIC collaboration, with five ACTs installed on La Palma, Canary Islands (Konopelko et al., 1999). Most of the current generation of ACTs employ this stereoscopic system (Table 1.1). Telescopes such as HESS<sup>22</sup> can measure the direction of a single  $\gamma$ -rays with resolution of 3–6 arcminutes, an energy resolution of around 15%, and a cosmic-ray rejection factor of 1% or better. This allows the detection of sources as faint as 1% the strength of the Crab Nebula ( $\nu F_\nu \sim 3 \times 10^{-13}$  erg cm<sup>-2</sup> s<sup>-1</sup> at  $\sim 1$  TeV) within 25 hours close to the zenith (Hinton & Hofmann, 2009).

The next generation of atmospheric Čerenkov telescope, the Čerenkov Telescope Array (CTA)<sup>23</sup>, is currently in a preparatory phase. It is foreseen that it becomes operational with full capacity in 2018 (Actis et al., 2011). With CTA (Figure 1.18) an in-depth study of individual sources as well as a wide-field survey can be made. By employing telescopes of different mirror area, CTA is also expected to cover a wide energy band ranging from below 100

Table 1.1: Properties of several currently-active ACTs, compiled from Hinton & Hofmann (2009). The mirror area is the combined area of all telescopes.

<sup>22</sup> High Energy Stereoscopic System, <http://www.mpi-hd.mpg.de/hfm/HESS>.

<sup>23</sup> <http://www.cta-observatory.org>



GeV to more than 10 TeV. A small number of very large telescopes, possibly four, with a 20–30 m diameter will be used to detect  $\gamma$ -rays of energies below 100 GeV. The so-called core energy range between 100 GeV to 10 TeV will be covered by a grid of telescopes with 10–15 m diameter spaced  $\sim 100$  m apart. The high-energy range above 10 TeV may be detected by a large number of small telescopes with diameter of a few meters spaced within the size of the Čerenkov light pool. CTA is planned to be built on two separate sites. A main site to be located in the southern hemisphere covering an area of 3 km<sup>2</sup> will observe the central region of the Milky Way. A complementary northern site covering an area of 1 km<sup>2</sup> will be devoted to extragalactic studies such as the observation of AGNs and GRBs.

Despite the low-duty cycle of CTA, its expected sensitivity is 1% Crab in the wide-field survey mode. The fast-slewing capabilities will be used to observe GRBs in their afterglow phase or even earlier in their prompt phase. In a recent simulation of follow-up GRB observations with CTA, Kakuwa et al. (2011) conclude that CTA could observe  $\sim 0.1$  GRBs per year during the prompt phase and  $\sim 0.5$  GRBs per year during the afterglow phase. It is possible that a fraction of these observed GRBs could also be observed in the TeV regime.

A COMPLEMENTARY method of VHE  $\gamma$ -ray detection can be performed by directly detecting the air-shower particles. This re-

Figure 1.18: An artistic impression of the Čerenkov Telescope Array (CTA), currently in the preparatory phase and is expected to be fully operational in 2018. Credit: G. Perez, SMM, IAC, <http://www.cta-observatory.org>



quires an array of a large number of particle detectors through which some of the particles should pass. This method of detection allows what ACTs could not provide: very high duty cycles (close to 100%) and very wide field of view ( $\sim 2$  sr). These advantages make particle shower arrays a suitable method to observe transient events such as GRBs, despite the fact that the point-source sensitivity of these detectors is almost two orders of magnitude worse than the best ACTs (Hinton & Hofmann, 2009). As mentioned in the previous section, a marginal detection of TeV  $\gamma$ -rays from GRB 970417A was reported by *Milagro* which is a particle air-shower detector array.

The main challenges faced by particle air-shower detectors is the discrimination of  $\gamma$ -ray showers with hadronic showers. One way to solve this problem is to put the detector at a high altitude in order to achieve a lower energy threshold (less than 1 TeV). Another way is to put the detector deep underground and observe high-energy muons which constitute the penetrating component of the shower. Muons from electromagnetic showers could be produced from hadronic photoproduction and the subsequent pion decay, as well as direct pair-production of muons from the interactions of  $\gamma$ -rays with atmospheric nuclei (Stanev, Vankov & Halzen, 1985; Halzen, Kappes & Ó Murchadha, 2009). Although the number of muons produced in an electromagnetic shower is relatively small compared to hadronic showers, a targeted search to a known source could produce a statistically significant excess over background.

In the 1980s there were a number of repeated detections of  $\gamma$ -ray-induced muons. Samorski & Stamm (1983) from the Kiel experiment and Marshak et al. (1985) from the Soudan-1 detector have detected muons from  $\gamma$ -rays with energies of  $10^{15}$  to  $10^{16}$  eV originating from the binary X-ray source Cygnus X-3, while Dzikowski et al. (1983) from the Łódź group detected a muon excess from  $\gamma$ -rays with energies of at least  $10^{16}$  eV from the Crab Nebula. Despite a promising start, interest in this method however appears to waned in the following decades (Weekes, 2003).

The high-altitude water Čerenkov approach pioneered by *Milagro* proved to be more successful, with contributions to the catalog of TeV sources (Abdo et al., 2007) and surveys of the diffuse  $\gamma$ -ray

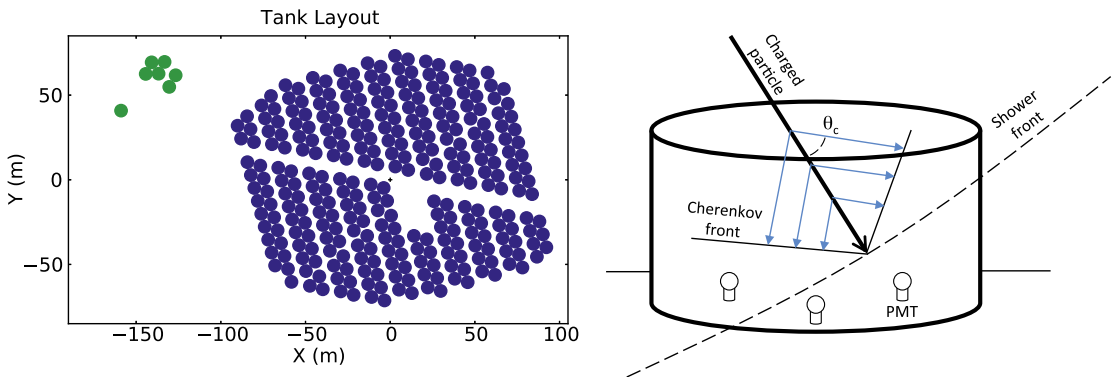


Figure 1.19: HAWC layout and operation principle. *Left:* The relative position of HAWC tanks (blue). The seven tanks at the top left are initial test array. *Right:* The principle of water Čerenkov detection. Particles produced in an air shower arrive at the ground and produce Čerenkov photons as they travel in the water tanks. The photons are emitted at a characteristic angle  $\theta_c$  with respect to the particle track. The photons will be detected by the photomultiplier tubes at the bottom of the tank. Figures reproduced from (Abeysekara et al., 2012).

<sup>24</sup> <http://hawc.umd.edu/>

emission of the Milky Way (Abdo et al., 2008). As we have seen in the previous section, Tibet AS $\gamma$  has also demonstrated the ability to detect TeV  $\gamma$ -rays from the Crab Nebula and several AGNs.

The High-Altitude Water Čerenkov (HAWC) observatory<sup>24</sup> will be the successor of *Milagro* and is expected to be completed in 2014. Located near the peak of Volcán Sierra Negra, Mexico, at an altitude of 4100 m, HAWC will consist of 300 steel tanks of 7.3 m diameter and 4.5 m deep, covering an instrumented area of about 22 000 m<sup>2</sup> (Figure 1.19). Each tank is filled with purified water and will contain four photomultiplier tubes (PMTs): three 20 cm PMTs will be placed near the bottom of each tank looking up to efficiently measure Čerenkov light, and an additional 25 cm PMT with higher quantum efficiency will be placed at the center of each tank. With sensitivity 15 times higher than *Milagro*, HAWC is expected to observe the brightest GRBs with significance of at least  $5\sigma$  (Abeysekara et al., 2012).

#### 1.4 The rise of neutrino telescopes

IDEAS to search for cosmic neutrino sources other than the Sun emerged soon after the discovery of Cowan et al. (1956) was published. In 1960, Kenneth Greisen (Figure 1.20) proposed to build a 3000 tons underground neutrino detector to observe the Crab Nebula. Although he admitted that the rate of cosmic neutrino events will be low, Greisen nevertheless was optimistic that “neu-

trino detection will become one of the tools of both physics and astronomy” (Greisen, 1960). On a more pessimistic note, Frederick Reines noted that “the problem of detecting the cosmic ray neutrino appears to be a most formidable one,” and warns that “the probability of a negative result even with detectors of thousands or possibly hundreds of thousands of gallons of  $\text{CCl}_4$  tends to dissuade experimentalists from making the attempt” (Reines, 1960). In other words, one must possess extreme patience and a readiness to face disappointment to undertake such an effort. Later on Soviet physicist Moisey Markov proposed “to install detectors deep in a lake or in the sea to determine the direction of charged particles with the help of Čerenkov radiation” (Markov, 1960). To isolate the neutrinos from cosmic-ray backgrounds it is necessary to observe neutrinos that have passed through the Earth since “all known particles with the exception of neutrinos are absorbed by scores of kilometres of the substance and thus are entirely screened by the planet” (Markov, 1961).

Even neutrinos with extremely-high energy can pass through a detector and remain undetected. The few that interact could create muons as well as electromagnetic and hadronic secondary particle showers. These charged particles will then produce Čerenkov photons that can be detected by a three-dimensional array of photomultiplier tubes that comprise the detector. In the years following Markov’s proposal, it was realized that the detector must be of at least a cubic kilometer in size.

In view of these requirements, three open and transparent media came into mind: the atmosphere, water, and ice. Instrumenting the atmosphere with omnidirectional detector does not provide sufficient shielding against cosmic-ray backgrounds. Furthermore, it is constantly lit-up by the Sun and the Moon except for only  $\sim 10\%$  of the time (Roberts, 1992).

Water is another option that give several advantages: If the detector is deep enough ( $\sim 2\text{--}4$  km from the surface), sunlight can not penetrate the depth and the layer above it could provide sufficient shielding against the muon background from cosmic rays. Water also has excellent optical qualities, with relatively long absorption and scattering lengths that lead to a good angular resolution in reconstructing the direction of the muon.



Figure 1.20: Kenneth Greisen in 1971, here shown celebrating a balloon flight which was the first to detect pulsed  $\gamma$ -rays with energies greater than 200 MeV from the pulsar in the Crab Nebula. Credit: David Koch, Cornell University.

Water is however contaminated with light from two sources: intermittent light from bioluminescent marine life present at all depths and radioactive decays of  $^{40}\text{K}$  that yields a constant rate of optical noise. There are numerous technological challenges in installing an array of detectors at the bottom of the sea. The photomultipliers must be encased in a transparent yet protective shell able to withstand the very high pressure of sea water (roughly 100 atmospheres per kilometer of depth) and the corrosive salt water. In addition, there must be a method to constantly monitor the positions of the photomultipliers which are changing due to the sea currents.

Ice provides a stable platform to work with and the optical background in the sterile ice is low. The scattering length of ice is however shorter than water leading to a lowering of the angular resolution.

THE FIRST and heroic effort to construct a large-scale neutrino detector was by the DUMAND<sup>25</sup> Collaboration. An early history of DUMAND was excellently written by Roberts (1992) and will be summarised here. The genesis of DUMAND happened in the 1973 International Cosmic Ray Conference in Denver, when a small group of physicists conceived an undersea muon detector to clarify an anomaly observed in the cosmic-ray depth-intensity curves. The anomaly disappeared later-on when other experiments were made, but it was realized that such an undersea muon detector could also be a neutrino detector. Most of the members of the group then agreed to put the idea of building an undersea muon detector into reality. Thus DUMAND was born.

During a series of DUMAND workshops between 1975–80, it was decided to deploy the detector 30 km off the coast of the Island of Hawaii, at a depth of 4.8 km. The ambitious early design was to construct a detector with  $1.22 \text{ km}^3$  volume, consisting of 20 000 photomultiplier tubes arranged in 1261 strings (Figure 1.21). Budgetary and technological constraints forced a constant redesign that considerably reduced the size of the detector after each iteration. The first of such was in 1980 which reduced the number of photomultipliers into 6000 and the volume into  $0.6 \text{ km}^3$ . Another redesign in 1982 reduced again the size of the de-

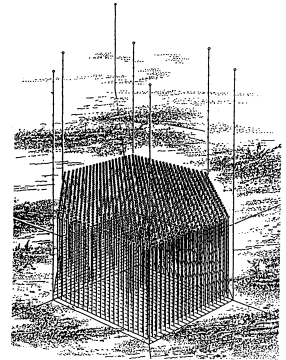
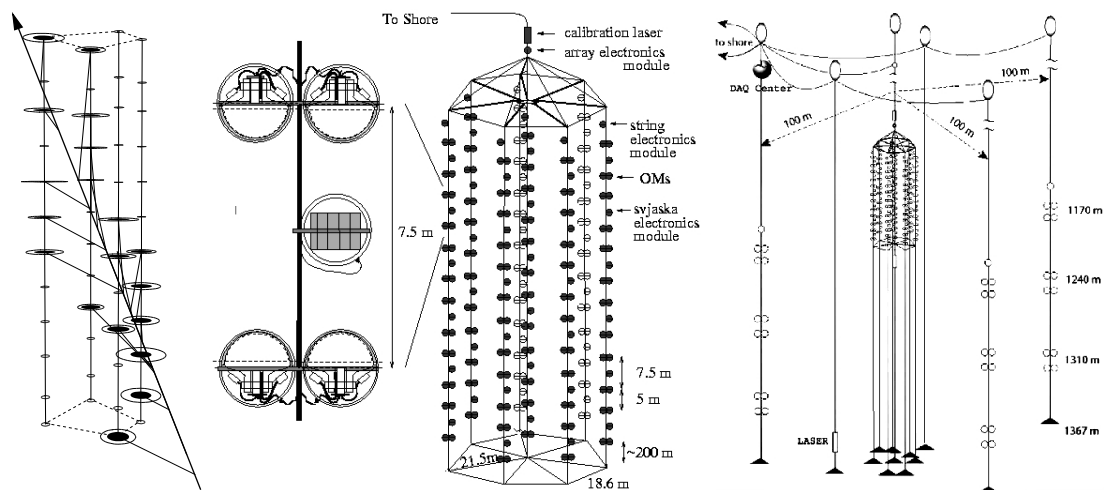


Figure 1.21: The early design of DUMAND: More than 20 000 photomultipliers are arranged in a hexagonal array 800 m on a side. The photomultipliers are tied into strings, each strings consist of 18 photomultipliers. There are 1261 strings, each spaced 50 m apart from each others. Figure reproduced from Roberts (1992).

<sup>25</sup> Deep Underwater Muon And Neutrino Detector, <http://www.phys.hawaii.edu/dmnd/>

It is interesting to note that Frederick Reines is in fact one of the physicists who conceived DUMAND and he was even the one who named it so (Roberts, 1992).



detector into 756 photomultipliers and a volume of  $0.03 \text{ km}^3$ , which also met the same fate with previous designs. The design that was finally accepted was a 9 strings detector, each with 24 photomultipliers, for a total of 216 photomultipliers. The strings were arranged in octagonal configuration, 40 m on a side, with the ninth string placed at the center.

In December 1993 the first string was finally deployed (Grieder, 1995). The deployment was a success. Unfortunately a leak occurred in one of the electrical connectors, resulting in a short circuit and a complete breakdown after 10 hours of operation. Despite a successful recovery of the damaged string one month later, in mid 1996 the US Department of Energy terminated further support and thus the venture to establish the first undersea neutrino telescope met its tragic end.

LAKE Baikal in Siberia, Russia, is the deepest fresh water lake in the world and it is here that the venerable Baikal Neutrino Telescope<sup>26</sup> is located. Several of the Soviet scientists involved in Baikal were previously part of the DUMAND Collaboration, however in the early 1980s they were excluded from the Collaboration because the Reagan administration threatened to cut funding should Soviet collaborators be involved (Roberts, 1992).

Figure 1.22: *Left:* One of the first upgoing muons from a neutrino, observed using the 4 strings of the detector in 1996. Figure reproduced from Balkanov et al. (1997). *Middle:* The design of the NT200 array of the Baikal Neutrino Telescope. Credit: Baikal Neutrino Telescope, <http://baikalweb.jinr.ru/>. *Right:* The upgraded Baikal Telescope NT200+: the old NT200 surrounded by three external long strings at 100 m radius from the center.

<sup>26</sup> <http://baikalweb.jinr.ru/>

The Baikal telescope is located in the southern part of Lake Baikal, 3.6 km from the shore at a depth of 1366 m. The first string of photomultipliers was deployed in 1984 and the first muons were detected soon afterwards (Bezrukov et al., 1984). In 1993 Baikal became the first collaboration to deploy three strings of photomultipliers (three is the minimum number of strings required for full spatial reconstruction of muon tracks) and was also the first to report the detection of a neutrino underwater (Figure 1.22, left). In April 1998, 192 photomultipliers were deployed in an array designated as NT200. The photomultipliers are supported by eight strings attached to an umbrella-like frame on top of them (Figure 1.22, middle). The configuration spans 72 m in height and 43 m in diameter.

Baikal is still taking data and upgrades are still carried out. Between February and April the lake is covered with a thick layer of ice, providing a convenient working platform for the construction and maintenance works. In 2005–07 Baikal was fenced by three distant, longer outer strings containing 36 photomultipliers in total (Figure 1.22, right). With this additional strings, named NT200+, the sensitivity of Baikal was increased by a factor of 4 (Aynutdinov et al., 2006).

The Baikal Collaboration will assure the continuing presence of a neutrino telescope in Lake Baikal with the plan to install the Gigaton Volume Detector (GVD). GVD will consist of strings grouped in clusters of eight (Figure 1.23). Each string will carry 24 photomultipliers spaced uniformly from a depth of 900 m down to about 1250 m depth. It is expected to achieve a detection volume of 0.3–0.8 km<sup>3</sup> for muons above 50 TeV (Avrorin et al., 2011).

EFFORTS to establish a neutrino observatory in ice was pioneered by the AMANDA Collaboration<sup>27</sup> in the late 1990s (Andrés et al., 2001). It was built in the 3 km-thick ice sheet at the Amundsen-Scott South Pole Station. Strings with photomultipliers are deployed into the ice by first drilling holes of 60 cm diameter into the ice with pressurised hot water. The strings are then lowered into the hole which subsequently refreezes.

During the 1993–94 Austral summer, 80 photomultipliers encased in protective vessels and mounted on four strings were low-

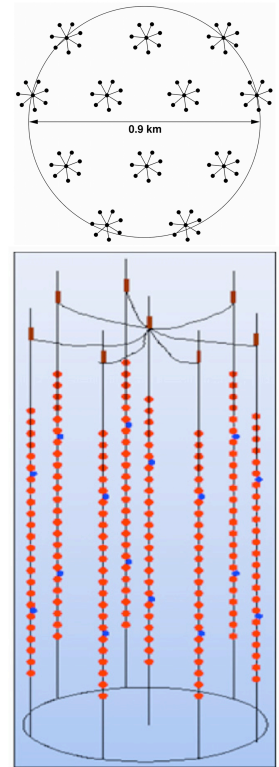


Figure 1.23: The design of the Gigaton Volume Detector (GVD). *Top*: Top view of GVD, showing the arrangement of the 12 clusters. *Bottom*: Schematic view of a cluster, containing 8 strings with 24 photomultipliers in each string. Figure reproduced from Avrorin et al. (2011).

<sup>27</sup> Antarctic Muon and Neutrino Detection Array, <http://amanda.uci.edu/>

ered into depths between 800 and 1000 m. No muon tracks were however observed. The problem was due to air bubbles trapped in the ice that makes the scattering length became as short as 50 cm, making track reconstruction impossible (Askebjerg et al., 1995).

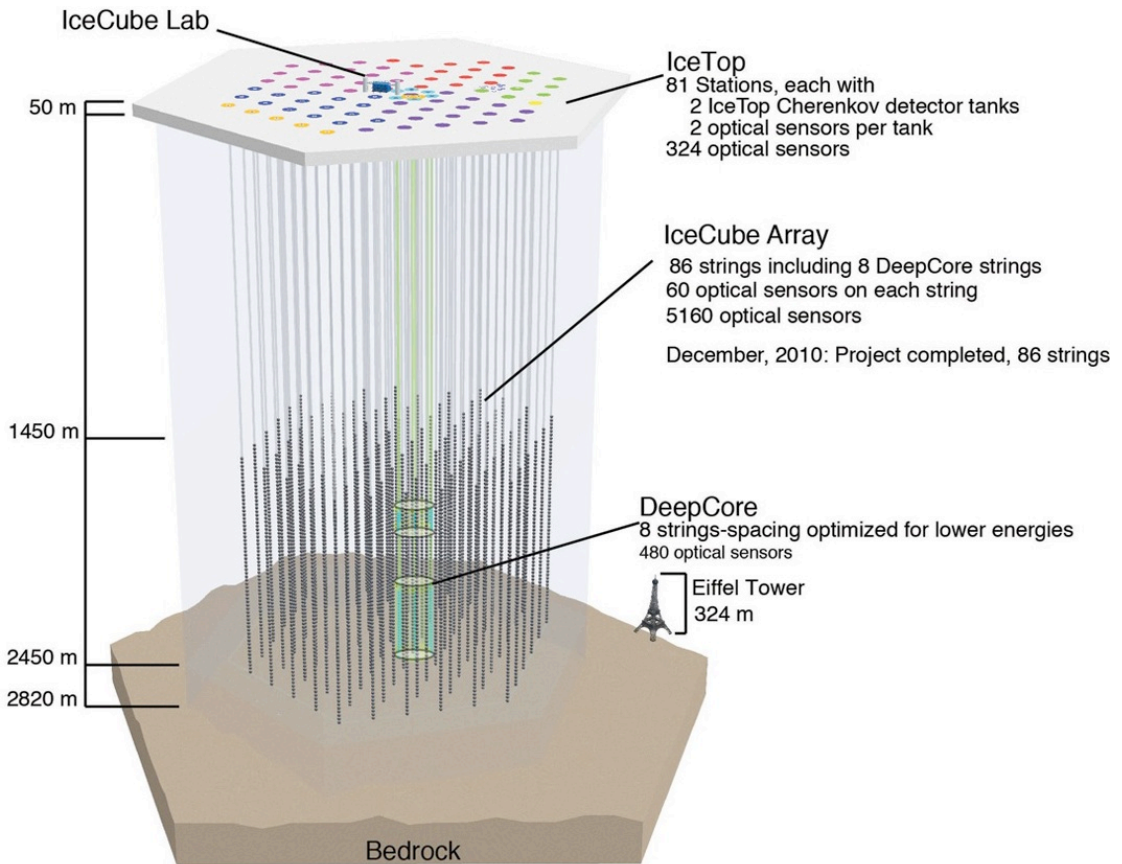
By observing that the scattering tends to decrease with depth it was predicted that the bubbles should disappear at a depth below 1400 m, as the high pressure would cause the bubbles to collapse. The deployment of four additional strings at depths between 1500 and 2000 m during the 1995–96 summer proved this to be the case, as analyses of the data showed that the scattering length is  $\sim 20$  m. While this is still considerably worse than water, nevertheless it is sufficient for track reconstruction (Ahrens et al., 2004). By 2000, AMANDA was completed, with 19 strings and 677 photomultipliers.

IceCube, the successor of AMANDA, began construction in January 2005. It consists of 5160 photomultipliers mounted on 86 strings at depths of 1450–2450 m (Figure 1.24). The 86 strings are spaced 125 m from each other, covering a surface area of roughly 1 km<sup>2</sup>. The photomultipliers are attached to the strings and vertically spaced 17 m from each others. An additional six strings, called DeepCore, are situated in the inner part of IceCube, spaced 72 m apart from each others. DeepCore strings have 50 photomultipliers per string and is installed in the very clear ice at depths between 2100 and 2450 m, where the effective scattering length is at least 50 m. The photomultipliers used in DeepCore strings have an enhanced quantum efficiency. This tighter spacing, better ice quality, and higher efficiency of the photomultipliers give DeepCore a lower energy threshold, possibly as low as 10 GeV (Halzen & Klein, 2010). IceCube was completed in 18 December 2010, when its 86th string was deployed. It is currently the largest neutrino telescope in the world.

DUMAND's efforts to establish an undersea neutrino telescope is continued by European groups. The NESTOR<sup>28</sup>, ANTARES, and NEMO<sup>29</sup> collaborations were established to explore the possibility of constructing an undersea neutrino telescope in the Mediterranean Sea. After an extensive research and development campaigns, the general atmosphere was an optimistic feeling that the

<sup>28</sup> Neutrino Extended Submarine Telescope with Oceanographic Research, <http://www.nestor.org.gr>

<sup>29</sup> Neutrino Mediterranean Observatory, <http://nemoweb.lns.infn.it/>



technological challenges to build an undersea detector has been overcome (ANTARES collaboration, 1997).

The ANTARES neutrino telescope was completed in 2008, proving that such an instrument is now within technological reach. It is currently the largest underwater neutrino telescope in the world and data are routinely taken. The detector is located at a depth of 2475 m, 40 km off Toulon, south of France. It consists of 12 detector strings, 11 strings have 25 floors with 3 photomultipliers and 1 string has 20 floors with 3 photomultipliers. The strings are anchored to the seabed and kept upright by a buoy at the top. Because of the long scattering length of more than 250 m and accurate positioning of all photomultipliers, muon tracks can be re-

Figure 1.24: Schematic view of the IceCube Neutrino Observatory, with 5160 photomultipliers in 86 strings within  $1 \text{ km}^3$  of natural ice. Also shown is the location of AMANDA and DeepCore. The Eiffel Tower is also shown as a size comparison. Credit: IceCube, <http://icecube.wisc.edu/>.



constructed with precision of  $\sim 0.2^\circ$  for muons of energies greater than 1 TeV (Brunner, 2011). More technical details on the ANTARES neutrino telescope and its track reconstruction technique will be described in Chapter 6.

The ambition to build a km-scale undersea neutrino telescope is continued by the KM<sub>3</sub>NeT Collaboration<sup>30</sup>, which was formed by the previously mentioned European groups together with deep-sea technology and marine science groups. The technical design phase has been completed. The first string of KM<sub>3</sub>NeT is expected to be deployed in 2013 and construction is expected to be completed in 2020.

<sup>30</sup> km<sup>3</sup> NEutrino Telescope,  
<http://www.km3net.org/>

### 1.5 *This thesis: Neutrino telescopes as $\gamma$ -ray observatories*

NEUTRINO telescopes can also operate as  $\gamma$ -ray observatories by observing the muon component of photon showers. With the establishment of very large volume neutrino telescopes in the last five years and plans to build larger telescopes, it is timely to revisit this old idea and analyse the now-available data.

The muon component of electromagnetic showers is however produced in small numbers. Thus the sensitivity of neutrino telescopes to  $\gamma$ -rays is weak. Muons induced from cosmic rays interacting with the atmosphere will be the main background. The thick layer of water or ice above the neutrino telescope provide shielding that reduces the background—as we shall see later on from analysis of ANTARES data in Chapter 8—to a small amount.

In principle this method of detection is applicable to any known TeV  $\gamma$ -ray sources, for example supernova remnants in the Galaxy or nearby AGNs. In reality, however, their measured fluxes are in the order of  $\sim 10^{-11}$  TeV<sup>-1</sup> cm<sup>-2</sup> s<sup>-1</sup>, which is much too low to be detected by neutrino telescopes (Halzen, Kappes & Ó Murchadha, 2009). After all, these TeV sources are steady sources and can be studied better with atmospheric Čerenkov telescopes.

GRBs are however an attractive target for neutrino telescopes due to the large flux of  $\gamma$ -rays during a very short time. Despite the fact that most of GRBs are located at cosmological distances, on rare occasions nearby GRB events do occur. The high duty cycle and wide field of view of neutrino telescopes are suitable to

observe nearby GRBs. Should a nearby GRB occur within the field of view of a neutrino telescope, detecting TeV  $\gamma$ -rays allows us to put constraints on the mechanisms of GRB jets and to search for origin of cosmic rays. Moreover, background can be considerably reduced by localizing the search to the specific direction and time of where and when the GRB happened.

Another way that can possibly increase the sensitivity of neutrino telescopes is by looking at the raw data when the GRB happened. Due to the large amount of data, filtering algorithms are employed to record events that are possibly caused by the passage of muons in the detector. However, the analysis of the raw data that coincide with a known GRB event can possibly lower the detection threshold and thus increase the potential to discover  $\gamma$ -ray signals from GRBs. The trigger to save all raw data can be provided by spaceborne  $\gamma$ -ray observatories that routinely detect  $\sim 1$  GRB per day. Together they form the GRB Coordinates Network (GCN)<sup>31</sup>, a system that distribute alert notices to its subscribers whenever any spacecraft that is part of this network detects a potential GRB (Barthelmy et al., 2000). Neutrino telescopes can use these alert information to save all raw data for offline analysis. At present five satellites are part of this network: HETE (Ricker et al., 2003), INTEGRAL<sup>32</sup> (Winkler et al., 2003), *Swift*<sup>33</sup> (Gehrels et al., 2004), *Fermi* (Moiseev, 2008), and AGILE<sup>34</sup> (Cocco et al., 2002).

DESPITE these potentials, detecting the TeV component of GRBs is not without pitfalls. One of the main problems that comes to mind is the attenuation of TeV  $\gamma$ -rays by ambient IR photons in the universe. Along their path from the source to the Earth, TeV  $\gamma$ -rays collide with ambient IR photons and annihilate themselves, creating pairs of electron–positron in the process. The cross section for such process is well-known but measuring the accurate spectral density of cosmic IR photons at all redshifts is still a main problem. This problem will be discussed in more details in Chapter 2 by confronting current attenuation models with observational data. This attenuation will limit possible observations only to the nearest GRBs.

Another crucial problem is to calculate the number of detectable muons produced from a  $\gamma$ -shower. Two production mechanisms

<sup>31</sup> <http://gcn.gsfc.nasa.gov/>

<sup>32</sup> INTERNATIONAL Gamma-Ray Astrophysics Laboratory, <http://www.esa.int/esaMI/Integral/>

<sup>33</sup> <http://heasarc.nasa.gov/docs/swift/swiftsc.html>

<sup>34</sup> Astrorivelatore Gamma a Immagini LEggero (Light-Imaging Gamma Astrophysical Detector), <http://agile.rm.iasf.cnr.it/>

are identified: photoproduction and direct muon-pair production. Both mechanisms have a small cross-section process and different energy dependence. The two mechanisms will be discussed in more detail in Chapter 3 and the necessary formula to determine the number of muon produced from  $\gamma$ -showers will be provided. In calculating the observed muon flux at detector level, the muon energy loss caused by their passage through seawater (Section 3.6) should also be taken into account. Using all this, the number of detectable muons for single GRB events at different redshifts are calculated (Chapter 4), as well as the prospect of detecting signal events from stacked GRB data (Chapter 5).

It is also necessary to quantify the performance of the detector. Part II of this dissertation will cover this question. After a description of the ANTARES neutrino telescope and the reconstruction technique in Chapter 6, simulations of the response of the ANTARES detector to downgoing muons will be described in Chapter 7. The statistical methods employed to analyse the data are presented in Chapter 8 and Chapter 9.

Part III of this dissertation deals with the analysis of the ANTARES data to search for TeV  $\gamma$ -ray signals from potential GRBs. A selection of potential targets among the known GRB events will be presented in Chapter 10, followed by the description of the data analysis in Chapter 11.

The conclusion that can be derived from this first attempt to operate a neutrino telescope as a  $\gamma$ -ray observatory will be discussed in Chapter 12. The overall prospect of this whole venture will also be discussed.

PART I

*Theory*



## 2 *The creation and propagation of TeV photons*

THE HIGH-ENERGY component of the Band function hints at the nonthermal nature of the very high energy  $\gamma$ -ray emission. It has been shown that the extension of the spectrum towards the GeV regime has been established in some GRBs (e.g. Hurley et al. 1994; Abdo et al. 2009), while there are evidences that GRBs also emit TeV  $\gamma$ -rays (e.g. Atkins et al. 2000b; Poirier et al. 2003).

On the theoretical side, the emission of very high energy  $\gamma$ -rays are expected within the standard fireball shock scenario. The emission could occur from the leptonic component of the fireball through the electron inverse Compton mechanism as well as from the hadronic component through proton synchrotron,  $\pi^+$  synchrotron emission and  $\pi^0$  decay.

This Chapter will elaborate on the various mechanisms within the fireball shock scenario that could give emission of TeV  $\gamma$ -rays (Section 2.1) and the calculations employed to describe the spectrum of a GRB with its physical parameters such as its luminosity and its distance (Section 2.2). The annihilation of TeV  $\gamma$ -rays by ambient infrared photons will also be discussed, along with some discussions on how the optical depth is calculated and how this can affect our observations (Section 2.3).

### 2.1 *VHE $\gamma$ -ray productions and the photon spectrum of a GRB*

WITHIN the fireball of a GRB, the emission of VHE  $\gamma$ -rays could occur within external shocks as well as within internal shocks in the prompt phase. In the external shocks, the likely mechanism to emit VHE  $\gamma$ -rays is through electron Inverse Compton (IC) mechanism (Zhang & Mészáros, 2001) as well as through proton synchrotron emission (Vietri, 1997). Synchrotron emission within internal shocks could also produce VHE  $\gamma$ -rays up to 30 GeV (Pe'er & Waxman, 2004). Emission of VHE  $\gamma$ -rays in the prompt phase via the Synchrotron Self-Compton (SSC) mechanism can also be expected (Wang, Dai & Lu, 2001a,b).

These are not an exhaustive list of mechanisms that can occur,

and not all of the processes may be operative at any one time. For example, if the GRB wind is strongly dominated by a Poynting flux,  $\gamma$ -rays are emitted due to dissipation of magnetic energy (Lyutikov & Blandford, 2003) and the internal shock components would be suppressed or absent (Zhang & Mészáros, 2004).

Before we move on to the descriptions of some of these mechanisms, let us first define the following three reference frames and their notation:

1. The comoving frame or the wind rest frame is the frame of the outflowing ejecta expanding with bulk Lorentz factor  $\Gamma$  with respect to the observer and the central engine. Quantities measured in this frame are denoted with primes.
2. The source rest frame is the frame of the GRB central engine which is located at redshift  $z$  from the observer frame.
3. The observer frame is the reference frame of the observer on Earth, which is related to the source rest frame by the redshift correction factor  $(1+z)$ .

### 2.1.1 Synchrotron emission

IT IS NATURAL to think that the nonthermal emission of GRBs is caused by synchrotron emission, i.e. radiation from relativistic electrons gyrating in magnetic fields, if we consider the fireball scenario. In calculating the photon energy spectrum due to synchrotron radiation, we can first assume that the energy of the electrons are distributed according to a broken power-law function (Sari & Esin, 2001; Gupta & Zhang, 2007):

$$\frac{dN_e}{d\epsilon'_e} \propto \begin{cases} \epsilon_e'^{-p}, & \epsilon'_{e,\min} \leq \epsilon'_e \leq \epsilon'_{e,c} \\ \epsilon_e'^{-(p+1)}, & \epsilon'_e < \epsilon'_{e,c} \end{cases} \quad (2.1)$$

in the case of slow cooling, where  $p$  is the spectral index of the distribution function and  $\epsilon'_{e,\min} = \gamma'_{e,\min} m_e c^2$  is the minimum injection energy of the electrons and  $\gamma'_{e,\min}$  is the minimum Lorentz factor of the electron. Energies in the source rest frame and the comoving frame are related as  $\epsilon = \Gamma \epsilon'$ . To keep the energy of the electrons finite, the spectral index must obey  $p > 2$ .  $\epsilon'_{e,c}$  is the

energy of an electron that loses its energy significantly during the dynamic timescale, defined as the cooling energy of the electrons.

If the electrons are cooling fast so that even the electrons with the minimum injection energy have cooled during the dynamical timescale, the electron distribution function is

$$\frac{dN_e}{d\epsilon'_e} \propto \begin{cases} \epsilon_e'^{-2}, & \epsilon_{e,c}' \leq \epsilon_e' \leq \epsilon_{e,\min}' \\ \epsilon_e'^{-(p+1)}, & \epsilon_{e,\min}' < \epsilon_e'. \end{cases} \quad (2.2)$$

If the electrons are accelerated behind a relativistic shock propagating through a uniform cold medium with particle density  $n$ , the energy density  $U$  behind the shock is  $U = 4\Gamma^2 n m_p c^2$ , where  $\Gamma$  is the Lorentz factor of the shocked fluid (Sari, Piran & Narayan, 1998). The energy density is related to the GRB isotropic luminosity  $L_{\text{iso}}$  in the source frame by

$$U = \frac{L_{\text{iso}}}{4\pi r_d^2 \Gamma^2 c'} \quad (2.3)$$

where  $r_d = \delta t \Gamma^2 c$  is the radius of the  $\gamma$ -ray emitting region in the source frame and  $\delta t$  is the time variability of the GRB in the source frame.

If we further assume that a constant fraction  $\epsilon_e$  and  $\epsilon_p$  of the shock energy goes to the electrons and to the protons respectively, we would then obtain the minimum injection energy of the electrons in the comoving frame to be

$$\epsilon_{e,\min}' = \gamma_{e,\min}' m_e c^2 = \frac{\epsilon_e}{\epsilon_p} \left( \frac{p-2}{p-1} \right) m_p c^2 \Gamma. \quad (2.4)$$

We could also assume that the magnetic energy density behind the shock is a constant fraction  $\epsilon_B$  of the shock energy, which would give us a magnetic field strength in the comoving frame (Sari, Piran & Narayan, 1998; Gupta & Zhang, 2007)

$$\begin{aligned} B' &= (32\pi m_p \zeta \epsilon_B n)^{1/2} \Gamma c \\ &\simeq 1.5 \times 10^7 \text{ G } \zeta^{1/2} \epsilon_B^{1/2} L_{\text{iso},51}^{1/2} \Gamma_{100}^{-3} \left( \frac{\delta t}{1 \text{ ms}} \right)^{-1}, \end{aligned} \quad (2.5)$$

where  $\zeta$  is the compression ratio which is  $\zeta \sim 7$  for strong shocks (Gupta & Zhang, 2007),  $L_{\text{iso},51} = L_{\text{iso}} / (10^{51} \text{ erg s}^{-1})$ , and  $\Gamma_{100} = 10^{-2} \Gamma$ .



Within the internal shocks, the total internal energy is distributed among electrons, protons, and the internal magnetic fields, and the relation  $\varepsilon_e + \varepsilon_p + \varepsilon_B = 1$  is maintained.

The electrons will lose their energy through synchrotron radiation as well as inverse-Compton scattering (Panaitescu & Meszaros 1998, see also Subsection 2.1.2). The cooling energy  $\varepsilon'_{e,c}$  that breaks the electron energy spectrum can be calculated by first calculating the cooling time  $t'_{\text{cool}}$ , which is a convolution of the cooling timescales for the synchrotron radiation  $t'_S$  and for the inverse-Compton (IC) scattering  $t'_{IC}$ :

$$\frac{1}{t'_{\text{cool}}} = \frac{1}{t'_S} + \frac{1}{t'_{IC}}. \quad (2.6)$$

If  $U_e$  and  $U_B$  are the energy densities of electrons and magnetic fields respectively, the energy density of the synchrotron radiation is (Sari & Esin, 2001)

$$U_{e,\text{syn}} = \frac{\eta_e U_e}{1 + Y_e} = \frac{\eta_e \varepsilon_e U}{1 + Y_e}, \quad (2.7)$$

here  $\eta_e$  is the radiation efficiency of the electron where  $\eta_e = (\varepsilon'_{e,c}/\varepsilon'_{e,\text{min}})^{2-p}$  for slow cooling and  $\eta_e = 1$  for fast cooling, and

$$Y_e = \frac{L_{e,IC}}{L_{e,S}} = \frac{U_{e,\text{syn}}}{U_B} = \frac{-1 + \sqrt{1 + 4\eta_e \varepsilon_e / \varepsilon_B}}{2} \quad (2.8)$$

is the relative importance between the IC and synchrotron components. Here  $L_{e,IC}$  and  $L_{e,S}$  are the luminosities of the radiations emitted from inverse Compton radiation and synchrotron emission, respectively. The inverse of the cooling time of the electrons is then the ratio between the power and the electron energy (Gupta & Zhang, 2007)

$$\frac{1}{t'_{\text{cool}}} = \frac{4}{3} \sigma_T \gamma'_{e,c} \frac{(U_B + U_{e,\text{syn}})}{m_e c^2} = \frac{4}{3} \sigma_T \gamma'_{e,c} \frac{c \varepsilon_B U}{m_e c^2} (1 + Y_e), \quad (2.9)$$

where  $\sigma_T = 6.625 \times 10^{-25} \text{ cm}^{-2}$  is the Thomson cross section. If the ratio between the cooling timescale  $t'_{\text{cool}}$  and the dynamical timescale  $t'_{\text{dyn}} \simeq \Gamma \delta t$  is denoted as  $f_c = t'_{\text{dyn}}/t'_{\text{cool}}$ , the electron

cooling energy is then (Gupta & Zhang, 2007)

$$\begin{aligned}\epsilon'_{e,c} &= \gamma'_{e,c} m_e c^2 = m_e c^2 \frac{3m_e c^2 f_c}{4\Gamma \delta t \sigma_T c U \epsilon_B (1 + Y_e)} \\ &= 5.3 \text{ keV} \left( \frac{\delta t}{1 \text{ ms}} \right) \left( \frac{f_c}{100} \right) \Gamma_{100}^5 L_{\text{iso},51}^{-1} \epsilon_B^{-1} (1 + Y_e)^{-1}.\end{aligned}\quad (2.10)$$

The cooling energy  $\epsilon'_{e,c}$  and the minimum injection energy  $\epsilon'_{e,\text{min}}$  of the electrons define two break energies in the photon spectrum due to synchrotron spectrum. The cooling break energy in the photon spectrum is (Gupta & Zhang, 2007)

$$\begin{aligned}\epsilon_{\gamma,c,S} &= \Gamma \frac{3h}{4\pi} \left( \frac{\epsilon'_{e,c}}{m_e c^2} \right)^2 \frac{eB'c}{m_e c^2} \\ &\simeq 2.8 \text{ meV} \left( \frac{\delta t}{1 \text{ ms}} \right)^{1/2} \left( \frac{f_c}{100} \right)^2 \xi^{1/2} L_{\text{iso},51}^{-3/2} \epsilon_B^{-3/2} \Gamma_{100}^8 (1 + Y_e)^{-2}.\end{aligned}\quad (2.11)$$

We can see that  $\epsilon_{\gamma,c,S}$  is very sensitive mainly to  $\Gamma$ , allowing it to become very large at the slightest increase of the bulk Lorentz factor.

The break energy in the photon spectrum due to the minimum electron injection energy is then

$$\begin{aligned}\epsilon_{\gamma,\text{min},S} &= \Gamma \frac{3h}{4\pi} \left( \frac{\epsilon'_{e,\text{min}}}{m_e c^2} \right)^2 \frac{eB'c}{m_e c^2} \\ &\simeq 85 \text{ MeV} \left( \frac{\epsilon_e}{\epsilon_p} \right)^2 \left( \frac{\delta t}{1 \text{ ms}} \right)^{-1} (\xi \epsilon_B L_{\text{iso},51})^{1/2} \Gamma_{100}^{-1}.\end{aligned}\quad (2.12)$$

Synchrotron radiation is also accompanied by absorption, in which radiated photons interact with a charge in magnetic fields and are absorbed, transferring its energy to the charge. This is called synchrotron self-absorption (Rybicki & Lightman, 1979). The synchrotron self-absorption (SSA) energy  $\epsilon_{\text{SSA}}$  within internal shocks will constitute the minimum cutoff in the photon energy spectrum, and can be expressed as (Gupta & Zhang, 2007)

$$\epsilon_{\text{SSA}} \simeq 3.57 \text{ keV} \left( \frac{\delta t}{1 \text{ ms}} \right)^{-5/7} L_{\text{iso},51}^{5/14} \Gamma_{100}^{-8/7} (\xi \epsilon_B)^{1/14} \left( \frac{\epsilon_e \eta_e}{1 + Y_e} \right)^{2/7}.\quad (2.13)$$

The photon energy spectrum due to synchrotron radiation for the case of slow-cooling relativistic electrons is then (Sari, Piran & Narayan, 1998; Gupta & Zhang, 2007)

$$\left. \frac{dN_\gamma}{d\epsilon_\gamma} \right|_S \propto \begin{cases} \epsilon_\gamma^{-2/3}, & \epsilon_{\text{SSA}} < \epsilon_\gamma \leq \epsilon_{\gamma, \text{min}, S}, \\ \epsilon_{\gamma, \text{min}, S}^{-2/3+(p+1)/2} \epsilon_\gamma^{-(p+1)/2}, & \epsilon_{\gamma, \text{min}, S} < \epsilon_\gamma \leq \epsilon_{\gamma, c, S}, \\ \epsilon_{\gamma, \text{min}, S}^{-2/3+(p+1)/2} \epsilon_{\gamma, c, S}^{1/2} \epsilon_\gamma^{-(p+2)/2}, & \epsilon_{\gamma, c, S} < \epsilon_\gamma. \end{cases} \quad (2.14)$$

The slow-cooling case happens when  $\epsilon_{e, c, S} > \epsilon_{e, \text{min}, S}$ . For the case of fast-cooling electrons, i.e.  $\epsilon_{e, c, S} < \epsilon_{e, \text{min}, S}$ , the spectrum will be

$$\left. \frac{dN_\gamma}{d\epsilon_\gamma} \right|_S \propto \begin{cases} \epsilon_\gamma^{-2/3}, & \epsilon_{\text{SSA}} < \epsilon_\gamma \leq \epsilon_{\gamma, c, S}, \\ \epsilon_{\gamma, c, S}^{5/6} \epsilon_\gamma^{-3/2}, & \epsilon_{\gamma, c, S} < \epsilon_\gamma \leq \epsilon_{\gamma, \text{min}, S}, \\ \epsilon_{\gamma, c, S}^{5/6} \epsilon_{\gamma, \text{min}, S}^{-3/2+(p+2)/2} \epsilon_\gamma^{-(p+2)/2}, & \epsilon_{\gamma, \text{min}, S} < \epsilon_\gamma. \end{cases} \quad (2.15)$$

As we can see, the photon energy spectrum consists of three segments. The low-energy part of the spectrum will always be the sum of the contribution of the tails of the emission of all electrons and thus is independent of the exact shape of the electron distribution. On the other hand, at the highest energy the most energetic electrons cool rapidly and practically transfer all their energy to the photons. Thus the high-energy part of the spectrum will have a power-law function that depends on the energy spectrum of the electrons.

Within the internal shock scenario, the total energy emitted in synchrotron radiation is  $E_{\text{iso}} \eta_e \epsilon_e (1 + Y_e)$ . Here  $E_{\text{iso}}$  is the total energy emitted by the GRB which is related to the luminosity  $L_{\text{iso}}$  by  $E_{\text{iso}} = L_{\text{iso}} T_{90} / (1 + z)$ , where  $T_{90}$  is the duration of the burst in the observer frame. The normalisation constant  $f_{\gamma, S}$  for the synchrotron photon energy spectrum can then be calculated:

$$f_{\gamma, S} \int_{\epsilon_{\text{SSA}}}^{\epsilon_{\gamma, \text{max}, S}} d\epsilon_\gamma \epsilon_\gamma \left. \frac{dN_\gamma}{d\epsilon_\gamma} \right|_S = E_{\text{iso}} \frac{\eta_e \epsilon_e}{(1 + Y_e)}, \quad (2.16)$$

where the maximum photon energy that can be radiated is (Gupta & Zhang, 2007)

$$\epsilon_{\gamma, \text{max}, S} = 102 \text{ GeV} \left( \frac{\Gamma_{100}}{1 + Y_e} \right). \quad (2.17)$$

### 2.1.2 Electron inverse-Compton scattering

IN INVERSE Compton (IC) scattering, ultrarelativistic electrons scatter low-energy ambient photons so that the photons gain energy at the expense of the electrons which subsequently lose their energy.

Assuming a spatially isotropic and homogeneous distribution of electrons and photons, the spectrum of accelerated photons per unit time per unit energy is (Blumenthal & Gould, 1970; Gupta & Zhang, 2007)

$$\left. \frac{dN}{d\epsilon_\gamma} \right|_{IC} = \int \int d\epsilon_e d\epsilon_\gamma W(\epsilon_e, \epsilon_\gamma, \epsilon_\gamma) \left. \frac{dN_e}{d\epsilon_e} \frac{dN_\gamma}{d\epsilon_\gamma} \right|_S, \quad (2.18)$$

where

$$W(\epsilon_e, \epsilon_\gamma, \epsilon_\gamma) = \frac{8\pi r_e^2 c}{\epsilon_e \eta} \left[ 2q \ln q + (1-q) \left( 1 + 2q + \frac{\eta^2 q^2}{2(1+\eta q)} \right) \right], \quad (2.19)$$

and

$$\eta = \frac{4\epsilon_\gamma \epsilon_e}{(m_e c^2)^2}, \quad q = \frac{\epsilon_\gamma}{\eta(\epsilon_e - \epsilon_\gamma)}. \quad (2.20)$$

Here  $W(\epsilon_e, \epsilon_\gamma, \epsilon_\gamma)$  defined in Equation 2.19 is the scattering probability which already take into account the Klein-Nishina effect. The parameter  $\eta$  in Equation 2.20 defines the domain of the scattering: For  $\eta \ll 1$  the photons take only a small fraction of the electron energy and thus scatterings occur in the Thomson regime, while for  $\eta \gg 1$  the photons take almost all the energy of the electrons in one scattering, which is called the Klein-Nishina regime.

Solving the integrals in Equation 2.18, the photon energy spectrum due to inverse-Compton scattering for slow-cooling of electrons is (Gupta & Zhang, 2007)

$$\left. \frac{dN_\gamma}{d\epsilon_\gamma} \right|_{IC} \propto \begin{cases} \epsilon_\gamma^{-2/3}, & \epsilon_{SSA,IC} < \epsilon_\gamma \leq \epsilon_{\gamma,min,IC}, \\ \epsilon_{\gamma,min,IC}^{-2/3+(p+1)/2} \epsilon_\gamma^{-(p+1)/2}, & \epsilon_{\gamma,min,IC} < \epsilon_\gamma \leq \epsilon_{\gamma,c,IC}, \\ \epsilon_{\gamma,min,IC}^{-2/3+(p+1)/2} \epsilon_{\gamma,c,IC}^{1/2} \epsilon_\gamma^{-(p+2)/2}, & \epsilon_{\gamma,c,IC} < \epsilon_\gamma \leq \epsilon_{\gamma,K}, \\ \epsilon_{\gamma,min,IC}^{-2/3+(p+1)/2} \epsilon_{\gamma,c,IC}^{1/2} \epsilon_{\gamma,K}^{(p-2)/2} \epsilon_\gamma^{-p}, & \epsilon_{\gamma,K} < \epsilon_\gamma \end{cases} \quad (2.21)$$

Here the break energies for the IC emission are related to the break energies for the synchrotron emission by the electron Lorentz factor  $\gamma'_{e,\min}$  and  $\gamma'_{e,c}$ :  $\epsilon_{\text{SSA},IC} = \gamma'^2_{e,\min} \epsilon_{\text{SSA}}$ ,  $\epsilon_{\gamma,\min,IC} = \gamma'^2_{e,\min} \epsilon_{\gamma,\min}$ , and  $\epsilon_{\gamma,c,IC} = \gamma'^2_{e,c} \epsilon_{\gamma,c}$ . In the case of fast cooling, where  $\epsilon_{\gamma,\min,IC} > \epsilon_{\gamma,c,IC}$ , the IC photon spectrum becomes

$$\left. \frac{dN_\gamma}{d\epsilon_\gamma} \right|_{IC} \propto \begin{cases} \epsilon_\gamma^{-2/3}, & \epsilon_{\text{SSA},IC} < \epsilon_\gamma \leq \epsilon_{\gamma,c,IC}, \\ \epsilon_{\gamma,c,IC}^{5/6} \epsilon_\gamma^{-3/2}, & \epsilon_{\gamma,c,IC} < \epsilon_\gamma \leq \epsilon_{\gamma,\min,IC}, \\ \epsilon_{\gamma,c,IC}^{5/6} \epsilon_{\gamma,\min,IC}^{(p-1)/2} \epsilon_\gamma^{-(p+2)/2}, & \epsilon_{\gamma,\min,IC} < \epsilon_\gamma \leq \epsilon_{\gamma,K}, \\ \epsilon_{\gamma,c,IC}^{5/6} \epsilon_{\gamma,\min,IC}^{(p-1)/2} \epsilon_{\gamma,K}^{(p-2)/2} \epsilon_\gamma^{-p}, & \epsilon_{\gamma,K} < \epsilon_\gamma. \end{cases} \quad (2.22)$$

Contrary to Equation 2.21, in Equation 2.22 the relation between the break IC energies with the break synchrotron energies are  $\epsilon_{\text{SSA},IC} = \gamma'^2_{e,c} \epsilon_{\text{SSA}}$ ,  $\epsilon_{\gamma,c,IC} = \gamma'^2_{e,c} \epsilon_{\gamma,c}$ , and  $\epsilon_{\gamma,\min,IC} = \gamma'^2_{e,\min} \epsilon_{\gamma,\min}$ .

In both Equations,  $\epsilon_{\gamma,K}$  is the energy at which IC scattering enters the Klein-Nishina (KN) regime and the KN effect becomes important (Fragile et al., 2004):

$$\epsilon_{\gamma,K} = 2.5 \text{ GeV} \left( \frac{\epsilon_{\gamma,\text{pk}}}{1 \text{ MeV}} \right)^{-1} \Gamma_{100}^2, \quad (2.23)$$

here  $\epsilon_{\gamma,\text{pk}} = \max[\epsilon_{\gamma,c,S}, \epsilon_{\gamma,\min,S}]$  is the energy at which the synchrotron spectrum peaks.

As the electrons scatter the ambient photons, they will lose their energy and cool down to a level in which they could no longer scatter photons. The timescale of the cooling is (Fragile et al., 2004)

$$t'_{IC} = 1.1 \times 10^{-5} \text{ s} \left( \frac{\delta t}{1 \text{ ms}} \right)^2 \Gamma_{100}^6 (\gamma'_e L_{\text{iso},51})^{-1}. \quad (2.24)$$

The cooling of the electrons would naturally impose a cutoff in the resulting IC  $\gamma$ -ray spectrum at maximum photon energy (Fragile et al., 2004)

$$\epsilon_{\gamma,\max,IC} = 852 \left( \frac{\delta t}{1 \text{ ms}} \right)^{1/2} \frac{\Gamma_{100}^{5/2}}{\epsilon_B^{1/4} L_{\text{iso},51}^{1/4}} \text{ GeV}. \quad (2.25)$$

Knowing the maximum energy of the photons emitted by IC scattering, the IC photon spectrum can then be normalized by (Gupta

& Zhang, 2007)

$$f_{\gamma,IC} \int_{\epsilon_{SSA,IC}}^{\epsilon_{\gamma,max,IC}} d\epsilon_{\gamma} \epsilon_{\gamma} \left. \frac{dN_{\gamma}}{d\epsilon_{\gamma}} \right|_{IC} = E_{iso} \frac{\eta_e \mathcal{E}_e Y_e}{(1 + Y_e)}. \quad (2.26)$$

The most likely origin for an extended high-energy afterglow component in GeV energies is from the electron IC scattering in the external shock (Zhang & Mészáros, 2001). In general, the detectability of the IC component is favoured by a high-density external medium, and it is possible that the late GeV emission occurred in GRB 940217 (Hurley et al., 1994) was caused by the IC component.

### 2.1.3 Proton synchrotron emission

THERE are two ways in which relativistic protons lose their energy. The first is by synchrotron emission and the second is—as mentioned in Chapter 1—by interacting with low-energy photons in the ambient medium to produce Delta resonances. The Delta resonances will subsequently decay into photopions ( $\pi^0, \pi^+$ ). The probabilities of  $\pi^0$  and  $\pi^+$  production are 1/3 and 2/3, respectively.  $\pi^0$ s primarily decay into  $\gamma$ -rays, i.e.  $\pi^0 \rightarrow \gamma\gamma$ , while  $\pi^+$ s decay into neutrinos (Equations 1.2–1.3). VHE  $\gamma$ -rays production from photopions will be discussed later-on in the next subsection, however since photopion productions affect proton synchrotron emission, some of the properties related to photopion production will also be discussed here.

The emission of VHE  $\gamma$ -rays from proton synchrotron was originally proposed by Vietri (1997). Vietri argued that cosmic rays of energies  $\sim 10^{20}$  eV could be produced from external shocks, and these protons could emit VHE  $\gamma$ -rays through synchrotron emission as they cross the acceleration region.

To calculate the photon energy spectrum due to proton synchrotron, let us first assume—analogueous to electron synchrotron emission—that the energy of the protons is distributed in a power-law function:

$$\frac{dN_p}{d\epsilon'_p} \propto \begin{cases} \epsilon'^{-p}, & \epsilon'_{p,min} \leq \epsilon'_p \leq \epsilon'_{p,c}, \\ \epsilon'^{-(p+1)}, & \epsilon'_{p,c} < \epsilon'_p, \end{cases} \quad (2.27)$$

here  $\epsilon_{p,\min} = \gamma'_{p,\min} m_p c^2 (p-2)/(p-1)$  is the minimum injection energy of the protons and  $\epsilon'_{p,c}$  is the break energy in the spectrum due to proton cooling. In this calculation only the slow-cooling scenario is considered since protons are poor emitters of photons.

The break energy of the proton spectrum can be calculated by comparing the comoving dynamical timescale  $t'_{\text{dyn}}$  with the cooling timescale  $t'_{\text{cool}}$  of the protons. The inverse of the cooling timescale  $t'_{\text{cool}}$  is equal to

$$\frac{1}{t'_{\text{cool}}} = \frac{1}{t'_S} + \frac{1}{t'_\pi}, \quad (2.28)$$

where  $t'_\pi$  is the photopion cooling timescale which is equal to  $1/t'_\pi \sim f_\pi/t'_{\text{dyn}}$ . Here  $f_\pi$  is the fraction of the proton energy that goes into pion production in  $p\gamma$  interactions. The cooling time due to photopion productions has been calculated by Waxman & Bahcall (1997) for the calculation of neutrino energy spectrum:

$$\begin{aligned} \frac{1}{t'_\pi} &\equiv -\frac{1}{\epsilon_p} \frac{d\epsilon_p}{dt} \\ &= \frac{c}{2\gamma_p'^2} \int_{\epsilon_0}^{\infty} d\epsilon \sigma_\pi(\epsilon) \xi(\epsilon) \epsilon \int_{\epsilon/2\gamma_p'}^{\infty} \frac{d\epsilon_\gamma}{\epsilon_\gamma^2} \frac{dN_\gamma}{d\epsilon_\gamma}, \end{aligned} \quad (2.29)$$

where  $\gamma'_p = \epsilon_p/m_p c^2$ ,  $\sigma_\pi(\epsilon)$  is the cross section for pion production for a photon with energy  $\epsilon$  in the proton rest frame,  $\xi(\epsilon)$  is the average fraction of energy lost to the pion, and  $\epsilon_0 = 0.15$  GeV is the threshold energy. The second integral is over the low-energy spectrum where  $dN_\gamma/d\epsilon_\gamma$  is the photon spectrum of the GRB in the frame of the protons. The solution to this integral is (Waxman & Bahcall, 1997)

$$\frac{1}{t'_\pi} \simeq \frac{U_\gamma}{2\epsilon_{\gamma b}} c \sigma_{p\gamma} \xi_{\text{peak}} \frac{\Delta\epsilon}{\epsilon_{\text{peak}}} \min(1, 2\gamma'_p \epsilon_{\gamma b} / \epsilon_{\text{peak}}), \quad (2.30)$$

where  $\sigma_{p\gamma} \simeq 5 \times 10^{-28}$  cm<sup>-2</sup> is the peak value of the  $p\gamma$  interaction cross section at the Delta resonance and  $\xi_{\text{peak}} \simeq 0.2$  is the value of  $\sigma$  and  $\xi$  at  $\epsilon = \epsilon_{\text{peak}} \sim 0.3$  GeV and  $\Delta\epsilon \simeq 0.2$  GeV is the width of the peak.

Using the relation between photon luminosity and the photon energy density shown in Equation 2.3, the fraction of energy lost

by protons to pions can be calculated:

$$f_{\pi}(\epsilon_p) \simeq \frac{\Gamma \delta t}{t'_{\pi}} = f_0 \begin{cases} \frac{\epsilon_p}{\epsilon_{pb}}, & \epsilon_p \leq \epsilon_{pb}, \\ 1, & \epsilon_p > \epsilon_{pb}, \end{cases} \quad (2.31)$$

where

$$f_0 = 16.2 \frac{L_{\text{iso},51}}{\Gamma_{100}^4} \left( \frac{\epsilon_{\gamma b}}{1 \text{ MeV}} \right)^{-1} \left( \frac{\delta t}{1 \text{ ms}} \right)^{-1}. \quad (2.32)$$

Here  $\epsilon_{\gamma b}$  is the break energy of the Band spectrum. In this formula the spectral indices of the Band function is assumed to be  $(\alpha, \beta) = (1, 2)$ . A more general formula can be found in Gupta & Zhang (2007). The proton break energy in Equation 2.31 is

$$\epsilon_{pb} = 3 \times 10^3 \Gamma_{100}^2 \left( \frac{\epsilon_{\gamma b}}{1 \text{ MeV}} \right)^{-1} \text{ TeV}. \quad (2.33)$$

The break energy  $\epsilon'_{p,c}$  in the proton spectrum due to proton cooling can be calculated by similar mean as in the previous section for the case of electrons:

$$\epsilon'_{p,c} = 6.25 \times 10^4 \text{ TeV} \left( \frac{f_c}{100} \right) \left( \frac{\delta t}{1 \text{ ms}} \right) \left( \frac{\Gamma_{100}^6}{\epsilon_B \Gamma_{100} + 1.51} \right) L_{\text{iso},51}^{-1}. \quad (2.34)$$

The photon energy spectrum from proton synchrotron is then (Gupta & Zhang, 2007)

$$\left. \frac{dN_{\gamma}}{d\epsilon_{\gamma}} \right|_{PS} \propto \begin{cases} \epsilon_{\gamma}^{-(p+1)/2}, & \epsilon_{\gamma, \text{min}, PS} < \epsilon_{\gamma} \leq \epsilon_{\gamma, c, PS}, \\ \epsilon_{\gamma}^{3/2} \epsilon_{\gamma}^{-(p+2)/2}, & \epsilon_{\gamma, c, PS} < \epsilon_{\gamma}, \end{cases} \quad (2.35)$$

here the minimum photon energy from proton synchrotron emission is related to the minimum photon energy from electron synchrotron by (Zhang & Mészáros, 2001)

$$\epsilon_{\gamma, \text{min}, PS} = \epsilon_{\gamma, \text{min}, S} \left( \frac{\epsilon'_{p, \text{min}}}{\epsilon'_{e, \text{min}}} \right)^2 \left( \frac{m_e}{m_p} \right)^3. \quad (2.36)$$

The cooling break energy  $\epsilon_{\gamma, c, PS}$  in the photon spectrum is the characteristic photon energy for proton of energy  $\epsilon'_{p,c}$ . It can be expressed as (Fragile et al., 2004)

$$\epsilon_{\gamma, c, PS} = 0.32 \text{ eV} \left( \frac{\delta t}{1 \text{ ms}} \right) \Gamma_{100}^8 (\epsilon_B L_{\text{iso},51})^{-3/2}. \quad (2.37)$$



To normalize the photon spectrum, the contribution of proton synchrotron relative to  $p\gamma$  interactions must be calculated. Similar to the calculation of  $Y_e$ , we can define (Gupta & Zhang, 2007)

$$Y_p = \frac{L_{p,p\gamma}}{L_{p,PS}} = \frac{\sigma_{p\gamma}}{\sigma_{p,T}} \frac{U_{e,S}}{U_B} = \frac{\sigma_{p\gamma}}{\sigma_{p,T}} Y_e, \quad (2.38)$$

where  $L_{p,p\gamma}$  and  $L_{p,PS}$  are the luminosities emitted in  $p\gamma$  and proton synchrotron respectively and  $\sigma_{p,T} = (m_e/m_p)^2 \sigma_{e,T}$  is the Thomson cross section for protons. Since  $\sigma_{p\gamma}$  is much larger than  $\sigma_{p,T}$ , most of the proton energy will go to the  $p\gamma$  interaction rather than to the proton synchrotron emission. The normalisation of the proton synchrotron photon spectrum is then

$$f_{\gamma,PS} \int_{\epsilon_{\gamma,\min,PS}}^{\epsilon_{\gamma,\max,PS}} d\epsilon_{\gamma} \epsilon_{\gamma} \left. \frac{dN_{\gamma}}{d\epsilon_{\gamma}} \right|_{PS} = E_{\text{iso}} \frac{\eta_p \epsilon_p}{(1 + Y_p)}, \quad (2.39)$$

where  $\eta_p = (\epsilon'_{p,c}/\epsilon'_{p,\min})^{2-\alpha}$ . Proton acceleration is also limited by synchrotron cooling which limits the maximum proton energy that can be achieved by proton acceleration (Totani, 1998a):

$$\epsilon_{p,\max,PS} = 4.26 \times 10^{17} \text{ eV} \left( \frac{\delta t}{1 \text{ ms}} \right)^{1/2} (\epsilon_B L_{\text{iso},51})^{-1/4} \Gamma_{100}^{5/2}, \quad (2.40)$$

which again imposes a cutoff in the resulting photon spectrum:

$$\epsilon_{\gamma,\max,PS} \simeq 5\Gamma_{300} \text{ TeV}. \quad (2.41)$$

Within the external shock scenario, already early-on Gallant & Achterberg (1999) showed the difficulty of accelerating protons in a fireball expanding into the ambient interstellar medium. For ambient Fermi-accelerated particles with initially isotropic momenta, they can gain a factor of  $\sim \Gamma^2$  in energy in the first shock crossing cycle but only a factor of 2 in the subsequent shocks, because the particles do not have time to become isotropic before being overtaken by the shock. This is in contradiction with the assumption of Vietri (1997) that the energy of the accelerated particle is multiplied by a factor of  $\Gamma^2$  after each shock crossing. Under the conditions imposed by Gallant & Achterberg (1999) the maximum energy attainable is well below  $10^{20}$  eV. To solve this problem, Gallant & Achterberg (1999) suggested that the shock expands into an already-relativistic medium such as the pulsar wind bubble.

Pulsars emit relativistic winds which should contain ions. These relativistic ions conserve their post-shock energy throughout a relativistic plasma bubble formed from the shock of the pulsar wind against the ambient gas. The presence of a pulsar wind bubble surrounding the GRB progenitor is plausible in the neutron-star-binary merger scenario.

#### 2.1.4 $\pi^0$ decay

FOR TYPICAL parameters of a GRB, a significant fraction of the energy of the protons accelerated to energies larger than the break energy,  $\epsilon_{pb}^{\text{ob}} \sim 10^4$  TeV, would be lost to pion production.  $\pi^0$ s typically carry  $\xi_{\text{peak}} \sim 20\%$  of the proton's energy and in the center of mass frame the  $\gamma$ -rays produced in the decay will equally share the available energy. The mean pion energy is then  $\langle \epsilon_{\pi^0} \rangle \sim \xi_{\text{peak}} \epsilon_p$ , and as the energy of the neutral pions will be shared equally among the  $\gamma$ -rays, each  $\gamma$ -ray will then have an average energy  $\langle \epsilon_\gamma \rangle \sim 0.5 \xi_{\text{peak}} \epsilon_p$ .

Assuming a photon with energy  $2m_e c^2 \sim 1$  MeV in the comoving frame, then in the source rest frame the energy of the photon is 400 MeV for  $\Gamma = 400$ . This photon could produce photopions by interacting with protons of minimum energy  $\epsilon_p \sim 120$  TeV (Gupta & Zhang, 2007). The minimum energy of the photons produced from  $\pi^0$  is then expected to be  $\langle \epsilon_\gamma \rangle \sim 12$  TeV.

The  $\gamma$ -ray spectrum due to  $\pi^0$  decay can be calculated, using the proton energy spectrum defined in Equation 2.27 and assuming the fraction  $f_\pi/3$  of the protons' energy goes into  $\pi^0$  (Fragile et al., 2004; Gupta & Zhang, 2007):

$$\left. \frac{dN_\gamma}{d\epsilon_\gamma} \right|_{\pi^0} \propto \frac{1}{3} \frac{f_\pi(\epsilon_\gamma)}{2} \begin{cases} \epsilon_\gamma^{2-p}, & \epsilon_\gamma \leq \epsilon_{\gamma,c,\pi^0}, \\ \epsilon_\gamma^{1-p}, & \epsilon_\gamma > \epsilon_{\gamma,c,\pi^0}, \end{cases} \quad (2.42)$$

where the break energy  $\epsilon_{\gamma,c,\pi^0}$  in the  $\gamma$ -ray spectrum due to pion decay is  $\epsilon_{\gamma,c,\pi^0} = 0.5 \xi_{\text{peak}} \epsilon_{pb}$ . The photon flux due to pion decay can then be normalized by

$$f_{\gamma,\pi^0} \int_{\epsilon_{\gamma,\text{min},\pi^0}}^{\epsilon_{\gamma,\text{max},\pi^0}} d\epsilon_\gamma \epsilon_\gamma \left. \frac{dN_\gamma}{d\epsilon_\gamma} \right|_{\pi^0} = \frac{1}{3} E_{\text{iso}} \frac{\eta_p \epsilon_p Y_p}{(1 + Y_p)}, \quad (2.43)$$

where  $\epsilon_{\gamma,\text{min},\pi^0} = 30\Gamma$  GeV and  $\epsilon_{\gamma,\text{max},\pi^0} = 0.1 \epsilon_{p,\text{max},PS}$ .

### 2.1.5 Internal absorption of VHE $\gamma$ -rays by low-energy photons

IN THE INTERNAL shock,  $\gamma$ -rays produced from the mechanisms described in previous subsections will interact with low-energy photons through the  $\gamma\gamma \rightarrow e^+e^-$  process, annihilating themselves and creating electron-positron pairs. A  $\gamma$ -ray with energy  $\epsilon_\gamma$  can produce a pair of electron-positron if it impacts a photon with threshold energy

$$\epsilon_{\text{th}} = \frac{2\epsilon_e^2}{\epsilon_\gamma(1 - \mu_i)}, \quad (2.44)$$

where  $\mu_i = \cos \theta_i$ , and  $\theta_i$  is the angle of impact between the two photons. For head-on collisions, the energy of the photons which will interact with passing  $\gamma$ -ray photons is then

$$\epsilon_{\text{th}} = 0.261 \left( \frac{1 \text{ TeV}}{\epsilon_\gamma} \right) \text{ eV}. \quad (2.45)$$

The cross section of the  $\gamma\gamma$  pair-production for photons of energies  $(\epsilon_1, \epsilon_2)$  is (Breit & Wheeler, 1934; Gould & Schröder, 1967)

$$\begin{aligned} \sigma(\epsilon_1, \epsilon_2, \mu_i) &= \frac{3}{16} \sigma_T (1 - \beta^2) \\ &\times \left[ (3 - \beta^4) \ln \left( \frac{1 + \beta}{1 - \beta} \right) + 2\beta(\beta^2 - 2) \right], \end{aligned} \quad (2.46)$$

in which  $\sigma_T$  is the Thomson cross section and  $\beta$  is the electron-positron velocity in the center-of-mass frame:

$$\beta = \sqrt{1 - \frac{2\epsilon_e^2}{\epsilon_1\epsilon_2(1 - \mu_i)}}. \quad (2.47)$$

The mean free path  $l_{\gamma\gamma}$  of a  $\gamma$ -ray with energy  $\epsilon'_\gamma$  interacting with low-energy photon of energy  $\epsilon'_L$  can then be calculated as (Gould & Schröder, 1967)

$$l_{\gamma\gamma}^{-1}(\epsilon'_\gamma) = \int_{-1}^1 d\mu_i (1 - \mu_i) \int_{\epsilon'_{\text{th}}}^{\infty} d\epsilon'_L \frac{dN_\gamma}{d\epsilon'_L} \sigma_{\gamma\gamma}(\epsilon'_\gamma, \epsilon'_L, \mu_i). \quad (2.48)$$

The low-energy photon spectrum is already known and is observed by BATSE and *Swift* as the Band spectrum. Theoretically this corresponds to the electron synchrotron component (Gupta & Zhang, 2007), which is related to the luminosity by

$$\int_{\epsilon'_{\text{SSA}}}^{\epsilon'_{\text{max},S}} d\epsilon'_L \epsilon'_L \frac{dN_\gamma}{d\epsilon'_L} = U_\gamma. \quad (2.49)$$

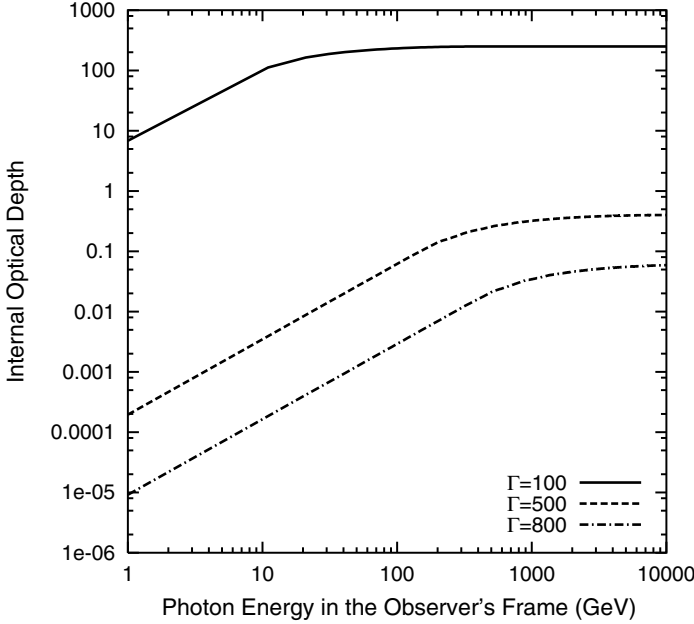


Figure 2.1: A plot of the internal optical depth  $\tau_{\gamma\gamma,\text{int}}$  as a function of energy in the observer frame, for different values of bulk Lorentz factor  $\Gamma$ , while all other values are kept the same. Here  $L_{\text{iso}} = 10^{51} \text{ erg s}^{-1}$ ,  $(\alpha, \beta) = (1, 2.25)$ ,  $\epsilon_{\gamma b} = 500 \text{ keV}$ ,  $\delta = 500 \text{ ms}$ , and  $z = 0.1$ . Figure reproduced from Bhattacharjee & Gupta (2003).

The integral in Equation 2.48 has been analytically solved by Baring & Harding (1997) and Bhattacharjee & Gupta (2003), and the internal optical depth is then

$$\tau_{\gamma\gamma,\text{int}}(\epsilon'_\gamma) = \frac{r_d}{\Gamma} l_{\gamma\gamma}^{-1}(\epsilon'_\gamma). \quad (2.50)$$

An example of how  $\tau_{\gamma\gamma,\text{int}}$  varies with observed  $\gamma$ -ray energy and Lorentz factor  $\Gamma$  is shown in Figure 2.1. As we can see, there is a high dependence of  $\tau_{\gamma\gamma,\text{int}}$  on the Lorentz factor  $\Gamma$ , which in turn will determine how compact the fireball is. The compactness of the fireball can be defined as  $l' = \Delta R n'_\gamma \sigma_T$ , where  $\Delta R = ct_{\text{dyn}}$  is the comoving width and  $n'_\gamma = \epsilon_e L_{\text{iso}} / (4\pi m_e c^3 \Gamma^2 r_d^2)$  is the comoving number density of photons of energy larger than the electron's rest mass,  $\epsilon_\gamma \geq m_e c^2$  (Pe'er & Waxman, 2004). The compactness parameter is thus

$$l' = \frac{\epsilon_e L_{\text{iso}} \sigma_T}{16\pi m_e c^4 \Gamma^5 \Delta t} = 2500 \left( \frac{\delta t}{1 \text{ ms}} \right)^{-1} L_{\text{iso},51} \epsilon_e \Gamma_{100}^{-5}. \quad (2.51)$$

A source with low Lorentz factor will then make the fireball very compact and increase the internal optical depth  $\tau_{\gamma\gamma,\text{int}}$ . According

to Pe'er & Waxman (2004), who performed a fully numerical treatment to the calculation of GRB prompt emissions, a fireball with large compactness parameter (small  $\Gamma$ ),  $l' > 100$ , should present a sharp cutoff in the photon spectra at  $\epsilon_\gamma \sim 10$  MeV. A small-to-moderate compactness parameter (large  $\Gamma$ ),  $l' \lesssim 10$ , would extend the spectra to  $\epsilon_\gamma \sim 10$  GeV. For fireballs with moderate-to-large compactness parameters, we could then expect a rapid expansion of the fireball and the escape of TeV  $\gamma$ -rays from the fireball, which could be observed as the VHE component of the prompt emission.

THE ENERGIES carried by the electron-positron pairs could be converted and re-radiated again as photons through either the  $e^+e^- \rightarrow \gamma\gamma$  process or through synchrotron emission. Calculations by Pe'er & Waxman (2004) and Gupta & Zhang (2007) shows that this feedback process does not contribute significantly to the resulting photon spectrum for fireballs with low compactness parameter. However, in fireballs with high compactness parameter, annihilations of electron-positron pairs will produce an additional peak of the photon spectrum at  $\sim 31.6\Gamma_{100}$  MeV (Pe'er & Waxman, 2004).

IT IS CLEAR then that observing the VHE component of a GRB would provide a strong constraint on the compactness parameter  $l'$  and thus on the fireball Lorentz factor  $\Gamma$ . For fireballs with large compactness, models predict suppression for energies  $\epsilon_\gamma \gtrsim 0.1$  GeV, which is weakly dependent on other parameters. On the other hand, fireballs with small compactness will exhibit emissions above 10 MeV and the low-energy spectrum will depend on  $\epsilon_B$  (Pe'er & Waxman, 2004).

### 2.1.6 *The detectability of each mechanism*

THE RELATIVE importance of the mechanisms described above depends on the equipartition parameters ( $\epsilon_e, \epsilon_p, \epsilon_B$ ). The effects of these parameters' change to each contribution has been investigated by Gupta & Zhang (2007).

The contribution from electron inverse Compton will decrease as  $\epsilon_e$  decreases while  $\epsilon_B$  is kept fixed. A low value of  $\epsilon_e$  and a high value of  $\epsilon_p$ , e.g.  $\epsilon_e/\epsilon_p \sim 10^{-3}$  will increase the proton syn-

chrotron contribution to the resulting  $\gamma$ -ray spectrum as well as the hadronic component. Pe'er & Waxman (2005) found out that the proton synchrotron emission suggested by Totani (1998b,a) to explain the 1 TeV  $\gamma$ -ray emission from GRB 970417a detected by Milagrito (Atkins et al., 2000b) requires a very low fraction of the energy carried by electrons,  $\epsilon_e \sim 10^{-3}$ . This is in contradiction with afterglow observations that imply  $\epsilon_e$  to be nearly in equipartition. The explanation favoured by Pe'er & Waxman (2005) is the photoproduction of pion decay, which could be the case if the magnetic field is well below equipartition,  $\epsilon_B \simeq 10^{-4}$ .

## 2.2 Normalising the observed photon spectrum

THE PHOTON spectrum of a GRB occurring at redshift  $z$  is assumed to be constant during the whole duration of the burst. The burst duration in the observer's frame is  $\Delta t = (1+z)\Delta t_*$ . The photon spectrum  $N(\epsilon)$  of a GRB is approximated by a broken but smoothly connected power law, known as the Band spectrum, which is a model based on BATSE observations of 54 GRB (Band et al., 1993):

$$N(\epsilon) = f_\gamma \left[ H(\epsilon_{\text{bk}} - \epsilon) \exp\left(- (b-a) \frac{\epsilon}{\epsilon_{\text{bk}}}\right) \left(\frac{\epsilon}{\epsilon_{\text{bk}}}\right)^{-(a+1)} + H(\epsilon - \epsilon_{\text{bk}}) \exp(a-b) \left(\frac{\epsilon}{\epsilon_{\text{bk}}}\right)^{-(b+1)} \right] \text{TeV}^{-1} \text{cm}^{-2} \text{s}^{-1}, \quad (2.52)$$

where  $a$  and  $b$  are respectively the spectral indices of the power law in the low- and high-energy regime demarcated by the break energy  $\epsilon_{\text{bk}}$ , and  $f_\gamma$  is the normalisation constant in unit of photons  $\text{TeV}^{-1} \text{cm}^{-2} \text{s}^{-1}$ . The function  $H(x)$  is the Heaviside step function defined as  $H(x) = 1$  for  $x \geq 0$  and  $H(x) = 0$  otherwise.

The break energy is related to the directly measurable peak energy  $\epsilon_{\text{pk}*}$ , which is the energy in which the function  $\nu f_\nu \equiv \epsilon^2 N(\epsilon)$  peaks, through

$$\epsilon_{\text{bk}} = \frac{b-a}{1-a} \epsilon_{\text{pk}}. \quad (2.53)$$

Throughout this dissertation, asterisks will be used to indicate terms in the source's frame, while terms without asterisk are terms in the observer's frame

Here  $\nu$  is the frequency of the  $\gamma$ -ray and is related to energy by  $\epsilon = h\nu$ , where  $h$  is the Planck constant.

BATSE observations extend only to several hundreds keV and in some cases to several MeV, but subsequent observations by later satellites confirmed that the power law extends to several GeV (e.g. Hurley et al. 1994; González et al. 2003; Abdo et al. 2009). Based on this we consider the case that this power law function extends to the TeV regime.

The normalisation constant  $f_\gamma$  is calculated by relating the energy spectrum in Equation 2.52 to its intrinsic isotropic-equivalent bolometric luminosity  $L_{\text{bol}*}^{\text{iso}}$ :

$$L_{\text{bol}*}^{\text{iso}} = 4\pi r_c^2(z)(1+z) \int_0^{\Delta t} dt \int_0^\infty d\epsilon N(\epsilon)\epsilon, \quad (2.54)$$

in which  $r_c(z)$  is its comoving distance at redshift  $z$ :

$$r_c(z) = \int_0^z dz' (1+z') \frac{dl}{dz'}, \quad (2.55)$$

where  $dl/dz$  is the cosmological line element defined as

$$\frac{dl}{dz} = \frac{c}{H_0} \frac{1}{(1+z)\sqrt{\Omega_\Lambda + \Omega_m(1+z)^3}}, \quad (2.56)$$

in which  $c$  is the speed of light,  $H_0 = 72 \text{ km s}^{-1} \text{ Mpc}^{-1}$  is the Hubble constant at the present epoch,  $\Omega_\Lambda = 0.742$  and  $\Omega_m = 0.258$  are respectively the present dark energy and matter density in the universe in units of the critical energy density. The critical energy density is related to the Hubble constant  $H_0$  and the gravitational constant  $G$  by  $3H_0^2/8\pi G$ . It is assumed that the GRB emission spectrum is constant during the whole burst duration. It is also important to note that  $L_{\text{bol}*}^{\text{iso}}$  is an isotropic-equivalent luminosity which assumes that the  $\gamma$ -ray emission is isotropic and is not beamed. The true, beamed, bolometric luminosity  $L_{\text{bol}*}^{\text{true}}$  is related to  $L_{\text{bol}*}^{\text{iso}}$  by

$$L_{\text{bol}*}^{\text{true}} = (1 - \cos \theta_j) L_{\text{bol}*}^{\text{iso}}, \quad (2.57)$$

where  $\theta_j$  is the opening angle of the jet. The average value of the opening angle is  $\langle \theta_j \rangle \sim 6^\circ$  (Ghirlanda et al., 2007), making  $L_{\text{bol}*}^{\text{true}} \sim 0.0055 L_{\text{bol}*}^{\text{iso}}$ .

The integration in Equation 2.54 can be solved by fixing the spectral index  $a$  to the typical value of  $a = 0$  (Preece et al. 2000; Natarajan et al. 2005) and letting the other values as free parameters. Solving the integration this way, we can obtain the photon flux  $f_\gamma$ :

$$f_\gamma = \frac{L_{\text{bol}*}^{\text{iso}}}{4\pi r_c^2(z)\Delta t_* \epsilon_{\text{bk}*}^2 \lambda_{\text{bol}}}, \quad (2.58)$$

in which  $\epsilon_{\text{bk}*} = \epsilon_{\text{bk}}(1+z)$  is the break energy in the source's frame and  $\lambda_{\text{bol}}$  is a bolometric correction to the flux, which is the result of the integration in energy. To avoid a divergent flux in the integration, we do not integrate it to infinite energy but instead cut the spectrum off at maximum energy  $\epsilon_{\text{max}*} = 300$  TeV. At the moment the upper cutoff of the photon spectrum is not known, and in fact the taking of 300 TeV as the limit of the integration is quite arbitrary. Taking this in mind, the value of  $\lambda_{\text{bol}}$  is then

$$\lambda_{\text{bol}} = \begin{cases} -\frac{1}{b} \exp(-b) + \frac{1}{b} + \frac{\exp(-b)}{1-b} \left[ \left( \frac{\epsilon_{\text{max}*}}{\epsilon_{\text{bk}*}} \right)^{1-b} - 1 \right], & \text{for } b \neq 1 \\ -\frac{1}{b} \exp(-b) + \frac{1}{b} + \exp(-b) \ln \left( \frac{\epsilon_{\text{max}*}}{\epsilon_{\text{bk}*}} \right), & \text{for } b = 1. \end{cases} \quad (2.59)$$

Thus given  $(L_{\text{bol}*}^{\text{iso}}, z, b, \Delta t_*, \epsilon_{\text{bk}*})$  as parameters, we can construct the photon spectrum of any GRB.

### 2.3 Photon absorption by ambient infrared photons

ALONG the path from the source to the Earth,  $\gamma$ -ray photons interact with extragalactic background light (EBL) through the  $\gamma\gamma \rightarrow e^+e^-$  process, annihilating themselves and creating pairs of electron-positron. For head-on collisions, the wavelength of EBL photons which will interact with passing TeV photons is then

$$\lambda_{\text{EBL}} \simeq \lambda_e \frac{\epsilon_\gamma}{2m_e c^2} = 1.2 \left( \frac{\epsilon_\gamma}{1 \text{ TeV}} \right) \mu\text{m}, \quad (2.60)$$

in which  $\lambda_e = h/(m_e c)$  is the Compton wavelength for an electron. We can see that TeV photons will interact strongly with infrared (IR) photons in the EBL.



The optical depth  $\tau_{\gamma\gamma}(\epsilon_\gamma, z)$  as a function of observed photon energy  $\epsilon_\gamma$  and redshift  $z$  can be calculated if we also know the differential number density of background photons  $n(\epsilon_{\text{bg}}, z)$  at energy  $\epsilon_{\text{bg}}$  and redshift  $z$ :

$$\begin{aligned} \tau_{\gamma\gamma}(\epsilon_\gamma, z) &= \frac{1}{2} \int_0^z dz \frac{dl}{dz} \int_{-1}^1 d\mu_i (1 - \mu_i) \\ &\times \int_{\epsilon_{\text{min}}}^{\infty} d\epsilon_{\text{bg}} n(\epsilon_{\text{bg}}, z) \sigma[\epsilon_\gamma(1+z), \epsilon_{\text{bg}}, \mu_i], \end{aligned} \quad (2.61)$$

in which  $\epsilon_{\text{min}} = \epsilon_{\text{th}}(1+z)^{-1}$ ,  $\frac{dl}{dz}$  is the cosmological line element defined in Equation 2.56, and  $\sigma(\epsilon_1, \epsilon_2, \mu_i)$  is the cross section of the  $\gamma\gamma$  pair production.

Directly observing EBL photons to obtain their photon distribution is difficult because of contamination issue from the instrument as well as from the zodiacal light. Source discrimination is also another issue: The Cosmic Infrared Background (CIB)—which is extragalactic in nature—must be discriminated from foreground objects such as discrete sources like stars and compact objects within the Galaxy, as well as diffuse sources such as light scattered and emitted by interplanetary dust and emission by interstellar dust (see Hauser & Dwek (2001) for a review on this matter).

There are many approaches in calculating the EBL photon density for all redshifts. One basic approach of doing it is by using “backward models,” in which we start from the existing galaxy count data and then model the luminosity evolution of these galaxies backward in time (e.g. Stecker, Malkan & Scully 2006). Another approach is the “forward evolution,” performed by assuming a set of cosmological theory and semi-analytic merger-tree models of galaxy formation to determine the star formation history of the universe (e.g. Primack, Bullock & Somerville 2005; Gilmore et al. 2009). Yet another approach is to focus on the properties and evolution of starlight, the primary source of CIB emission. This model integrates stellar formation rates and properties over time to obtain the amount of light emitted (e.g. Kneiske et al. 2004; Finke, Razzaque & Dermer 2010).

In this dissertation three different attenuation models are considered: The “best-fit” model of Kneiske et al. (2004), the fidu-

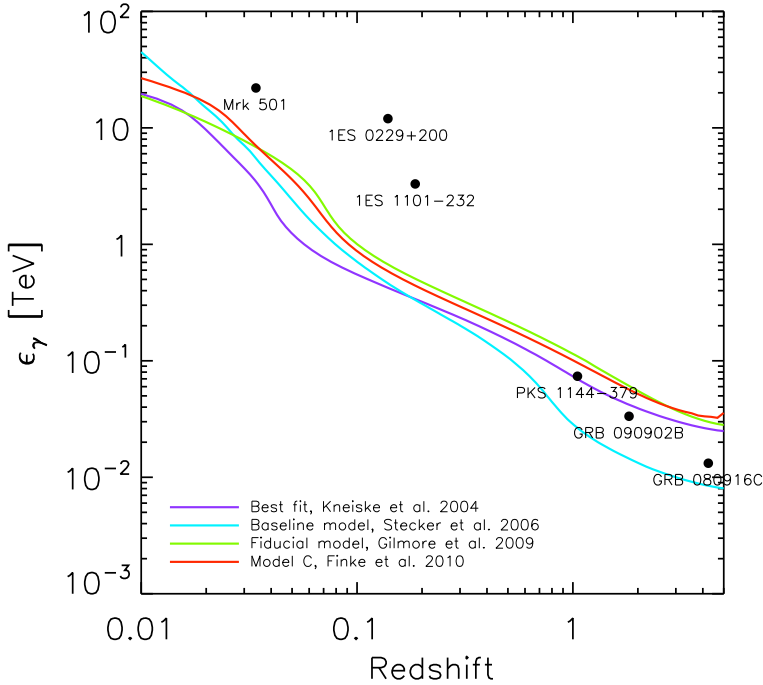


Figure 2.2: A plot of the Fazio-Stecker Relationship (Fazio & Stecker, 1970) for several attenuation models, as a function of redshift. Also shown are the redshifts and highest energy photons  $\epsilon_{\max}$  of various objects observed by Atmospheric Čerenkov Telescopes and *Fermi*-LAT (Finke & Razzaque, 2009; Abdo et al., 2010).

cial model of Gilmore et al. (2009), and the recent “Model C” by Finke, Razzaque & Dermer (2010). These models, along with the Baseline Model of Stecker, Malkan & Scully (2006), are compared in the plot of the Fazio-Stecker relation (Fazio & Stecker, 1970) in Figure 2.2. The Fazio-Stecker relation is the  $(\epsilon_\gamma, z)$  value that gives  $\tau_{\gamma\gamma} = 1$ . This is interpreted to be the redshift at which the flux of photons of a given energy is attenuated by a factor  $e$  and is called the  $\gamma$ -ray horizon. In this plot, for all models except those of Stecker, Malkan & Scully (2006), for redshift  $\lesssim 5$  the universe is optically thin to photons with energy  $\lesssim 20$  GeV. At very low redshifts however, the models are relatively consistent with each other, but the differences start to become apparent at  $z \gtrsim 1$ . The model calculated by Stecker, Malkan & Scully (2006), which predicts higher attenuation at higher redshifts, has in recent times contradicted MAGIC (Albert et al., 2008) and *Fermi* (Abdo et al., 2010) observations and thus can be ruled out with high con-

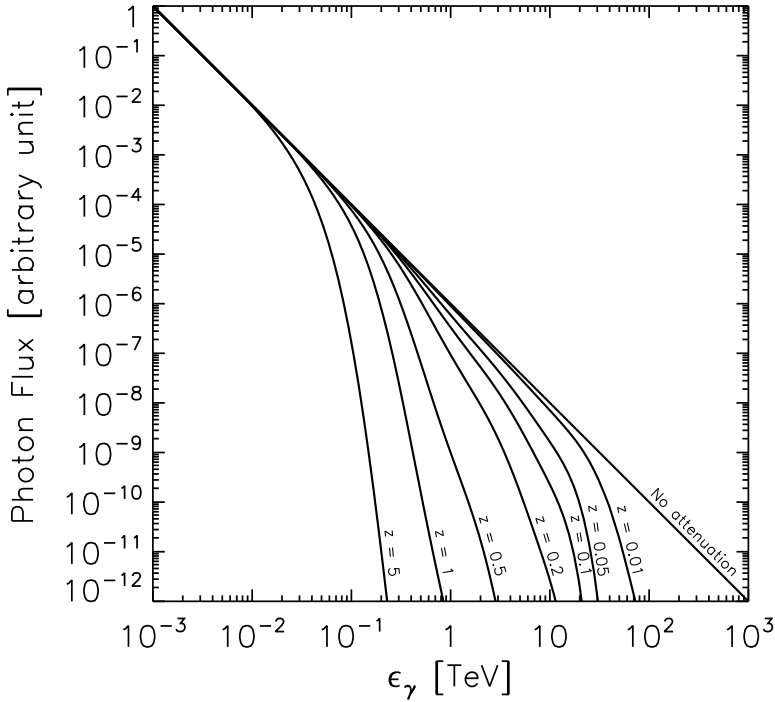


Figure 2.3: An illustration of the effect of attenuation to a photon spectrum. Attenuation is calculated using the model by Finke, Razzaque & Dermer (2010). The shape of the photon spectrum of a source located at redshifts indicated beside each curve is shown. Energies are in the observer frame of reference. The further a source is located, more attenuation is suffered by the highest energy photons. The curve is normalized to unity at  $\epsilon_\gamma = 1$  GeV.

confidence (furthermore, Figure 3 in Abdo et al. (2010) indicate that models by Finke, Razzaque & Dermer (2010); Gilmore et al. (2009); Franceschini, Rodighiero & Vaccari (2008) are the favourable ones) and will not be used in further calculations.

Thus, knowing the attenuation function, we can then estimate the total number of photons emitted from a GRB at redshift  $z$  per unit energy arriving at the top of the Earth's atmosphere per unit area per unit time to be

$$\gamma_0(\epsilon_\gamma) = \gamma(\epsilon_\gamma, t = 0) \equiv f_\gamma \left( \frac{\epsilon_\gamma}{\epsilon_{\text{bk}}} \right)^{-(b+1)} e^{-\tau_{\gamma\gamma}(\epsilon_\gamma, z)}, \quad (2.62)$$

where  $f_\gamma$  is as derived in Equation 2.59 and  $\gamma(\epsilon, t)$  is the notation for the photon flux at slant depth  $t$  in the atmosphere, as introduced in Rossi & Greisen (1941). Slant depth  $t = 0$  means the top of the atmosphere. In this equation only the high-energy part of Equation 2.52 is used, because this is precisely the concern of this

study and henceforth this equation will be the working equation.

To give an illustration of the effect of attenuation to a photon spectrum, the shape of the photon spectrum curve of several sources emitting at different redshifts is showed in Figure 2.3. As a comparison an unattenuated photon spectrum is also shown. The curves are normalized to an arbitrary unit. From the shape of the curves, the more distant the source is located, the more the photon spectrum curve is distorted due to attenuation effects. This imposes a limit on the number of TeV photons that we can observe from a given source.

### 3 *Muon production in the atmosphere*

HIGH-ENERGY  $\gamma$ -rays produce muons when they interact with the Earth's atmosphere. These muons will then traverse down to the bottom of the sea, producing Čerenkov light that can be detected by the detector array. This idea of detecting  $\gamma$ -induced showers by detecting the produced muons has been around for a long time. However, early calculations performed in the 1960s seem to indicate that  $\gamma$ -induced showers are muon-poor, having only less than 10% the muon content of proton-induced showers (Stanev, Gaisser & Halzen, 1985). These calculations are contradicted when muons were firmly detected at underground detectors, coming from the direction of Cygnus X-3 (e.g. Marshak et al. 1985). Despite the low rates and weak signals, these detections raised the interest to build large-area detectors that can detect high-energy muons and thus operate as  $\gamma$ -ray observatory. Stanev, Vankov & Halzen (1985) then identify two channels in which muons can be produced in  $\gamma$  showers: photoproduction and direct muon-pair production. In photoproduction, muons are produced from the (semi)leptonic decay of pions or kaons produced by the interaction of high-energy photons with the atomic nucleus of the atmosphere. This is the most important channel to produce muons in the GeV regime. In direct muon-pair production, muons are created directly via the channel  $\gamma + Z \rightarrow Z + \mu^+ + \mu^-$ , in which  $Z$  is a nucleus of the atmosphere. Whereas muon production through photoproduction dies away with increasing energy, the cross section for muon-pair production increases with energy and thus muon-pair production is the dominant muon producing channel in the TeV regime.

In the following subsections we will describe the necessary formulation to calculate the muon flux generated in gamma-induced showers. For convenience, all units of length are converted into radiation lengths in the air  $\lambda_{\text{rad}}$ , which is taken to be  $37.1 \text{ g cm}^{-2}$ .

### 3.1 The cascade equation: Approximation A

HIGH-ENERGY photons interact with atoms in the atmosphere and initiate electromagnetic showers of particles that will cascade on their way through the atmosphere. Through materialization or Compton collision, pairs of electron-positron will be produced, which in turn emit additional photons by way of bremsstrahlung. At each step the number of particles increases but their average energy decreases (Rossi & Greisen, 1941). Nevertheless these secondary photons can also produce muons that can be detected by the detector array, and thus it is important to calculate the total number of photons produced in such a photon shower.

This problem of counting particles produced in electromagnetic showers can be solved if we consider only radiation phenomena and electron-pair production, which can be described by the asymptotic formula for complete screening. This solution is called Approximation A (Rossi & Greisen, 1941) and allows us to calculate the photon flux at some depth  $t$  in the atmosphere, given the initial photon energy spectrum. If the initial spectrum is in the form of a power law such as  $\gamma(\epsilon) \propto \epsilon^{-(b+1)}$ , then the resulting spectrum at depth  $t$  is (Rossi & Greisen 1941; Halzen, Kappes & Ó Murchadha 2009)

$$\gamma(\epsilon, t) = \gamma(\epsilon, t = 0) \frac{(\sigma_0 + \lambda_1)(\sigma_0 + \lambda_2)}{\lambda_2 - \lambda_1} \times \left[ \frac{\exp(\lambda_1 t)}{\sigma_0 + \lambda_1} - \frac{\exp(\lambda_2 t)}{\sigma_0 + \lambda_2} \right] \quad (3.1)$$

In this Equation as well as the in the following calculations,  $t$  is the slant depth in units of radiation length (in the atmosphere, 1 radiation length equals  $36.62 \text{ g cm}^{-2}$ ),  $\sigma_0 = 7/9$  is the probability per radiation length that an electron pair production will take place (in a case of complete screening), and  $\lambda_{1,2}$  are the scale lengths factor of the shower growth and dissipation in the atmosphere. The formula to calculate  $\lambda_{1,2}$  as a function of spectral index  $b$ , as well as its tabulation, is given in Rossi & Greisen (1941). For  $b < 1$ ,  $\lambda_1$  is positive while for  $b > 1$ ,  $\lambda_1$  is negative. This would mean that in the former case the shower would grow as it penetrates the atmosphere while in the latter it will dissipate. Thus for a general case of an arbitrary value of  $b$ , the photon flux

can be decomposed into its spectrum at the top of the atmosphere and its scale factor at depth  $t$ , i.e

$$\gamma(\epsilon, t) = \gamma_0(\epsilon)\gamma_2(t). \quad (3.2)$$

Particularly important is the case for  $b = 1$  since  $\lambda_1 = 0$  and  $\lambda_2 < 0$ , and this would make the second exponential term in Equation 3.1 essentially zero after several radiation length, making the photon spectrum independent of depth:

$$\gamma(\epsilon_\gamma, t) = 0.567\gamma(\epsilon_\gamma, t = 0), \quad (3.3)$$

where the photon spectrum at the top of the atmosphere  $\gamma(\epsilon_\gamma, t = 0)$  is as described in Equation 2.62.

### 3.2 Pion decay

THE INTERACTION of high-energy photons with atomic nuclei in the atmosphere can produce pions through the reaction  $\gamma + N \rightarrow \pi + X$  followed by leptonic decay of pions into a positive muon and a muon neutrino, or a negative muon and a muon antineutrino:

$$\pi^\pm \rightarrow \mu^\pm + \nu_\mu(\bar{\nu}_\mu), \quad (3.4)$$

with a probability of close to 100% to occur. The formulation to calculate the muon spectrum from this channel has been calculated using the linear cascade equation and assuming a power-law photon spectrum with spectral index  $b = 1$  by Drees, Halzen & Hikasa (1989), and its generalisation to an arbitrary spectral index by Halzen, Kappes & Ó Murchadha (2009).

For the case of  $b \neq 1$ , this paper will closely follow that of Halzen, Kappes & Ó Murchadha (2009), which begins by an ansatz that the differential pion spectrum in the atmosphere can be factorized as

$$\pi(\epsilon, t) = \gamma(\epsilon, t = 0)\pi_2(\epsilon, t), \quad (3.5)$$

in which  $\pi_2(\epsilon, t)$  can be split in two regimes: the high energy regime where pion interactions dominate over decay, and the low

energy regime where pion interactions are neglected. The pion spectrum at high energy is

$$\pi_2^{\text{HE}}(t) = \left[ \frac{\exp(\lambda_1 t) - \exp(-t/\Lambda_\pi)}{(\sigma_0 + \lambda_1)(\lambda_1 + \frac{1}{\Lambda_\pi})} - \frac{\exp(\lambda_2 t) - \exp(-t/\Lambda_\pi)}{(\sigma_0 + \lambda_2)(\lambda_2 + \frac{1}{\Lambda_\pi})} \right] \times \frac{z_{\gamma\pi}}{\lambda_{\gamma A}} \frac{(\sigma_0 + \lambda_1)(\sigma_0 + \lambda_2)}{\lambda_2 - \lambda_1}, \quad (3.6)$$

while the spectrum at low energy is

$$\pi_2^{\text{LE}}(\epsilon, t) = \frac{z_{\gamma\pi}}{\lambda_{\gamma A}} \frac{(\sigma_0 + \lambda_1)(\sigma_0 + \lambda_2)}{\lambda_2 - \lambda_1} \times \int_0^t dt' \left( \frac{t'}{t} \right)^\delta \left[ \frac{\exp(\lambda_1 t')}{\sigma_0 + \lambda_1} - \frac{\exp(\lambda_2 t')}{\sigma_0 + \lambda_2} \right], \quad (3.7)$$

in which  $\delta = t/d_\pi$ , where  $d_\pi$  is the decay length

$$d_\pi = \frac{\epsilon t \cos \theta}{\epsilon_\pi}, \quad (3.8)$$

here  $\epsilon_\pi = 115$  GeV is the pion decay energy constant.

The integral in Equation 3.7 can be expanded into series:

$$\int_0^t dt' \left( \frac{t'}{t} \right)^\delta \frac{\exp(\lambda_i t')}{\sigma_0 + \lambda_i} \approx \frac{1}{\sigma_0 + \lambda_i} \sum_{j=1}^{100} \frac{\lambda_i^{j-1} t^j}{(j-1)!(\delta+j)}. \quad (3.9)$$

In Equation 3.6 and 3.7,

$$\Lambda_\pi = 173 \text{ g cm}^{-2} = 4.66 \text{ radiation lengths} \quad (3.10)$$

is the effective pion interaction length in the atmosphere,

$$z_{\gamma\pi} = \frac{\sigma_{\pi\pi}}{\sigma_{\gamma N}} = \frac{2}{3} \quad (3.11)$$

is the ratio between cross sections  $\sigma_{\gamma \rightarrow \pi}$  and  $\sigma_{\gamma N}$ , and

$$\lambda_{\gamma A} = 446.14 \text{ radiation lengths} \quad (3.12)$$

is the interaction length of photons in atmospheric nuclei. These values are assumed to vary little for different spectral indices and energy.



Due to the unavailability of an analytical expression for both energy regime, taking a smooth transition from one regime to another is difficult. The pion spectrum at all energy regime is then

$$\pi(\epsilon, t) = \gamma(\epsilon, t = 0) \min \left[ \pi_2^{\text{HE}}(t), \pi_2^{\text{LE}}(\epsilon, t) \right]. \quad (3.13)$$

The muon flux at the surface of the Earth can then be obtained by using standard 2-body decay kinematics, assuming no muon decay and energy loss in the atmosphere:

$$\frac{dN_\mu}{d\epsilon_\mu} = \int_0^{t_{\text{max}}} dt B_{\mu\pi} \int_\epsilon^{\epsilon/r} \frac{d\epsilon'}{(1-r)\epsilon'} \frac{\pi(\epsilon', t)}{d\pi(t)}, \quad (3.14)$$

in which  $r = (m_\mu/m_\pi)^2$  and  $B_{\mu\pi} = 1$  is the number of muons produced for each decaying pion. The maximum depth  $t_{\text{max}}$  is determined using

$$t_{\text{max}} = \lambda_{e^+e^-} \ln \left[ \frac{\epsilon_{\text{max}} \langle x \rangle_{\gamma \rightarrow \mu}}{\epsilon} \right], \quad (3.15)$$

where  $\lambda_{e^+e^-} = 9/7$  is the electromagnetic cascade length and  $\langle x \rangle_{\gamma \rightarrow \mu} = 0.25$  is the fraction of  $\gamma$ -ray energy that goes into the final muon for the case of pion decays.

For the special case of  $b = 1$ , we calculate the muon spectrum using the formulation by Drees, Halzen & Hikasa (1989):

$$\frac{dN_\mu}{d\epsilon_\mu} = \gamma(\epsilon_\mu, t = 0) \frac{\Lambda_\pi}{\lambda_{\gamma A}} z_{\gamma\pi} \frac{L_\gamma}{1 + (L_\gamma/H_\gamma)\epsilon_\mu \epsilon_\pi \cos \theta'} \quad (3.16)$$

where

$$L_\gamma = \frac{1-r^2}{2(1-r)} \frac{t_{\text{max}}}{\Lambda_\pi}, \quad H_\gamma = \frac{1-r^3}{3(1-r)} \left[ 1 + \ln \frac{t_{\text{max}}}{\Lambda_\pi} \right]. \quad (3.17)$$

The constant terms ( $\Lambda_\pi, z_{\gamma\pi}, \lambda_{\gamma A}$ ) in the Equations above are the same as in Equations 3.10–3.12

### 3.3 Direct muon-pair production

THE FEYNMAN diagram for direct lepton-pair production  $\gamma + N \rightarrow N + l^+ + l^-$  is pictured in Figure 3.1. This reaction occurs when an impacting photon interacts with a photon within the

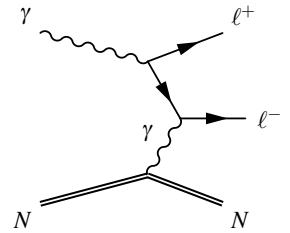


Figure 3.1: Feynman diagram for lepton-pair production in the presence of a nucleus  $N$

electric field of a nucleus, producing a pair of leptons. The second photon is necessary to maintain the conservation of 4-momentum, transferring the required momentum from the nucleus. Lepton-pair production is related to bremsstrahlung by a substitution rule and the calculation of the cross section can be done if we know how to calculate bremsstrahlung by electrons (Tsai, 1974). For the interaction of a photon with nuclear electrons to produce muon-pair, the photon energy threshold must then be

$$\epsilon_{\text{th}} = \frac{2m_{\mu}}{m_e} (m_{\mu} + m_e) \simeq 43.9 \text{ GeV}, \quad (3.18)$$

where  $m_e$  is the electron mass and  $m_{\mu}$  is the muon mass.

To calculate an approximate formula of muon-pair production, what is usually done is taking the Bethe-Heitler result for electron-pair production (Bethe & Heitler, 1934) and substitute the electron mass with that of muon. This generalization would not be correct, however, because the atomic form factor involved in the calculation must be integrated over the transferred momentum in which the upper limit is approximately the mass of the lepton involved (Halzen, Kappes & Ó Murchadha, 2009).

We will now discuss the necessary calculations to obtain the accurate formula for the cross section of muon-pair production.

The impacting photon energy will be fully shared by the resulting muon-pair according to

$$\epsilon_{\gamma} = \epsilon_{\mu}^{+} + \epsilon_{\mu}^{-}, \quad (3.19)$$

or in terms of fraction of photon energy:

$$x_{+} = \frac{\epsilon_{\mu}^{+}}{\epsilon_{\gamma}}, \quad x_{-} = \frac{\epsilon_{\mu}^{-}}{\epsilon_{\gamma}}, \quad x_{+} + x_{-} = 1. \quad (3.20)$$

To take into account the atomic and nuclear form factors, we need the differential cross section equation as a function of the momentum transfer. Since this work concerns very high-energy photons, we can use the ultrarelativistic approximation written as (Bethe & Heitler, 1934)

$$\frac{d\sigma}{dx_{+}} = 4\alpha Z^2 \left( r_0 \frac{m_e}{m_{\mu}} \right)^2 \left[ (x_{+}^2 + x_{-}^2) \Phi_1(\delta) + \frac{2}{3} x_{+} x_{-} \Phi_2(\delta) \right],$$

$$(3.21)$$

where  $\alpha$  is the fine-structure constant,  $Z$  is the charge of the nucleus—for the Earth's atmosphere  $Z = 7.37$  (Rossi, 1952),  $r_0$  is the classical electron radius, and  $\delta$  is the screening parameter equal to the necessary minimum momentum transfer from the nucleus:

$$\delta \simeq q_{\min} = \frac{m_{\mu}^2}{2\epsilon_{\gamma}x_+x_-}. \quad (3.22)$$

The functions  $\Phi_{1,2}$  are integrals of form factors over transferred momentum  $q$ . Whereas electron-pair production involves only the atomic form factors, in the case of muon-pair production it is also necessary to consider the nuclear form factors since the momentum involved is much larger than the inverse square of the atomic radius (Tsai, 1974). The functions  $\Phi_{1,2}$  would then be

$$\Phi_{1,2}(\delta) = \int_{\delta}^{q_{\max}} \frac{dq}{q^3} [F_n(q) - F_a(q)]^2 \psi_{1,2}(q, \delta), \quad (3.23)$$

where  $F_n$  and  $F_a$  are respectively the nuclear and atomic form factors and  $\psi_{1,2}$  are the wave functions of the nucleus.

Equation 3.23 has been solved with several assumptions. We take the solution of Kelner, Kokoulin & Petrukhin (1995) in which a single function  $\Phi(\delta) = \Phi_1 = \Phi_2$  is used for the case of complete screening. By taking the effects of complete screening into account we consider the fact that atoms are essentially neutral at large distance. This is because the electric charge of the nucleus get "screened" by the atomic electrons, i.e. their field are canceled by opposite electric charge of the atomic electrons, reducing the effective charge according to distance and thus limiting the maximum distance at which photons can still interact.

The contribution from inelastic form factors is also considered. This must also be taken into account since muon bremsstrahlung occurs on electrons bound in the atom and not on free electrons (Kelner, Kokoulin & Petrukhin, 1995).

Having considered both elastic and inelastic form factors, Equation 3.21 then becomes

$$\frac{d\sigma}{dx}(x, \epsilon_{\gamma}) = 4\alpha Z^2 \left(r_0 \frac{m_e}{m_{\mu}}\right)^2 \left[1 - \frac{4}{3}x(1-x)\right] \left[\Phi_{\text{el}}(\delta) + \frac{1}{Z}\Phi_{\text{in}}(\delta)\right].$$

$$(3.24)$$

The elastic contribution  $\Phi_{\text{el}}(\delta)$  is in the form of

$$\Phi_{\text{el}}(\delta) = \ln \left[ \Phi_{\infty} \frac{1 + (D_n e^{1/2} - 2)\delta/m_{\mu}}{1 + BZ^{-1/3} e^{1/2} \delta/m_e} \right], \quad (3.25)$$

where

$$\Phi_{\infty} = \frac{BZ^{-1/3} m_{\mu}}{D_n m_e}, \quad \delta = \frac{m_{\mu}^2}{2\epsilon_{\gamma} x(1-x)}, \quad e^{1/2} = 1.6187 \dots$$

$$\begin{array}{lll} B = 202.4 & D_n = 1.49 & \text{for Hydrogen, and} \\ B = 183 & D_n = 1.54A^{0.27} & \text{otherwise.} \end{array} \quad (3.26)$$

Here  $A$  is the atomic number of the nuclei involved. For our case of the Earth's atmosphere,  $A = 14.78$  (Rossi, 1952).

The inelastic contribution  $\Phi_{\text{in}}(\delta)$  is

$$\Phi_{\text{in}} = \ln \left[ \frac{m_{\mu}/\delta}{m_{\mu}\delta/m_e^2 + e^{1/2}} \right] - \ln \left[ 1 + \frac{1}{B'Z^{-2/3} e^{1/2} \delta/m_e} \right], \quad (3.27)$$

where  $B' = 1429$ . We can see that the differential cross section is symmetric in  $x_+$  and  $x_-$ , thus we can write

$$x_+ x_- = x - x^2,$$

where  $x$  substitutes either  $x_+$  or  $x_-$  and the other becomes  $(1-x)$ .

In Figure 3.2 Equation 3.24 for various values of photon energy  $\epsilon_{\gamma}$  is shown. We can see that due to the "screening" effect the cross section does not increase indefinitely but saturates as  $\epsilon_{\gamma}$  increases. I integrate the differential cross section over  $x$  to obtain the total cross section as a function of photon energy and the result is shown in Figure 3.3. In the figure it is shown that saturation of the cross section occurs when the impacting photon energy  $\epsilon_{\gamma} \approx 10$  TeV.

Using the cascade equation, we can calculate the muon-pair flux at sea level:

$$\frac{dN_{\mu}}{d\epsilon_{\mu}} = 2\lambda_{\text{rad}} \frac{N_A}{A} \gamma_0(\epsilon_{\mu}) \int_0^1 dx x^b \frac{d\sigma}{dx} \left( x, \frac{\epsilon_{\mu}}{x} \right) \int_0^{t_{\text{max}}} dt \gamma_2(t, b), \quad (3.28)$$

where  $N_A$  is the Avogadro number.

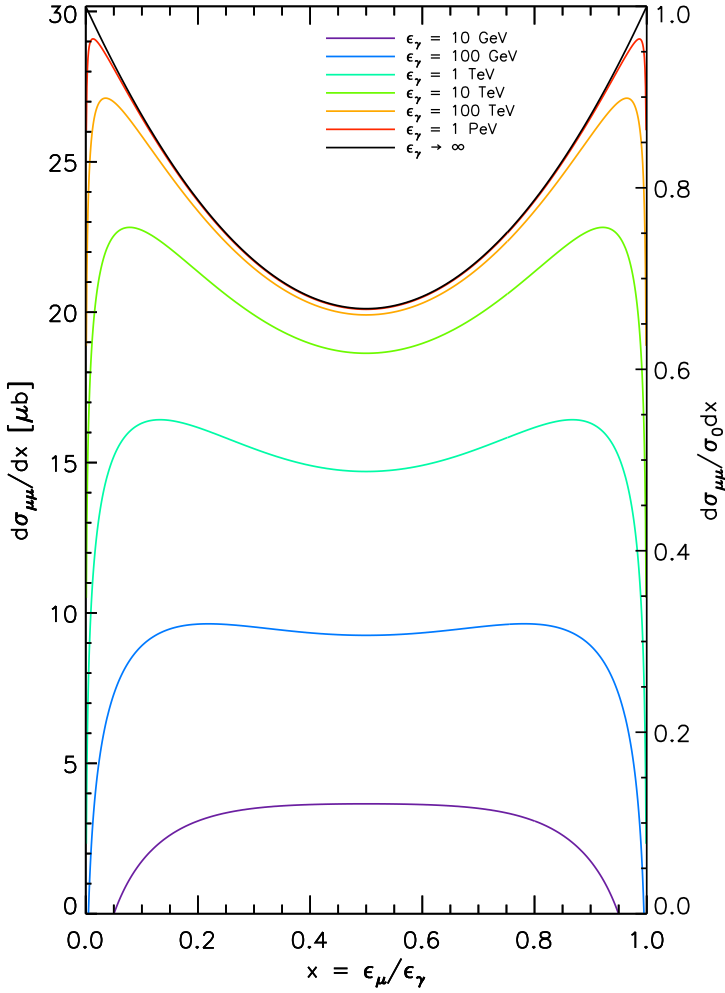


Figure 3.2: Differential cross section of muon-pair production (Equation 3.24) in the Earth's atmosphere for various values of impacting photon energy  $\epsilon_\gamma$ , as a function of  $x = \epsilon_\mu / \epsilon_\gamma$  which is the ratio between the resulting muon energy and the photon energy. The atomic and mass number of the atmosphere is taken to be  $(A, Z) = (14.78, 7.37)$ .

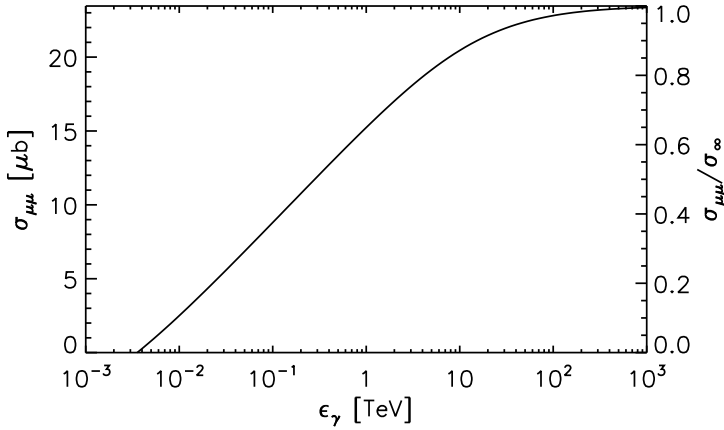


Figure 3.3: Total cross section of the process  $\gamma \rightarrow \mu^+ \mu^-$  in the Earth's atmosphere as a function of impacting photon energy  $\epsilon_\gamma$ . Due to screening effect which limits the maximum distance in which high-energy photons can still interact with the nucleus, the cross section saturates for impacting photon energy  $\epsilon_\gamma \gtrsim 10$  TeV.

### 3.4 Other channels of muon production

A  $\gamma$ -SHOWER can also produce kaons and the hadronic decay of kaons can produce a positive muon and a muon neutrino or a negative muon and a muon antineutrino:

$$K^\pm \rightarrow \mu^\pm + \nu_\mu (\bar{\nu}_\mu). \quad (3.29)$$

This reaction has only  $\sim 63.5\%$  chance of occurring (Gaisser, 1990). Furthermore, results from Halzen, Kappes & Ó Murchadha (2009) showed that the muon yield from kaon decays and other channels involving kaons can be neglected.

Positrons produced in  $\gamma$ -showers can also produce pairs of muon by interaction with an atomic electron through reaction  $e^+ e^- \rightarrow \mu^+ + \mu^-$ . However, cross section for this reaction is very small and peaked at  $\sim 61$  GeV and falls rapidly with energy and is essentially zero for  $\epsilon_\mu \gtrsim 700$  GeV (Halzen, Kappes & Ó Murchadha, 2009). Thus this production channel can also be neglected altogether.

### 3.5 Cosmic ray-induced muon background

IN ORDER to calculate the detection significance of photon-induced muons, we need to know the amount of the background in our observation. In our case of photon-induced muons detection, the

background consists of cosmic-ray induced muons. These muons are produced mainly through leptonic decay of pions, which is essentially the same channel discussed in Section 3.2. Leptonic decay of Kaons is also another channel of muon production albeit it is less important.

The energy spectrum of cosmic-ray induced muons, as a function energy and zenith distance, has already been parametrized by Gaisser (1990) as

$$\frac{dN_\mu}{d\epsilon_\mu} \approx 0.14\epsilon_\mu^{-2.7} \left[ \frac{1}{1 + \frac{1.1\epsilon_\mu \cos\theta}{115\text{GeV}}} + \frac{0.054}{1 + \frac{1.1\epsilon_\mu \cos\theta}{850\text{GeV}}} \right] \text{GeV}^{-1} \text{cm}^{-2} \text{s}^{-1} \text{sr}^{-1}. \quad (3.30)$$

This parametrization overestimates the actual measured muon flux for energies below 10 GeV because at that energy regime muon decay and muon energy loss become important factors (see Figure 6.1 in Gaisser 1990). However, this will not be our concern since this is far below the energy regime we are interested in, and Equation 3.30 fits perfectly well for high-energy regime. This equation estimates the muon flux at sea level, thus if we want to estimate the muon background at detector we have to apply the appropriate muon energy loss formula for seawater. We will discuss this later in Section 3.6.

### 3.6 Passage of muons through seawater

UPON traversing a medium, energetic muons lose their energy through ionization and radiative processes. This energy loss can be treated by taking the standard formula to calculate the average energy loss (Barrett et al., 1952)

$$-\frac{d\epsilon}{dx} = a(\epsilon) + b(\epsilon)\epsilon, \quad (3.31)$$

in which  $a(\epsilon)$  is the ionization contribution of the energy loss, while  $b(\epsilon) = b_p(\epsilon) + b_b(\epsilon) + b_n(\epsilon)$  is the radiative contribution consisting of  $e^+e^-$  pair production ( $b_p$ ), bremsstrahlung ( $b_b$ ), and photonuclear interaction  $b_n$ .

Here I take the approach of Klimushin, Bugaev & Sokalski (2001) by splitting  $a(\epsilon)$  into two separate processes,  $a(\epsilon) = a_c(\epsilon) + a_e(\epsilon)$ , where  $a_c$  is the classical ionization process sufficiently described by the ‘‘Bethe’’ equation (Nakamura & Particle Data Group, 2010) and  $a_e$  is the  $e$  diagrams for bremsstrahlung treated as part of an ionization process.  $a_c$  can thus be approximated by

$$a_c(\epsilon) = a_{c_0} + a_{c_1} \ln \left( \frac{W_{\max}}{m_\mu} \right), \quad W_{\max} = \frac{\epsilon}{1 + \frac{m_\mu^2}{2m_e\epsilon}}, \quad (3.32)$$

in which  $W_{\max}$  is the maximum transferable energy to the electron and  $m_{\mu,e}$  are respectively the masses of muon and electron. The coefficients, in units of ( $10^{-6}$  TeV cm<sup>2</sup> g<sup>-1</sup>), are  $(a_{c_0}, a_{c_1}) = (2.106, 0.0950)$  for  $\epsilon \leq 45$  GeV and  $(a_{c_0}, a_{c_1}) = (2.163, 0.0853)$  for  $\epsilon > 45$  GeV. For  $a_e$ , a polynomial approximation is used:

$$a_e(\epsilon) = 3.54 + 3.785 \ln \epsilon + 1.15 \ln^2 \epsilon + 0.0615 \ln^3 \epsilon \quad 10^{-9} \text{ TeV cm}^2 \text{ g}^{-1}, \quad (3.33)$$

where  $\epsilon$  is in units of GeV.

The terms of  $b$  are parametrized in a polynomial function in the form

$$b_i(\epsilon) = \sum_{j=0}^4 b_{ij} \ln^j \epsilon, \quad \text{where } i = p, b, n. \quad (3.34)$$

Here the energy input  $\epsilon$  is also in units of GeV. The values of coefficients for  $b_{ij}$  is already calculated by Klimushin, Bugaev & Sokalski (2001) and is tabulated in their Table II. These formulations of energy loss are expected to still valid for  $\epsilon_{\text{detector}} = 30 \text{ GeV} - 5 \text{ TeV}$  and slant depth (3 – 12) km with errors up to  $\pm(6 - 8)\%$  (Klimushin, Bugaev & Sokalski, 2001).

Taking into account these contributions, the total muon energy loss in seawater as a function of energy is shown in Figure 3.4. In this figure we can see that at high energies radiative processes are more important than ionization. The critical energy at which the energy loss from ionization and radiative processes are equal can be calculated by solving  $\epsilon_{\mu c} = a(\epsilon_{\mu c})/b(\epsilon_{\mu c})$ . In the case of seawater this is  $\epsilon_{\mu c} \sim 590$  GeV. Below this critical energy the dominant process is ionization while above this limit the radiative processes starts to dominate.



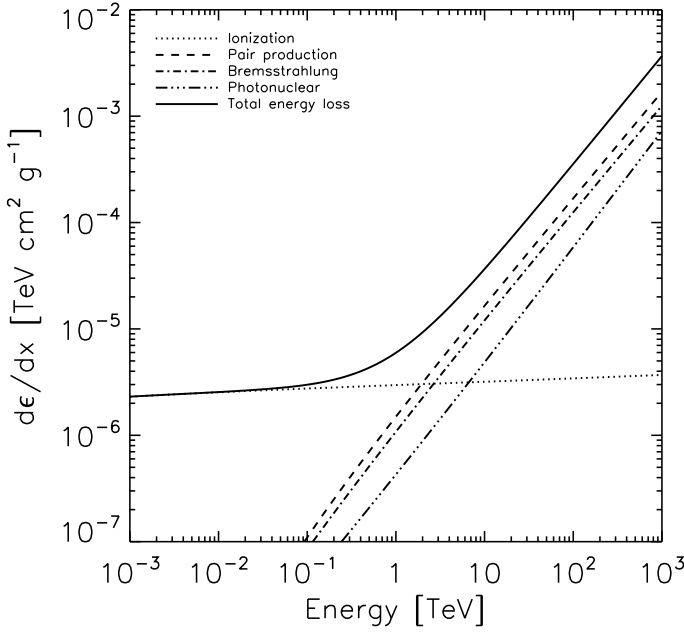


Figure 3.4: The muon energy loss in seawater as a function of energy, calculated from Equations 3.32 to 3.34. The total energy loss (solid line) is decomposed into contributions from different processes, indicated in the legend. This Figure is made using the values of Klimushin, Bugaev & Sokalski (2001).

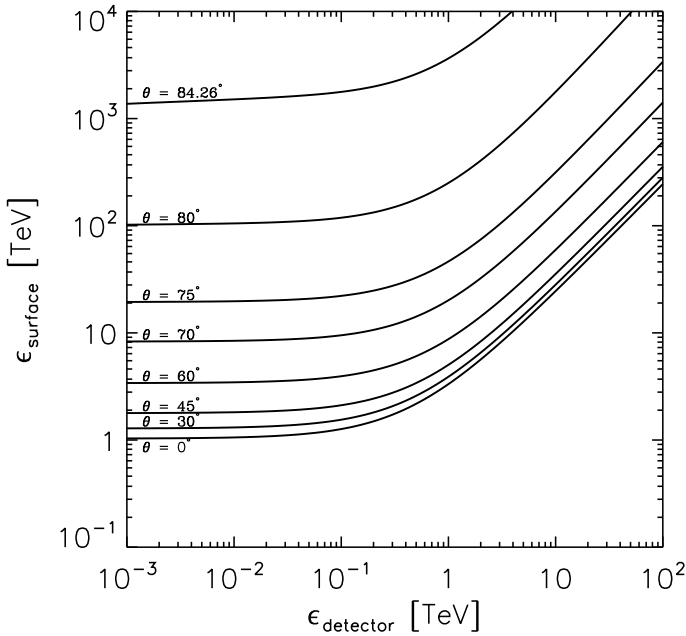


Figure 3.5: The muon energy loss by passing a layer of seawater with vertical depth  $d = 2475$  m is pictured here in the form of muon energy at the surface of the sea  $\epsilon_{\text{surface}}$  as a function of muon energy at the detector level  $\epsilon_{\text{detector}}$ . We plot the energy loss for different zenith distance  $\theta$ , thus the path length is  $R = d / \cos \theta$ .

If we integrate Equation 3.31 we can obtain the integral equation

$$\int_{\epsilon_{\text{surface}}}^{\epsilon_{\text{detector}}} \frac{d\epsilon}{a(\epsilon) + b(\epsilon)\epsilon} + R = 0, \quad (3.35)$$

in which  $\epsilon_{\text{surface}}$  is the energy at the surface of the sea and  $\epsilon_{\text{detector}}$  is the energy at detector level, located at slant depth  $R = d / \cos \theta$  where  $d$  is the vertical distance of the detector and  $\theta$  is the zenith distance from which the source came. The slant depth formula assumes a plane-parallel layers of the sea which does not take into account the curvature of the Earth. This is however a good approximation for zenith distances less than  $\sim 85^\circ$ , which is the range of zenith distances we are interested in.

Solving Equation 3.35, we can obtain  $\epsilon_{\text{surface}}$  if  $\epsilon_{\text{detector}}$  is the input and vice versa. I solve Equation 3.35 to obtain  $\epsilon_{\text{surface}}$  as a function of  $\epsilon_{\text{detector}}$ . The result for ANTARES depth of  $d = 2475$  m below sea level is shown in Figure 3.5 for several slant depths.

The relation between  $\epsilon_{\text{surface}}$  as a function of  $\epsilon_{\text{detector}}$  is particularly useful to obtain the muon flux at detector level:

$$\frac{dN}{d\epsilon_{\text{det}}}(\epsilon_{\text{det}}, R) = \frac{dN}{d\epsilon_{\text{sur}}}(\epsilon_{\text{sur}}) \left. \frac{d\epsilon_{\text{sur}}}{d\epsilon_{\text{det}}} \right|_{\epsilon_{\text{det}}, R} \quad (3.36)$$

With these in mind, we can now proceed to calculate the muon spectrum of a GRB based on its observed photon spectrum at the top of the atmosphere.

### 3.7 On the multiplicity of downgoing muons

THE CALCULATIONS of muon production developed in this Chapter is a time-averaged model and thus is incapable of predicting the rate of muon bundles due to the occurrence of several muons produced in a  $\gamma$ -induced shower. It is important, however, to quantify accurately the rate of downgoing muon bundles, as they can be misidentified as signals expected from  $\gamma$ -induced muons.

To this end, simulations of muon production from  $\gamma$  showers have been performed with CORSIKA (Heck et al., 1998), a program built to simulate in detail extensive air showers initiated by cosmic-ray particles, including high-energy photons. A number of showers with primary photons ranging from 1 TeV to 100 TeV

$\epsilon_\gamma$	$N_\gamma$	$N_\mu$	$N_\mu(\epsilon_\mu \geq 0.7 \text{ TeV})$	$N_\mu(\epsilon_\mu \geq 0.9 \text{ TeV})$
1	$1 \times 10^7$	1 647 016	223 (0.014%)	55 (0.003%)
2	$1 \times 10^7$	3 652 709	1271 (0.035%)	772 (0.021%)
5	$1 \times 10^7$	10 389 534	3924 (0.038%)	2573 (0.025%)
10	$4 \times 10^6$	9 119 416	3515 (0.039%)	2228 (0.024%)
50	$2 \times 10^6$	28 121 835	9802 (0.035%)	6420 (0.023%)
100	$6 \times 10^5$	18 345 064	6016 (0.033%)	3960 (0.022%)

is produced (see Table 3.1 for details on the number of showers produced for each energy of the primary photon). Hadronic interactions in the atmosphere are simulated with the QGSJET model while the electromagnetic interactions are simulated with the EGS4 package. The photon source is fixed to an assumed position in the sky, with an azimuth angle of  $0^\circ$  (toward the North) and zenith distance of  $30^\circ$ .

The result of the simulation can be seen in Table 3.2 and Figure 3.6. Table 3.2 shows the rate of single muon events produced in each photon shower with given photon energy  $\epsilon_\gamma$ . For each primary energies, single muon rates are shown for three different muon energy threshold: No threshold at all,  $\epsilon_\mu \geq 0.7 \text{ TeV}$ , and  $\epsilon_\mu \geq 0.9 \text{ TeV}$ . For each threshold, two quantities are shown: The number of showers that produce at least one muon passing the energy threshold and the number of shower producing only single muons passing the energy threshold.

Figure 3.6 shows the distribution of the muon multiplicity. For each shower with given photon energy  $\epsilon_\gamma$  the distribution of the

Table 3.1: A summary of the  $\gamma$ -induced electromagnetic shower simulations performed with CORSIKA. All simulations are performed with zenith distance  $\theta = 30^\circ$ . Each row summarises the simulation results for photons with a given primary energy  $\epsilon_\gamma$ .  $N_\gamma$  is the number of showers simulated;  $N_\mu$  is the total number of muons produced from all simulations;  $N_\mu(\epsilon_\mu \geq 0.7 \text{ TeV})$  and  $N_\mu(\epsilon_\mu \geq 0.9 \text{ TeV})$  are the total number of muons with energies greater or equal than respectively 0.7 TeV and 0.9 TeV.

Table 3.2: The rate of single muons for each shower with given primary energy  $\epsilon_\gamma$ . For each given threshold energy, two quantities are shown: The number of showers that produce at least one muon with energy equal or larger than the given threshold and the number of showers that produce only one muon passing the given energy threshold.

$\epsilon_\gamma$ [TeV]	No threshold			$\epsilon_\mu \geq 0.7 \text{ TeV}$			$\epsilon_\mu \geq 0.9 \text{ TeV}$		
1	792740	529689	(66.82%)	208	208	(100.00%)	55	55	(100.00%)
2	945618	604308	(63.91%)	699	630	(90.13%)	435	415	(95.40%)
5	2181219	1203441	(55.17%)	2135	1914	(89.65%)	1365	1194	(87.47%)
10	1218344	511458	(41.98%)	1602	1409	(87.95%)	1020	905	(88.73%)
50	993949	21334	(2.15%)	3990	3207	(80.38%)	2746	2287	(83.28%)
100	599983	121	(0.02%)	4698	3652	(77.74%)	3215	2559	(79.60%)

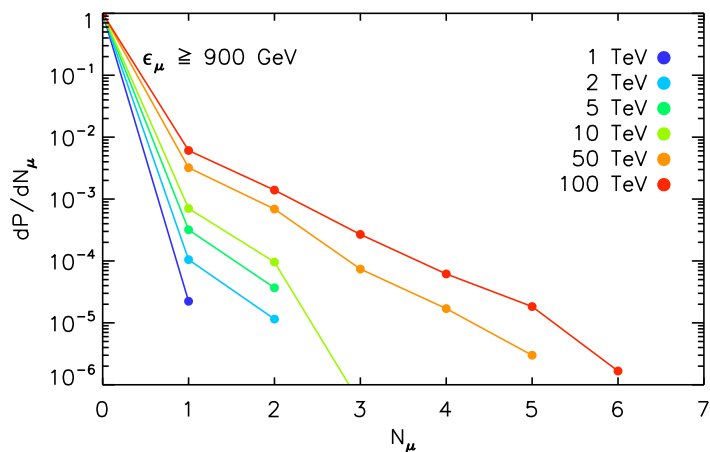
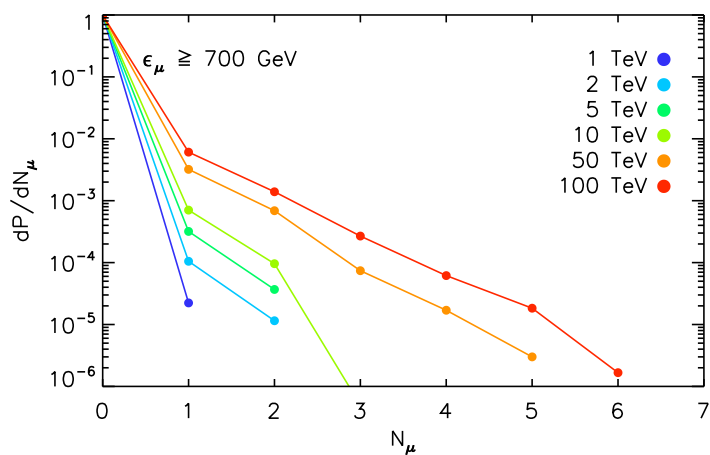
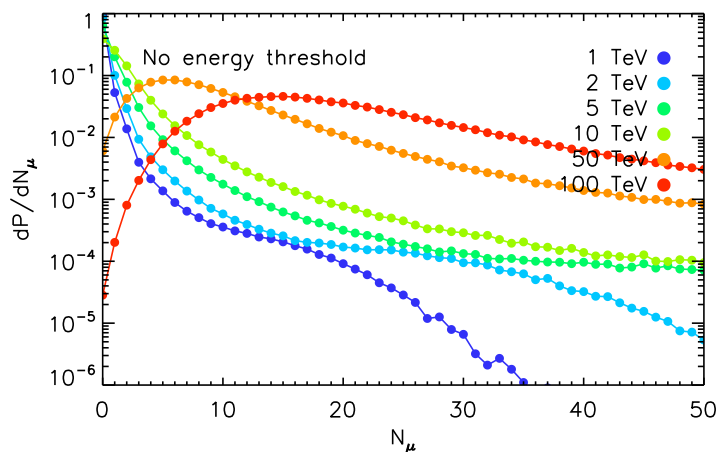


Figure 3.6: The distribution of muon multiplicity  $N_\mu$  at the surface of the sea. Each curve shows the fraction of  $N_\mu$  produced from showers with given photon-primary with energy  $\epsilon_\gamma$ . Photons with energy  $\epsilon_\gamma \gtrsim 10$  TeV can produce large muon bundles. However, if a certain muon energy threshold is applied (middle and bottom plots), we can see that the majority of the events are single muons.

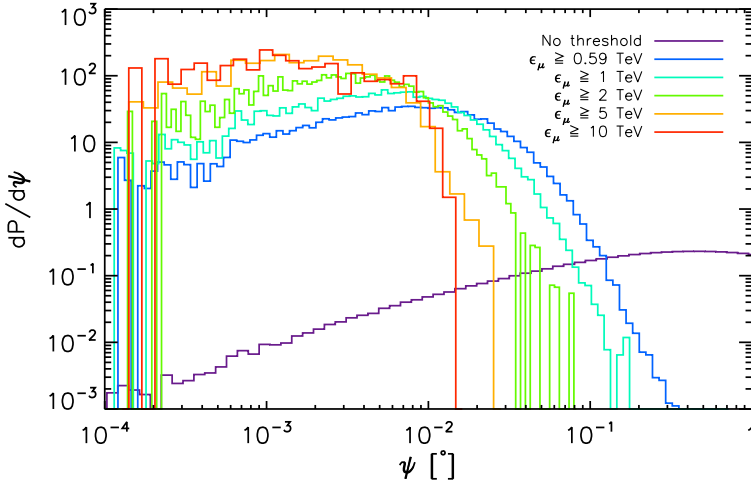


Figure 3.7: The distribution of the angular separation  $\psi$  of the original TeV photon track and the track of muons produced in the atmosphere. In addition to the distribution of  $\psi$  for all muons, the  $\psi$  distribution for six different muon energy thresholds are also shown. We can see that for TeV muons, the angular separations with the original photon tracks are very small they are practically parallel with them.

number of muons  $N_\mu$  produced in the shower, at the surface of the sea, is shown. The top plot shows the distribution of  $N_\mu$  for muons with any energy. We can see that for photon primaries with energy  $\epsilon_\gamma \lesssim 10$  TeV, the majority of the showers produce no muons at all, with a probability of  $\sim 20\%$  producing at least one muon. At higher primary energies, there is a higher chance to produce multiple muons within a shower. However, the muons must penetrate the depth of the sea in order to be detected by the ANTARES telescope. Thus only muons with sufficiently high energy are detected. If we only count muons with energy larger than 700 GeV (middle plot of Figure 3.6) or 900 GeV (bottom plot of Figure 3.6), it is clear that the majority of events contain a single muons and that high-energy muon bundles are rare. Table 3.2 shows that in the photon energy range of  $2 \text{ TeV} \leq \epsilon_\gamma \leq 10 \text{ TeV}$ , at most  $\sim 11\%$  of the muons with  $\epsilon_\mu \geq 0.9 \text{ TeV}$  arrive in bundles. The rate of muon bundles is thus rather low.

If the very high energy muon bundles pass through the detector, it is still possible to reconstruct a track. At this energy, the muons will travel essentially at parallel angles and could therefore be reconstructed as a single muon track. This is due to the limited two-track resolution of the detector that hinders the abil-

ity to distinguish multiple muon tracks coming at approximately the same time (Halzen, Kappes & Ó Murchadha, 2009). From the CORSIKA simulation, we could calculate the angular separation  $\psi$  of the tracks with respect to the original photon directions. In Figure 3.7 the distribution of  $\psi$  is plotted for muons with any energy as well as for muons passing a certain energy threshold. Six energy thresholds are considered, ranging from 590 GeV to 10 TeV. We can see that for TeV muons, the distribution of  $\psi$  is peaked at around  $\sim 0.001^\circ$ , which is much smaller than the angular resolution of the ANTARES detector.

Consequently, the simulations of ANTARES' sensitivity to down-going muons can then be performed by generating single muon tracks. We will discuss this simulation in Chapter 7.

## 4 Muon event rate from single GRBs

ONCE we know how to produce gamma ray-induced muons in the atmosphere and how they lose their energy in seawater, we are now in the position to calculate the muon yield both on the surface of the sea and at detector level.

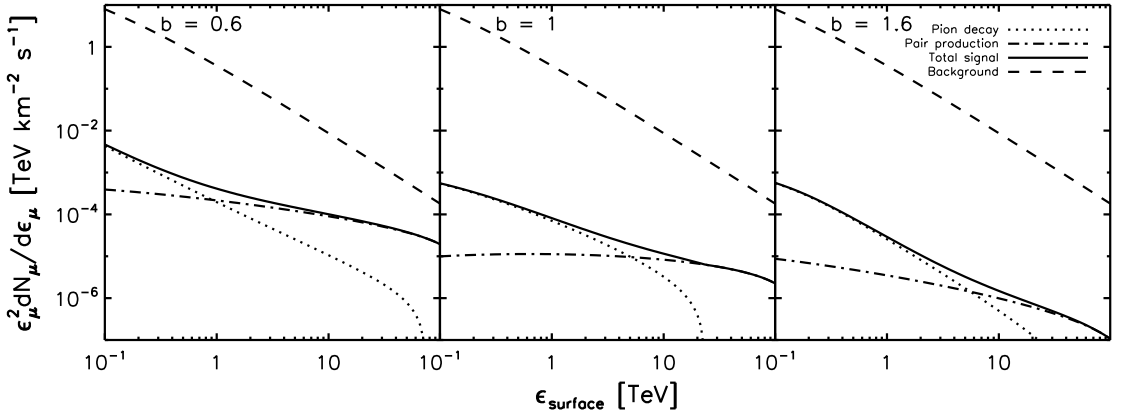
### 4.1 Muon flux from a fictive test source

I FIRST calculate muons produced from a fictive, unattenuated test source with fluence  $f_\gamma = 10^{-1} \text{ TeV}^{-1} \text{ km}^{-2} \text{ s}^{-1}$  at 1 TeV. The source is a point source with negligible diameter, assumed to be located at zenith distance  $\theta = 30^\circ$ . The muon flux is calculated for three spectral indices  $b = (0.6, 1, 1.6)$  and cutoff energy at  $\epsilon_{\text{max}} = 300 \text{ TeV}$ . For the background estimation, the opening angle of the search cone is taken to be  $\theta_{\text{cone}} = 1^\circ$ . The results are shown in Figure 4.1 and compared to a background of cosmic ray-induced muons flux for the same zenith distance.

These results are reasonably consistent with the results of Halzen, Kappes & Ó Murchadha (2009). We can see that the dominant channel of muon-production at low energies is by pion decay. However the number of muons that can be created from this way goes down with photon energy. At high energies, because the cross-section of the muon-pair production goes up with photon energy before reaching saturation point at  $\epsilon_\gamma \gtrsim 10 \text{ TeV}$ , the dominant muon production mechanism is direct-pair production.

A COMPARISON is also made using CORSIKA. Simulations are performed for fictive sources with the same zenith distances and spectral indices as in the previous calculation, but with cutoff energy at  $\epsilon_{\text{max}} = 1000 \text{ TeV}$ . The photon spectrum is normalized so that the fluence will be  $f_\gamma = 10^{-1} \text{ TeV}^{-1} \text{ km}^{-2} \text{ s}^{-1}$  at 1 TeV. The results of the simulations and the analytical calculations for the same parameters are shown in Figure 4.2.

For  $b = 1$ , there is a good agreement between CORSIKA and the analytical calculation. However for  $b = 0.6$ , the CORSIKA results are systematically lower while the shape of the muon spectrum is



consistent. For  $b = 1.6$ , the difference at lower muon energy is even more pronounced.

These systematic differences however appear only at sub-TeV energies. At TeV energies the shape of the muon spectrum is reasonably in agreement, barring the fluctuations caused by low statistics at very-high energy energies.

#### 4.2 Muon flux from single GRB

CONFIDENT with the consistency of the calculation, I proceed by calculating the muon flux for single GRB events located at different redshifts. Using Equation 2.62, the photon flux arriving at the top of the atmosphere from GRBs with spectral indices  $b = (0.5, 1, 1.25, 1.5)$ , redshifts  $z = (0.05, 0.1, 0.2, 0.5)$ , and zenith distances  $\cos\theta = (0.5, 1)$  can be determined. A typical GRB power spectrum measured by BATSE is  $b \simeq 1.25$  (Preece et al., 2000), however measurement inconsistencies have been reported and thus the shape of the spectral index at high energy is still debatable and might not be in the form of a simple power law (see e.g. Kaneko et al. 2008 and González et al. 2003). Until this debate is clarified, it is reasonable to assume a soft spectrum with index  $b \simeq 1$ . The other spectral indices,  $b = 0.5$  and  $b = 1.5$  which corresponds respectively to a harder and softer spectrum, while not entirely impossible nevertheless have a small possibility

Figure 4.1: The  $\nu f_\nu$  spectrum of a fictive, unattenuated test source with fluence  $f_\gamma = 10^{-1} \text{ TeV}^{-1} \text{ km}^{-2} \text{ s}^{-1}$  at 1 TeV, for photon spectral indices  $b = (0.6, 1, 1.6)$ , photon energy cutoff  $\epsilon_{\text{max}} = 300 \text{ TeV}$ , and zenith distance  $\theta = 30^\circ$ . The spectrum is decomposed into its major contributing components: Pion decay and direct pair production. For a comparison, the spectrum of cosmic ray-induced muons for the same zenith distance is also shown, (see Equation 3.30). The search cone has an opening angle of  $1^\circ$ . The result is largely consistent with that of Halzen, Kappes & Ó Murchadha (2009).



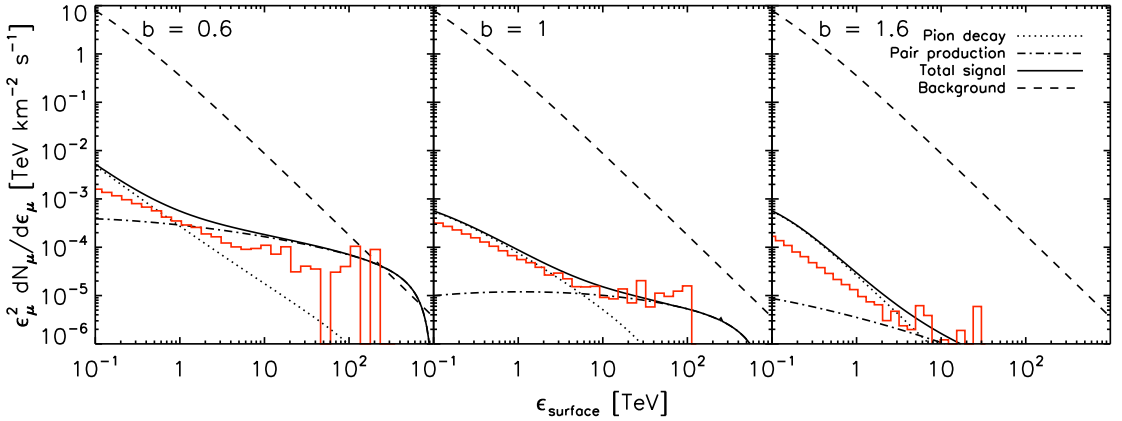


Figure 4.2: The same as in Figure 4.1, but for cutoff photon energy  $\epsilon_{\max} = 1000$  TeV. Red histogram is the result from CORSIKA simulations using the same parameters as the analytical calculation.

of occurring and is thus also considered to study their possibility of observing the muon signal.

Throughout the calculation, the values  $\Delta t_* = 10$  s,  $\epsilon_{\text{bk}*} = (b - a)\epsilon_{\text{pk}*}/(1 - a) = (b - 1)400$  keV, and  $L_{\text{bol}*}^{\text{iso}} = 8.9 \times 10^{52}$  erg are used. These values are the average values determined from *Swift* observations (Butler et al., 2007; Butler, Bloom & Poznanski, 2010). After calculating the number of photons at the top of the atmosphere, the muon flux at the surface of the sea is then determined by means of Equation 3.14 or 3.16—depending on the spectral index considered—and Equation 3.28. The muon flux at the surface is then transformed to the muon flux at detector level by way of Equation 3.36, and the corresponding energy at detector level is calculated by solving Equation 3.35.

The results of this series of calculations are shown in Figure 4.3 using the attenuation model by Finke, Razzaque & Dermer (2010). One panel in each of these Figures plot the muon flux of GRBs for one spectral index. For each spectral index, the muon flux from GRBs at different redshifts is also shown and indicated with the colour scheme shown in the legend. For each redshift, an area is drawn to show their dependence on zenith distance. The the borders of the area drawn for each redshifts are the the muon flux at zenith distance  $\theta = 0$  (solid lines) and at  $\theta = 60^\circ$  (dashed lines). Anything in between those two lines are then the amount of sig-

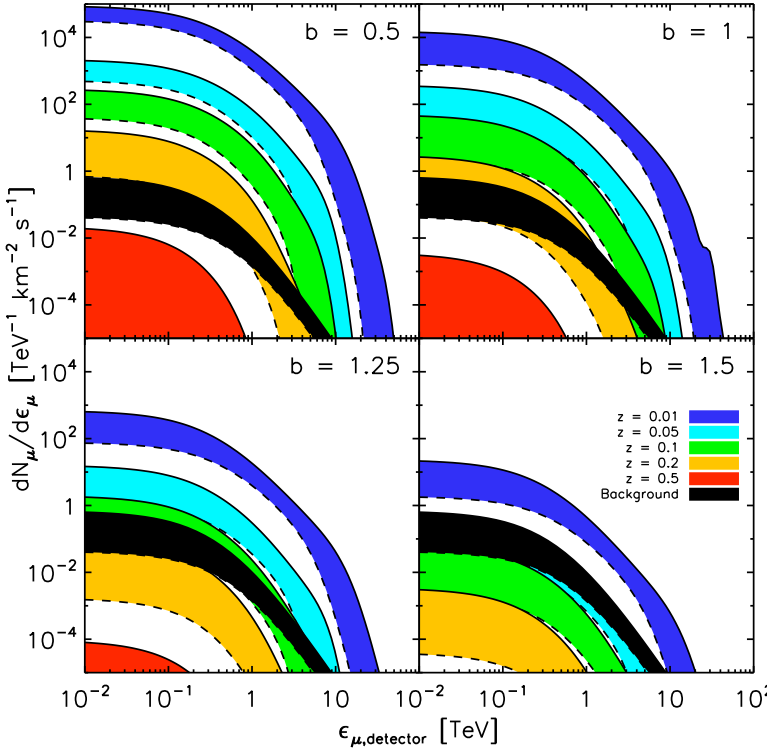


Figure 4.3: The muon flux at the detector (depth of 2475 m) for single GRBs emitted from different redshifts indicated by the colour coding on the legend. The black area is the background flux from cosmic ray-induced muons, calculated using Equation 3.30 assuming a search cone with an opening angle of  $1^\circ$ . For each colour, the muon flux drawn by the dashed-line is the flux from zenith distance  $\theta = 60^\circ$  while those drawn by the solid line is the flux straight from the zenith (i.e.  $\theta = 0$ ). The filled-area indicates all possible fluxes from all zenith distance between  $\theta = 0^\circ$  and  $\theta = 60^\circ$ . Attenuation is determined by using a model by Finke, Razzaque & Dermer (2010).

nals from any zenith distance between the borders. A background flux due to cosmic ray induced-muons calculated from Equation 3.30 is also shown for the same limit of zenith distances, indicated by the black area. The search cone (or the opening angle) is taken to be  $1^\circ$ . The same calculations for other attenuation models were made, but upon inspection of the numbers, results indicate that the magnitude of attenuation does not differ much for nearby universe, i.e.  $z \lesssim 0.2$ . Hence here only results calculated using the calculation by Finke, Razzaque & Dermer (2010) are shown.

The results shown in Figure 4.3 indicate that the number of muons reaching the detector depends heavily on the GRB's distance from us and its power spectrum. The redshift is an important factor because it determines the number of photons that survives all the way from the GRB to the top of the atmosphere, and the power spectrum determines the number of photons produced in

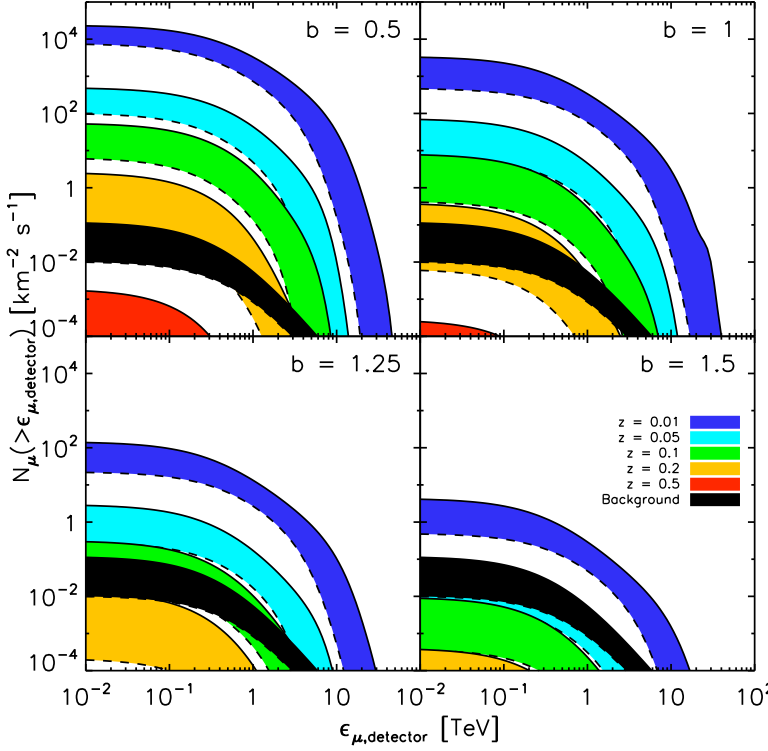


Figure 4.4: The expected number of muons with energies higher than a given muon energy  $\epsilon_{\mu,\text{detector}}$  at the detector (depth of 2475 m) for single GRBs emitted from different redshifts. The colour coding and line styles are the same as in Figure 4.3.

the GRB.

The muon spectrum is then integrated to obtain a muon event rate with energies higher than  $\epsilon_{\mu,\text{detector}}$ :

$$N_{\mu}(> \epsilon_{\mu,\text{detector}}) = \int_{\epsilon_{\mu,\text{detector}}}^{\infty} d\epsilon_{\mu} \frac{dN_{\mu}}{d\epsilon_{\mu}} \quad (4.1)$$

The result of this integration is shown in Figure 4.4, using the attenuation model by Finke, Razzaque & Dermer (2010). This result can give us an idea of how many muon events per unit area per unit time we can expect from any GRB event with the given power spectrum, redshift, and zenith distance.

To explore further the effect of distance on the muon event rate at the detector, in Figure 4.5 the event rate of muons with energies higher than 0.1 TeV per unit area per unit time,  $N_{\mu}(\epsilon_{\mu,\text{detector}} > 0.1 \text{ TeV})$ , is plotted as a function of redshift. The black horizontal

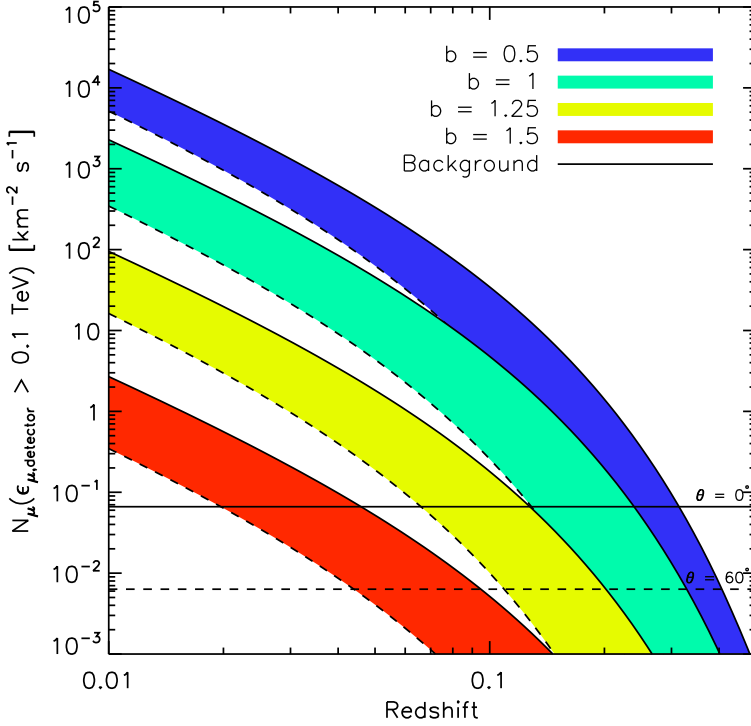


Figure 4.5: The muon count rate with energies  $\epsilon_{\mu,\text{detector}} > 0.1$  TeV for GRB events occurring at different redshifts. As in Figure 4.3, dashed lines are for GRBs at zenith distance  $\theta = 60^\circ$  while solid lines are for GRBs at  $\theta = 0^\circ$ .

lines are the background rate from cosmic ray-induced muons at zenith distances  $\theta = [0^\circ, 60^\circ]$ .

Figure 4.5 tells us the minimum redshift and maximum zenith distance to observe, for example, at least one muon event per kilometer square per second. For example, a GRB event with power spectrum  $b = 1.25$  that occurs at the zenith must have a redshift of  $z \lesssim 0.07$  if we want to observe at least one muon per kilometer square per seconds. The number of muons produced from a photon spectrum with  $b = 0.5$  and those from  $b = 1.5$  exhibit a large deviation, ranging from  $N_\mu \sim 1$  to  $N_\mu \sim 10^4 \text{ km}^{-2} \text{ s}^{-1}$ . This is because a photon flux with a hard spectrum can produce electromagnetic showers that grow in the atmosphere, while fluxes with softer spectrum produce showers that instead dissipate in the atmosphere.

The number of detectable muons depends also on the size of

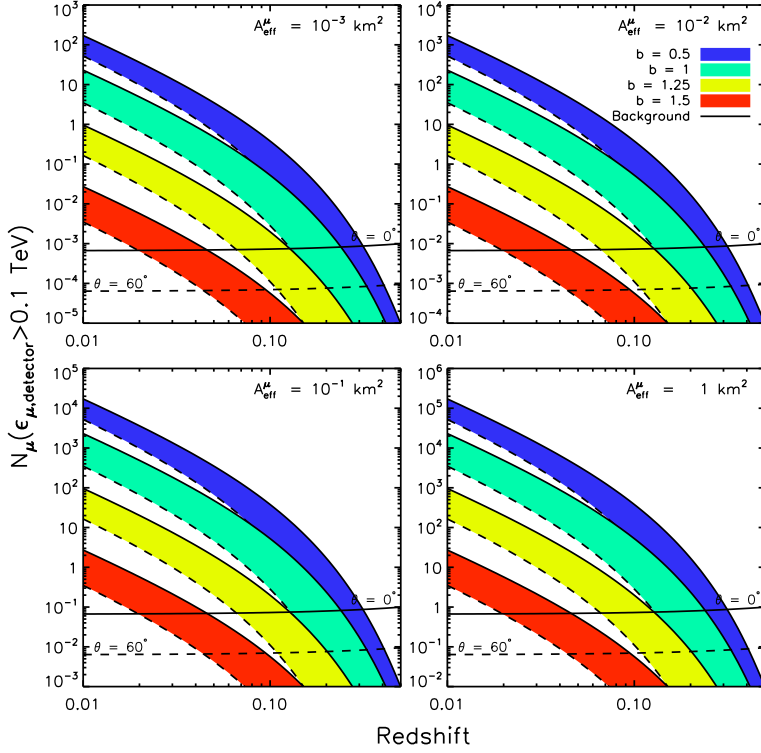


Figure 4.6: The total number of muons with energies  $\epsilon_{\mu,\text{detector}} > 0.1$  TeV for GRBs from different redshifts and different spectral index as indicated by the colour code in the legend. The intrinsic burst duration  $\Delta t_*$  is assumed to be 10 sec, thus making  $t_{90} = (1+z)\Delta t_*$ . The total muon count is calculated by assuming different detector sizes, which are assumed to be independent of energy.

the detector. ANTARES is projected to have an effective muon area of  $A_{\text{eff}}^{\mu} \sim 10^{-2}$  km<sup>2</sup> while IceCube is expected to have an area of  $A_{\text{eff}}^{\mu} \sim 1$  km<sup>2</sup> (Halzen, Kappes & Ó Murchadha, 2009). In Figure 4.6, I calculate the total number of detectable muons during the whole duration of the burst for four different detector sizes. The downgoing muon effective areas considered are  $A_{\text{eff}}^{\mu} = (10^{-3}, 10^{-2}, 0.1, 1)$  km<sup>2</sup>, which are assumed to be constant with respect to the muon energy.

With a larger detector we can see farther GRBs, up to  $z \sim 0.3$  for  $b = 0.5$ . Using a detector with the size of ANTARES, however, one can only detect at least one muon from GRBs at a redshift up to  $z \sim 0.2$  for the same spectral index.

Since we know the number of signal and noise events in our detector, we can now calculate the expected detection significance of each individual GRB as a function of redshift. The significance

$S$  is calculated according to the procedure outlined by Li & Ma (1983). The total signal  $N_{\text{on}}$  is the number of muon events within a  $1^\circ$  search cone and during the  $t_{\text{on}} = t_{90}$  time interval, while the total number of background  $N_{\text{off}}$  is the number of muons within the same search cone but some amount of time  $t_{\text{off}}$  before the GRB took place. The statistical significance  $S$  (the number of standard deviation above background) is determined using the likelihood ratio method:

$$\begin{aligned}
 S = \sqrt{2} \left\{ N_{\text{on}} \ln \left[ \frac{1 + \alpha}{\alpha} \left( \frac{N_{\text{on}}}{N_{\text{on}} + N_{\text{off}}} \right) \right] \right. \\
 \left. + N_{\text{off}} \ln \left[ (1 + \alpha) \left( \frac{N_{\text{off}}}{N_{\text{on}} + N_{\text{off}}} \right) \right] \right\}^{1/2}, \quad (4.2)
 \end{aligned}$$

where  $\alpha$  is the ratio  $\alpha \equiv t_{\text{on}}/t_{\text{off}}$ . The time  $t_{\text{off}}$  to measure the background rate is taken to be 2 hours, i.e.  $t_{\text{off}} = 7200$  s, thus making  $\alpha$  very low. The results of these calculation is shown in Figure 4.7, again for four different detector sizes.

These results correspond to the detection significance of observing GRBs with a certain power spectrum, zenith distance, and redshift. We can also use this result to determine the maximum redshift where a GRB has to occur if we want to have at least  $3\sigma$  or  $5\sigma$  detection significance. As an example, for an ANTARES-sized detector to detect a GRB signal with  $5\sigma$  significance, a GRB event at zenith must be closer than  $z \lesssim 0.05$  if its power spectrum is  $b = 1$ .

### 4.3 Conclusions

THE MOST important factors in detecting a possible TeV component of a GRB are the redshift, the spectral index, and the effective area of the detector. The redshift determines the number of photons that survive to the top of the atmosphere, while the hardness of the spectrum determines whether the electromagnetic spectrum grows or dissipate in the atmosphere. The dependence of these two quantities is presented in Figure 4.8. A typical GRB has a spectral index  $b = 1-1.25$  (Preece et al., 2000; Kaneko et al., 2008). For an ANTARES-type telescope, a typical GRB must then be located at redshift  $z \lesssim 0.05$ , while a larger telescope with a muon collecting area of  $A_{\mu}^{\text{eff}} = 1 \text{ km}^2$  can see up to  $z \lesssim 0.1$ .

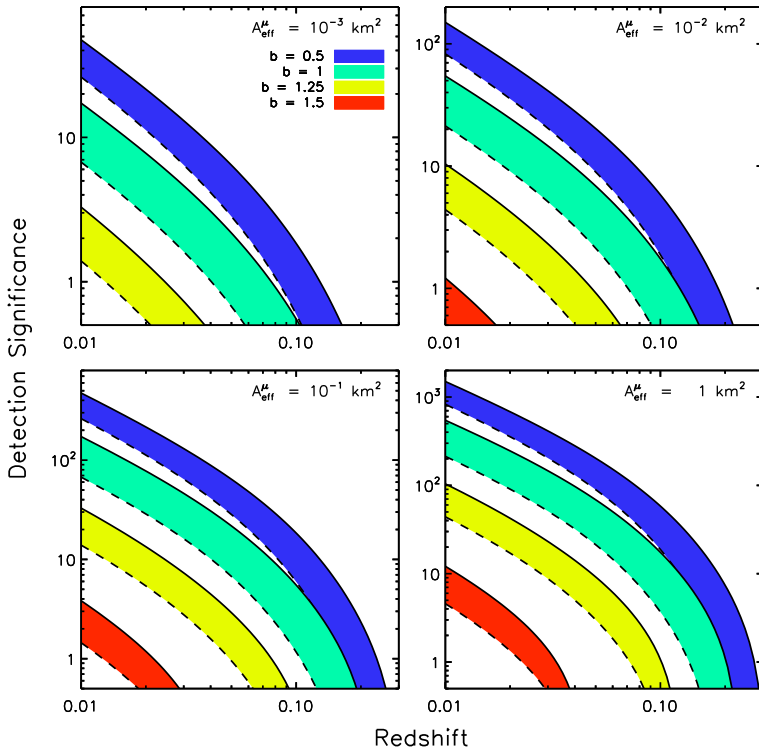


Figure 4.7: The muon signal detection significance for GRB events located at different redshifts and different spectral indices as indicated by the colour code in the legend. The detection significance is calculated using the Li & Ma (1983) formula, and using the results shown in Figure 4.6.

A recent analysis of *Fermi* GRB data by Zhang et al. (2011) suggests that the peak of the distribution in  $b$  has shifted to  $b \sim 1.6$ , a much steeper slope than what was suggested by previous observations. Consequently, the maximum redshift that permits a  $3\sigma$  detection is lower: Redshift  $z \lesssim 0.005$  for an ANTARES-type telescope and  $z \lesssim 0.01$  for a  $\text{km}^3$  neutrino telescope. In the analysis of Zhang et al. (2011), the peak distribution of integral index  $a$  is  $a \sim -0.1$ , which is not significantly different with previous results.

The limitation pertaining to distance proves to be a great hindrance to the detection of TeV  $\gamma$ -rays from GRBs, as there are not many GRBs with known redshift that took place at so close distance. Recent analysis of 425 *Swift* GRBs suggests that the redshift distribution of GRBs is peaked at  $z \sim 1$  (Butler, Bloom & Poznanski, 2010). Within this data set, there are 144 GRBs with known

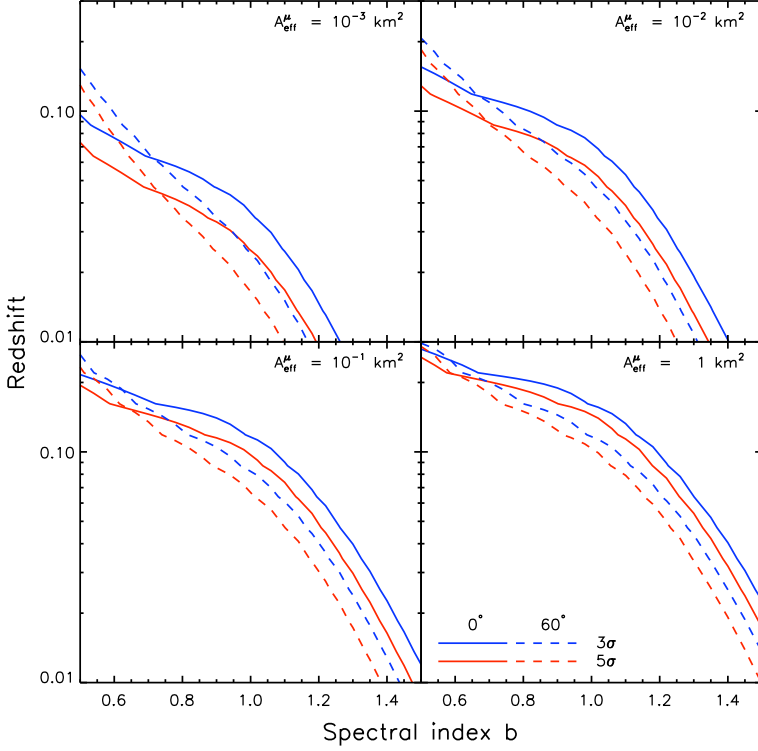


Figure 4.8: The combination of redshift  $z$  and spectral index  $b$  that gives a detection significance of  $3\sigma$  (blue lines) and  $5\sigma$  (red lines), for GRB photons that came from zenith distances of  $0^\circ$  (solid lines) or  $60^\circ$  (dashed lines).

redshift and 3 of them have  $z \leq 0.15$ . This corresponds roughly to a fraction of  $P(z \leq 0.15) \sim 7 \times 10^{-3}$ .

From these results we can conclude that a role of neutrino-telescopes as a gamma-ray telescope can only be played-out restrictively to the nearest GRB sources. As nearby GRBs tend to belong to a different population (i.e. short GRB) than the ones farther away, other considerations must also be taken in view of the different luminosity and burst duration of this population.

The rate of muon signals calculated in this Chapter does not yet include the detection efficiency of the detector. To understand this effect a Monte Carlo simulation of the detector response to the muon signals must be performed. This will be discussed in Chapter 7.



# 5 *Muon event rate and discovery potential from stacked GRB events*

FROM the results in Chapter 4, we could now investigate how long do we have to wait before a sufficiently nearby GRB event takes place, or in another words, how frequent can we observe a GRB with  $z \lesssim 0.1$ ? Aside from this question, a second aim of this Chapter is to calculate the integrated muon flux of any number of simulated GRB events. To do this, a Monte Carlo method to simulate GRB events is developed, using a distribution functions of several GRB parameters. These distribution functions are known collectively as the GRB world model (Butler, Bloom & Poznanski, 2010).

## 5.1 *GRB world model*

THE STUDY of GRBs distribution functions has been intensified due to the wealth of data from *Swift*. The latest data release contains 425 bursts in which 147 of them have a measured redshift. This data set largely supersedes previous GRB analyses (Butler et al., 2007; Butler, Bloom & Poznanski, 2010). As shown in Section 2.1, given  $(L_{\text{bol}}, z, b, \Delta t, \epsilon_{\text{bk}})$  we can simulate a GRB event. The distribution functions of these parameters have been determined. In this Section the form and parameters of these functions will be described. The data set used for comparison in this section is taken from Butler et al. (2007); Butler, Bloom & Poznanski (2010). For all cases a criterion of signal-to-noise ratio of  $S/N > 10$  is applied. In cases where redshift information is needed (e.g. Luminosity function, redshift distribution), the redshift data are further selected using the criteria suggested by Jakobsson et al. (2006). These criteria select only redshifts measured under favorable conditions such that the distance is reliably measured. These criteria include the public availability of X-ray positioning within 12 hours; low Galactic foreground, i.e.  $A_V < 0.5$ ; the burst took place no less than  $55^\circ$  from the Sun; no nearby bright star; and the burst should not be located at a polar declination, i.e.  $|\delta| < 70^\circ$ .

A catalog of GRBs<sup>1</sup> passing these redshift measurement criteria is then used to select *Swift* measurements. At the end of this selection procedure, 89 GRBs with high-quality measurements and redshift information is obtained.

<sup>1</sup> Available at <http://www.raunvis.hi.is/~pja/GRBsample.html>.

### 5.1.1 GRB luminosity function

THE GRB luminosity function  $\phi(\log L)$  is traditionally defined as the probability to find a GRB in a luminosity interval between  $\log L$  and  $\log L + d \log L$ . This function is usually assumed to be of the form of a smoothly broken power law:

$$\phi(\log L) = \frac{dN}{d \log L} = \begin{cases} \left(\frac{L}{L_{\text{pk}}}\right)^{-a_L} & \text{for } L \leq L_{\text{pk}}, \\ \left(\frac{L}{L_{\text{pk}}}\right)^{-b_L} & \text{for } L > L_{\text{pk}}. \end{cases} \quad (5.1)$$

This function is normalized to the interval from zero to infinity. Recent results from *Swift* indicates that the bolometric luminosity function is well-described by the indices  $(a_L, b_L) = (0.27, 3.46)$  and the peak luminosity  $\log L_{\text{pk}} = 52.95$  (Butler, Bloom & Poznanski, 2010). Figure 5.1 shows the luminosity function compared to a histogram of 89 *Swift* GRBs with measured redshift (Butler et al., 2007; Butler, Bloom & Poznanski, 2010). The bolometric luminosity  $L_{\text{bol}}$  is calculated using Equation 9 in Butler, Bloom & Poznanski (2010).

### 5.1.2 The distribution of burst duration $T_{90}$

THE COMMONLY used definition for the burst duration is  $T_{90}$ , defined as the time interval in which the background-subtracted integrated counts from the GRB increase from 5% to 95% of the total counts (Kouveliotou et al., 1993, 1996). Based on this parameter, Kouveliotou et al. (1993) found a bimodality in the distribution of  $\log T_{90}$  and thus introduced two distinct groups of GRBs: The short and the long duration GRBs, with  $T_{90}$  shorter or longer than 2 seconds.

Further analysis using the BATSE 3B catalog (Meegan et al., 1996), however, exhibit a possibility that the distribution of  $\log T_{90}$  can also be well-fitted using a trimodal Gaussian thus indicating the existence of a third, intermediate, class of GRB (Horváth,

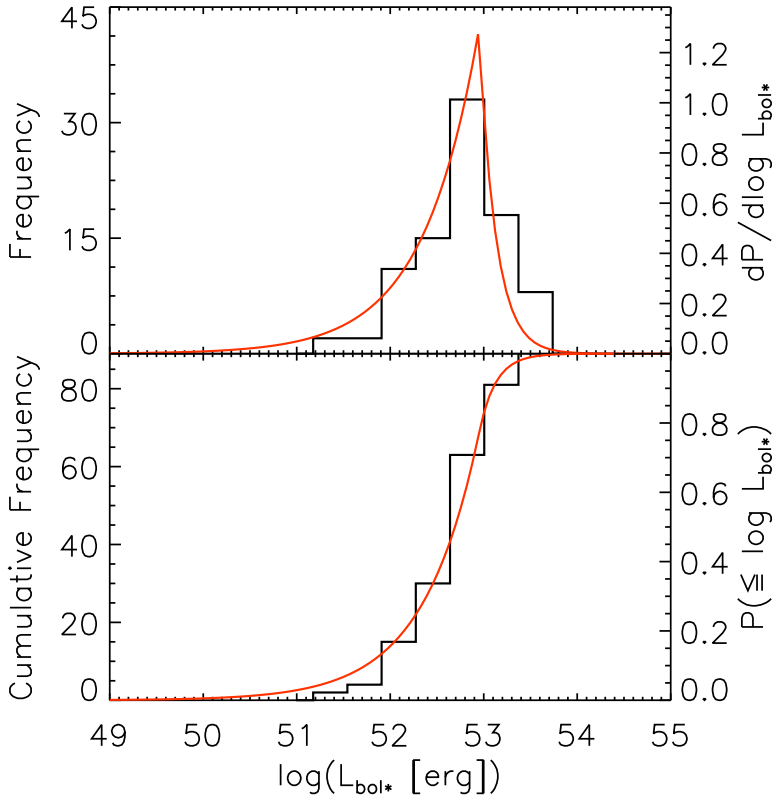


Figure 5.1: The top graph shows the luminosity probability density function while the bottom graph is the cumulative probability function. Red curves represent the best-fit GRB world model for the luminosity function (Butler, Bloom & Poznanski, 2010), compared to 89 selected *Swift* data with measured redshift (Butler et al., 2007; Butler, Bloom & Poznanski, 2010) and passing the redshift measurement criteria suggested by Jakobsson et al. (2006). The left side of the vertical axis is the actual number of data in each bin while the right side is the value of the probability function.

1998). Various statistical methods applied to different data sets from different satellites (e.g. BATSE (Horváth et al., 2006), BepoSAX (Horváth, 2009), *Swift* (Horváth et al., 2008)) seem to indicate that this third class is real and not an artifact or bias from one particular satellite. While the short and long GRB can be explained as two distinct physical phenomena, the third class is still lacking any physical interpretation.

A trimodal Gaussian function is used to model the distribution function of  $\log T_{90}$ :

$$\frac{dN}{d \log T_{90}} = \sum_{k=s,l,i} \frac{w_k}{\sigma_k \sqrt{2\pi}} \exp \left[ -\frac{\log^2(T_{90} / \log \mu_{T_{90},k})}{2\sigma_k^2} \right], \quad (5.2)$$

in which  $(s, l, i)$  is the notation for respectively the short, long, and

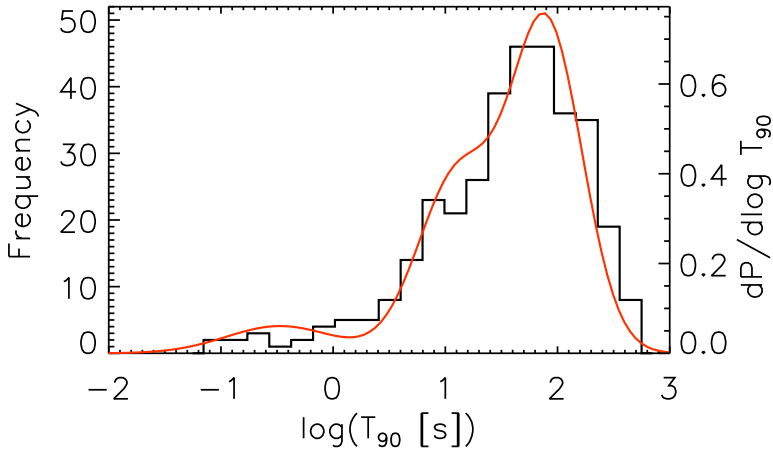


Figure 5.2: The red curve is the  $T_{90}$  distribution function from Horváth et al. (2008) compared to 345  $T_{90}$  measurement by *Swift* (Butler et al., 2007; Butler, Bloom & Poznanski, 2010) with signal-to-noise ratio larger than 10. The parameters for the distribution function is shown in Table 5.1.

Terms	$k$ subscript	$\mu_{T_{90},k}$	$\sigma_k$	$w_k$
short	$s$	-0.473	0.48	0.073
long	$l$	1.903	0.32	0.582
intermediate	$i$	1.107	0.35	0.345

Table 5.1: The parameters for the trimodal Gaussian distribution function of  $\log T_{90}$  (Horváth et al., 2008).

intermediate duration GRB,  $w_k$  is the weight of the Gaussian function where  $w_s + w_i + w_l = 1$  applies,  $\mu_{T_{90},k}$  is the mean in  $\log T_{90}$  and  $\sigma_k$  is the standard deviation. We use the parameters calculated by Horváth et al. (2008) for the *Swift* data, shown in Table 5.1. In Figure 5.2 the distribution function is shown alongside the  $T_{90}$  data measured by *Swift*. There are 345 *Swift* GRB measurement with signal-to-noise ratio  $S/N > 10$ . The lack of a physical interpretation for the intermediate class should not be a concern because the aim of this study is to accurately simulate the observational features and not to deduce any physical interpretation of these features.

### 5.1.3 The intrinsic peak energy $\epsilon_{pk^*}$ distribution

THE INTRINSIC peak energy  $\epsilon_{pk^*}$  is the energy in which the  $\nu f_\nu$  spectrum peaks. It is calculated by performing a spectral fit to the measured energy spectrum of a GRB. What one obtains from this procedure is the observed peak energy  $\epsilon_{pk}$ . For the Band spectrum

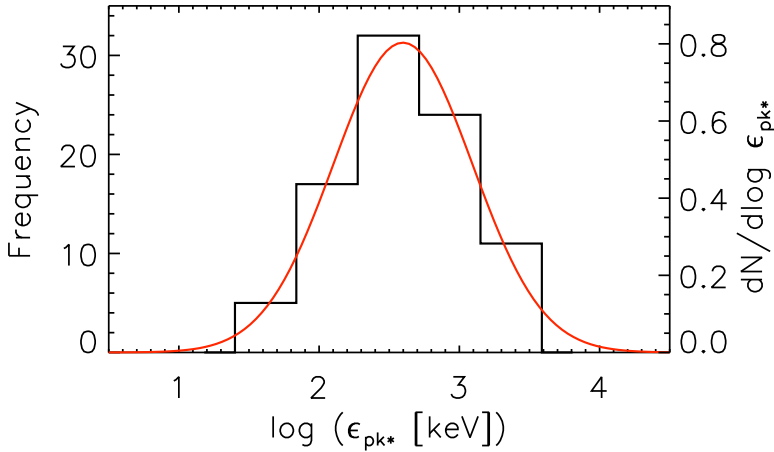


Figure 5.3: The logarithm of intrinsic peak energy  $\epsilon_{\text{pk}^*}$  histogram of 89 *Swift* GRB with measured redshift (Butler et al., 2007; Butler, Bloom & Poznanski, 2010). The histogram is compared to a best-fit Gaussian function in  $\log \epsilon_{\text{pk}^*}$ .

(Equation 2.52), the peak energy is related to the break energy  $\epsilon_{\text{bk}}$  through

$$\epsilon_{\text{bk}} = \frac{b-a}{1-a} \epsilon_{\text{pk}^*}. \quad (5.3)$$

The distribution function of  $\epsilon_{\text{pk}^*}$  can be modelled reasonably well by the normal distribution in  $\log \epsilon_{\text{pk}^*}$ :

$$\frac{dN}{d \log \epsilon_{\text{pk}^*}} = \frac{1}{\sqrt{2\pi\sigma_{\epsilon_{\text{pk}^*}}^2}} \exp \left[ -\frac{\log^2(\epsilon_{\text{pk}^*}/\epsilon_{\text{pk}^*,0})}{2\sigma_{\epsilon_{\text{pk}^*}}^2} \right]. \quad (5.4)$$

The mean and variance of the distribution is found to be  $(\log \epsilon_{\text{pk}^*,0}, \sigma_{\epsilon_{\text{pk}^*}}) = (2.58 \pm 0.05, 0.50 \pm 0.03)$ . The corresponding function is shown as the red curve in Figure 5.3.

#### 5.1.4 The redshift distribution of GRBs in the universe

THE REDSHIFT distribution function is calculated using the physical model formulated by Le & Dermer (2007), which includes the effects of beaming by incorporating a distribution function for the jet opening angle. This model sets out by assuming a GRB energy

spectrum  $\nu F_\nu = \epsilon^2 N(\epsilon)$  in the form of a broken power law, i.e.

$$\nu F_\nu \equiv f_{\epsilon_{\text{pk}}} \left[ H(\epsilon_{\text{pk}} - \epsilon) \left( \frac{\epsilon}{\epsilon_{\text{pk}}} \right)^\alpha + H(\epsilon - \epsilon_{\text{pk}}) \left( \frac{\epsilon}{\epsilon_{\text{pk}}} \right)^\beta \right], \quad (5.5)$$

where  $\alpha (> 0)$  and  $\beta (< 0)$  are the spectral indices of the energy spectrum,  $\epsilon_{\text{pk}}$  is the peak energy, and  $H(x)$  is the Heaviside function. Using this energy spectrum, just as in Equation 2.54, we can calculate the bolometric fluence of the GRB:

$$F = \int_0^{\Delta t} dt \int_0^\infty d\epsilon \frac{\nu F_\nu}{\epsilon} = \lambda_{\text{bol}} f_{\epsilon_{\text{pk}}} \Delta t, \quad (5.6)$$

where the bolometric correction  $\lambda_{\text{bol}}$  in this case is simply  $\lambda_{\text{bol}} = (\alpha^{-1} - \beta^{-1})$ . Following Le & Dermer (2007), here the bolometric correction is always taken to be  $\lambda_{\text{bol}} = 5$  to simplify the situation.

Taking into account beaming effects, which means that the burst is collimated to a bipolar jet with opening angle  $\theta_j$ , the beaming-corrected energy release  $L_{\gamma^*}$  is given by

$$L_{\gamma^*} = 4\pi r_L^2 (1 - \cos \theta_j) \frac{F}{1+z}, \quad (5.7)$$

where  $r_L$  is the luminosity distance, related to the comoving distance as  $r_L = (1+z)r_c$ . Inserting Equation 5.6 into Equation 5.7, the peak flux is then given by

$$f_{\epsilon_{\text{pk}}} = \frac{L_{\gamma^*}}{4\pi r_L^2(z)(1 - \cos \theta_j) \Delta t_* \lambda_{\text{bol}}}. \quad (5.8)$$

The number of GRB events per unit redshift per unit solid angle with spectral flux greater than  $f_{\epsilon_{\text{pk}}}$  can then be calculated using the formula

$$\frac{dN(> f_{\epsilon_{\text{pk}}})}{d\Omega dz} = \frac{c}{H_0} \Theta(z) \frac{n_c(z) r_L^2(z)}{(1+z)^3 \sqrt{\Omega_\Lambda + \Omega_m(1+z)^3}}, \quad (5.9)$$

where  $\Theta(z)$  is the jet opening angle distribution integrated over all possible opening angle:

$$\Theta(z) = \int_{\cos \theta_{j,\text{max}}}^{\cos \theta_{j,\text{min}}} d \cos \theta_j g(\cos \theta_j) (1 - \cos \theta_j). \quad (5.10)$$

The form for the jet opening angle distribution  $g(\cos \theta_j)$  is unknown, but Le & Dermer (2007) consider the form

$$g(\cos \theta_j) = g_0(1 - \cos \theta_j)^s H(\cos \theta_j; \cos \theta_{j,\max}, \cos \theta_{j,\min}), \quad (5.11)$$

where  $s$  is the power-law index of  $g(\cos \theta_j)$  and  $H(x; a, b)$  is the Heaviside function such that it is  $H(x; a, b) = 1$  when  $a \leq x \leq b$  and zero elsewhere. This distribution is normalized to unity, thus

$$g_0 = \frac{1 + s}{(1 - \cos \theta_{j,\max})^{1+s} - (1 - \cos \theta_{j,\min})^{1+s}}. \quad (5.12)$$

The final form of the GRB rate per unit redshift per spatial opening angle is then (Le & Dermer, 2007)

$$\frac{dN(> f_{\epsilon_{\text{pk}}})}{d\Omega dz} = \frac{c g_0}{H_0(2+s)} \frac{n_c(z) r_L^2(z)}{(1+z)^3 \sqrt{\Omega_\Lambda + \Omega_m(1+z)^3}} \times \left\{ [1 - \max(\hat{\mu}_j, \mu_{j,\min})]^{2+s} - (1 - \mu_{j,\max})^{2+s} \right\}, \quad (5.13)$$

here  $\mu_j = \cos \theta_j$  and

$$\hat{\mu}_j \equiv 1 - \frac{L_{\gamma^*}}{4\pi r_L^2(z) \Delta t_* \hat{f}_\epsilon \lambda_{\text{bol}}}, \quad (5.14)$$

where  $\hat{f}_\epsilon$  is the  $\nu F_\nu$  flux threshold sensitivity of *Swift*, taken to be  $\hat{f}_\epsilon = 10^{-8} \text{ erg cm}^{-2} \text{ s}^{-1}$ .

The function  $n_c(z)$  is the comoving star formation rate from Hopkins & Beacom (2006) which is in the form of

$$n_c(z) = \frac{1 + (a_2 z / a_1)}{1 + (z / a_3)^{a_4}}, \quad (5.15)$$

where  $a_1 = 0.015$ ,  $a_2 = 0.10$ ,  $a_3 = 3.4$ , and  $a_4 = 5.5$  are the best-fit parameters (Le & Dermer, 2007).

The unknown parameters in Equation 5.13 can be calculated by performing a fit of the function to the observed GRB redshift distribution. Le & Dermer (2007) obtained a best-fit values of  $L_{\gamma^*} = 4 \times 10^{51} \text{ ergs}$ ,  $\theta_{j,\min} = 0.05 \text{ rad}$ ,  $\theta_{j,\max} = 0.7 \text{ rad}$ , and  $s = 1.25$ . The form of the function with the best-fit values is shown

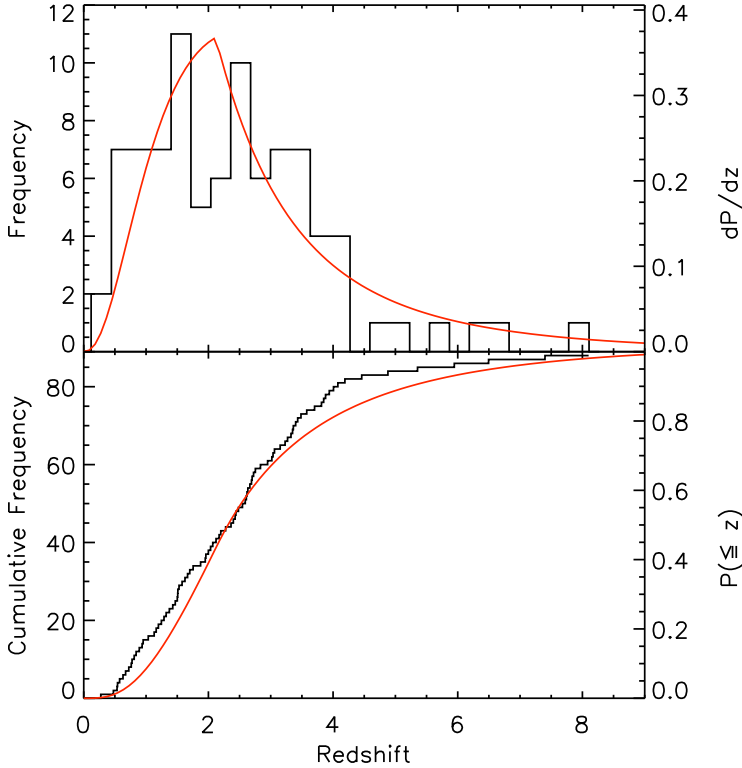


Figure 5.4: The GRB redshift distribution compared to the distribution function of Le & Dermer (2007). The best-fit values of  $L_{\gamma^*} = 4 \times 10^{51}$  ergs,  $\theta_{j,\min} = 0.05$  rad,  $\theta_{j,\max} = 0.7$  rad, and  $s = 1.25$  are used.

in Figure 5.4, as compared to the observed redshift distribution.

With this distribution function, we can estimate the probability to observe a GRB of redshift  $z \lesssim 0.1$ . Figure 5.5 shows a more detailed view of Figure 5.4 in low-redshift area. Le & Dermer (2007) estimated that the probability to observe a GRB of redshift  $z \lesssim 0.1$  is  $P(z \leq 0.1) \sim 7 \times 10^{-5}$ , and that  $P(z \leq 0.2) \sim 6.5 \times 10^{-4}$ . Assuming that 1 GRB is detected per day by any satellites, from these number we can expect to observe 1 GRB with  $z \leq 0.1$  every  $\sim 40$  years and 1 GRB every  $\sim 4.2$  years to have a redshift of  $z \leq 0.2$ . The second number is still within the expected operation time of neutrino telescopes, which is approximately 5–10 years.

Despite these discouragingly low numbers predicted by theo-



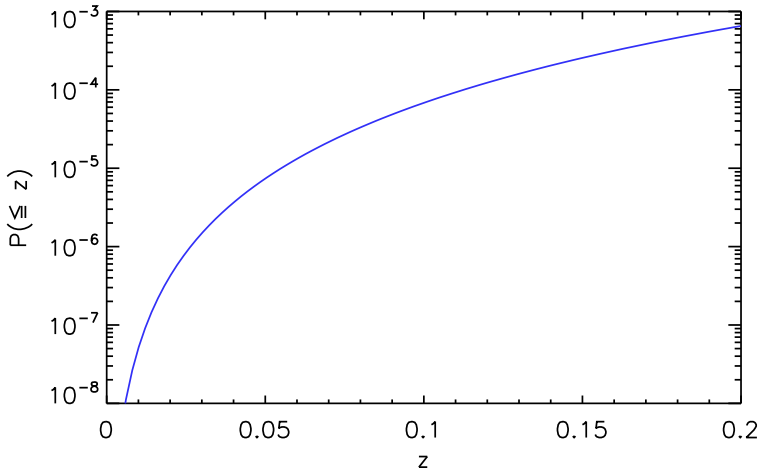


Figure 5.5: A more detailed view of the GRB redshift distribution function of Le & Dermer (2007) for low-redshift area.

retical calculations, in the last 14 years we have observed at least 6 GRBs with  $z \leq 0.1$  and 12 GRBs with  $z \leq 0.2$  within the same time period<sup>2</sup>. These facts alone show us the still-uncertain nature of the GRB redshift distribution and that this venture is still worth-pursuing.

<sup>2</sup> From the GRB index of GRBox, <http://lyra.berkeley.edu/grbox>, retrieved on August 30 2012.

## 5.2 GRB event generation and muon flux calculations

GENERATIONS of GRB events are performed for several data taking period (in years)  $n_{\text{yr}} = \{1, 2, 3, 5, 10\}$  yr. It assumed that 1 GRB is detected per day, thus making the number of GRBs generated to be  $n_{\text{GRB}} = 365 \times n_{\text{yr}}$ . For each data taking period, each GRB is generated by randomly generating the six parameters using the inverse-transform method (Nakamura & Particle Data Group, 2010). The zenith distance  $\cos \theta$  of each GRB is randomly generated assuming an isotropic spatial distribution in the sky. The azimuth angle is not generated as it does not have any effect on the resulting muon spectrum.

Only GRBs above the horizon are then selected for further calculations. the six parameters  $(L_{\text{bol}}, z, b, \Delta t, \epsilon_{\text{bk}}, \theta)$  is then used to calculate the muon spectrum at detector depth  $d = 2475$  km, following the prescriptions described in Chapters 2–3.

The on-period of each GRB observation is defined to be equal to  $T_{90}$  and the off-period is taken to be 1 hour before the GRB took place, at the same zenith distance as the observed GRB. The number of expected event at detector depth could then be calculated, and the number of expected background during the off-period.

The total number of events from GRBs above the horizon during the observation period are then summed, thus stacking all observed sources as if they are a single observation. The significance  $S$  of the observation during the data-taking period is then calculated using the Li & Ma (1983) significance formula written in Equation 4.2.

Due to the stochastic nature of GRB events, this simulation is repeated  $10^6$  times in order to analyze the distribution of the significance and to estimate the discovery potential.

### 5.3 *Result and conclusions*

THE RESULT of the simulation is shown in Figure 5.6. Each panel in the Figure describes the probability do make a detection with significance greater than any given  $S$ , for 4 different detector size (i.e.  $A_\mu^{\text{eff}} = \{10^{-3}, 10^{-2}, 0.1, 1\}$  km<sup>2</sup>) and for 5 different data-taking period.

The result in Figure 5.6 indicates that an ANTARES-sized detector of  $A_\mu^{\text{eff}} = 10^{-2}$  km<sup>2</sup> is still too small make a discovery. Even a sub-km<sup>3</sup> detector with  $A_\mu^{\text{eff}} = 0.1$  km<sup>2</sup> still has very little chance to make a discovery with at  $3\sigma$  significance, as it has only 5% probability of making a  $3\sigma$  discovery or better (for a data-taking period of 5 years).

A km-sized detector can have a better chance of making a  $3\sigma$  detection. After an operation of 5 years, it has  $\sim 50\%$  probability to detect TeV photon signals with  $3\sigma$  significance or better, and  $\sim 25\%$  probability for a  $5\sigma$  detection or better.

From these results it can be safely concluded that a neutrino telescope that can be taken seriously must have an instrumented volume of at least 1 km<sup>3</sup>, which enables it not only to detect astrophysical high-energy neutrinos but also plays its secondary role as a VHE  $\gamma$ -ray observatory.

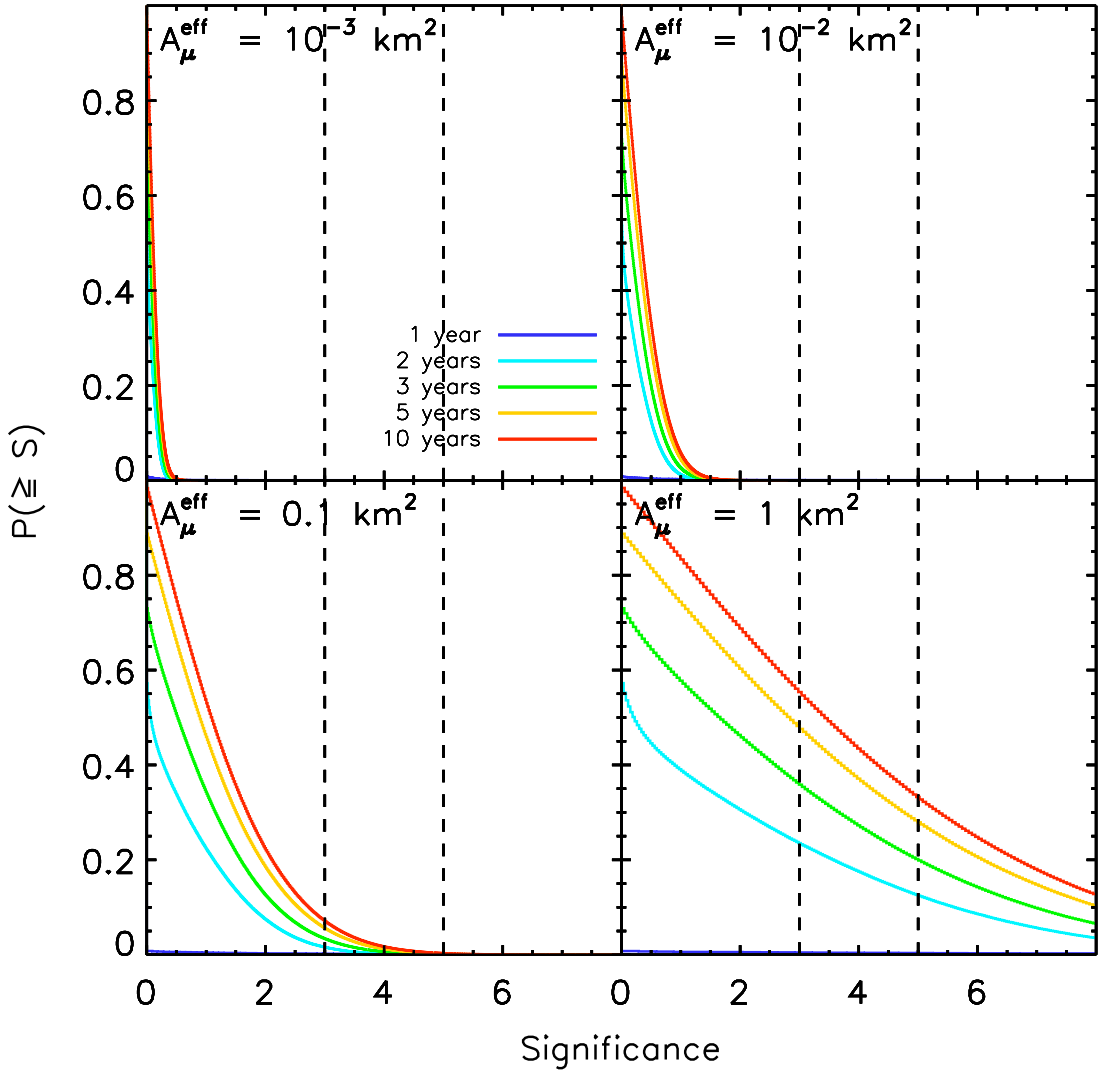


Figure 5.6: The distribution of the detection significance  $S$  of stacked GRB observations, here plotted for four different detector size and 5 different data-taking period. The larger the detector size, the better the chance to detect events with  $3\sigma$  and  $5\sigma$  significance or better, as indicated by the dashed vertical lines.

PART II

*Detector & simulations*



## 6 The ANTARES neutrino telescope

ON MAY 29th 2008, the 12th line of the ANTARES neutrino telescope was put in operation thus completing the construction which has begun in 2006 (Ageron et al., 2011). This makes ANTARES the largest neutrino telescope in the northern hemisphere and the second largest neutrino telescope in the world.

Due to the location at the bottom of the sea, at a depth of 2475 m, many technical challenges had to be met to overcome the problems that can arise from deep-sea environments. Following a discussion on the basic detection principle of a neutrino telescope, this Chapter will discuss the architecture of the ANTARES telescope and the method to reconstruct muon tracks that pass through the detector.

### 6.1 Čerenkov photons

WHEN a charged particle such as a muon traverses a medium with velocity  $\beta$  greater than the speed of light in that medium,  $u = 1/n$ , where  $n$  is the refraction index of the medium, an electromagnetic shock-wave will be generated along the trajectory of the particle (Figure 6.1). This shock-wave is in the form of coherent radiation of photons emitted at a characteristic angle  $\theta_C$  with respect to the particle's trajectory, which is determined by (Čerenkov, 1937)

$$\cos \theta_C = \frac{1}{\beta n}, \quad \beta > \frac{1}{n}. \quad (6.1)$$

For relativistic particles with velocities  $\beta \simeq 1$  traversing through water ( $n = 1.33$ ), the angle is  $\theta_C \simeq 41.2^\circ$ .

This radiation is named after Pavel Čerenkov who first noticed a very weak visible radiation from pure liquids under the influence of  $\gamma$ -rays in his experiments (Čerenkov, 1934, 1937). This happened because the electromagnetic field of the traversing particle distorts the atoms such that they will be polarized toward the trajectory of the particle. The atoms will then emit photons as they return to equilibrium (Jelley, 1958). The number of photons

Here velocities  $\beta$  and  $u$  are expressed in fractions of the speed of light in vacuum  $c$ .

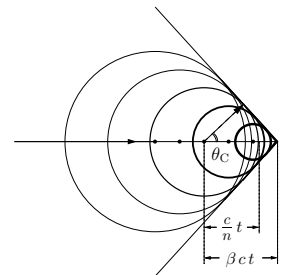


Figure 6.1: An illustration of the Čerenkov wavefront of the photons emitted at an angle  $\theta_C$ . Figure reproduced from Lim (2011).

emitted per unit wavelength per unit unit distance is

$$\frac{dN}{d\lambda dx} = \frac{2\pi\alpha Z^2}{\lambda^2} \left(1 - \frac{1}{n^2\beta^2}\right), \quad (6.2)$$

where  $\alpha$  is the fine structure constant,  $Z$  is the electric charge of the moving particle, and  $\lambda$  is the wavelength of the photons. If we integrate Equation 6.2 over  $\lambda$ , we obtain the number of photons emitted within a range of wavelength between  $\lambda_1$  and  $\lambda_2$  (Jelley, 1958):

$$\frac{dN}{dx} = 2\pi\alpha Z^2 \left(\frac{1}{\lambda_1} - \frac{1}{\lambda_2}\right) \left(1 - \frac{1}{n^2\beta^2}\right). \quad (6.3)$$

Thus for a relativistic muon with  $\beta \simeq 1$  in water, approximately 30 000 photons in the visible spectrum ( $350 \text{ nm} \leq \lambda \leq 750 \text{ nm}$ ) are emitted per meter.

## 6.2 Detection principle of a neutrino telescope

WHEN A COSMIC neutrino passes through the Earth, it may interact via the charged current interactions to produce a muon that could come out of the other side of the Earth (Figure 6.2). The muon will travel in the same direction as the neutrino with minor deviation. An upgoing track will confirm the neutrino origin of the muon since no other known particles can traverse the entire Earth.

In order to detect the faint Čerenkov light, no other source of light—such as sunlight or manmade light source—should be detected. The detector must also be deep enough to veto as much atmospheric muons as possible. Atmospheric muons are muons resulting from the interaction of cosmic rays with the atmosphere. They can have sufficient energy to penetrate great depths, but they should be detected as downgoing muon tracks (Figure 6.2). These muons will constitute a background if the direction is not accurately reconstructed. Another background is due to atmospheric neutrinos, which are also the result of cosmic-ray interactions with the atmosphere. They are indistinguishable from cosmic neutrinos.

The wavefront of the Čerenkov photons is a cone. To detect these photons, a neutrino telescope comprises a three-dimensional

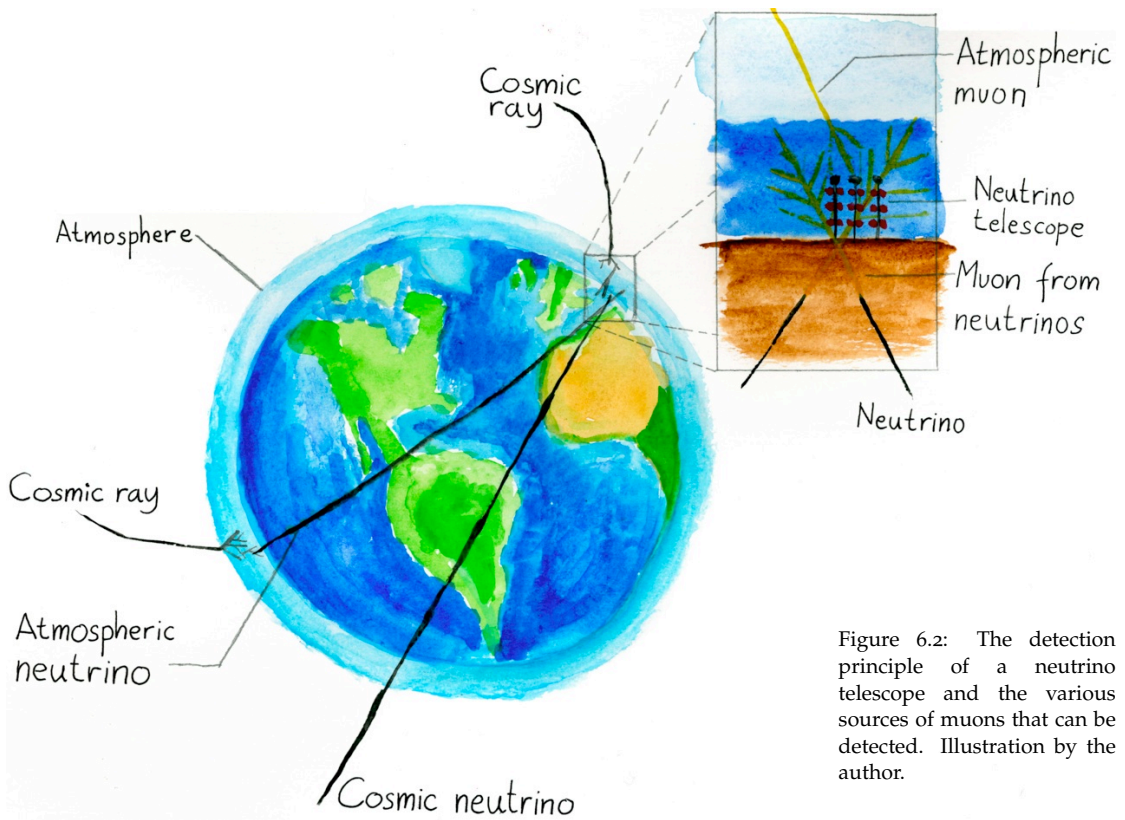


Figure 6.2: The detection principle of a neutrino telescope and the various sources of muons that can be detected. Illustration by the author.

arrangement of light-sensitive detectors, usually photomultiplier tubes (PMT). The PMTs record the arrival time and amplitude of the Čerenkov photons. For an underwater detector such as ANTARES, the PMTs are housed in a transparent pressure casing to protect the PMTs and its electronic instruments against the hostile environment of the deep sea.

### 6.3 The ANTARES detector

THE SITE of ANTARES is approximately 40 km to the southeast of Toulon, south of France (Figure 6.3). The control station of ANTARES is located at La Seyne-sur-Mer, a commune located at the west of Toulon. Power to the detector and data from the detector



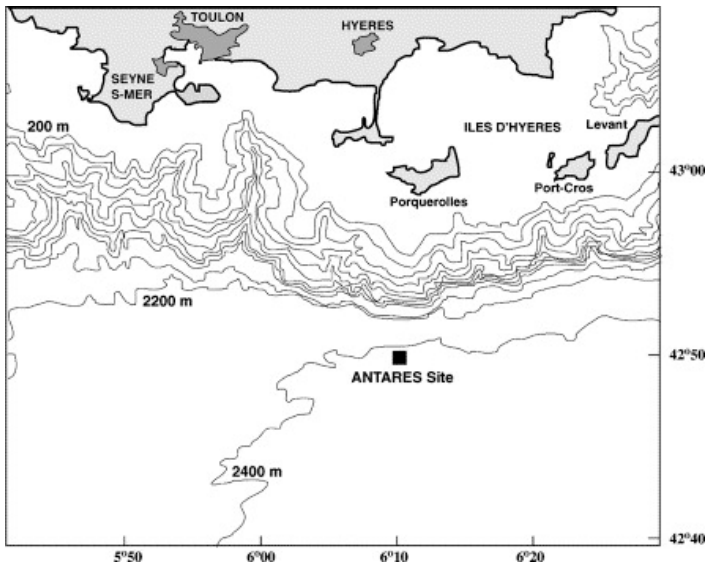


Figure 6.3: The depth contour of the Mediterranean Sea around the site of ANTARES. ANTARES is located approximately 40 km off the coast of Toulon, south of France, at a depth of 2475 m.

are transmitted through an electro-optical cable that connects the detector to the control station on the shore.

ANTARES is located on the seabed at a depth of 2475 m. All components of the detector must then be able to withstand a hydrostatic pressure between 200 and 256 bar and resist the corrosion of sea water for a minimum detector lifetime of 10 years (Ageron et al., 2011). The following subsections will give a brief description of the most important components of ANTARES. A more complete overview is given in Ageron et al. (2011).

### 6.3.1 The Optical Module (OM)

THE BASIC element of ANTARES is a glass sphere with a PMT inside, called optical module (OM), shown in Figure 6.4. The glass sphere has a diameter of 43 cm and 15 mm thickness. The material is a transparent Vitrovex<sup>®</sup> glass sphere with >95% transmission for light with wavelength above 350 nm. The glass sphere contains a PMT and a magnetic shield, kept in place by an optical gel. The gel is a two-component silicon rubber with elasticity soft enough absorb the sphere diameter reduction by the deep sea pressure and yet stiff enough to hold the PMT in place (Amram et al., 2002).

The photomultiplier tube is the Hamamatsu 10" PMT model

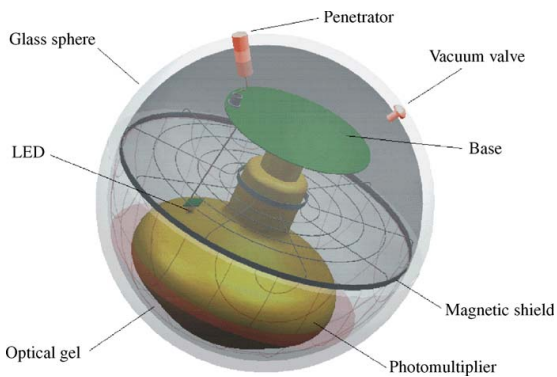


Figure 6.4: *Left:* Schematic view of an ANTARES optical module (OM). *Right:* A Hamamatsu R7081-20 10'' photomultiplier tube. Figures reproduced from Amram et al. (2002).

R7801-20 (Figure 6.4, right). It is a large hemispherical PMT of 25 cm in diameter and an effective sensitive area of 440 cm<sup>2</sup>. It is sensitive to photons with wavelength in the visible spectrum between 300–600 nm, with peak quantum efficiency (QE) of 23% at wavelength of 350–450 nm. At a voltage of 1760 V the PMT has a nominal gain of  $5 \times 10^7$ . The accuracy of the measurement of the arrival time of a photon at the photocathode is determined by the Transit Time Spread (TTS). From the measurements of 912 PMTs, the TTS is found to be  $2.79 \pm 0.15$  ns and the dark noise rate to be  $1.88 \pm 1.08$  kHz (Aguilar et al., 2005a).

The PMT is surrounded by a mesh of  $\mu$ -metal wires to minimize the influence of the Earth's magnetic field. The size of the wire mesh is  $68 \times 68$  mm<sup>2</sup> with a wire diameter of 1.08 mm, resulting in a shadowing effect of less than 4% of the photocathode area while reducing the magnetic field effects by a factor of 2.5 (Amram et al., 2002).

The high voltage system to power the PMT adopts the Cockcroft-Walton scheme (Cockcroft & Walton, 1932) to limit the power consumption to less than 300 mW. This is a factor 10 reduction compared to standard converters and passive dividers (Amram et al., 2002). The system has two independent high-voltage chains. The first chain produces a constant focusing voltage (800 V) to be applied between photocathode and first dynode, while the second

$\mu$ -metal is a nickel-iron alloy that has a very-high magnetic permeability for low-intensity magnetic fields.

chain gives the amplification voltage which can be adjusted from 400 to 1600 V by an external DC voltage (Ageron et al., 2011). A 48 V DC power supply powers the HV generator.

The OM is also equipped with a LED system used for internal calibration, especially for the calibration of the TTS. This system consists of a fast blue light-emitting diode (LED) with peak intensity around 470 nm. The LED is glued on the back of the PMT to optimally illuminate the photocathode through the aluminium coating of the tube (Amram et al., 2002). The LED is activated by an externally-driven pulser circuit.

### 6.3.2 Floors, sectors, and detector lines

THE OPTICAL modules are grouped together in triplets to form a floor or storey (Figure 6.5). The PMTs point downwards at  $45^\circ$  angle relative to the vertical to optimize photon collection from up-going muon tracks. The frame that hold them together, the optical module frame (OMF), also holds the local control module (LCM). The LCM is a Titanium cylinder housing the readout electronics. The OMF also supports various instruments for calibration and monitoring.

Floors are connected with each other by an electromechanical cable (EMC). The EMC contains 21 optical fibres for data transmission as well as 9 electrical conductors for power distribution. The distance between each floors is 14.5 m. Five connected floors make up a sector and a sector is an individual unit as far as power supply and data transmission are concerned. In each sector, one of the five LCMs is a Master LCM (MLCM) that manages data transfer between all LCMs and in the sector and the shore.

A single detector line (Figure 6.6) consists of 25 floors (or 5 sectors) linked together by the EMC. The line is anchored to the seabed by a Bottom String Structure (BSS). The BSS also allows line recovery by means of two parts: an unrecoverable deadweight on the seabed and a recoverable part on top of it, which are connected together by a release system remotely controlled by acoustic signals (Ageron et al., 2011). The BSS also contains a String Control Module (SCM) and a String Power Module (SPM). The SCM contains electronics that manages the data transmission between sectors in the line and the shore. The SPM provides indi-

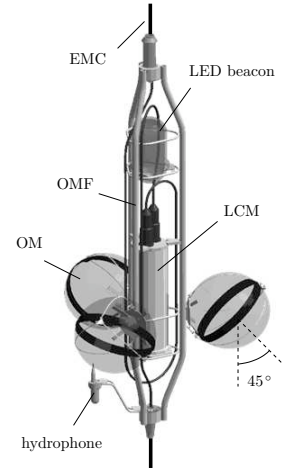


Figure 6.5: Schematic view of an ANTARES floor and its component. Figure reproduced from Lim (2011).

vidual power supplies for all sectors in the line.

The distance between the seabed to the lowest floor of each line is 100 m, to maximize the development of the Čerenkov cone for upgoing muon tracks. At the top of each line, a buoy is placed to keep the line vertical.

THE FULL ANTARES detector (Figures 6.7) consists of 12 detector lines distributed in an octagonal configuration and a dedicated instrumentation line (IL). The instrumentation line is equipped with instruments dedicated for acoustic neutrino detection (Aguilar et al., 2011b) and environmental monitoring. The last line, Line 12, contains only 20 floors. The lines are separated by an average distance of  $\sim 60$  m. The BSS of each line is connected to the junction box (JB) which is the main distribution point of data and power supply between the detector lines and the shore. The junction box is connected to the shore by a  $\sim 40$  km main electro-optical cable (MEOC).

Altogether, the 885 OMs in the 12 detector lines that comprise ANTARES cover an instrumented volume of approximately  $1.1 \times 10^7$  m<sup>3</sup>.

## 6.4 Data acquisition (DAQ) system

THE MAIN purpose of the data acquisition (DAQ) system is to convert the analogue signals from the PMTs into a format suitable for physics analysis. This process consists of several steps: The preparation for data taking, digitization of the analogue signals from the PMTs, transporting the data to shore, filtering the physics signals from backgrounds, storing and archival (Aguilar et al., 2007). Some of these aspects will be discussed below.

### 6.4.1 Signal digitization

WHEN A photon hits the photocathode of a PMT, an electron may be emitted through photoelectric effect. The electron is then accelerated through the dynode structure of the PMT and multiplied. The quantum efficiency of the PMT determines whether a photon in a certain wavelength could be detected.

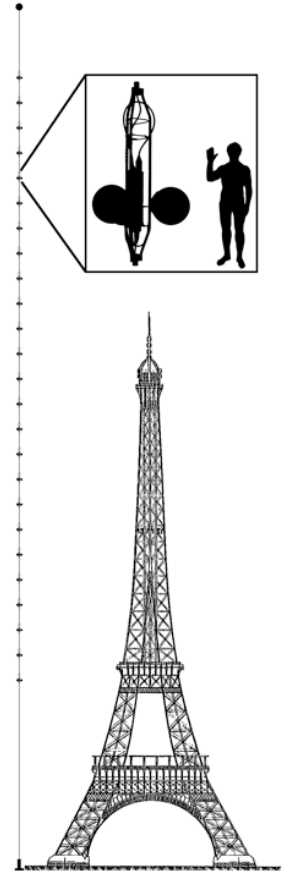


Figure 6.6: A schematic view of an ANTARES detector line and its floors, compared with the Eiffel Tower (324 m). Also shown at the inset is the comparison of an ANTARES floor to the *Pioneer* plaque man (168 cm). Figure courtesy of Guillard (2011).

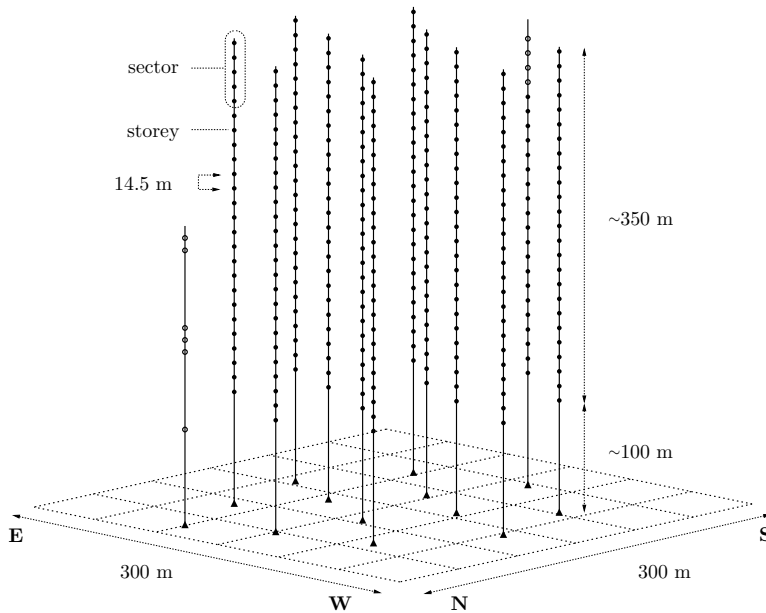


Figure 6.7: A schematic view of the full ANTARES detector, which consists of 12 detector lines of 25 floors each, and an instrumentation line (IL) of 6 storeys. Line 12 has only 20 floors. Figure reproduced from Lim (2011).

Digitization of the analogue signal occurs when the amplitude of the signal exceeds a predetermined voltage threshold. The threshold is typically set to a 0.3 of the single photoelectron signal, to suppress the PMT dark current. Signal digitization is performed by a custom-made front-end chip called the Analogue Ring Sampler (ARS). The ARS timestamps the signal when it crosses the threshold. The time is defined with respect to a reference time provided by a local clock which is synchronized with the onshore master clock. The timing resolving is better than 0.4 ns (Aguilar et al., 2010).

The change of the analogue signals is measured with an 8-bit Analogue-to-Digital Converters (ADC), with an integration gate typically set to about 35 ns to minimize the contribution of electronic noise (Aguilar et al., 2007). A dead time of  $\sim 250$  ns is introduced when the ARS is processing signals. Therefore two ARS chips are used in order to minimize this dead time. The minimum time difference between two consecutive hits in the same PMT can thus be as low as 38 ns (Aguilar et al., 2010).

The combined charge and time information of a PMT signal is called a level zero (L0) hit. All 6 ARS chips in an LCM are read-out by a Field Programmable Gate Array (FPGA) that arranges the hits produced in a preset time window into a dataframe, and buffers these in a 64 MB Synchronous Dynamic Random Access Memory (SDRAM). The complete set of dataframes from all ARSs corresponding to the same time window is called a time slice.

#### 6.4.2 *Data transfer, storage and filtering*

DURING data taking, all signals recorded by the PMTs and digitized by the ARS chips are transported to the shore station without any selection. This concept is known as the all-data-to-shore concept. All raw data are then available on shore in which further analysis can be applied.

Each LCM contains a CPU connected to the onshore computer farm through the main electro-optical cable. The buffered data stored in the SDRAM are sent as single packet to shore using TCP/IP (Aguilar et al., 2007). Each LCM CPU is connected to the MLCM through a bidirectional Fast Ethernet link of 100 Mb/s. In the MLCM, these links are multiplexed using an Ethernet switch into two unidirectional 1 Gb/s links, one for incoming control signals and one for outgoing data.

Data transport between the detector and the shore station employs the dense wavelength division multiplexing (DWDM). Multiple wavelengths are used to transmit different streams of data along a single fibre (Aguilar et al., 2007).

As a consequence of the all-data-to-shore concept, the rate of data is typically at 0.3–0.5 Gb/s (Aguilar et al., 2007). The vast majority of these data are due to the optical background in the sea. A filtering system must be employed to reduce the demand for data storage. A computer farm in the shore station is used for this purpose. The algorithms implemented are designed to search for a physics signal by looking for space-time correlations between hits. The algorithm looks for a set of causally-connected hits. If such event is found, all hits during a preset time window are stored.

## 6.5 Calibrations

THERE are various calibrations performed to operate the detector optimally: The time calibration is necessary to precisely determine the arrival time of the Čerenkov photons at each PMT. Because of sea currents and the flexibility of the electromechanical cables, the detector lines can sway sideways and thus displace the position of each PMT relative to the vertical. Position calibration is performed to determine the accurate location of all PMTs at any given time.

A precise measurement of the photon arrival time and the position of each PMTs allows tracks to be reconstructed with an accurate angular resolution, which is expected to be  $\lesssim 0.3^\circ$  for muons of energies above 10 TeV (Ageron et al., 2007). The charge calibration is used to convert the data into units photoelectrons.

### 6.5.1 Time calibration

THE RELATIVE arrival times of the Čerenkov photons between PMTs are essential for an accurate reconstruction of the muon direction. The difference of each local clock relative to the onshore master clock thus has to be known. The time resolution of the clock is limited by the transit time spread (TTS) of the signal in the PMTs and by the scattering and chromatic dispersion of light in seawater which typically has  $\sigma \sim 1.5$  ns (Aguilar et al., 2005b).

Time calibration should reach a precision below the nanosecond level. Several complementary, independent calibration systems are implemented to this end.

The internal clock calibration system sends signals between the onshore master clock and the local clock in each LCMs. The time offset between all LCM clocks can be measured by recording the time delays of the return signals of each floor relative to the original clock signal emission time. A resolution of  $\sim 0.1$  ns is obtained from measurements in real conditions (Aguilar et al., 2011a).

The blue LED inside each OMs is used to measure the relative variation of the PMT transit time. Using this method, the path traversed by the signal from the PMT photocathode up to read-out electronics can be monitored. Over an eight month period, the variation of the transit time is found to be less than  $\sim 0.2$  ns (Aguilar et al., 2011a).

The optical beacon system allows the relative time calibration of different OMs to be determined as well as the influence of water properties on the light propagation to be monitored (Ageron et al., 2007). The optical beacon system consists of a series of pulsed light sources distributed throughout the detector. An LED beacon is composed of several LEDs, pulsed by dedicated electronic circuits. Four blue LED (470 nm) beacons are located in every line of the detector at floors 2, 9, 15, and 21 (counted from bottom to top), and two green (532 nm) laser beacons are located on the BSS of lines 7 and 8 (Aguilar et al., 2011a). Once per week a time calibration is done using the LED and laser beacons.

Calibration using the optical beacon system yield a time resolution of  $\sim 0.5$  ns. The time resolution is thus dominated by contributions from the transit time spread of the PMT, and the contributions from the scattering and chromatic dispersion of light in water (Aguilar et al., 2011a).

Absolute timing is performed by synchronizing the onshore master clock with the Global Positioning System (GPS) time, which provides a time accuracy of  $\sim 100$  ns (Aguilar et al., 2011a).

### 6.5.2 *Position calibration*

THE SWAY of the detector lines due to sea currents is measured by two independent systems: an acoustic positioning system and a tiltmeter-compass system (Ardid, 2009).

A High Frequency Long Baseline (HFLBL) acoustic system is used to determine the three-dimensional position of hydrophones along a detector line. The positions are obtained by triangulation from emitters anchored in the base of the line and autonomous transponders on the sea floor. This method has an accuracy of 10 cm.

The tiltmeter-compass system gives the local measurements of tilts (roll, pitch) and heading of storeys. The system has a measurement accuracy of  $0.2^\circ$  in tilt and  $1^\circ$  in heading. The measurements of the tilt and heading of each detector line is performed every 2 minutes.

The swaying of the detector line is reconstructed using a global  $\chi^2$  fit of a line shape model to the data. The line shape model is then employed to calculate the position of all OMs at any given



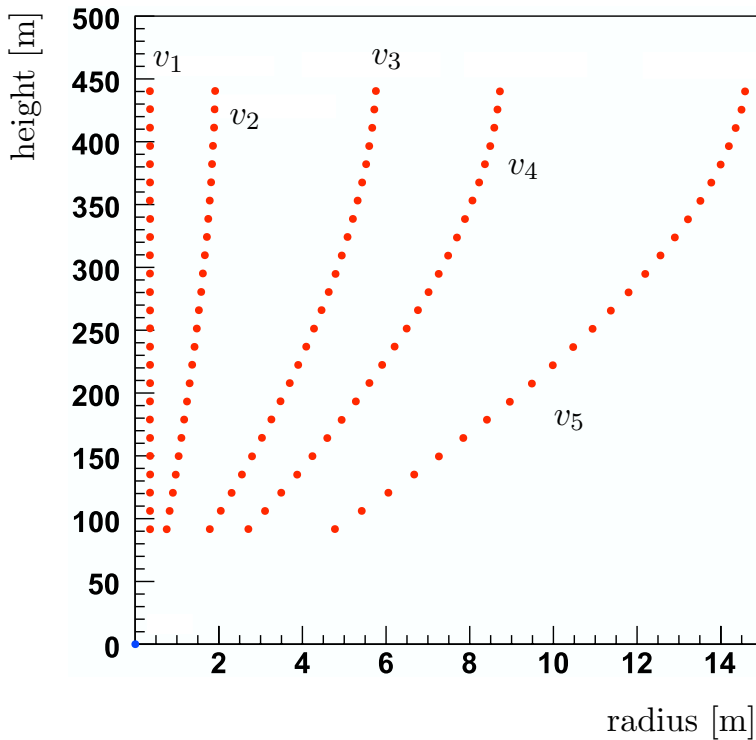


Figure 6.8: The shape of a detector line due to sea current. The swaying is shown for various sea current velocities:  $v_1 = 0.01$  cm/s,  $v_2 = 7$  cm/s,  $v_3 = 12.6$  cm/s,  $v_4 = 16$  cm/s, and  $v_5 = 20$  cm/s. The horizontal scale is exaggerated for illustration purpose. Figure reproduced from Fritsch (2010).

time, relative to the position of the BSS. The absolute position of the BSS itself is determined during the deployment of the BSS with a remotely operated vehicle (ROV). This is performed by acoustic positioning of the ROV and knowing the GPS location of the ship at the surface. The reconstructed detector line shape due to various values of sea current velocities is shown in Figure 6.8.

## 6.6 Triggering and track reconstruction

THE MAJORITY of the data taken by ANTARES will come from random backgrounds due to the decay of the radioactive Potassium isotope  $^{40}\text{K}$ , and bioluminescence.

The decay of  $^{40}\text{K}$  will introduce a continuous baseline rate of  $\sim 35$  kHz (Figure 6.9) in the measurement of photon rate by the PMTs (Amram et al., 2000). Bioluminescence, which is caused

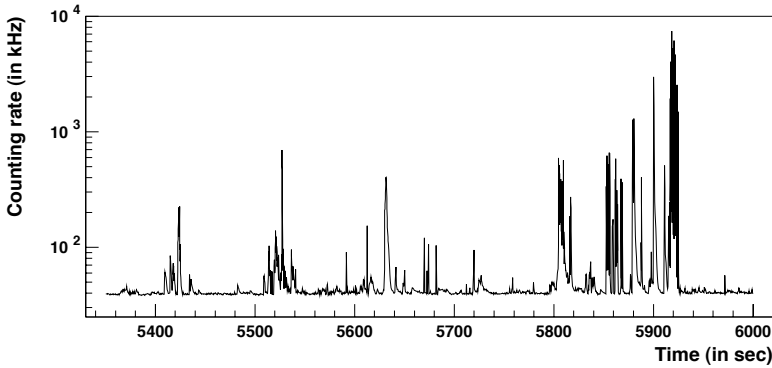


Figure 6.9: A typical measurement of the photon counting rate at 0.3 pe level. A continuous baseline rate of  $\sim 35$  kHz can be observed here, which is due to the  $^{40}\text{K}$  decay. We can also see an occasional burst of photon rate which is due to bioluminescence. Figure reproduced from Amram et al. (2000).

by marine life, will give rise to bursts with rates up to several orders of magnitude above the baseline rate. Long-term observations show that these burst due to bioluminescence have seasonal variations that correlate with the sea current.

A reduction of this background noise can be obtained by searching for hits within a 20 ns window in PMTs of the same floor or single hits with an amplitude higher than 3 pe. Hits satisfying these criteria are called level one (L1) hits. By searching for L1 hits satisfying the causality relation one can reduce the background rate by a factor of  $\sim 10^4$  (de Jong, 2005).

### 6.6.1 Causality relation

PHOTON hits due to the emission of Čerenkov radiation from a muon track should be causally related in space-time. In Figure 6.10 the track of a muon passing through a part of the detector is depicted. Consider a pair of hits detected in  $\text{PMT}_i$  and  $\text{PMT}_j$  respectively at time  $t_i$  and time  $t_j$ . If we assume that both hits are Čerenkov photons emitted by the same muon, the time of the hits and the distance between the PMTs must then satisfy the causality relation

$$|t_i - t_j| = r_{ij} \frac{n}{c}, \quad (6.4)$$

where  $r_{ij}$  is the distance between the two PMTs,  $n$  is the refractive index of seawater, and  $c$  is the speed of light (Figure 6.10). This Equation can be used to look for a cluster of hits. If the cluster

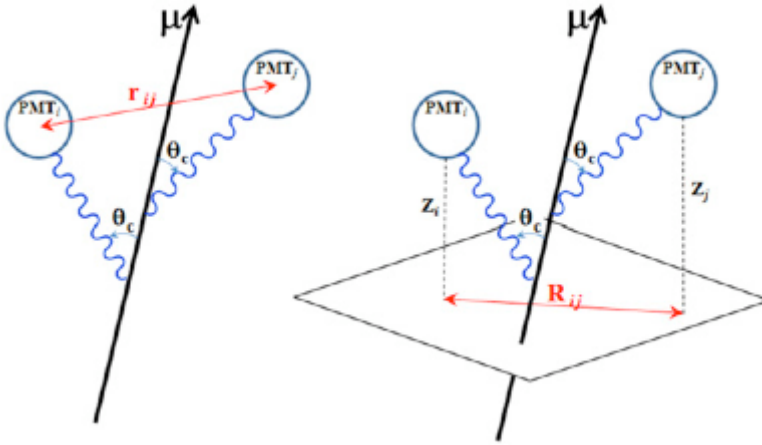


Figure 6.10: *Left*: Definitions employed in the causality criterion. *Right*: Definitions employed in a directional trigger. Figure reproduced from Ageron et al. (2011).

contains at least 5 L1 hits or a local cluster of neighbouring L1 hits, then the event will be stored.

A directional trigger can be applied which includes a scan over a number of directions. Two hits can be considered to come from the same muon track if they satisfy the direction-specific causality relation

$$(z_i - z_j) - R_{ij} \tan \theta_C \leq c(t_i - t_j) \leq (z_i - z_j) + R_{ij} \tan \theta_C, \quad (6.5)$$

where  $z_{i,j}$  refers to the positions of PMT  $i, j$  along the muon direction,  $R_{ij}$  is the distance between the two PMTs in the plane perpendicular to the muon direction, and  $\theta_C$  is the Čerenkov angle in water. If a cluster contains at least 5 L1 hits within  $R_{ij} \leq 90$  m, the event will be triggered.

### 6.6.2 Onshore filtering system and the GRB Coordinates Network (GCN)

THE PC FARM that comprises the onshore filtering system is also linked to the GRB Coordinates Network (GCN). Whenever an alert from GCN is received, all raw data currently being processed are immediately saved to disk. The data stored in memory, which were taken before the alert is received, are also saved to disk. This is possible because the data filtering PCs serve also as a buffering system that delay the filtering process and store the raw data

memory as long as possible. This allows us to save the raw data up to 4 minutes taken before the alert was received (Bouwhuis, 2005). It is possible to store all the raw data up to 3 minutes after the alert is received, this depends on the size of the raw data itself. This linking of onshore filtering system to GCN alert system allows the sensitivity of ANTARES to transient sources such as GRBs or X-ray flares to be maximized.

### 6.6.3 Track reconstruction

THE GOAL of track reconstruction is to obtain the position and direction of the muon track based on the recorded photon hits. The trajectory of the muon can be expressed by the normalized direction  $\mathbf{d} \equiv (d_x, d_y, d_z)$ , the position  $\mathbf{p} \equiv (p_x, p_y, p_z)$  at a fixed time  $t_0$ . We can also express the direction in terms of azimuth  $\phi$  and zenith distance  $\theta$ , i.e.  $\mathbf{d} = (\sin \theta \cos \phi, \sin \theta \sin \phi, \cos \theta)$ , which explicitly reduces the number of directional parameters to two. There are thus five independent parameters that we seek.

The reconstruction algorithm is performed in four consecutive procedures, in which the final procedure gives the most accurate result but requires an *a priori* estimate of the track parameters that should be close to the true values (Heijboer, 2004).

In general, the fitting is based on the time residuals of the recorded hits:

$$r_i = t_i - t_{i,\text{th}}, \quad (6.6)$$

where  $t_i$  is recorded time of a hit and  $t_{i,\text{th}}$  is the theoretical time of hit should it comes from a Čerenkov photon, given the track parameters.

To calculate the theoretical time of hit  $t_{i,\text{th}}$  we must first know the distance between the track and the PMT in which it is recorded. In Figure 6.11, the geometry is described. Let us first define  $\mathbf{v} = \mathbf{q} - \mathbf{p}$ . We can project  $\mathbf{v}$  to the track to obtain  $\|\mathbf{l}\| = \mathbf{v} \cdot \mathbf{d}$ . The length of vector  $\mathbf{k}$  can then be computed by

$$\|\mathbf{k}\| = (\|\mathbf{v}\|^2 - \|\mathbf{l}\|^2)^{1/2}. \quad (6.7)$$

The theoretical time of hit is then

$$t_{i,\text{th}} = t_0 + \frac{1}{c} \left( \|\mathbf{l}\| - \frac{\|\mathbf{k}\|}{\tan \theta_C} \right) + \frac{\|\mathbf{k}\|}{v_g \sin \theta_C}, \quad (6.8)$$

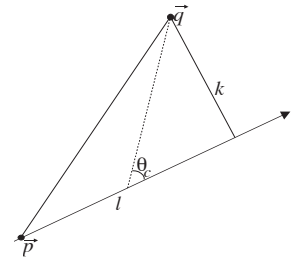


Figure 6.11: Geometry of the detection of a Čerenkov photon. A muon with direction  $\mathbf{d}$  goes through point  $\mathbf{p}$ . A Čerenkov photon is emitted at an angle  $\theta_C$  and is detected by an OM located at  $\mathbf{q}$ . The vector between  $\mathbf{p}$  and  $\mathbf{q}$  is  $\mathbf{v}$ , and  $\mathbf{k}$  is the vector towards  $\mathbf{q}$  that is perpendicular to  $\mathbf{d}$ . Figure reproduced from Heijboer (2004).

where  $v_g$  is the group velocity of light.

THE FIRST STAGE of track reconstruction is the linear prefit. Let us first denote the position of the  $i$ -th hit as  $(x_i, y_i, z_i)$ . In the prefit it is assumed that the hits occur on points located on the muon track. This assumption can be a reasonable approximation if the length of the muon track in the detector is much larger than the attenuation length of light (Heijboer, 2004). The following relation thus holds:

$$\mathbf{y} = \mathbf{H}\Theta, \quad (6.9)$$

here  $\mathbf{y}$  is a vector containing the hit positions,

$$\mathbf{y} = [x_1, y_1, z_1, \dots, x_n], \quad (6.10)$$

$\Theta$  is a vector containing the track parameters

$$\Theta = [p_x, d_x, p_y, d_y, p_z, d_z]^T, \quad (6.11)$$

and  $\mathbf{H}$  is a matrix containing the hit times

$$\mathbf{H} = \begin{pmatrix} 1 & ct_1 & 0 & 0 & 0 & 0 \\ 0 & 0 & 1 & ct_1 & 0 & 0 \\ 0 & 0 & 0 & 0 & 1 & ct_1 \\ 1 & ct_2 & 0 & 0 & 0 & 0 \\ 0 & 0 & 1 & ct_2 & 0 & 0 \\ \vdots & \vdots & \vdots & \vdots & \vdots & \vdots \\ 0 & 0 & 0 & 0 & 1 & ct_n \end{pmatrix}. \quad (6.12)$$

The estimate of the track parameters  $\hat{\Theta}$  can be calculated by minimizing the  $\chi^2$ ,

$$\chi^2 = [\mathbf{y} - \mathbf{H}\hat{\Theta}]^T \mathbf{V}^{-1} [\mathbf{y} - \mathbf{H}\hat{\Theta}], \quad (6.13)$$

where  $\mathbf{V}$  is the covariance matrix of the error estimates on the hit positions, which usually is assumed to be diagonal. By minimizing  $\chi^2$  we can obtain

$$\hat{\Theta} = [\mathbf{H}^T \mathbf{V}^{-1} \mathbf{H}]^{-1} \mathbf{H}^T \mathbf{V}^{-1} \mathbf{y}. \quad (6.14)$$

FOR THE SECOND STAGE, an M-estimator fit is performed. This fit works by maximising a function  $g(r)$ . The fit is not very sensitive

to the accuracy of the starting value, so it seems a logical continuation of the previous stage. The function of the time residuals  $r_i$  that provides good results are found to be

$$g(r_i) = -2\sqrt{1 + r_i^2/2} + 2. \quad (6.15)$$

The hits used in this stage are based on the result of the linear prefit. The time residual  $r_i$  must satisfy  $-150 \text{ ns} \leq r_i \leq 150 \text{ ns}$  and a distance from the fitted track no larger than 100 m.

THE THIRD STEP is a maximum-likelihood fit where the hit selection is based on the results of the M-estimator fit. The residuals used in this stage must satisfy  $-0.5 \times R \leq R_i \leq R$ , where  $R$  is the root mean square of the residuals used for the M-estimator fit. Hits that are part of a coincidence are also selected. The maximum-likelihood fit is performed by searching for parameters that maximize

$$P(\text{event}|\text{track}) = \prod_i P(t_i|t_{i,\text{th}}, a_i, b_i, A_i). \quad (6.16)$$

Here  $P(t_i|t_{i,\text{th}}, a_i, b_i, A_i)$  is a probability distribution function (PDF) of  $t_i$  given  $(t_{i,\text{th}}, a_i, b_i, A_i)$ , where  $A_i$  is the amplitude of the hit, and

$$b_i = \frac{\|\mathbf{k}_i\|}{\sin \theta_C} \quad (6.17)$$

is the length of the photon path, and

$$a_i = [\mathbf{v} - \mathbf{d} (\|\mathbf{l}\| - b)] \cdot \mathbf{w} \quad (6.18)$$

is the cosine of the angle of incidence of the photon on the OM. Here  $\mathbf{w}$  is the direction where the OM points. For a head-on collision of a photon with the photocathode,  $a = -1$ , whereas  $a = 1$  means that the photon hits the insensitive rear of the OM.

The PDF used in this fit was developed by Hubaut (1999), and is shown in Figure 6.12. This PDF does not take photon hits due to backgrounds into account.

THE LAST TWO steps are then repeated with different starting points as input tracks. The different starting points are calculated

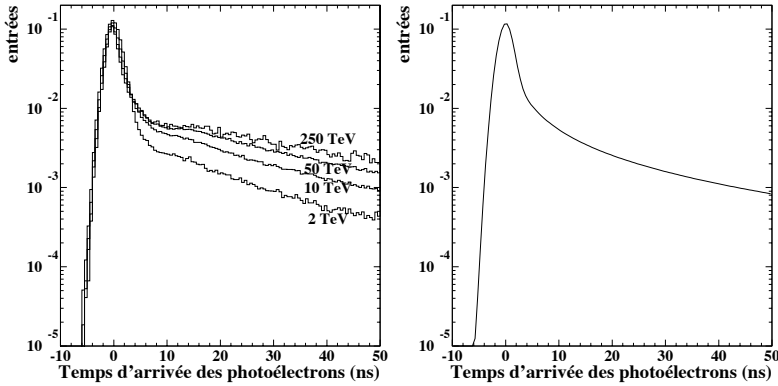


Figure 6.12: The shape of the PDF used in the maximum-likelihood. On the left is the PDF based on simulations, for Čerenkov photons coming from muons of different energies. On the right is a parametrisation of the PDF for a muon of energy 10 TeV. Figures reproduced from Hubaut (1999).

by performing a series of rotations and translations. The result with the best likelihood per degree of freedom is then kept. The number of starting points that result in track estimates compatible with the preferred result (those that give the same track direction to within  $1^\circ$ ) is called  $N_{\text{comp}}$ .

THE FINAL STEP is then to use the starting point obtained from the previous step as a starting point for the maximum-likelihood fit with an improved PDF, which is the sum of the PDF for signal hits and optical background hits:

$$P(t_i | t_{i,\text{th}}, a_i, b_i, A_i) = \frac{1}{N_{\text{total}}} (P_{\text{sig}} N_{\text{sig}} + R_{\text{bg}}), \quad (6.19)$$

here  $N_{\text{total}}$  and  $N_{\text{sig}}$  are the total number of hits and the number of signal hits, and  $R_{\text{bg}} = N_{\text{bg}} / \Delta t = N_{\text{bg}} P_{\text{bg}}$  is the optical background rate.  $\Delta t$  is the time window of the selection of hits in the event and  $N_{\text{bg}}$  is the expected number hits due to background. For this fit only hits with residuals between  $-250$  ns and  $250$  ns and hits within local coincidences are used.

The final quality of the fit can be characterized by the quantity  $\Lambda$  which is defined to be

$$\Lambda \equiv \frac{\log L}{N_{\text{DOF}}} + 0.1(N_{\text{comp}} - 1), \quad (6.20)$$

where  $L$  is the likelihood at maximum and  $N_{\text{DOF}}$  is the degree of freedom. A higher  $\Lambda$  value means a better-reconstructed event.

The covariance matrix  $\mathbf{V}$  can also be calculated by calculating the second derivatives of the likelihood function at the fitted maximum:

$$[\mathbf{V}^{-1}]_{ij} = -\frac{\partial^2 \log L}{\partial \mathbf{x}_i \partial \mathbf{x}_j}, \quad (6.21)$$

where  $\mathbf{x} = (p_x, p_y, p_z, \theta, \phi)$ . From this covariance matrix we can extract the covariance matrix for the reconstructed azimuth  $\hat{\phi}$  and the reconstructed zenith distance  $\hat{\theta}$ :

$$\hat{\sigma} = \begin{bmatrix} \sigma_{\hat{\phi}}^2 & \sigma_{\phi\theta} \\ \sigma_{\phi\theta} & \sigma_{\hat{\theta}}^2 \end{bmatrix} \quad (6.22)$$

The error estimate of the direction of the reconstructed muon track  $\sigma_\psi$  can then be obtained from the covariance matrix, i.e.

$$\sigma_\psi = \left( \sin^2 \hat{\theta} \sigma_{\hat{\phi}}^2 + \sigma_{\hat{\theta}}^2 + 2 \sin \hat{\theta} \sigma_{\phi\theta} \right)^{1/2}. \quad (6.23)$$

These two parameters,  $\Lambda$  and  $\sigma_\psi$ , are often used for event selections. In later chapters these parameters will be used to evaluate the quality of the fit and as basis for cuts.

Knowing how the ANTARES telescope works and how muon tracks are reconstructed, we can then proceed to the simulations of downgoing muon events in order to investigate the sensitivity of the ANTARES telescope high-energy  $\gamma$ -rays.



# 7 *Simulation of the detector response to downgoing muons*

THIS CHAPTER will discuss the results of Monte Carlo simulations of the response of the ANTARES detector to downgoing muon signals. There are two reasons why this study is necessary: First, the photomultipliers (PMT) are pointing downward to optimize the detection of upgoing neutrino-induced muons, hence the detection efficiency of downgoing muons will be different. This will affect the energy threshold of muon detection as well as the angular resolution of the track reconstruction. Secondly, downgoing muon events in previous analyses are treated only as backgrounds and not as possible signal. In this work downgoing muon events are treated both as signal and background.

## 7.1 *Simulation chains*

HERE we are interested in how downgoing muons are seen by the detector. The simulations are thus performed in the environment around the detector. This volume is called the *can*, a cylindrical volume with the detector placed at the centre. The size of the can covers the detector with a margin of a few times the attenuation length of light. With this definition, the Čerenkov photons produced outside the can do not reach the PMTs and thus do not need to be simulated.

Muon tracks are generated with *gentra*, a simpler version of *genhen* (Bailey, 2002), developed specifically to generate single muon tracks coming from a fixed zenith distance. The muons are generated with initial positions at the surface of the can. The azimuthal directions are isotropic but directed towards the inside of the can, while the zenithal directions are according to the provided zenith distance range. It is also possible to generate zenithal directions for a single value of zenith distance.

The energy of the muons are generated according to the power-law spectrum  $dN_\mu/d\epsilon_\mu \sim \epsilon_\mu^{-\alpha}$ , where  $\alpha$  is usually fixed to  $\alpha = 2$ . The generated energy range is between 10 GeV and 1 PeV. In the

first part of the simulation, the zenith distance range is from  $0^\circ$  (coming straight from the zenith) to  $90^\circ$  (parallel to the horizon), equally divided into six bins each  $15^\circ$  wide. For each zenith distance bin,  $10^7$  muon tracks are generated. For convenience this data set will be referred to as SIMULATION 1.

The propagation of the muon towards the detector, the generation of Čerenkov photons, and the generation of hits recorded by the PMTs are simulated with the km3 program (Navas & Thompson, 1999; Bailey, 2002). km3 uses a modified version of the MUSIC<sup>1</sup> package (Antonioli et al., 1997) to propagate the muon. MUSIC simulates both the energy loss and multiple scattering, and treat all manners of muon interaction with matter as a stochastic processes. The tracking of every photon emitted is very inefficient, thus a set of tables is constructed by taking into account the absorption and scattering of light and storing the average photon fields produced by muons for various distances, positions, and orientations of the PMTs with respect to the track. The number of the hits and the times on the optical modules are then sampled from these tables.

The next step is then simulated with the TriggerEfficiency (de Jong, 2009) program. This program simulates the PMTs and data acquisition system. Optical background is also added, the rates can either be provided by the user or generated according to a Poisson distribution based on measured rates. The latter can be chosen when one is interested to reproduce the conditions of a specific data taking period. Signal and background hits are then generated by simulating the response of the PMTs such as TTS and electronic, the charge threshold, time integration, and dead time. The hits are then processed based on the filtering algorithm discussed in Section 6.6.1. The events used in this analysis are triggered with the  $3N$  trigger. This trigger is not only the standard trigger that is always present in ANTARES data taking, but it also has a high purity, i.e. has a directional information which is important for sources with known directions such as GRBs.

In TriggerEfficiency, the random background hits are generated according to the normal distribution, its rate is set to 100 kHz. The number of triggered physics events for each zenith distance is shown in the 4th column of Table 7.1.

<sup>1</sup> MUon Simulation Code

Zenith distance [ $^{\circ}$ ]	Can area [ $\text{km}^2$ ]	$N_{\text{gen}}$	$N_{\text{phys}}$	$N_{\text{reco}}$	$N_{\text{reco}}(\psi \leq 1^{\circ})$
$0 \leq \theta \leq 15$	0.18	$10^7$	34556 (0.35%)	33308 (96.39%)	3956 (11.88%)
$15 \leq \theta \leq 30$	0.22	$10^7$	17979 (0.18%)	17713 (98.52%)	3887 (21.94%)
$30 \leq \theta \leq 45$	0.26	$10^7$	17783 (0.18%)	17659 (99.30%)	5143 (29.12%)
$45 \leq \theta \leq 60$	0.27	$10^7$	24982 (0.25%)	24881 (99.60%)	8376 (33.66%)
$60 \leq \theta \leq 75$	0.27	$10^7$	42374 (0.42%)	42279 (99.78%)	16374 (38.73%)
$75 \leq \theta \leq 90$	0.25	$10^7$	81080 (0.81%)	80073 (98.76%)	35772 (44.67%)

The tracks are then reconstructed with the `aafit v0r9pre` algorithm, which employs the track reconstruction algorithm discussed in Section 6.6.3.

From the fitting result of `aafit` we can obtain the goodness-of-fit  $\Lambda$ , which is the fit likelihood per number of degrees of freedom. The direction of the reconstructed track in azimuth angle  $\hat{\phi}$  and zenith distance  $\hat{\theta}$  is obtained as well as the covariance matrix  $\hat{\sigma}$ . The difference between the true track direction and the reconstructed track direction can be calculated from the dot product of the direction vectors of the true muon directions and the reconstructed directions:

$$\begin{aligned} \cos \psi &= \mathbf{x}_{\text{true}} \cdot \mathbf{x}_{\text{reco}}, \\ &= x_{\text{true}}x_{\text{reco}} + y_{\text{true}}y_{\text{reco}} + z_{\text{true}}z_{\text{reco}}, \end{aligned} \quad (7.1)$$

where  $\mathbf{x}_{\text{true}} = \{x_{\text{true}}, y_{\text{true}}, z_{\text{true}}\}$  and  $\mathbf{x}_{\text{reco}} = \{x_{\text{reco}}, y_{\text{reco}}, z_{\text{reco}}\}$  are the direction vectors of respectively the true muon direction and the reconstructed muon direction.

From the error covariance matrix  $\hat{\sigma}$  (Equation 6.22) we would

Table 7.1: A summary of the simulation results. The can area used in each zenith distance bin is the median value of the can area for each muon track within the bin.  $N_{\text{gen}}$  is the number of generated muon tracks at the edge of the can.  $N_{\text{phys}}$  is the number of triggered events.  $N_{\text{reco}}$  is the number of tracks successfully reconstructed by `aafit` algorithm, and  $N_{\text{reco}}(\psi \leq 1^{\circ})$  is the number of tracks reconstructed to better than  $1^{\circ}$  from its true direction. The percentages in shown in a column is calculated relative to the previous column.

Table 7.2: A summary of the simulation results for the fixed zenith distance source.

Zenith distance [ $^{\circ}$ ]	Can area [ $\text{km}^2$ ]	$N_{\text{gen}}$	$N_{\text{phys}}$	$N_{\text{reco}}$	$N_{\text{reco}}(\psi \leq 1^{\circ})$
0	0.14	$10^7$	44654 (0.45%)	43385 (97.16%)	22357 (51.53%)
15	0.20	$10^7$	23496 (0.23%)	22908 (97.50%)	3446 (15.04%)
30	0.24	$10^7$	16499 (0.16%)	16332 (98.99%)	4301 (26.33%)
45	0.27	$10^7$	19889 (0.20%)	19784 (99.47%)	6213 (31.40%)
60	0.28	$10^7$	30997 (0.31%)	30905 (99.70%)	11070 (35.82%)
75	0.27	$10^7$	56895 (0.57%)	56793 (99.82%)	23622 (41.59%)

then obtain the angular error estimate  $\sigma_\psi$  (Equation 6.23).

It is assumed that the detector is running with all 12 lines operational, which means that it is assumed that the detector is running with full capacity.

TABLE 7.1 summarised the results after each stage of simulation is passed. The numbers suggest that less than  $\sim 1\%$  of the generated events are actually detected and reconstructed. While this number look discouraging, a look at Figure 7.1 however indicate that the majority of the undetected events are low-energy muons with energy  $\epsilon_\mu \lesssim 50$  GeV. This can thus be interpreted as the threshold energy of ANTARES for downgoing muons. As we can see in column 5,  $\sim 99\%$  of the detected events can be reconstructed albeit with varying degree of qualities. Column 6 tells us the number of reconstructed tracks with accuracy  $\psi \leq 1^\circ$ . The percentage varies with zenith distance, i.e. the shallower the tracks, the better its reconstruction quality.

To simulate a GRB event, separate simulations have also been performed with *gentra*. The simulations generate muon tracks from a fixed zenith distance. Six cases of zenith distances are simulated, from  $\theta = 0$  to  $\theta = 75^\circ$ , with  $15^\circ$  intervals. The generated tracks are then processed using the same procedure. A summary of the simulation results is shown seen in Table 7.2. We will refer to this data set as SIMULATION 2.

## 7.2 Detector performance

SEVERAL aspects of the simulations pertaining to the performance of ANTARES will be discussed in this Section, namely the shape of the energy spectrum, the effects of quality cuts, and the effective areas.

### 7.2.1 The muon energy spectrum

FIGURE 7.1 depicts the muon energy spectrum for SIMULATION 1 at various stages of the simulation. As mentioned in Section 7.1, a minimum threshold at muon energy  $\epsilon_\mu \sim 50$  GeV can be seen. The detection efficiency increases with energy and at TeV scale the majority of muon tracks can be succesfully reconstructed. The

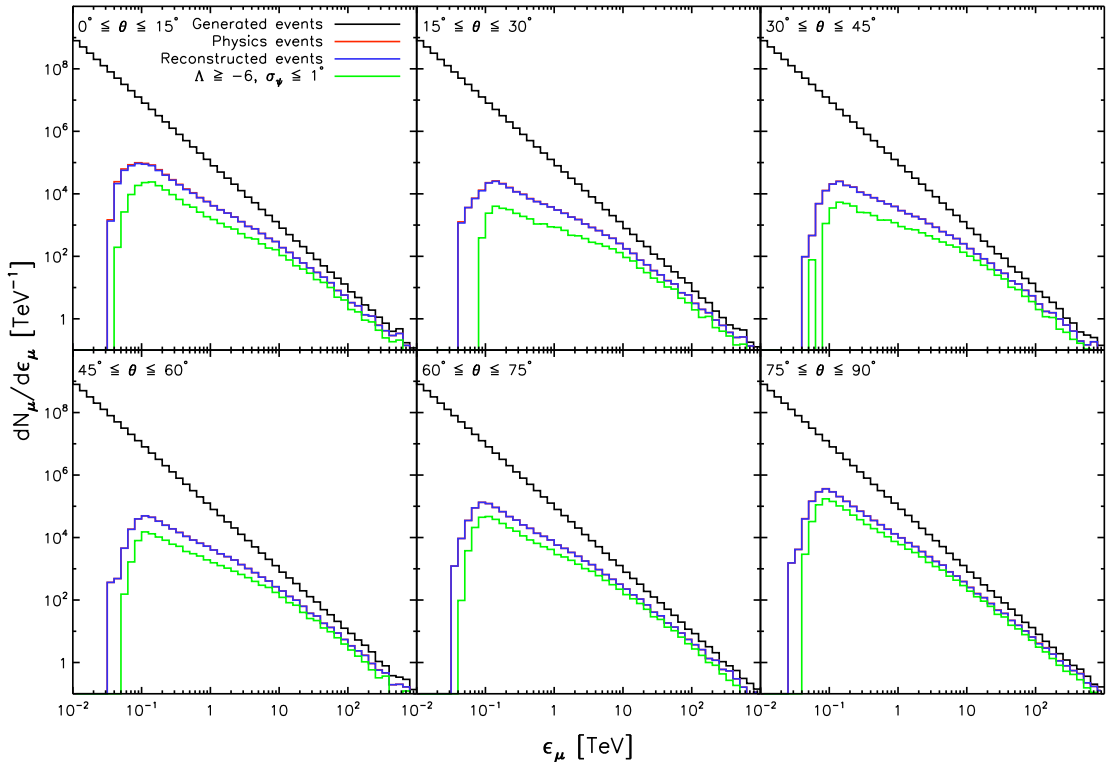


Figure 7.1: The development of the muon spectrum after each stage of the simulation. Black histogram shows the initial spectrum of the muons when they are generated with `gentra`, while red histogram corresponds to the events that pass the `TriggerEfficiency` program as triggered events. The dark blue histogram shows all events successfully reconstructed by the `aafit` `v0r9pre` algorithm. The green histogram shows all events satisfying the quality cuts indicated at the legend.

plot of the muon detection efficiency  $\eta_\mu$  as a function of muon energy  $\epsilon_\mu$  is shown in Figure 7.8.

The shape of the reconstructed energy spectrum also varies with zenith distance bins. Except for the bins containing sources from the zenith, in general the detection efficiency increases with zenith distance. This effect could arise from the geometry of the detector. In the next section I will qualitatively discuss this relation between the detector geometry and the reconstruction quality.

### 7.2.2 *The quality of the reconstructed tracks and the preliminary cuts*

THE DISTRIBUTION of the true angular resolution  $\psi$  (the difference between the reconstructed angle and the true angle), error estimate  $\sigma_\psi$  (the statistical estimate of  $\psi$ ), and the goodness-of-

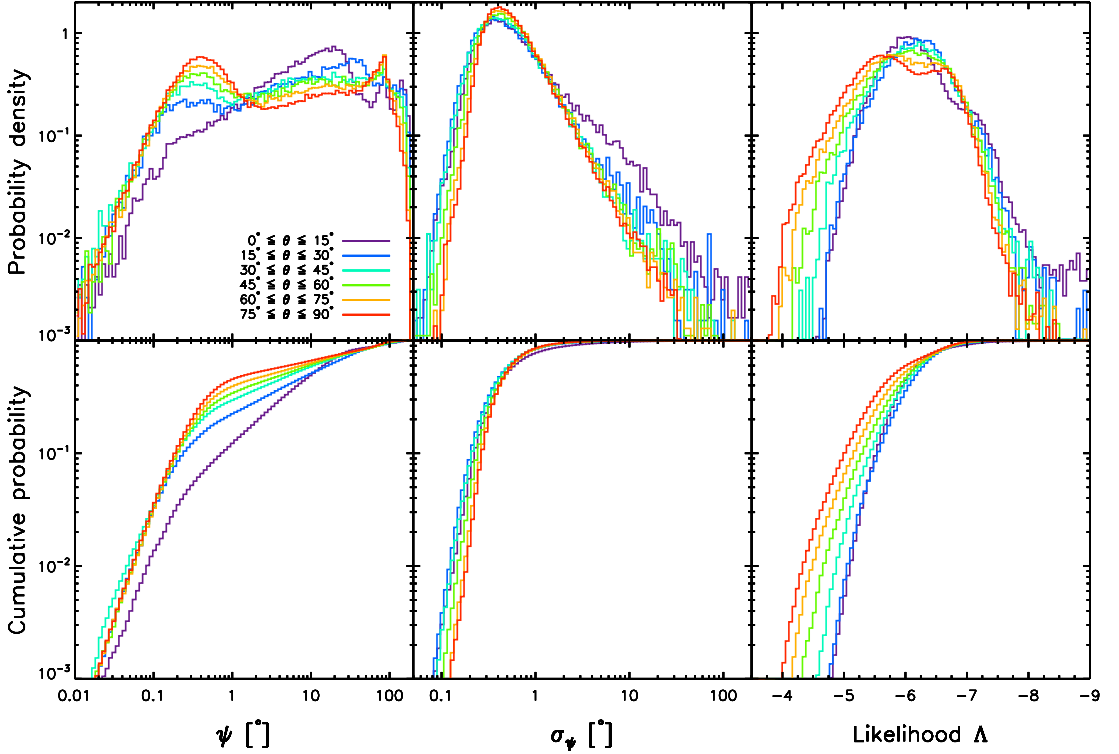


Figure 7.2: *Top:* The probability distribution function (PDF). *Bottom:* The cumulative distribution function (CDF). Both functions are shown for the true angular resolution  $\psi$  (left), the angular uncertainty  $\sigma_\psi$  (center), and the fit likelihood  $\Lambda$  (right). Different color indicates different zenith distance according to the legend.

fit  $\Lambda$  is shown in Figure 7.2 for all six cases of zenith distance bins. The top row plots the probability distribution function (PDF) while the bottom row plots the cumulative distribution function (CDF) of each parameter. Table 7.3 summarises the effects of quality cuts.

From Figure 7.2, we can see that for all bins,  $\sim 80\%$  of all the muon tracks have an error estimate of  $\sigma_\psi \lesssim 1^\circ$  (this can also be seen from column 3 in the top part of Table 7.3). The distribution of  $\sigma_\psi$ , however, does not completely reflect the distribution of  $\psi$ . As we can see in the left column of Figure 7.2 as well as the the rightmost column in Table 7.1, at best only  $\sim 45\%$  of the reconstructed muon tracks (coming from zenith distances  $75^\circ \leq \theta \leq 90^\circ$ ) are actually accurate to better than  $1^\circ$ , at worst only  $\sim 12\%$  (coming from zenith distances  $0^\circ \leq \theta \leq 15^\circ$ ). Thus

Table 7.3: A summary of the applied quality cuts.  $N_{\text{reco}}$  is the number of tracks successfully reconstructed by aafit algorithm and its percentage relative to  $N_{\text{phys}}$ . The first part of the table—under the first heading—shows the results of selecting reconstructed muon tracks with  $\sigma_\psi \leq 1^\circ$ . The second part under the second heading are for the results from selection of all tracks with  $\Lambda_{\text{aafit}} \geq -6$ , and the last part shows the results from selecting muon tracks with both quality:  $\sigma_\psi \leq 1^\circ$  and  $\Lambda_{\text{aafit}} \geq -6$ . For each part,  $N_{\text{sel}}$  is the number of tracks passing the applied quality cuts and its percentage relative to  $N_{\text{reco}}$ ;  $N_{\text{sel}}(\psi \leq 1^\circ)$  is the number of tracks with good accuracy (i.e.  $\psi \leq 1^\circ$ ) and its percentage relative to  $N_{\text{sel}}$ ;  $N_{\text{sel}}(\psi > 1^\circ)$  is the number of poorly-reconstructed tracks and its percentage relative to  $N_{\text{reco}}$ ; and finally  $N_{\text{false}}$  is the number of false-negative tracks i.e. the number of tracks that did not get selected by the cuts even though they are accurately reconstructed to better than  $1^\circ$ . The percentage given in  $N_{\text{false}}$  is relative to  $N_{\text{reco}}(\psi \leq 1^\circ)$ , shown in the rightmost column of Table 7.1.

Zenith Distance	$N_{\text{reco}}$	$N_{\text{sel}} = N_{\text{reco}}(\sigma_\psi \leq 1^\circ)$			$N_{\text{false}}$
		$N_{\text{sel}}$	$N_{\text{sel}}(\psi \leq 1^\circ)$	$N_{\text{sel}}(\psi > 1^\circ)$	
$0 \leq \theta \leq 15$	33308	25459 (76.44%)	3602 (14.15%)	21857 (85.85%)	354 (8.95%)
$15 \leq \theta \leq 30$	17713	14665 (82.79%)	3805 (25.95%)	10860 (74.05%)	82 (2.11%)
$30 \leq \theta \leq 45$	17659	14845 (84.06%)	5018 (33.80%)	9827 (66.20%)	125 (2.43%)
$45 \leq \theta \leq 60$	24881	20691 (83.16%)	8158 (39.43%)	12533 (60.57%)	218 (2.60%)
$60 \leq \theta \leq 75$	42279	35149 (83.14%)	15874 (45.16%)	19275 (54.84%)	500 (3.05%)
$75 \leq \theta \leq 90$	80073	67746 (84.61%)	34849 (51.44%)	32897 (48.56%)	923 (2.58%)
Zenith Distance	$N_{\text{reco}}$	$N_{\text{sel}} = N_{\text{reco}}(\Lambda_{\text{aafit}} \geq -6)$			$N_{\text{false}}$
		$N_{\text{sel}}$	$N_{\text{sel}}(\psi \leq 1^\circ)$	$N_{\text{sel}}(\psi > 1^\circ)$	
$0 \leq \theta \leq 15$	33308	13916 (41.78%)	3602 (25.88%)	10314 (74.12%)	354 (8.95%)
$15 \leq \theta \leq 30$	17713	5897 (33.29%)	3399 (57.64%)	2498 (42.36%)	488 (12.55%)
$30 \leq \theta \leq 45$	17659	7045 (39.89%)	4602 (65.32%)	2443 (34.68%)	541 (10.52%)
$45 \leq \theta \leq 60$	24881	11129 (44.73%)	7652 (68.76%)	3477 (31.24%)	724 (8.64%)
$60 \leq \theta \leq 75$	42279	21661 (51.23%)	15278 (70.53%)	6383 (29.47%)	1096 (6.69%)
$75 \leq \theta \leq 90$	80073	46705 (58.33%)	34171 (73.16%)	12534 (26.84%)	1601 (4.48%)
Zenith Distance	$N_{\text{reco}}$	$N_{\text{sel}} = N_{\text{reco}}(\sigma_\psi \leq 1^\circ, \Lambda_{\text{aafit}} \geq -6)$			$N_{\text{false}}$
		$N_{\text{sel}}$	$N_{\text{sel}}(\psi \leq 1^\circ)$	$N_{\text{sel}}(\psi > 1^\circ)$	
$0 \leq \theta \leq 15$	33308	11769 (35.33%)	3317 (28.18%)	8452 (71.82%)	639 (16.15%)
$15 \leq \theta \leq 30$	17713	5573 (31.46%)	3356 (60.22%)	2217 (39.78%)	531 (13.66%)
$30 \leq \theta \leq 45$	17659	6640 (37.60%)	4516 (68.01%)	2124 (31.99%)	627 (12.19%)
$45 \leq \theta \leq 60$	24881	10484 (42.14%)	7509 (71.62%)	2975 (28.38%)	867 (10.35%)
$60 \leq \theta \leq 75$	42279	20237 (47.87%)	14912 (73.69%)	5325 (26.31%)	1462 (8.93%)
$75 \leq \theta \leq 90$	80073	43828 (54.74%)	33432 (76.28%)	10396 (23.72%)	2340 (6.54%)

between zenith distances of  $0^\circ$  to  $90^\circ$ , the number of tracks accurately reconstructed to better than  $1^\circ$  ranges from  $\sim 12\%$ – $45\%$ . This means that without any quality cuts, the majority of the reconstructed tracks actually have poor accuracy.

Another thing that we can see from the distribution of  $\psi$  is that although a relatively large number of tracks coming from  $0^\circ \leq \theta \leq 15^\circ$  can be successfully reconstructed compared to the following three zenith distance bins (see Column 5 in Table 7.1), almost 90% of them are actually poorly-reconstructed as compared to 70%–80% for the other bins. In other words, tracks coming from steep zenith distances (close to the zenith) can be efficiently reconstructed but with relatively low quality. This effect can be attributed to the geometry of the detector. More detector lines can participate in the detection of the Čerenkov photons when the muon passes the detector at a shallow angle, but only one or two detector lines participate in the detection when the muon is coming at a very steep angle. When only the PMTs from one or two lines detect photons, a symmetry in the data remains that results in an ambiguity of the track direction.

The relative number of poorly-reconstructed tracks could be reduced by applying selection cuts. The selection cuts are based on a combination of goodness-of-fit  $\Lambda_{\text{aafit}}$  and angular resolution estimate  $\sigma_\psi$ . The distribution of  $\psi$  are influenced by the combination of these two values.

We have seen that the angular error estimate  $\sigma_\psi$  is not entirely correlated with  $\psi$ . This is more apparent in Figure 7.3, in which the 2 dimensional histogram of  $\sigma_\psi$  and  $\psi$  is shown. For all bins of zenith distance, if we select all tracks with  $\sigma_\psi \leq 1^\circ$ , we reject a large number of low-accuracy tracks. However, a considerable number of poorly-reconstructed tracks (with an angular deviation even as far as  $180^\circ$ ) will contaminate the resulting subsample, assuming that the background distribution is approximately the same as the signal distribution. As we can see in Table 7.3, as much as  $\sim 86\%$  and as little as  $\sim 50\%$  of the subsample will still contain tracks with accuracy worse than  $1^\circ$ .

A tighter correlation exists between goodness-of-fit  $\Lambda_{\text{aafit}}$  and  $\psi$ , as we can see in the 2D histogram of  $\Lambda_{\text{aafit}}$  and  $\psi$  shown in Figure 7.4. We can also see a progression of a bimodality in the dis-



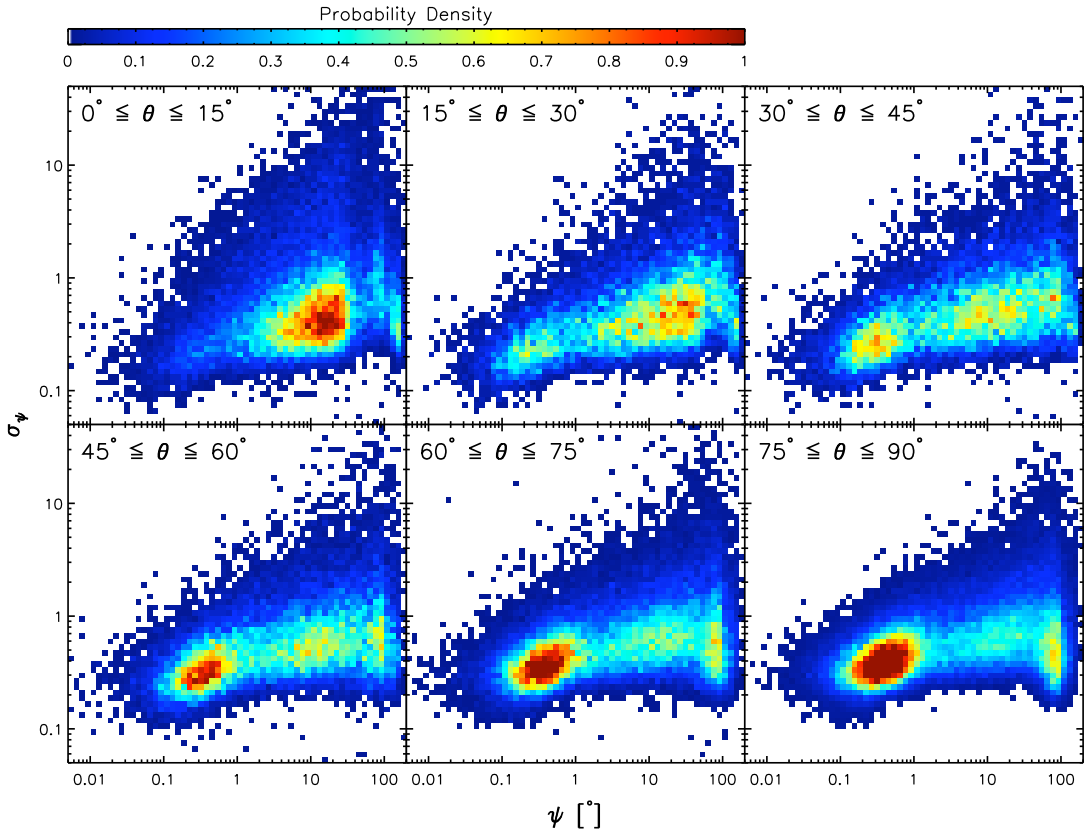


Figure 7.3: Two dimensional histogram of  $\sigma_\psi$  and  $\psi$ . We can see that  $\sigma_\psi$  is not entirely correlated with  $\psi$ . Tracks with estimated error  $\sigma_\psi \leq 1^\circ$  can actually be reconstructed with low accuracy, even as far as  $180^\circ$  from its actual direction.

tribution, in which there seems to be two peaks centered around  $\psi \lesssim 1^\circ$  and  $\psi \sim 100^\circ$ . In zenith distance range  $0^\circ \leq \theta \leq 15^\circ$ , the distribution is concentrated at  $(\psi, \Lambda_{\text{aafit}}) \sim (20^\circ, -6.25)$ . In general, the distribution of the good quality tracks is concentrated around  $\Lambda_{\text{aafit}} \gtrsim -5.5$ . If we accept all tracks with  $\Lambda_{\text{aafit}} \geq -6$ , we can obtain a good majority of the high-quality tracks while rejecting a considerable number of poorly-reconstructed tracks. In the middle part of Table 7.3, in Column 4, we can see that as much as  $\sim 70\%$  of the high-quality tracks can be kept.

Having seen the effects of both quality cuts separately, we could also see their combined effects on the distribution of  $\psi$ . Such effects are shown in Figure 7.6, in which four combinations of qual-

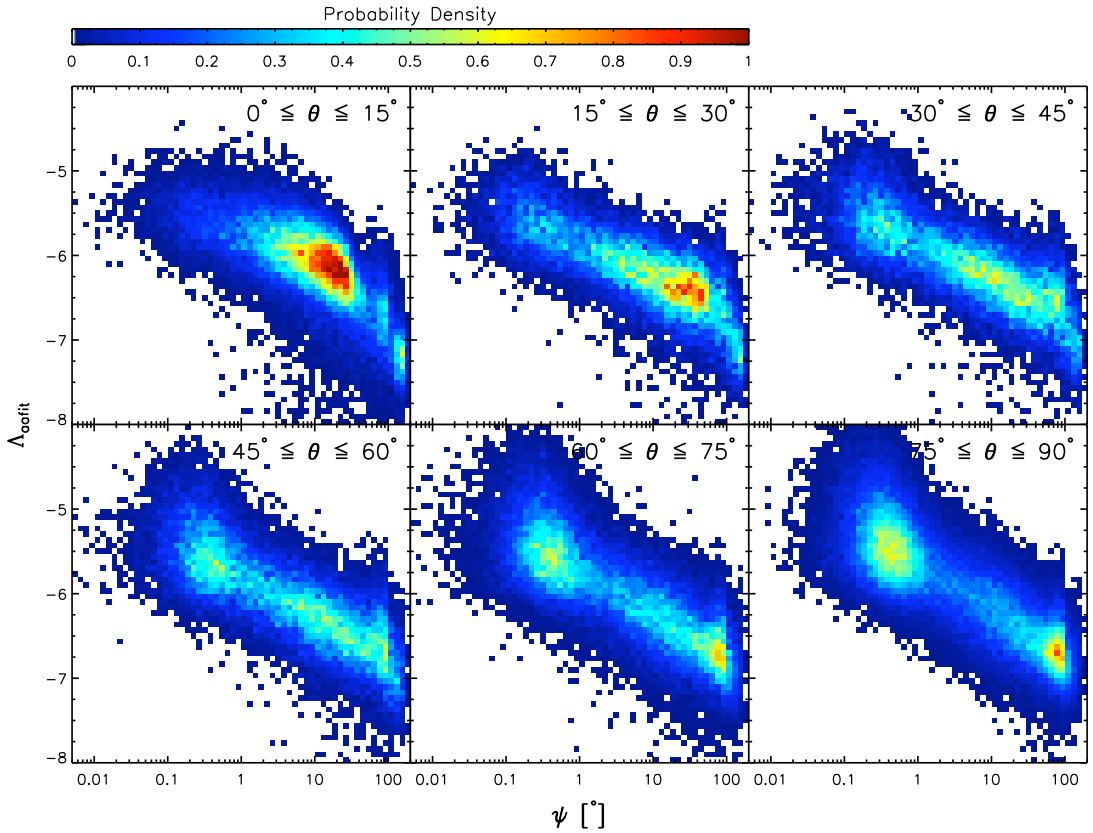


Figure 7.4: Two dimensional histogram of  $\Lambda_{\text{aoft}}$  and  $\psi$ . A progression of a bimodality can be seen in the distribution with increasing zenith distance. The majority of tracks reconstructed to better than  $1^\circ$  are concentrated above  $\Lambda_{\text{aoft}} \sim -5.5$ , while the poorly-reconstructed tracks (e.g. worse than  $10^\circ$ ) are concentrated below  $\Lambda_{\text{aoft}} \sim -6.5$ .

ity cuts are considered, and their effects on the PDF and CDF of the true angular resolution  $\psi$  are shown. With very loose quality cuts, shown as the purple-colored histogram, remains a considerable number of poorly-reconstructed tracks. With very tight quality cuts, shown as the red-colored histogram, a vast majority of the poorly-reconstructed muon tracks is rejected, but leaves only  $\sim 10\%$  of all reconstructed events. This considerably decreases the detection efficiency.

Preliminary selection criteria of  $\sigma_\psi \leq 1^\circ$  and  $\Lambda_{\text{aoft}} \geq -6$  have been defined to compute the median accuracy of the reconstruction of downgoing muons. Figure 7.7 shows the cumulative distribution function of  $\psi$  after such quality cuts are applied. Although

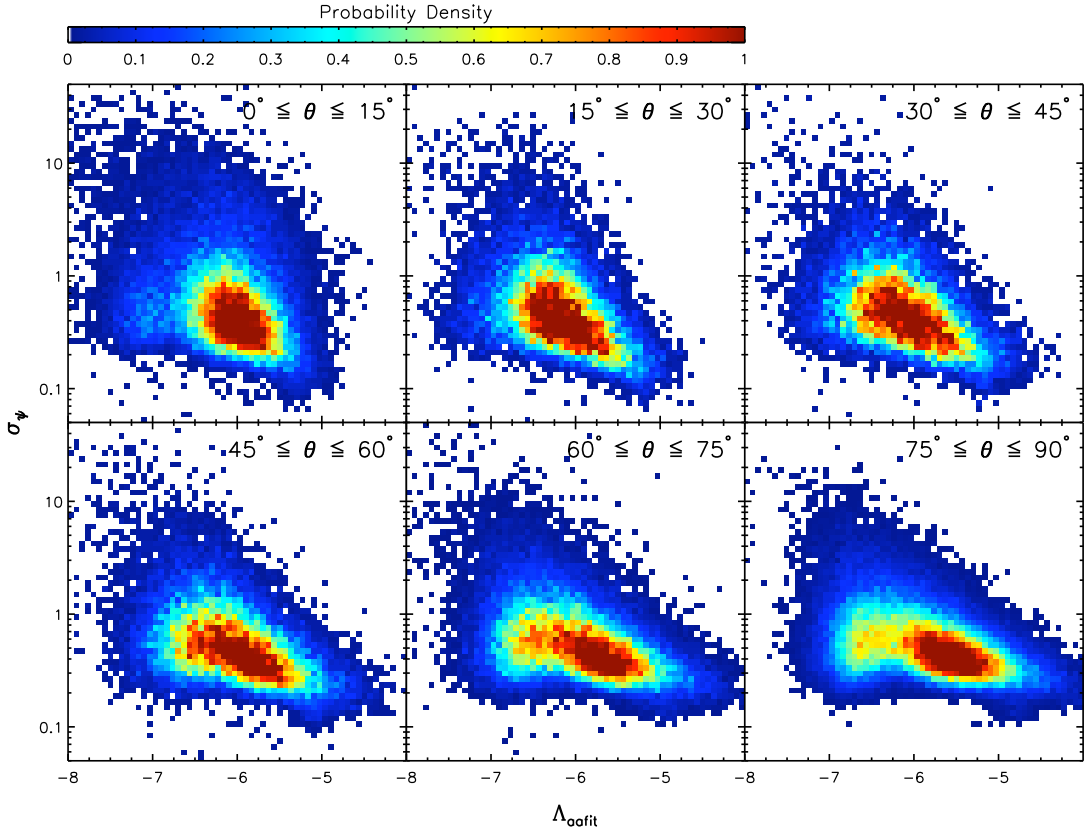


Figure 7.5: Two dimensional histogram of  $\sigma_\psi$  and  $\Lambda_{\text{aaFit}}$ .

at steep zenith distances, i.e.  $0^\circ \leq \theta \leq 15^\circ$ , the median accuracy is  $\psi \sim 3^\circ$ , in general the median accuracy is  $\psi \sim 0.4^\circ$ .

The appropriate cut that could provide a good compromise between reliable background rejection and detector efficiency will be defined in Section 8.2, in which we include background data into the analysis.

### 7.2.3 Effective areas

THE DETECTION efficiency of the ANTARES detector as a function of energy, defined as the ratio between the number of recon-

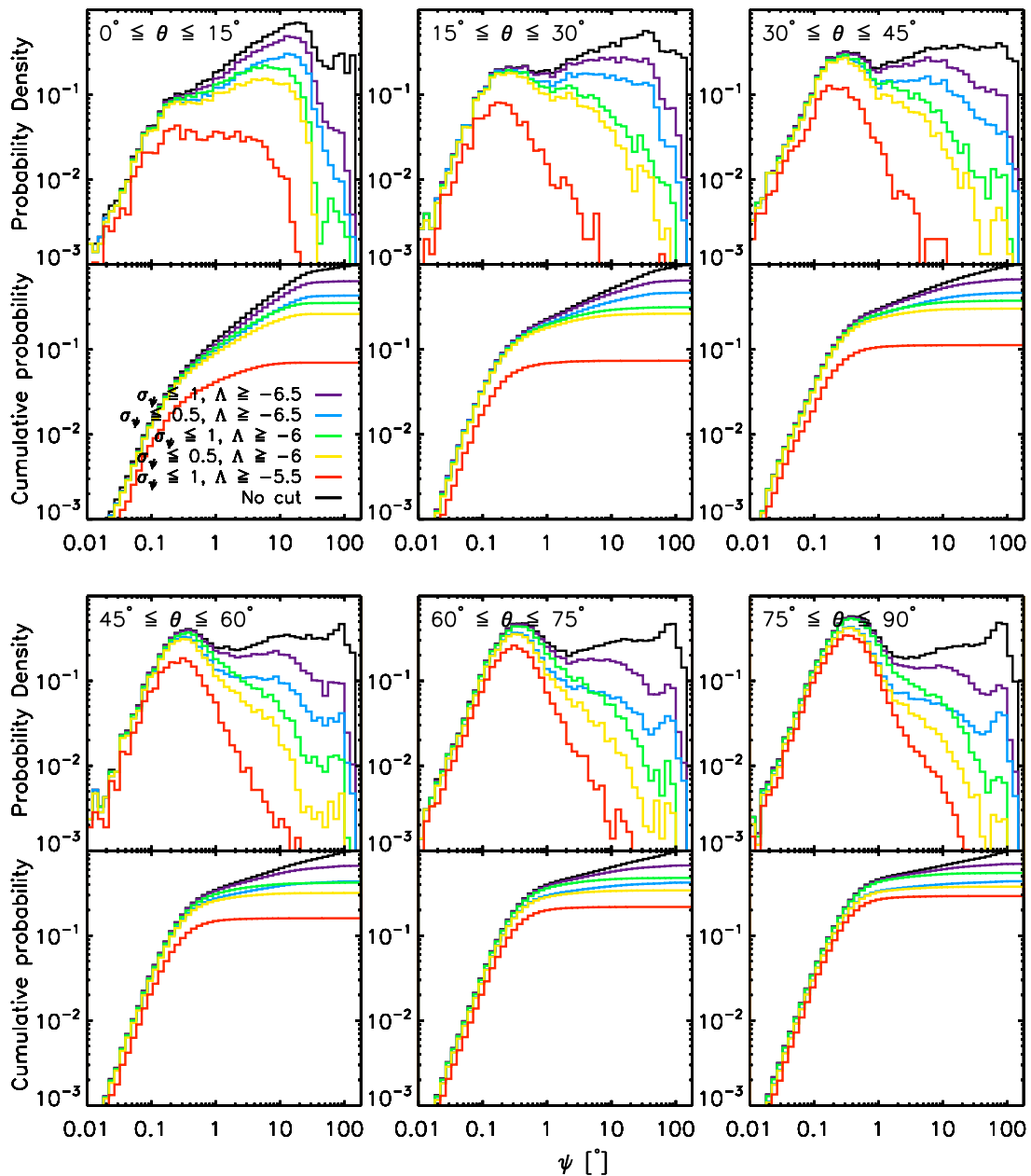


Figure 7.6: The effect of several quality cuts (indicated by different color coding shown in the legends) to the PDF and CDF of the angular resolution  $\psi$ .

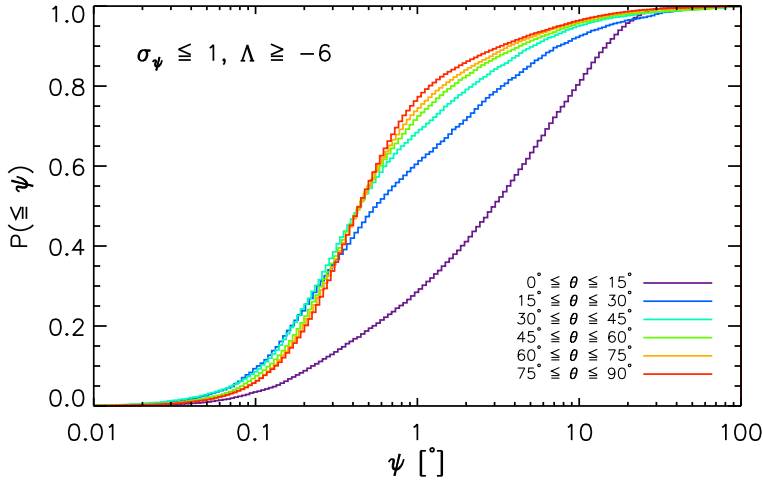


Figure 7.7: The CDF of the true angular resolution  $\psi$  after the quality cuts  $\sigma_\psi \leq 1^\circ$  and  $\Lambda_{\text{aafit}} \geq -6$  have been applied. Only  $\sim 30\%$  of the signals coming from very steep zenith distances,  $0^\circ \leq \theta \leq 15^\circ$ , are going to be reconstructed to better than  $1^\circ$ , but other zenith distances will reconstruct to better than  $1^\circ$  between  $\sim 60\text{--}75\%$  of the signals satisfying the applied cuts.

structed muon tracks and generated tracks in each energy bin,

$$\eta_\mu(\epsilon_\mu) = \frac{dN_{\mu,\text{rec}}}{dN_{\mu,\text{can}}}, \quad (7.2)$$

is shown in Figure 7.8. The top graphic depicts the efficiency if all events are admitted while the bottom graphic is for all events satisfying the quality criteria  $\sigma_\psi \leq 1^\circ$  and  $\Lambda_{\text{aafit}} \geq -6$ . The muon effective area  $A_\mu^{\text{eff}}$  as a function of energy is also shown in Figure 7.8. The effective area is simply the detection efficiency multiplied by the generation area given in the second column of Table 7.1.

The muon detection efficiency and effective area for point sources corresponding to six considered cases of zenith distances (the SIMULATION 2 data set) are shown in Figure 7.9.

It is also possible to calculate the photon effective area  $A_\gamma^{\text{eff}}$  as a function of the photon energy  $\epsilon_\gamma$ . First we must calculate the muon spectrum at the surface of the sea, assuming that the electromagnetic shower is initiated by a single photon with energy  $\epsilon_\gamma$ . The photon spectrum at the top of the atmosphere would then be

$$\gamma_0(\epsilon) = \gamma(\epsilon, t = 0) \equiv \delta(\epsilon - \epsilon_\gamma), \quad (7.3)$$

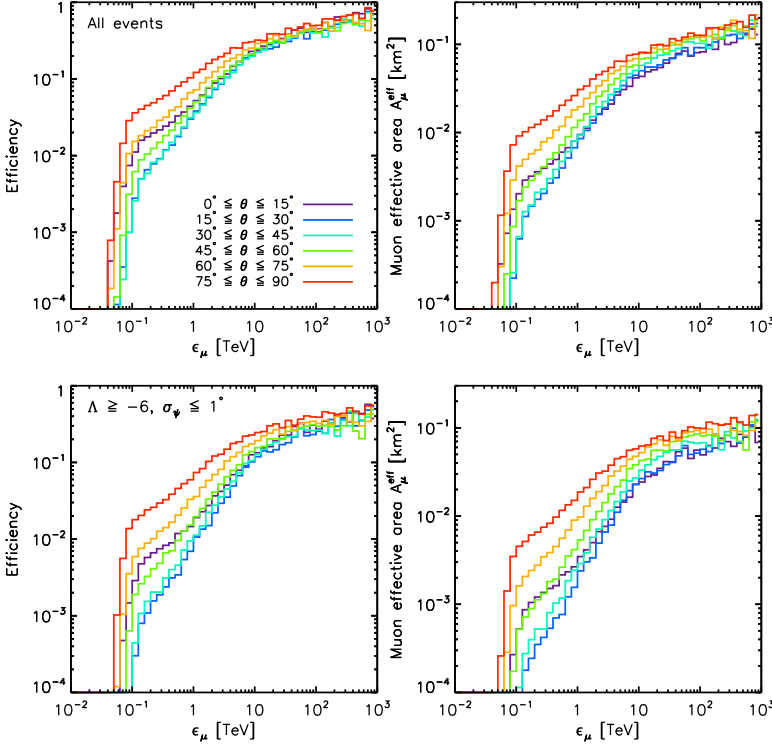


Figure 7.8: *Top*: The muon detection efficiency (left) and the muon effective area  $A_{\mu}^{\text{eff}}$  (right). *Bottom*: The same, but for events satisfying the quality cuts  $\Lambda \geq -6$  and  $\sigma_{\psi} \leq 1^{\circ}$ . The efficiency and effective area are calculated using the data set in SIMULATION 1.

where  $\delta$  is the Dirac delta function.

The development of the photon spectrum in the atmosphere could be determined using a discrete approximation, in which the atmosphere is segmented in layers of depth  $\lambda_R \ln 2$  and that leptonic particles lose half their energy after passing each layer. At depth  $t = n \lambda_R \ln 2$ , the shower would contain  $2^n/3$  photons with energy  $\epsilon_{\gamma}/2^n$ . This would mean that the shape of the photon spectrum at depth  $t$  is

$$\gamma(\epsilon, t) = \frac{2^n}{3} \delta\left(\epsilon - \frac{\epsilon_{\gamma}}{2^n}\right). \quad (7.4)$$

Using this formula we could then calculate the muon flux from pair-production by using Equation 3.28, as well as the muon flux from pion decay (Drees, Halzen & Hikasa, 1989). The result of this analytical calculation is compared with results from CORSIKA

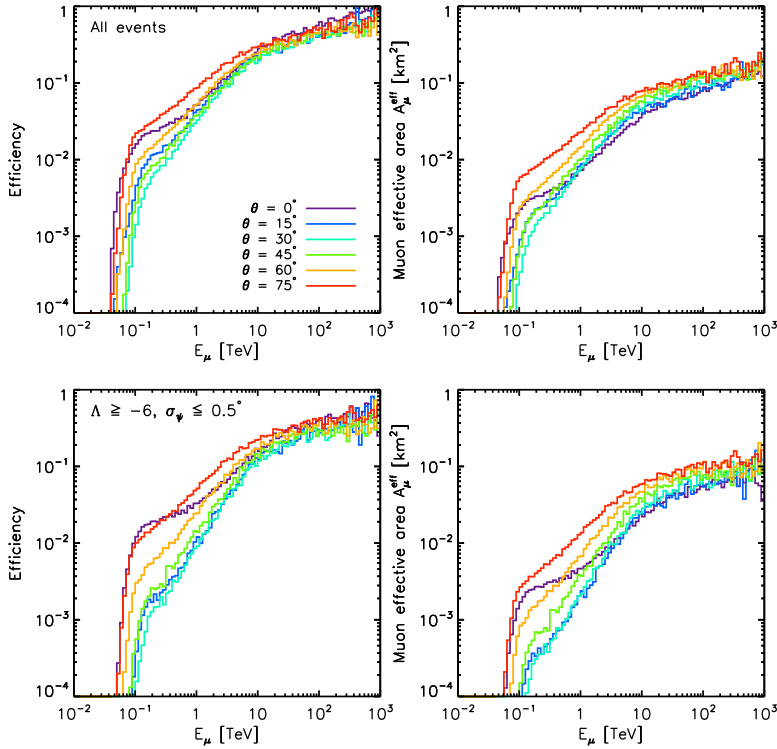


Figure 7.9: The same as in Figure 7.8, but for SIMULATION 2.

for a number of photons with energy  $\epsilon_\gamma = \{1, 2, 5, 10, 50, 100\}$  TeV (Figure 7.10). We can see that there is a good agreement between theoretical calculations and the simulations. We can now calculate the muon spectrum at the detector using the manners described in Section 3.6. The muon spectrum at the detector, before and after reconstruction, is shown in Figure 7.11. Once we know the shape of the muon spectrum after reconstruction, it is straightforward to calculate the photon effective area. The photon detection efficiency would simply then be

$$\eta_\gamma(\epsilon_\gamma) = \frac{dN_{\mu, \text{rec}}}{d\epsilon_\mu}. \quad (7.5)$$

The photon effective area  $A_\gamma^{\text{eff}}$  is then the photon detection efficiency multiplied by the generation area (column 2 in Table 7.2). The photon effective area as a function of energy is showed in

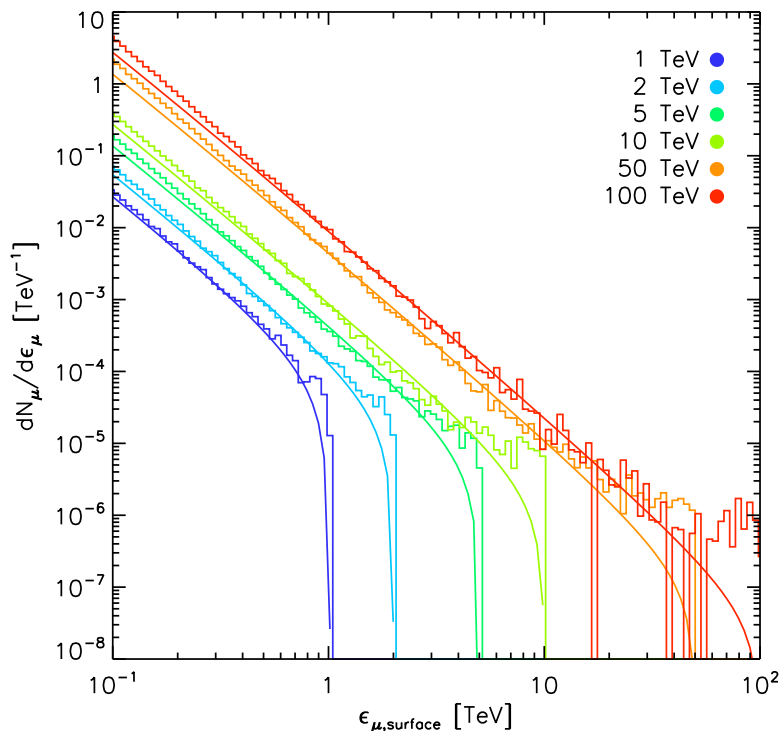


Figure 7.10: The muon flux at the sea surface, induced by single photons. The energy of the single photon is given in the legend. Results of the analytical calculations are also given as a comparison.

Figure 7.12. The photon effective area of other (spaceborne)  $\gamma$ -ray observatories is also shown for comparisons, namely *Fermi*-LAT, EGRET, and AGILE, which parameterization has been calculated by Le & Dermer (2009).

We can see that the photon effective area of ANTARES increases where other satellites are decreasing, thus complementing these instruments in higher energy ranges.



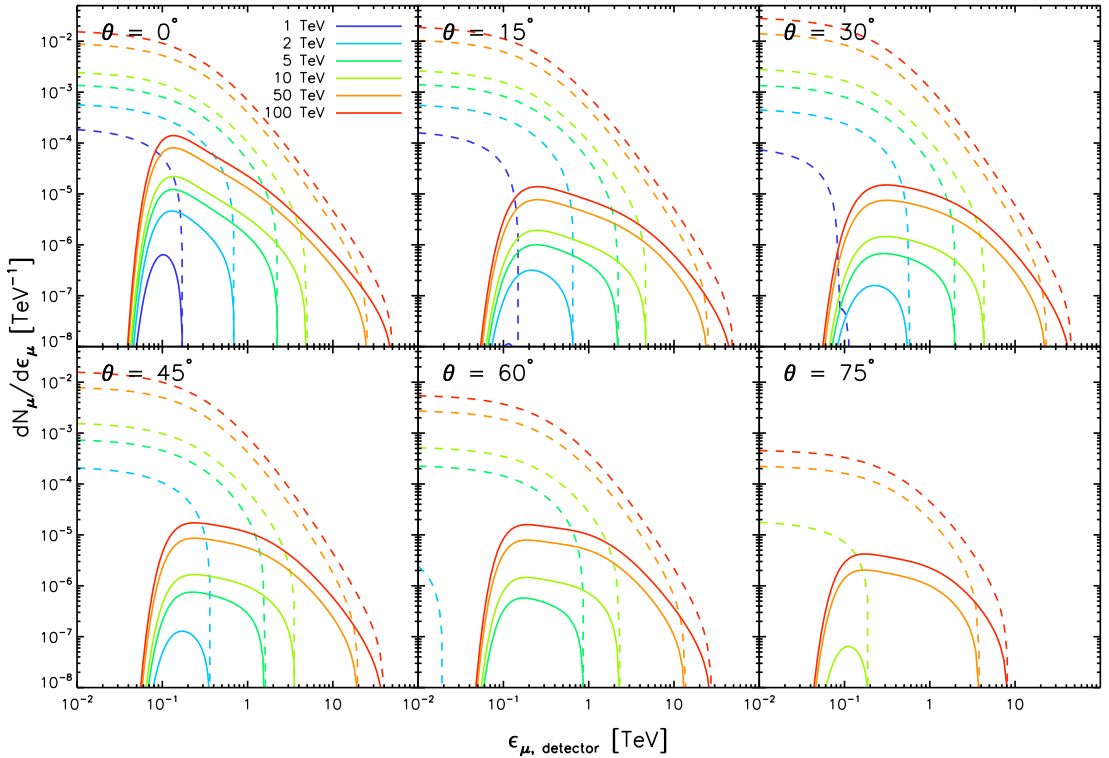


Figure 7.11: The shape of the muon spectrum induced by single photons, at detector level. The dashed lines are for spectrums of muons arriving at the detector, while the solid lines are after detection efficiency function is included. Each panel is for a different zenith distance.

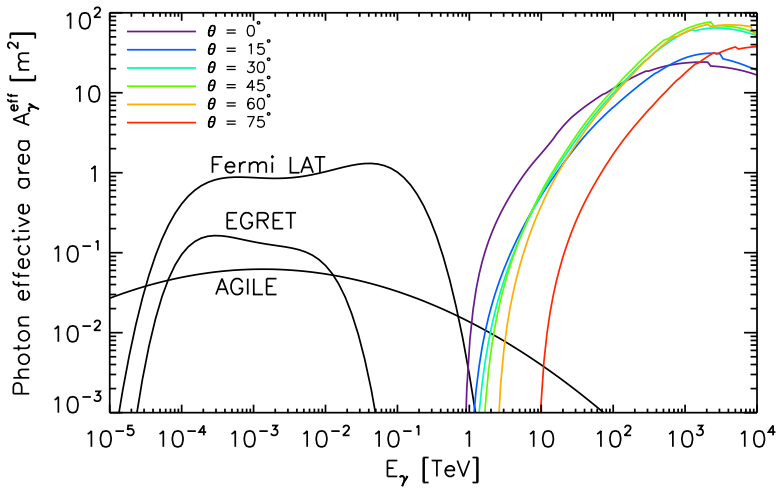


Figure 7.12: The ANTARES telescope photon effective area  $A_{\gamma}^{\text{eff}}$  compared to spaceborne  $\gamma$ -ray observatories.

# 8 *The point spread function and the optimization of quality cuts*

IN THIS Chapter, the analysis involving both signal and background data will be described. Rather than reproducing background data with simulations, the input is taken from ANTARES data that have been successfully reconstructed with `aafit`. The data used for this analysis is the data taken in 2008 with 12 lines. During this period, the lifetime of the data taking period is  $6.46 \times 10^6$  s or roughly  $\sim 75$  days. There are approximately  $6.9 \times 10^7$  reconstructed muon events within this period.

## 8.1 *Background data*

VARIOUS maps of the muon events in local ANTARES coordinates are shown in Figure 8.1. In these maps, the celestial sphere is divided into bins of equal area using the `healpix` algorithm (Górski et al., 2005). It is then easy to calculate the total number events in each bins. Dividing the number of events with the total lifetime of the experiment and the size of the bin will give the background event rate in units of Hz per square degree, as indicated by the fill colour of each bin.

These maps give an overview of the background rate as a function of azimuth and zenith distance. In general the background is essentially about 1 mHz per square degree. For the unfiltered events, the background distribution is not the same in azimuthal directions. This can be attributed to the detector geometry. Events coming close to a detector line will be more likely to be reconstructed than those coming at a considerable distance from any detector line. This effect becomes less if we apply some quality cuts. At the bottom plot, only background events with  $\Lambda_{\text{aafit}} \geq -6$  and  $\sigma_\psi \leq 1^\circ$  are accepted. We can see that the anisotropy has diminished.

Figure 8.2 shows an azimuth-averaged muon rate as a function of zenith distance. The red line is a polynomial fit to the data, which will be useful for further calculations. We can also compare

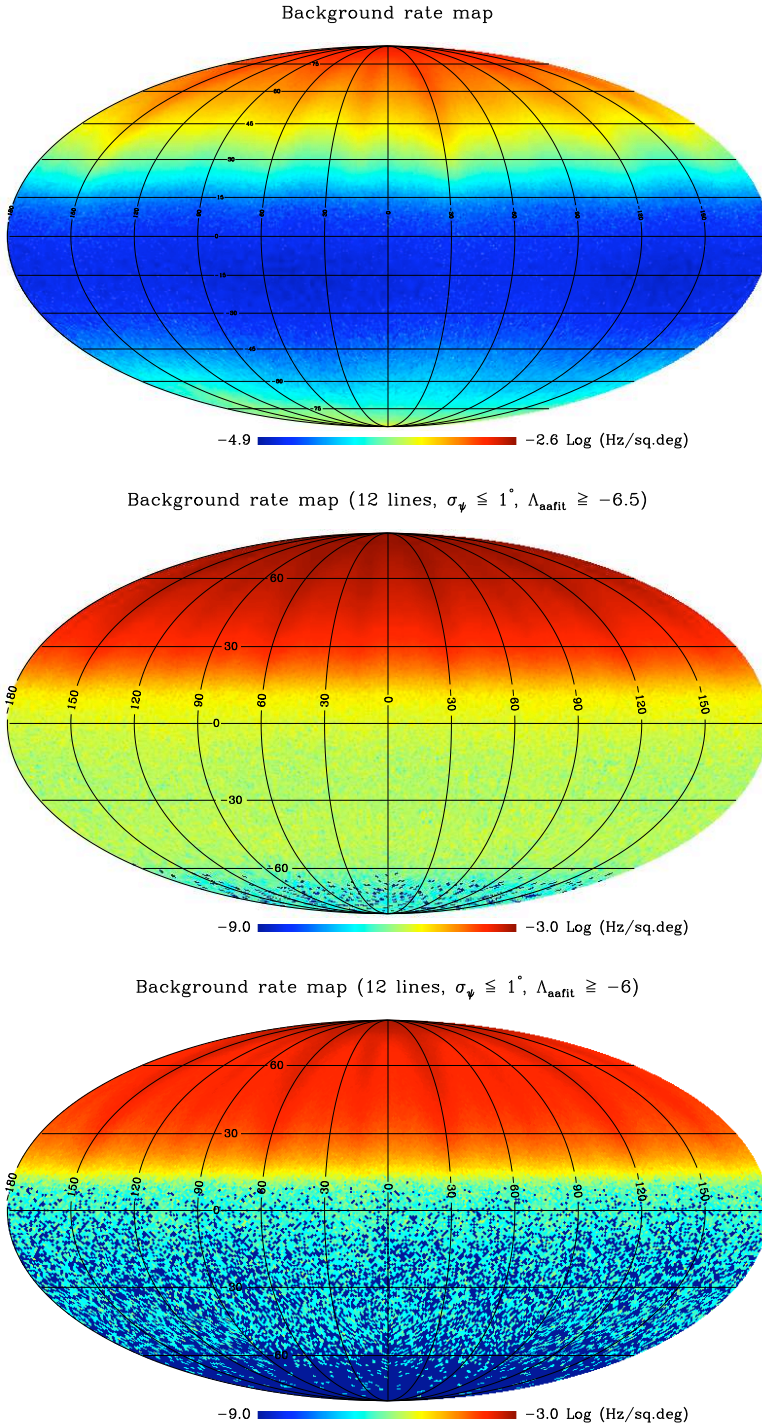


Figure 8.1: Mollweide projections of the Altitude-Azimuth distribution of reconstructed muon events detected with the ANTARES telescope during the 12-line period in 2008 ( $\sim 75$  days of data taking). The top plot shows all reconstructed events without any quality cuts, while the middle and bottom plots shows all reconstructed events satisfying, respectively, loose cuts of  $\Lambda \geq -6.5$  and  $\sigma_\psi \leq 1^\circ$ , and tighter cuts of  $\Lambda \geq -6$  and  $\sigma_\psi \leq 1^\circ$ . For the unfiltered events, the azimuthal distribution is not really isotropic. This can be attributed to the detector geometry. This anisotropy is diminished somewhat when quality cuts are applied. These maps are made using the healpix algorithm (Górski et al., 2005) that pixelize the celestial sphere into cells of equal area and then count the number of events within each cell.

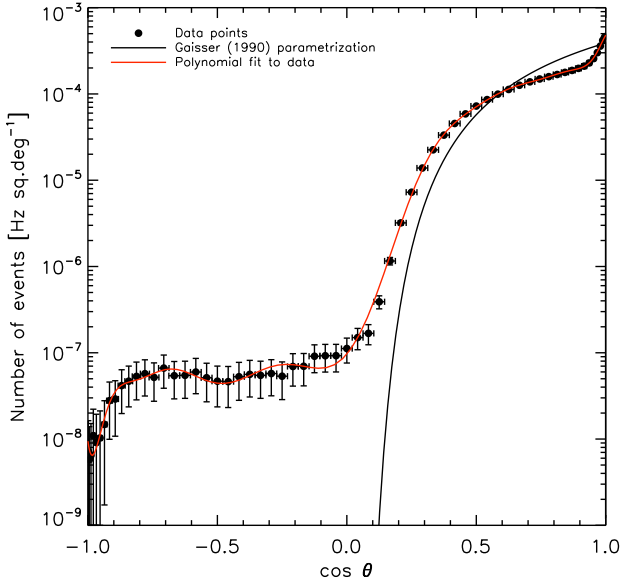


Figure 8.2: The azimuth-averaged muon event rate as a function of zenith distance  $\theta$ . A polynomial fit to the data is shown as the red line. A comparison with the parametrization of Gaisser (1990) is also shown as the solid black line.

the observed rate with the expected muon rate parameterized by Gaisser (1990).

A comparison between simulated signal and observed background events in the  $\sigma_\psi$ - $\Lambda_{\text{aafit}}$  space is shown in Figure 8.3. This comparison indicates that the signal and background look rather similar, despite the different origin ( $\gamma$ -induced muons events versus cosmic ray induced muon events).

## 8.2 Weighting scheme and the point spread function

THE POINT spread function (PSF) of downgoing muons could be determined from the simulated events. The determination of the PSF is necessary as a first step in hypothesis testing (which will be described in more detail in Chapter 9). The events that constitute the PSF, however, are results from simulations of fictitious events, which energies are generated according to simple power law. Actual GRB events, however, do not follow a simple power law. For example, at higher energy the spectrum is cut due to attenuations by extragalactic infrared background photons. The

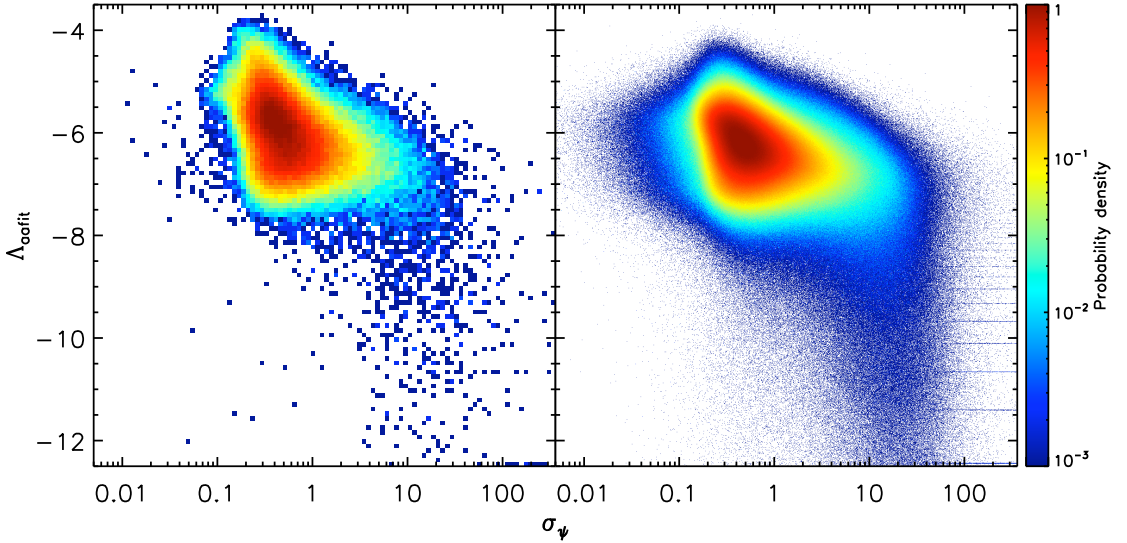


Figure 8.3: A comparison of signal (left plot) and background (right plot) events in the  $\sigma_\psi$ - $\Lambda_{\text{aaifit}}$  space.

severity of the attenuation depends on the redshift and the energy band in question.

The simulated muon events must then be weighted accordingly so that the muon spectrum reproduces the energy spectrum of a GRB event. The background events must also be weighted, since they are taken from an exposure time much longer than an actual GRB events, with a different detector configuration and varying detector conditions. The following subsection will describe the weighting scheme employed in this analysis before we move on to the modelling of the PSF.

### 8.2.1 Weighting scheme

FOR UNWEIGHTED events, the normalisation of a histogram following a power law function is straightforward. For the  $j$ -th bin of the histogram, the total number of reconstructed event per unit energy would simply be

$$\frac{dN}{dE_j} = \frac{1}{E_j \ln(10)} \frac{N_j}{\Delta \log E_j'} \quad (8.1)$$

Par.	Definition	Value
$\alpha$	spectral index at low energy	1
$\beta$	spectral index at high energy	2
$\epsilon_{\text{pk}}$	the energy at which the spectrum peaks	400 keV
$L_{\text{bol}}^{\text{iso}}$	isotropic bolometric luminosity	$8.9 \times 10^{52}$ erg
$t_{\text{exp}}$	rest-frame burst duration	10 s
$d$	ANTARES depth	$2.475 \times 10^5$ cm

Table 8.1: The adopted values used to calculate the muon energy spectrum at can level.

where  $E_j$  is the energy at the midpoint of the  $j$ -th bin,  $N_j$  is the total number of events in the  $j$ -th bin, and  $\Delta \log E_j$  is the binwidth in  $\log E_j$ .

Equation 8.1 implies that all events have the same weight. Summing up all the weights of events within the  $j$ -th bin would result in the actual event rate. The number of reconstructed events in the  $j$ -th bin is related to the total number of generated events in the same bin by way of

$$\frac{dN_{\text{rec}}}{dE_j}(E_j, \theta, z) = \frac{dN_{\text{can}}}{dE_j}(E_j, \theta, z) \eta_{\mu}(E_j, \theta) A_{\text{can}}(\theta) t_{\text{exp}}, \quad (8.2)$$

where  $dN_{\text{can}}/dE_j(E_j, \theta, z)$  is the number of generated events at the edge of the can as a function of energy  $E_j$ , zenith distance  $\theta$ , and the redshift  $z$  of the GRB source, in units of  $\text{TeV}^{-1} \text{cm}^{-2} \text{s}^{-1}$ ,  $\eta_{\mu}(E_j, \theta)$  is the muon reconstruction efficiency as a function of energy and zenith distance,  $A_{\text{can}}(\theta)$  is the generated can area at the given zenith distance, and  $t_{\text{exp}}$  is the time exposure. Using the prescription described in Chapters 2–3, we can now determine the number of photon-induced muons at the detector. The values used to construct the GRB spectrum are the standard values shown in Table 8.1.

We can also see that the energy spectrum of the reconstructed events also relates to the weight of individual events through

$$\frac{dN_{\text{rec}}}{dE_j}(E_j, \theta, z) = \frac{1}{E_j \ln(10)} \frac{\sum_{i=1}^{N_j} w_{i,j}}{\Delta \log E_j}. \quad (8.3)$$

By combining equation 8.3 with 8.2, the modified weight for

the  $i$ -th event in the  $j$ -th bin would then be

$$w_{i,j}(E_j, \theta, z) = \frac{dN_{\text{can}}}{dE_j}(E_j, \theta, z) \eta_{\mu}(E_j, \theta) A_{\text{can}}(\theta) t_{\text{exp}} E_j \Delta \log E_j \ln(10) N_j^{-1}. \quad (8.4)$$

We can see from Equation 8.4 that for a GRB source located at given  $\theta$  and redshift  $z$ , the individual weight  $w_{i,j}$  would just be a function of the energy in the  $j$ -th bin. Thus all events inside the same bin will have the same weight, provided the bin width is sufficiently small.

The weighting of the background events follows a different but simpler approach. They would just simply be weighted according to ratio of the time exposure and the lifetime of the data taking:

$$w_{\text{bg}} = \frac{t_{\text{exp}}}{t_{\text{lifetime}}}. \quad (8.5)$$

In this, we assume a fixed detector configuration. The muon event rate as a function energy is shown in Figure 8.4, for different values of zenith distances and redshifts. In this, a standard GRB is assumed (see Table 8.1). In this Figure, the black lines correspond to the muon energy spectrum at the edge of the can, while the blue lines correspond to the spectrum of the reconstructed events. The red lines correspond to the events satisfying the quality criteria  $\sigma_{\psi} \leq 1^{\circ}$  and  $\Lambda_{\text{aafit}} \geq -6$ . The spectrum of the background muons—calculated using Gaisser’s (1990) parametrization—is shown as the dashed lines. We can see that given a short exposure time and small cone angle, the background is very low.

### 8.2.2 *The point spread function*

THE ANGULAR distributions of the weighted signal and background events are shown in Figure 8.5 for various values of zenith distances  $\theta$  and redshifts  $z$ . In this, the preliminary cuts are applied. The angular distribution of the events is depicted in the Lambert azimuthal equal-area projection, which project the celestial sphere onto a disk centered at a given direction in the celestial sphere. By choosing this projection, the shape of the distribution around the center of the disk, which is chosen to be

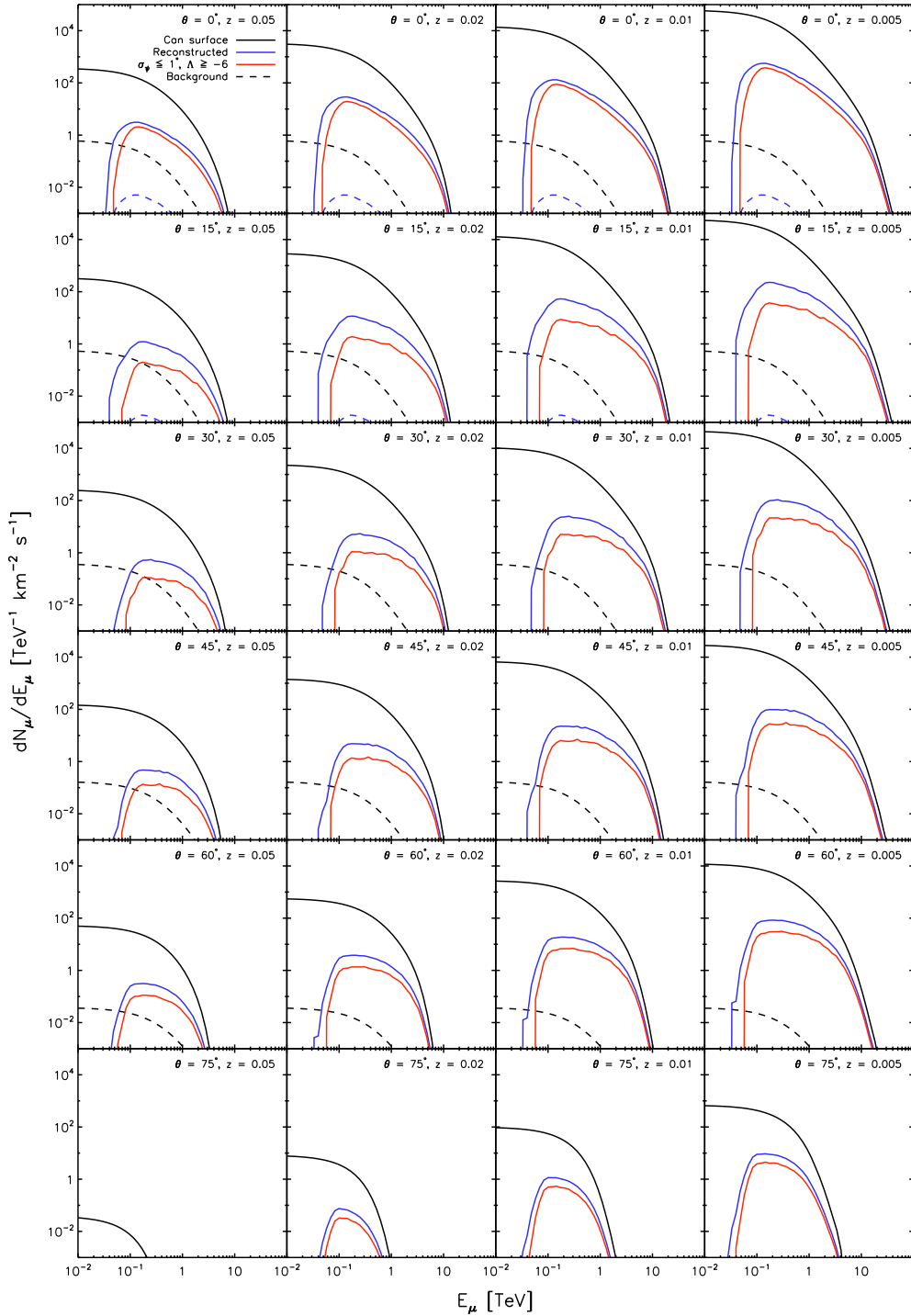


Figure 8.4: The muon event rate as a function of energy. Each event is weighted according to the scheme in Equation 8.4. The rate is calculated for different zenith distances and redshifts.



coincident with the assumed direction of the GRB, is free from distortions and thus making shape and numerical comparison between event distributions at different zenith distance straightforward. From now on the angular distribution will be referred as the point spread function (PSF).

A glance at the PSF in Figure 8.5 seems to indicate that the most interesting signal events are well-reconstructed to better than  $\sim 0.5^\circ$  from the supposed direction of the GRB. We can also see that for any GRB with redshift closer than  $z \lesssim 0.01$ , an excess of signal over background will be immediately apparent in the PSF distribution, except when the zenith distance of the source is very close to the horizon (e.g.  $\theta = 75^\circ$ ).

The PSF depicted here are shown for events satisfying the preliminary quality cuts, which were chosen rather arbitrarily. In the following section we will discuss the optimization of cuts that maximize the discovery potential.

### 8.3 Optimization for discovery: The model discovery potential

WITHIN the context of frequentist statistics, one can claim a discovery when the probability that the effect will be mistaken as a background fluctuation is very small. What is agreed as small is generally in the order of  $\alpha = 5.73 \times 10^{-7}$  (an area in a two-sided  $5\sigma$  Gaussian distribution tails). Thus in a counting experiment using Poisson statistics, for a given  $\alpha$ , we can calculate the critical number of events  $n_{\text{crit}}$  in which

$$P(\geq n_{\text{crit}}|\mu_b) \leq \alpha = 5.73 \times 10^{-7}, \quad (8.6)$$

which is the minimum number of events that has to be detected, for a given background rate  $\mu_b$ , so that the probability that the observed number of events are caused by random background fluctuation is equal of less than  $5.73 \times 10^{-7}$ . Should we also expect to detect signal events with rate  $\mu_s$ , we could then calculate the probability to observe a number of events greater than  $n_{\text{crit}}$  given the expected rate  $\mu_s + \mu_b$ :

$$P(\geq n_{\text{crit}}|\mu_s + \mu_b) = 1 - \beta. \quad (8.7)$$

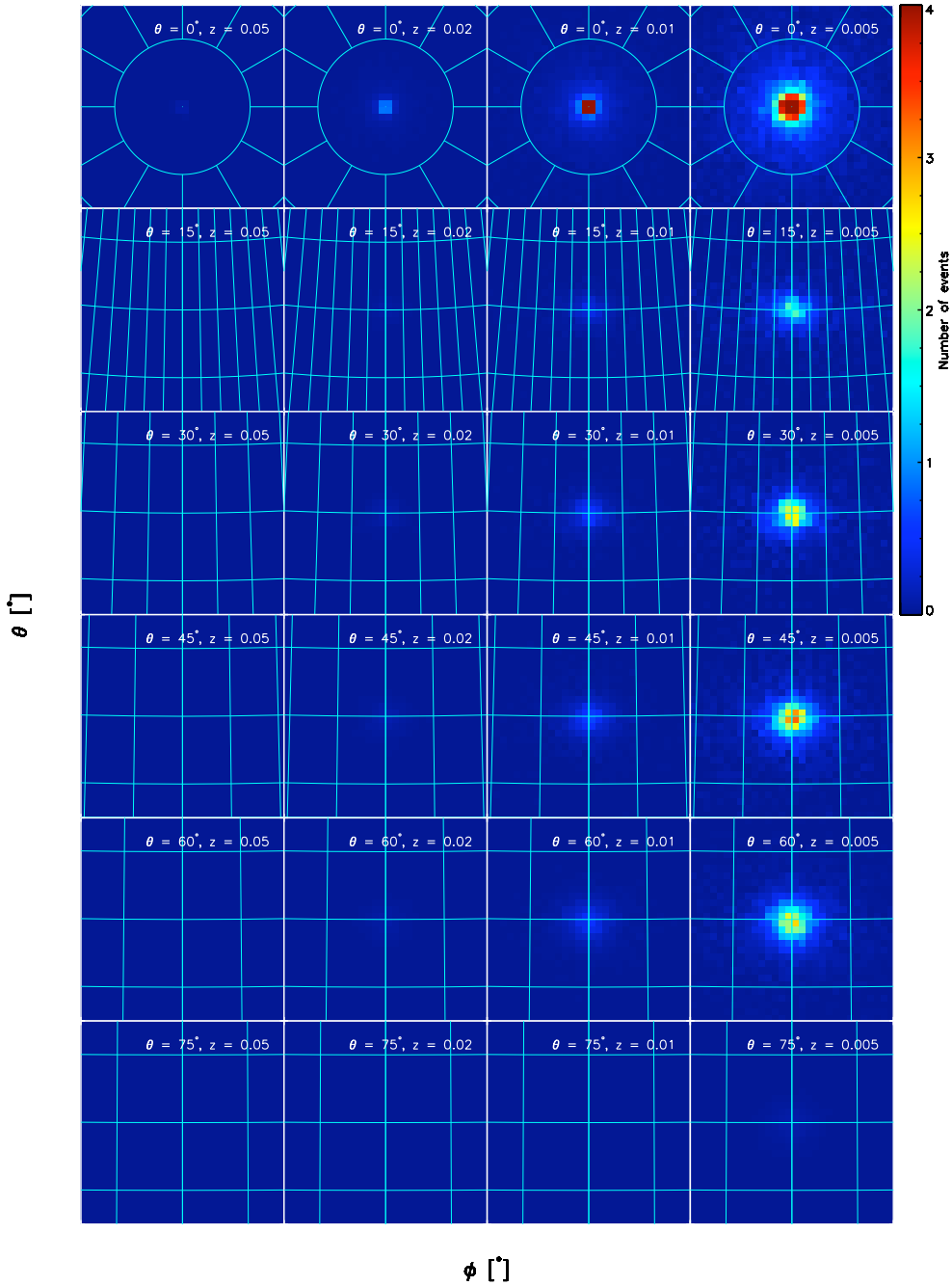


Figure 8.5: The angular distribution of signal and background events for different zenith distances and redshifts. Different rows correspond to different zenith distances  $\theta$  and different columns correspond to different redshifts  $z$ . Each plot is centered on the supposed direction of the GRB. The blue lines indicate an equally-spaced grids at  $1^\circ \times 1^\circ$ . The events are mapped in Lambert azimuthal equal-area projection.

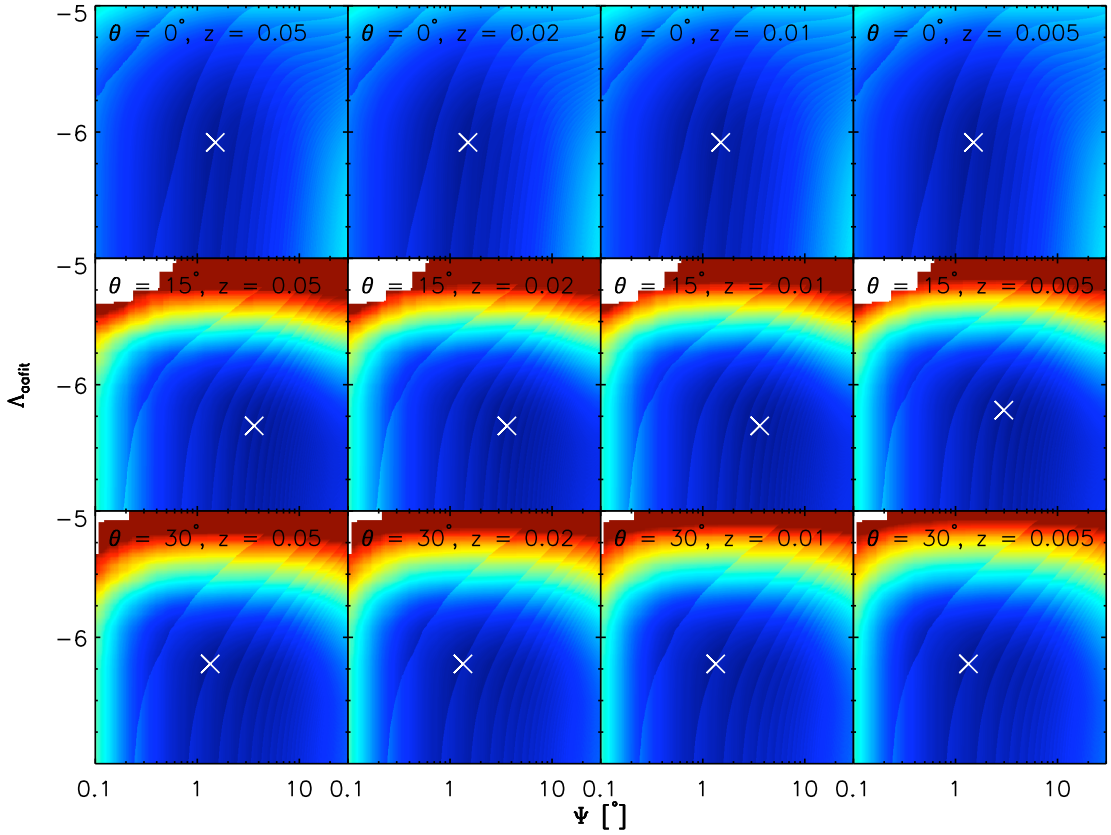


Figure 8.6: The model discovery potential (MDP) for 50% chance of making a  $5\sigma$  discovery, plotted as a function of opening radius  $\Psi$  and  $\Lambda_{\text{aaifit}}$ . For each point in the plot, the MDP is determined from the background contained within the radius  $\Psi$  from the supposed direction of the GRB and with a minimum reconstruction likelihood  $\Lambda_{\text{aaifit}}$ . The top, middle, and bottom rows correspond respectively to zenith distances  $0^\circ$ ,  $15^\circ$ , and  $30^\circ$ . The left, middle, and right columns correspond respectively to redshifts 0.05, 0.02, 0.01, 0.005.

The value  $1 - \beta$  is the usually called the *discovery potential*. If we fix  $1 - \beta$  to a certain value, e.g.  $1 - \beta = 0.5$ , we could then calculate the minimum signal required such that Equation 8.7 is satisfied. The value of  $\mu_s$  satisfying Equation 8.7 could then be interpreted as the *least detectable signal*  $\mu_{\text{lds}}$ .

The ratio between this least detectable signal  $\mu_{\text{lds}}$  and the expected number of signal  $\mu_s$  is called the Model Discovery Potential or MDP. If we choose the cut criteria that minimize the MDP, we would then minimize the required signal that will give a probability  $1 - \beta$  it would yield an observation at significance level  $\alpha$ . For this minimization of the MDP, I choose two cut criteria: the maximum opening radius  $\Psi$  around the supposed direction of the

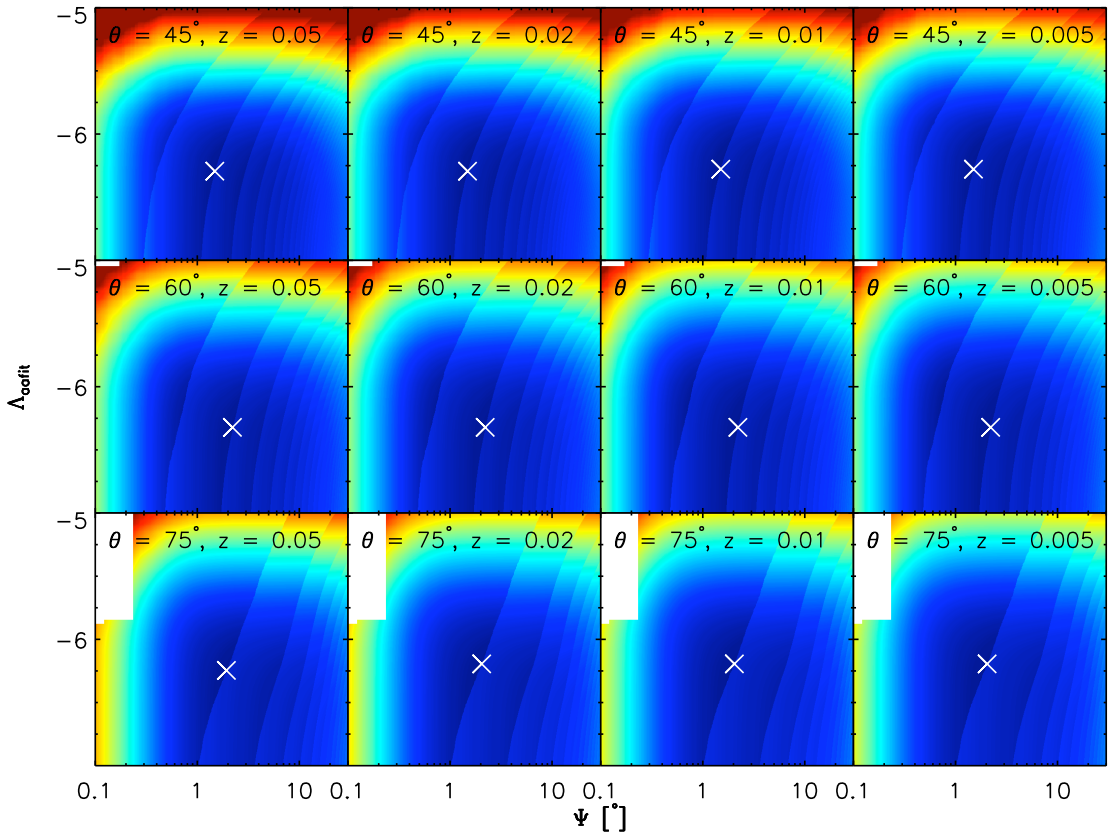
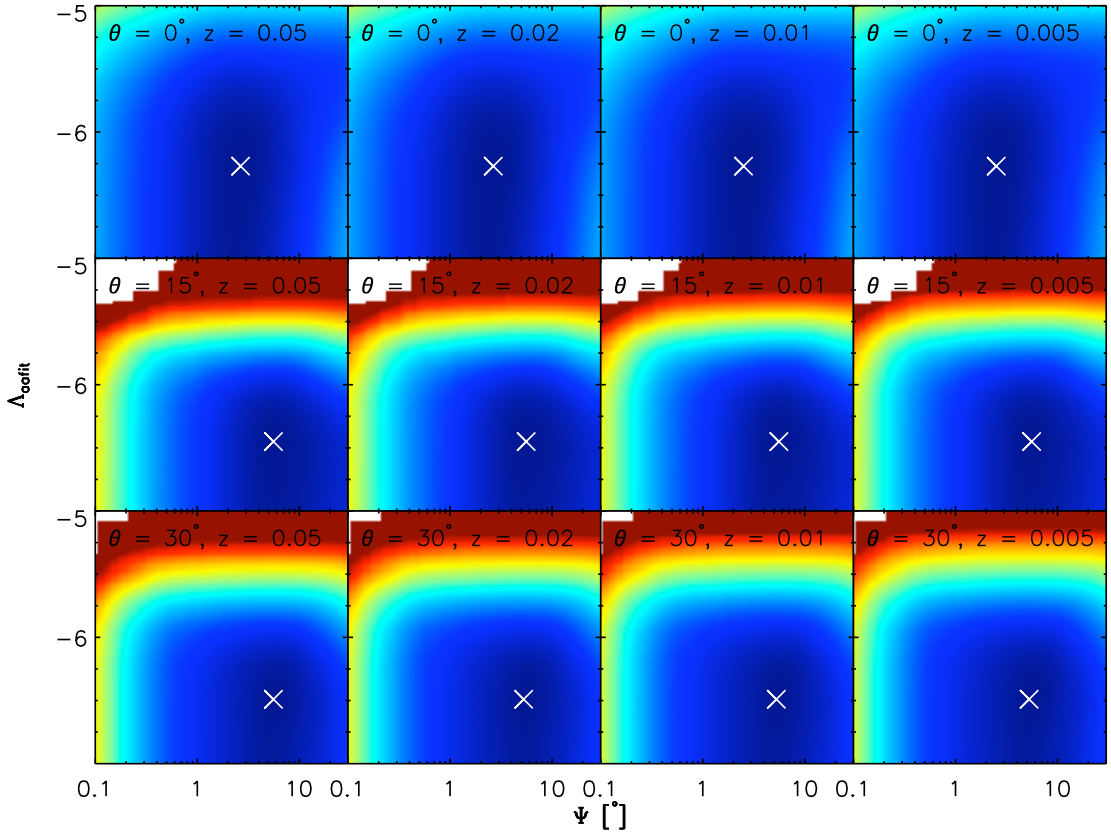


Figure 8.7: The same as in Figure 8.6, but the top, middle, and bottom rows correspond respectively to zenith distances  $45^\circ$ ,  $60^\circ$ , and  $75^\circ$ .

GRB and the minimal  $\Lambda_{\text{aaifit}}$  value.

The result of this minimization is given in Figures 8.6 and 8.7 for  $\alpha = 5\sigma$  and  $1 - \beta = 0.5$ . For various fictitious GRB events at 4 different redshifts and 6 different zenith distances, the MDP is calculated as a function of the opening radius  $\Psi$  and the minimum likelihood  $\Lambda_{\text{aaifit}}$ . At each point in the  $\Psi$ - $\Lambda_{\text{aaifit}}$  space, all events satisfying the cuts are admitted to calculate the MDP, and the point that give the minimum MDP is then marked in the Figures as a white cross.

We can see in these Figures that the position of the minimum MDP does not change significantly with redshift and changes only slightly with zenith distance. This is a good result because this



means that MDP is an unbiased estimator, i.e. the minimized true signal rate  $\mu_{\text{lds}}$  is independent of the expected signal rate  $\mu_s$ . Table 8.2 summarizes the combination of cut values that minimizes the MDP for all zenith distances.

#### 8.4 Optimization for sensitivity: The model rejection factor

A METHOD commonly used to set an unbiased sensitivity limit is the Model Rejection Factor (MRF) technique (Hill & Rawlins, 2003). With this method the selection cut that minimizes the expected upper limit of the experiment—assuming that no true signal is present—can be determined.

Suppose we choose events satisfying a certain selection cuts,

Figure 8.8: The model discovery factor (MRF) for 90% confidence limit as a function of opening radius  $\Psi$  and  $\Lambda_{\text{aafit}}$ . For each point in the plot, the MRF is determined from background events contained within the radius  $\Psi$  from the supposed direction of the GRB and with a minimum reconstruction likelihood  $\Lambda_{\text{aafit}}$ . The top, middle, and bottom rows correspond respectively to zenith distances  $0^\circ$ ,  $15^\circ$ , and  $30^\circ$ . The left, middle, and right columns correspond respectively to redshifts 0.05, 0.02, 0.01, 0.005.

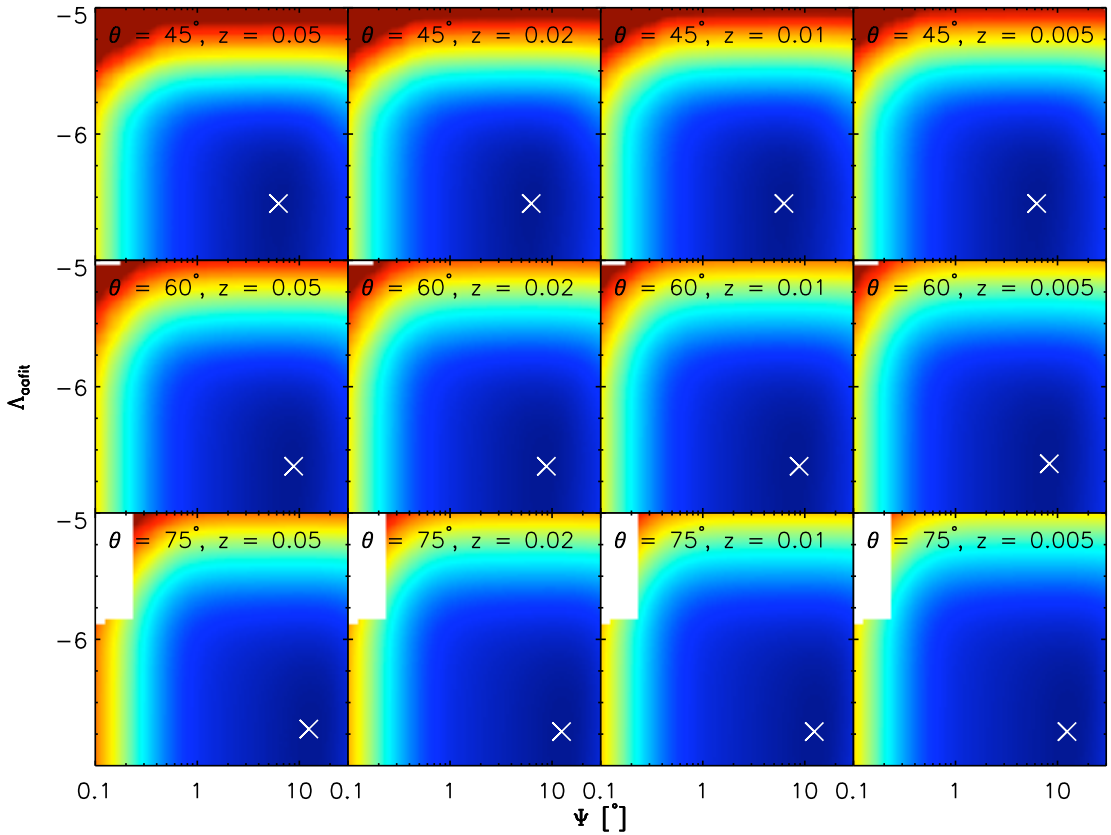


Figure 8.9: The same as in Figure 8.8, but the top, middle, and bottom rows correspond respectively to zenith distances  $45^\circ$ ,  $60^\circ$ , and  $75^\circ$ .

we then obtain an expected background rate  $\mu_b$  and an expected signal rate  $\mu_s$ . We can then simulate the experiment and obtain a number of observed events  $n_{\text{obs}}$ . Given  $\mu_b$  and  $n_{\text{obs}}$ , we can then calculate the confidence interval  $\mu_\alpha = (\mu_1, \mu_2)$  using the Feldman–Cousins unified approach (Feldman & Cousins, 1998).

Since we do not know the actual upper limit until we are looking at the data, we can determine the average upper limit that would be observed after we performed a hypothetical repetition of the experiment (assuming that the background rate is  $\mu_b$  and there is no true signal) and obtain all possible outcomes of the observed number of events  $n_{\text{obs}}$ . This average upper limit would then be the sum of all upper limits for the possible numbers of

$\theta$ [ $^\circ$ ]	MDP		MRF	
	$\Psi$	$\Lambda_{\text{aafit}}$	$\Psi$	$\Lambda_{\text{aafit}}$
0	1.50	-6.08	2.66	-6.27
15	3.61	-6.33	5.58	-6.45
30	1.34	-6.21	5.58	-6.49
45	1.48	-6.29	6.25	-6.55
60	2.21	-6.32	8.80	-6.63
75	1.93	-6.25	12.39	-6.71

Table 8.2: The combination of cut values that minimizes the MDP and the MRF.

$n_{\text{obs}}$  weighted by their Poisson probability of occurring:

$$\bar{\mu}_\alpha(\mu_b) = \sum_{n_{\text{obs}}=0}^{\infty} \mu_\alpha(n_{\text{obs}}, \mu_b) \frac{\mu_b^{n_{\text{obs}}}}{n_{\text{obs}}!} \exp(-n_b) \quad (8.8)$$

By calculating  $\bar{\mu}_\alpha$  after the cut are applied, we can then determine the MRF which is the quantity  $\bar{\mu}_\alpha / \mu_s$ . We could optimize the cuts by finding the combination of cut values that would minimize the MRF.

The result of the MRF minimization is shown in Figures 8.8 and 8.9 for a 90% confidence interval. For various fictitious GRB events at 4 different redshifts and 6 different zenith distances, the MRF is shown as a function of the opening radius  $\Psi$  and the minimum likelihood  $\Lambda_{\text{aafit}}$ . The point that give the minimum MRF is marked in the Figures as a white cross. Table 8.2 summarizes the combination of cut values that minimizes the MRF.

The cut that minimize the MRF is looser than that of the MDP minimization. This is because we aim to optimize for sensitivity. The short exposure time practically reduces the background rate to zero. Consequently, the cuts should be looser. This is apparent especially at angles close to the horizon. At these angles the expected background rates is very low hence the search cone can be very large and the  $\Lambda_{\text{aafit}}$  cut very loose. As a result, one will accept admit more events.

## 9 Hypothesis testing

ONCE the optimal quality cuts have been defined and the data have been obtained, we can test whether the data are compatible with a signal plus background hypothesis or the background-only hypothesis. These two hypotheses are traditionally referred to as  $H_0$  for the background-only hypothesis and  $H_1$  for the hypothesis that the data contain signal events in addition to background events.

The hypothesis testing is usually performed with the likelihood ratio method. The likelihood ratio  $Q$  is the ratio of probabilities for the results from the two hypotheses:

$$Q = -2 \ln \frac{\mathcal{L}(\text{data}|H_1)}{\mathcal{L}(\text{data}|H_0)} \quad (9.1)$$

The likelihood  $\mathcal{L}(\text{data}|H_1)$  and  $\mathcal{L}(\text{data}|H_0)$  are the products of all the probabilities for the events under the given hypothesis:

$$\mathcal{L}(\text{data}|H_1) = \prod_i P(\mathbf{X}_i|H_1), \quad (9.2)$$

$$\mathcal{L}(\text{data}|H_0) = \prod_i P(\mathbf{X}_i|H_0), \quad (9.3)$$

where  $P(\mathbf{X}_i|H_1)$  and  $P(\mathbf{X}_i|H_0)$  are the probability density functions that describe the probability of an event with observable parameters  $\mathbf{X}_i$  to agree with the  $H_1$  hypothesis and the  $H_0$  hypothesis, respectively.

For the modelling of the probability distribution function (PDF) for the signal, we could use the point spread function (Chapter 8) centered at the supposed direction of the GRB. The PDF would simply return the probability to find a signal event at a given azimuth  $\psi$  and zenith distance  $\theta$ . The closer the signal is to the supposed direction of the GRB, the higher its likelihood to be a



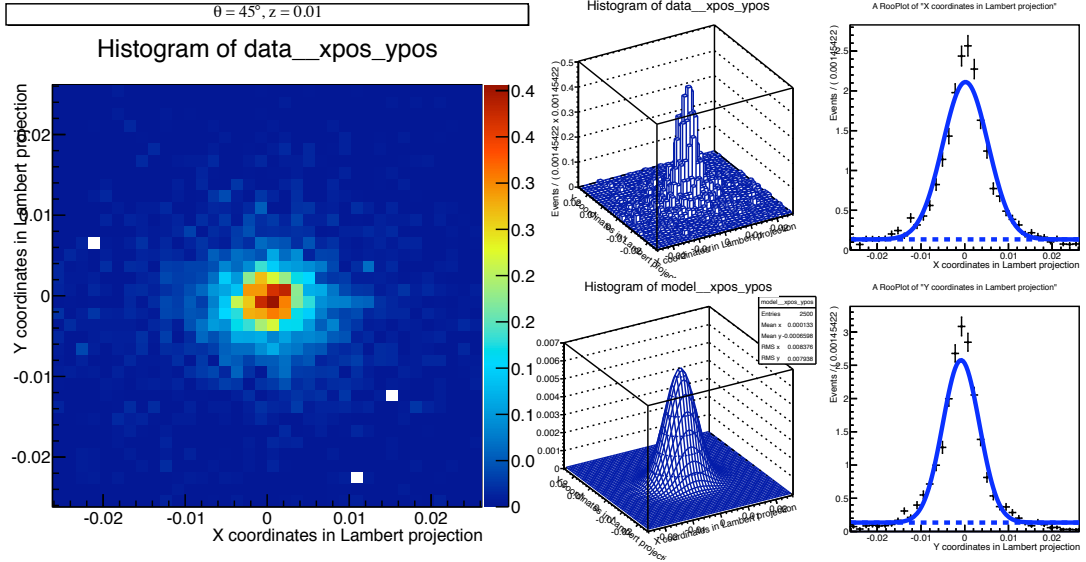


Figure 9.1: The probability density function for signal and background. The leftmost plot is the distribution of all events centered around the direction of a fictional GRB event located at zenith distance  $45^\circ$  and redshift 0.01. The  $x$  and  $y$  abscissa are the coordinates in Lambert azimuthal equal-area projection and are related to the azimuth  $\psi$  and zenith distance  $\theta$  in local coordinates. The middle-top plot is the same histogram as in the leftmost plot, but in the form of a lego plot. The middle-bottom plot is the bivariate normal distribution that fits the event distribution. The rightmost plots are the projections of the distribution. The dashed line is the fit to the background distribution which is assumed to be a constant.

signal event. The PDF for the signal events will thus be

$$P_s(x, y | \mu_x, \mu_y, \sigma_x, \sigma_y, \rho) = \frac{1}{2\pi\sigma_x\sigma_y\sqrt{1-\rho^2}} \times \exp\left(-\frac{1}{2(1-\rho^2)} \times \left[ \frac{(x-\mu_x)^2}{\sigma_x^2} + \frac{(y-\mu_y)^2}{\sigma_y^2} + \frac{2\rho(x-\mu_x)(y-\mu_y)}{\sigma_x\sigma_y} \right]\right), \quad (9.4)$$

where  $\rho$  is the correlation between  $x$  and  $y$ .

The probability distribution for the background events is taken to be a constant function for all  $\psi$  and  $\theta$ . This approximation is still valid if we consider the background data within a small opening angle ( $\psi \sim 1^\circ$ ) around the source direction. Figure 9.1 shows the two-dimensional distribution of combined background and signal events along with a fit of a bivariate normal distribution to the data. We can see that the fit describes reasonably well the signal and background data.

Since we now have all the ingredients for the test statistics, we

can evaluate  $Q$  by seeking the values of the parameters that maximize

$$\log P_s(\text{data}|\mathbf{p}_s^{\max}) = \sum_i^{\text{data}} \log P_s(x_i, y_i|\mu_x, \mu_y, \sigma_x, \sigma_y, \rho), \quad (9.5)$$

where  $\mathbf{p}_s^{\max} = (\hat{\mu}_x, \hat{\mu}_y, \hat{\sigma}_x, \hat{\sigma}_y, \hat{\rho})$  is the vector of parameters that maximize said Equation.

To see how the test statistics are distributed, we perform Monte Carlo experiments that simulate all possible outcomes of the observation. In this, a number of background events according are generated according to the expected rate  $\mu_b$ . The distributions of the test statistics for the background-only experiments are shown in the left part of Figures 9.2–9.4, for various zenith distances.

Using the cumulative distribution function  $Q$  for the background-only experiment, we can compute the critical value of  $Q_c$ , i.e. the maximum value of  $Q$  in which the probability that the data sample contains not only background events but also signal events at a given confidence level  $\alpha$ . Per definition,

$$1 - \alpha = P(Q \leq Q_c|H_0). \quad (9.6)$$

Figures 9.2–9.4 show the critical values for the  $3\sigma$  and  $5\sigma$  confidence levels, respectively  $Q_c^{3\sigma}$  and  $Q_c^{5\sigma}$ . The determination of  $Q_c^{3\sigma}$  is straightforward, however the determination of  $Q_c^{5\sigma}$  requires an extrapolation of the CDF due to an insufficient number of experiments. For each zenith distance, a set of  $6 \times 10^5$  background-only experiment is performed.

We can now move on to see how  $Q$  is distributed when there are a number of signal events in the data in addition to the background. In this second run of experiments, a fixed number of signal events is added to the background. The number of signal events added are  $n_s = \{1, 3, 5, 8, 10, 12, 15, 18, 20\}$ . For each value of  $n_s$ , first a fit is performed to obtain the parameters that maximizes the probability for the signal plus background hypothesis and then the value of  $Q$  is evaluated. The probability density function of  $Q$  for this signal plus background case is shown in the right part of Figures 9.2–9.4. The red histogram is the distribution of  $Q$  for the background-only case, while the other histograms correspond to the distributions for different numbers of signal counts.

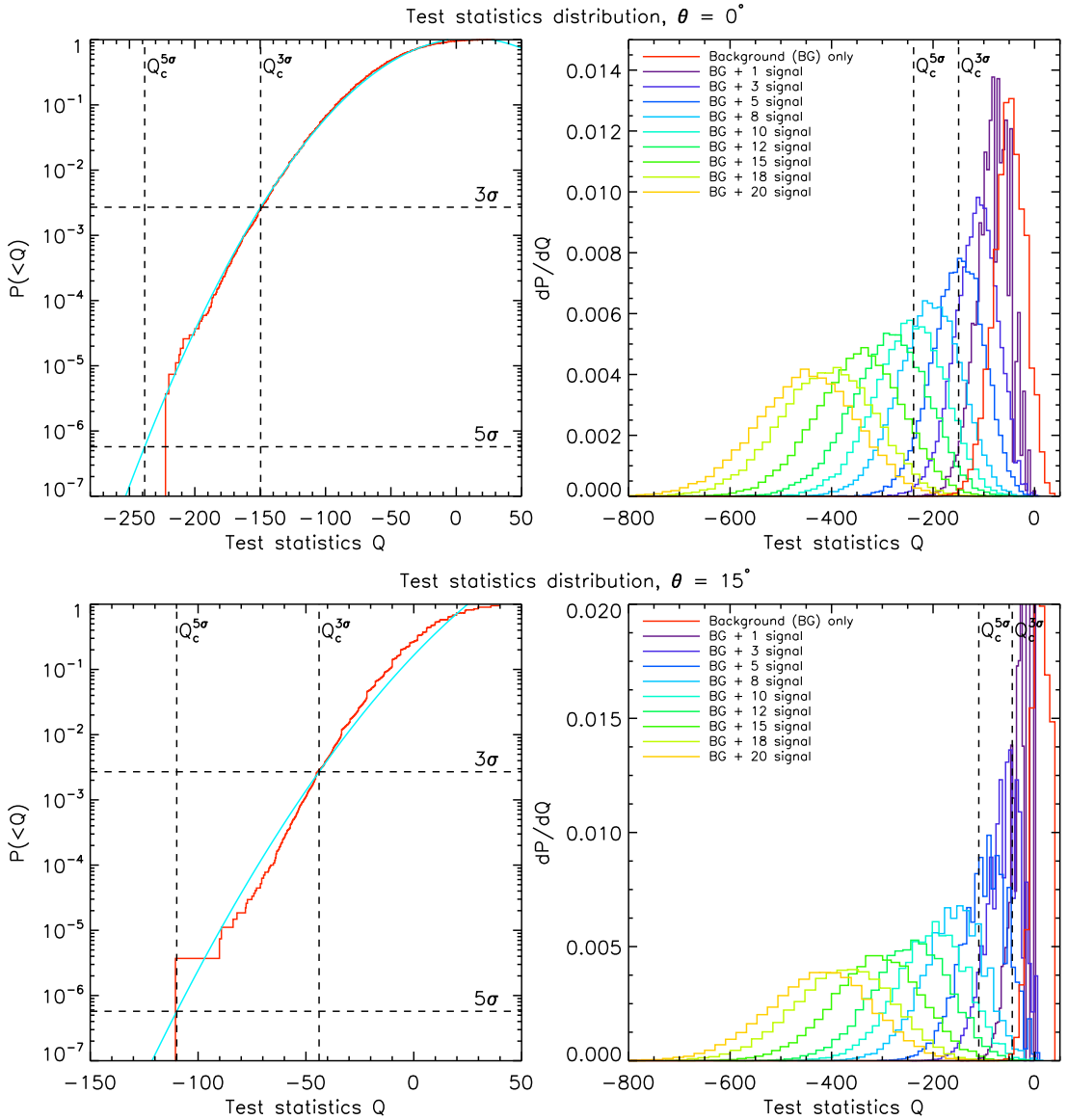


Figure 9.2: The distribution of test statistics  $Q$ . The left part shows the cumulative distribution of  $Q$  for the background-only experiments, while the right part shows the probability density distribution of  $Q$  for the background-only experiments (red histogram) and for a number of signal events added to the background. The number of signals added to the experiment is indicated in the legend. For the background-only experiments, a parabolic function is fitted to the logarithm of the cumulative function in order to extrapolate the CDF to the  $5\sigma$  level. The critical value of  $Q$  at the  $3\sigma$  and  $5\sigma$  level is also shown. The top and bottom rows correspond respectively to zenith distances  $0^\circ$  and  $15^\circ$ .

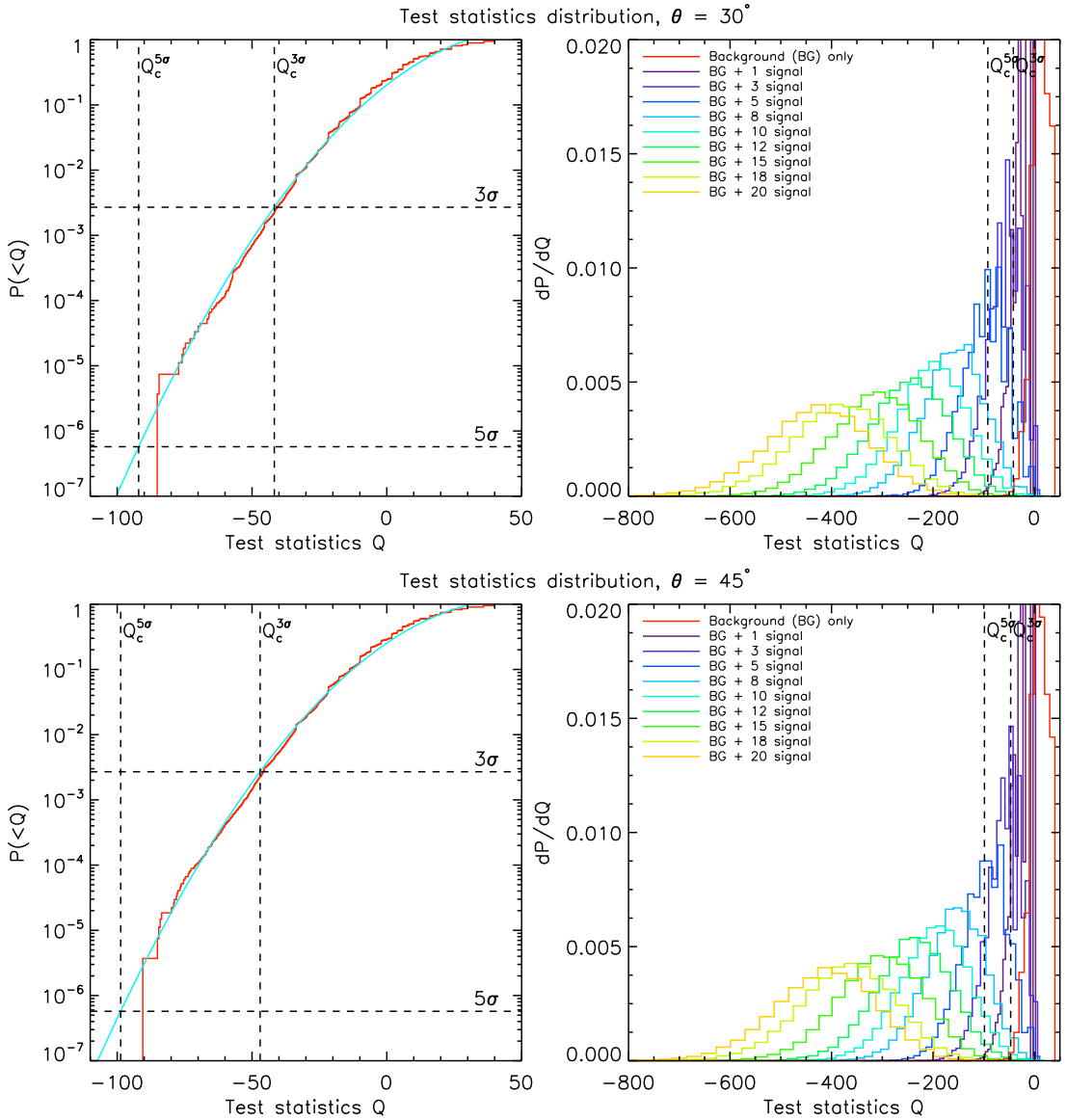


Figure 9.3: The same as in Figure 9.2. The top and bottom rows correspond respectively to zenith distances  $30^\circ$  and  $45^\circ$ .

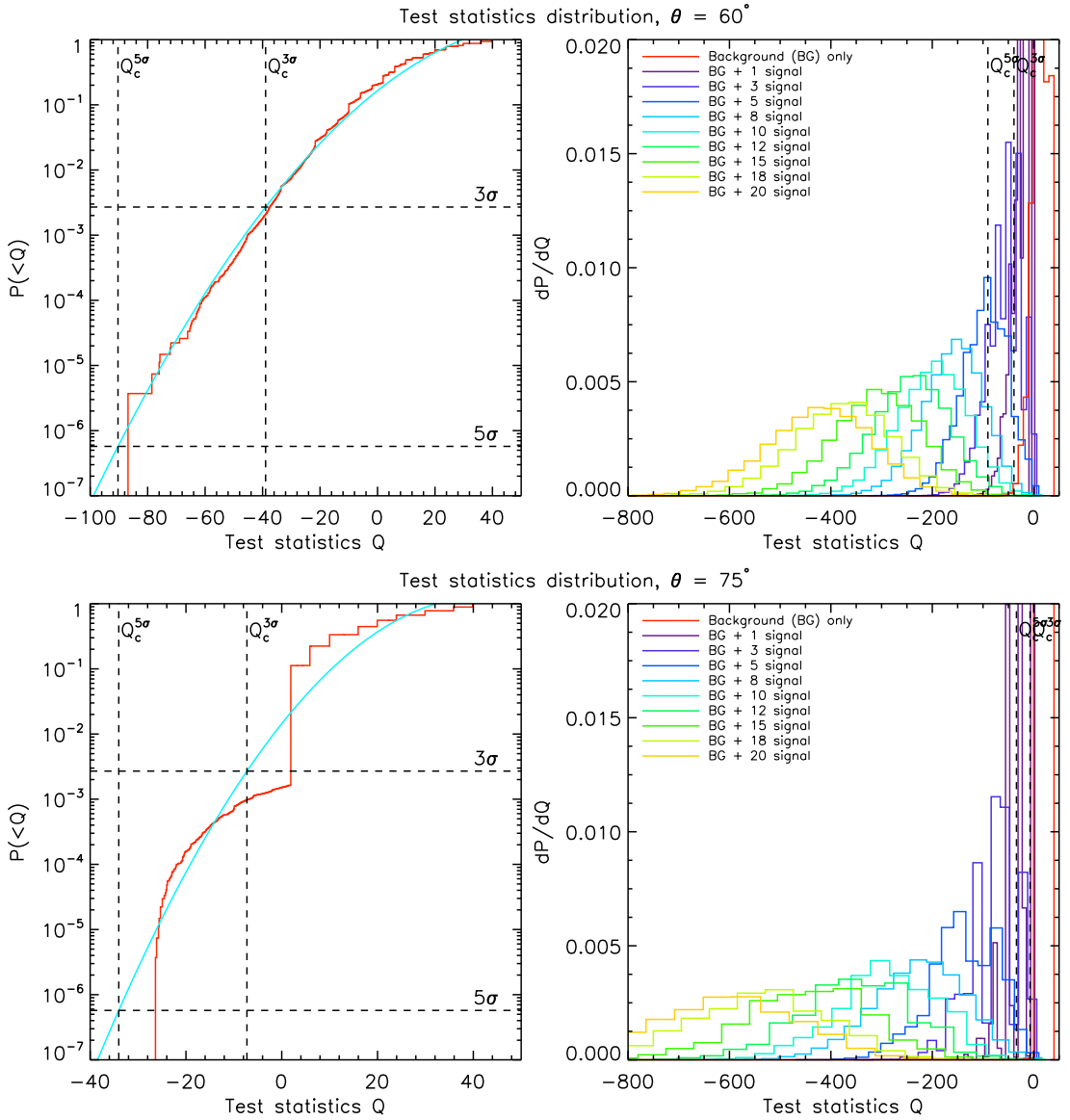


Figure 9.4: The same as in Figure 9.2. The top and bottom rows correspond respectively to zenith distances  $60^\circ$  and  $75^\circ$ .

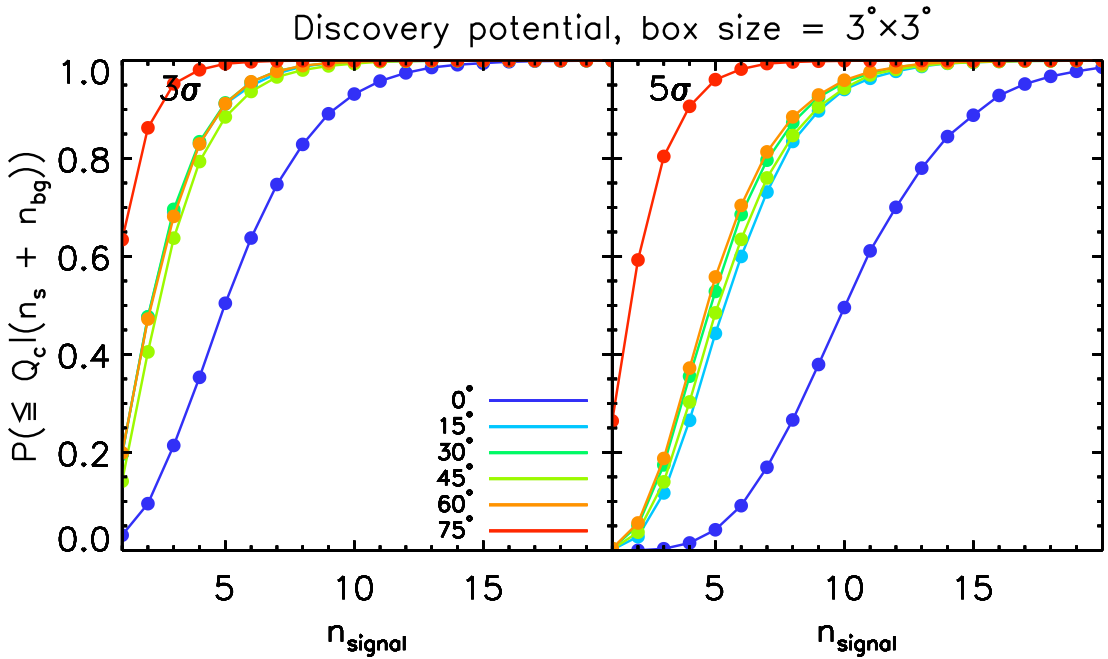


Figure 9.5: The discovery potential as a function of the number of signal events  $n_s$  present in the data. Each line with different colors plots the discovery potential for different zenith distance, indicated by the color-coding in the legend.

We can see that the more signal events are added, the better we can separate between background-only case and the signal plus background case. The minimum number of signal events required to claim a discovery depends on the background rate  $\mu_b$ . Since the background rate varies primarily with the zenith distance, it is possible to determine the minimum number of signal events required to claim discovery as a function of zenith distance only. Figure 9.5 plots the discovery potential as a function of the number of signals for six different values of zenith distance. In general we can see that for most cases there is a 90% chance of making a discovery with  $3(5)\sigma$  significance when there are 5(9) signal events present in the data. For the most extreme cases, such as sources coming straight from the zenith ( $\theta = 0^\circ$ ), the number of required signal events is higher due to the higher background rate relative to the other zenith distances. For sources close to the horizon, here for example at  $\theta = 75^\circ$ , the required number of signal events is less due to the low background rate.



PART III

*Data analysis*





# 10 *Prospective GRB sources*

IN THIS Chapter the procedure for selecting prospective GRB sources will be described as well as a description of the target GRB proposed to the ANTARES Collaboration to be observed.

## 10.1 *Selection Procedure*

A NUMBER of GRB events from the past  $\sim 6$  years has been compiled from various GRB catalogues and ranked in order of their expected signal  $\mu_s$ . The catalogues used to compile the events and the number of GRBs obtained are:

1. *Swift* GRB Table, [http://swift.gsfc.nasa.gov/docs/swift/archive/grb\\_table.html/](http://swift.gsfc.nasa.gov/docs/swift/archive/grb_table.html/), 729 GRBs as of 29 January 2012.
2. *Fermi* GRB Table, [http://fermi.gsfc.nasa.gov/ssc/observations/types/grbs/grb\\_table/](http://fermi.gsfc.nasa.gov/ssc/observations/types/grbs/grb_table/), 26 GRBs as of 29 January 2012.
3. GRBweb compilation, <http://grbweb.icecube.wisc.edu/> (Aguilar, 2011), 568 GRBs as of 29 January 2012.
4. GRBox, <http://lyra.berkeley.edu/grbox/grbox.php>, 1 GRB (GRB 080109A) that turns out to be an X-ray transient.

In these catalogues, most of the six physical properties required to construct the photon spectrum and to estimate the expected number of signal  $\mu_s$  are available. Furthermore, whenever available, the properties in the initial catalogue are superseded with those of the values calculated by Butler et al. (2007); Butler, Bloom & Poznanski (2010) for the *Swift* GRBs and from Zhang et al. (2011) for the *Fermi* GRBs. For these papers, the authors have rigorously analyzed the spectra of the detected GRBs and have calculated the values that best fit their spectral profile. If there is still an unknown value, the standard values shown in Table 10.1 are used. These “most likely” values are obtained from the statistical analysis of GRBs measured by Butler et al. (2007); Butler, Bloom & Poznanski (2010).

Par.	Definition	Value
$\alpha$	spectral index at low energy	1
$\beta$	spectral index at high energy	2
$\epsilon_{\text{pk}}$	the energy at which the spectrum peaks	400 keV
$L_{\text{bol}}^{\text{iso}}$	isotropic bolometric luminosity	$8.9 \times 10^{52}$ erg
$\Delta t_*$	source-frame burst duration	30 s
$z$	redshift	0.97

Table 10.1: The standard values of GRB physical properties used to estimate the expected number of signal events  $\mu_s$ .

The redshifts of each individual GRBs are treated differently depending on the available data. If the redshift is directly measured by a ground-based telescope, this measurement will be immediately used. Unfortunately, due to the transient nature of GRBs, only a small minority of GRBs have measured redshift. If the redshift is unknown, the following scheme is employed in descending order of priority:

1. If the apparent  $\gamma$ -ray flux  $F_{\text{iso}}$  is measured, I transform this measured flux from the instrument band into the standard bolometric band of 1–10<sup>4</sup> keV. The transformation is performed by assuming that the bolometric flux is related to the measured flux by

$$F_{\text{iso}}^{\text{bol}} = f_I F_{\text{iso}}^{\text{inst}}, \quad (10.1)$$

where  $f_I$  is the conversion factor from the instrument band to the bolometric band. If we know that the photon energy spectrum is in the form of the Band function, then both  $F_{\text{iso}}^{\text{bol}}$  and  $F_{\text{iso}}^{\text{inst}}$  can be calculated by integrating the Band function  $N(\epsilon)$  described in Equation 2.52 in their respective energy band:

$$\int_{1 \text{ keV}}^{10^4 \text{ keV}} d\epsilon N(\epsilon_\gamma) \epsilon = f_I \int_{\epsilon_1}^{\epsilon_2} d\epsilon N(\epsilon) \epsilon, \quad (10.2)$$

where  $(\epsilon_1, \epsilon_2)$  is the energy range of the detector involved. The solution to the integral on both side for  $\alpha = 1$  is given in Equation 2.59. However, various values of  $\alpha$  have been measured and it is necessary to solve the integral for a general value of  $\alpha$ :

$$\lambda_{\text{bol}}(\alpha, \beta, \epsilon_{\text{bk}}, \epsilon_1, \epsilon_2) = \epsilon_{\text{bk}}^2 (\lambda_{\text{low}} + \lambda_{\text{high}}), \quad (10.3)$$

where

$$\lambda_{\text{low}} = \left( \frac{\epsilon_1}{\epsilon_{\text{bk}}} \right)^{2-\alpha} E_{\alpha-1} \left( (\beta - \alpha) \frac{\epsilon_1}{\epsilon_{\text{bk}}} \right) - E_{\alpha-1}(\beta - \alpha), \quad (10.4)$$

$$\lambda_{\text{high}} = \exp(\alpha - \beta) \times \begin{cases} \frac{1}{2-\beta} \left[ \left( \frac{\epsilon_2}{\epsilon_{\text{bk}}} \right)^{2-\beta} - 1 \right], & \beta \neq 2, \\ \ln \left( \frac{\epsilon_2}{\epsilon_{\text{bk}}} \right), & \beta = 2, \end{cases} \quad (10.5)$$

where  $E_n(x)$  in Equation 10.4 is the exponential integral (Abramowitz & Stegun, 1964)

$$E_n(x) = \int_1^{\infty} dt \frac{e^{-xt}}{t^n}, \quad (n = 0, 1, 2, \dots; \Re x > 0). \quad (10.6)$$

Solving both integrals, the conversion factor  $f_I$  can then be obtained.

The redshift is then calculated by assuming that the isotropic bolometric luminosity is  $L_{\text{bol}}^{\text{iso}} = 8.9 \times 10^{52}$  erg.

2. If no flux is measured, the most probable value of  $z = 0.97$  is used and the bolometric luminosity is assumed to be  $L_{\text{bol}}^{\text{iso}} = 8.9 \times 10^{52}$  erg.

The same scheme is also employed to calculate  $L_{\text{bol}}^{\text{iso}}$ . If a measured redshift is available and the flux is also measured, the luminosity is calculated first by transforming the measured flux to the standard bolometric band, and then use it along with the measured redshift to calculate the luminosity. If any of those values are unavailable, the standard value from Table 10.1 is used.

After all of the six values are determined, we can then proceed by calculating the expected number of signal event  $\mu_s$ :

$$\mu_s = t_{\text{exp}} \int_0^{\infty} d\epsilon_{\mu} \frac{dN_{\mu}}{d\epsilon_{\mu}}(a, b, T_{90}, \epsilon_{\text{pk}}, L_{\text{bol}}^{\text{iso}}, z, \theta) A_{\mu}^{\text{eff}}(\epsilon_{\mu}), \quad (10.7)$$

where  $t_{\text{exp}}$  is the exposure time of the data taking and is assumed to be equal to the measured  $T_{90}$  or 30 seconds if it is not measured;  $A_{\mu}^{\text{eff}}(\epsilon_{\mu})$  is the muon effective area as a function of the muon energy  $\epsilon_{\mu}$  and is already presented in Section 7.2.3;  $dN_{\mu}/d\epsilon_{\mu}$  is the muon spectrum of the GRB at detector level, given the six physical parameters of the GRB and its zenith distance  $\theta$ . It can be calculated using the prescription formulated in Chapters 2–3.

The expected number of background event  $\mu_{bg}$  parallel with the direction of the GRB is calculated by counting all the events from the reconstructed data that are within the circle of the optimum radius centered on the zenith distance  $\theta$  of the GRB and weight them according to Equation 8.5.

All the GRBs in the catalogue are selected according to these preliminary criteria:

1. The GRB must occur after the first light of ANTARES, which is on 2 March 2006.
2. The GRB must be above the horizon of ANTARES when it is occurring.
3.  $\mu_s \geq 10^{-9}$ .

Using these three criteria alone, 14 GRBs satisfying all three criteria are found. They are shown in Table 10.2, sorted in descending order of  $\mu_s$ . In the last column of this Table the Li & Ma (1983) significance is also calculated. In calculating the Li & Ma significance, the on-time is taken to be equal to  $T_{90}$  and the off-time is taken to be 1800 seconds (30 minutes) long.

By looking at the number of expected signal  $\mu_s$ , it is apparent that the collecting area of ANTARES still too small to observe interesting TeV sources. It was proposed that the top two prospective GRBs will be observed, i.e. GRB 090709A and GRB 070220. Even if in the end we do not find any signal-like events, it possible to set up a confidence limit on ANTARES sensitivity to TeV  $\gamma$ -rays.

Before further analysis of ANTARES data can be performed, an optimum quality cut needs to be found. In order to do this, the number of expected signal and background need to be estimated. To achieve the former, a full Monte Carlo simulation from the top of the atmosphere to the detector volume needs to be performed. The latter can be estimated by analysing the data already obtained by ANTARES in the past years. The upper limit of signal event rate  $\mu_s$  can be determined by calculating the upper limit of the Feldman-Cousins confidence interval, given the estimated number of background  $\mu_b$ , the number of observed events  $n_{obs}$  and the required confidence limit  $\alpha = 90\%$ .

Table 10.2: The list of prospective GRBs in which the top 2 were proposed to be unblinded.

No.	Name	$\alpha$ [ $^{\circ}$ ]	$\delta$ [ $^{\circ}$ ]	Az [ $^{\circ}$ ]	Alt [ $^{\circ}$ ]	$F_{\text{iso}}$ [erg cm $^{-2}$ ]	$a$	$b$	$E_{\text{pk}}$ [keV]	$T_{90}$ [s]	$z$	$L_{\text{iso}}$ [ $10^{52}$ erg]	$\mu_{\text{sig}}$	$\mu_{\text{bg}}$	S
1	090709A	289.94	60.73	331.62	25.09	$1.55 \times 10^{-3}$	0.06 <sup>b</sup>	1 <sup>c</sup>	283.24 <sup>b</sup>	344.85 <sup>b</sup>	0.13/	5.50 <sup>c</sup>	$3.72 \times 10^{-4}$	0.0516	0.30
2	070220	34.80	68.80	4.68	22.05	$5.02 \times 10^{-4}$	0.29 <sup>b</sup>	1 <sup>c</sup>	350.45 <sup>b</sup>	150.67 <sup>b</sup>	0.22/	5.50 <sup>c</sup>	$3.65 \times 10^{-7}$	0.0169	0.18
3	060505	331.77	-27.82	176.54	19.39	$9.44 \times 10^{-7}$	0.29 <sup>b</sup>	1 <sup>c</sup>	400 <sup>c</sup>	4.00 <sup>f</sup>	0.089 <sup>f</sup>	0.0049 <sup>f</sup>	$1.64 \times 10^{-7}$	0.0003	0.02
4	080325	277.91	36.52	98.27	68.77	$1.06 \times 10^{-4}$	0.67 <sup>b</sup>	1 <sup>c</sup>	36.63 <sup>b</sup>	183.92 <sup>b</sup>	0.46 <sup>f</sup>	5.50 <sup>c</sup>	$1.48 \times 10^{-7}$	0.1221	0.48
5	101225A	0.20	44.57	284.15	75.88	$1.90 \times 10^{-6}$	0.82 <sup>a</sup>	1 <sup>c</sup>	400 <sup>c</sup>	1088.00 <sup>a</sup>	0.4 <sup>d</sup>	0.21 <sup>d</sup>	$8.33 \times 10^{-8}$	1.0500	1.28
6	080727C	32.64	64.13	32.60	36.23	$1.44 \times 10^{-4}$	-0.06 <sup>b</sup>	1 <sup>c</sup>	202.10 <sup>b</sup>	99.84 <sup>b</sup>	0.40 <sup>f</sup>	5.50 <sup>c</sup>	$6.12 \times 10^{-8}$	0.0331	0.25
7	081022	226.58	12.41	225.37	51.76	$9.25 \times 10^{-5}$	-0.07 <sup>b</sup>	1 <sup>c</sup>	83.70 <sup>b</sup>	149.60 <sup>b</sup>	0.49 <sup>f</sup>	5.50 <sup>c</sup>	$4.46 \times 10^{-8}$	0.0733	0.38
8	081126	323.53	48.71	303.49	41.18	$1.10 \times 10^{-4}$	-0.06 <sup>b</sup>	1 <sup>c</sup>	261.38 <sup>b</sup>	59.60 <sup>b</sup>	0.45 <sup>f</sup>	5.50 <sup>c</sup>	$3.80 \times 10^{-8}$	0.0240	0.22
9	070616	32.10	56.95	332.06	19.64	$4.88 \times 10^{-4}$	0.33 <sup>b</sup>	1 <sup>c</sup>	99.47 <sup>b</sup>	443.52 <sup>b</sup>	0.22 <sup>f</sup>	5.50 <sup>c</sup>	$2.49 \times 10^{-8}$	0.0350	0.25
10	110825A	46.00	13.80	128.84	51.08	$5.45 \times 10^{-5}$	0.23 <sup>b</sup>	1.04 <sup>i</sup>	245.74 <sup>b</sup>	6.90 <sup>j</sup>	0.49 <sup>f</sup>	5.50 <sup>c</sup>	$1.94 \times 10^{-8}$	0.0033	0.08
11	080319A	206.35	44.08	294.34	45.20	$9.46 \times 10^{-5}$	0.64 <sup>b</sup>	1 <sup>c</sup>	38.10 <sup>b</sup>	45.63 <sup>b</sup>	0.48 <sup>f</sup>	5.50 <sup>c</sup>	$7.26 \times 10^{-9}$	0.0195	0.20
12	070704	354.71	66.26	21.78	27.06	$1.77 \times 10^{-4}$	0.59 <sup>b</sup>	1 <sup>c</sup>	91.91 <sup>b</sup>	384.78 <sup>b</sup>	0.36 <sup>f</sup>	5.50 <sup>c</sup>	$4.31 \times 10^{-9}$	0.0667	0.35
13	060512	195.75	41.21	275.73	68.31	$2.32 \times 10^{-7}$	-0.55 <sup>b</sup>	1 <sup>c</sup>	34.50 <sup>b</sup>	8.37 <sup>b</sup>	0.4428 <sup>d</sup>	0.02 <sup>g</sup>	$2.73 \times 10^{-9}$	0.0055	0.10
14	080515	3.17	32.56	100.02	61.87	$4.92 \times 10^{-5}$	-0.74 <sup>b</sup>	1 <sup>c</sup>	46.27 <sup>b</sup>	22.05 <sup>b</sup>	0.66 <sup>f</sup>	5.50 <sup>c</sup>	$2.31 \times 10^{-9}$	0.0135	0.16

<sup>a</sup> *Swift* GRB table, [http://heasarc.gsfc.nasa.gov/docs/swift/archive/grb\\_table/](http://heasarc.gsfc.nasa.gov/docs/swift/archive/grb_table/)

<sup>b</sup> Butler et al. 2007, 2010

<sup>c</sup> Assumed value.

<sup>d</sup> Observation.

<sup>e</sup> Calculated from measured fluence and assumed  $L_{\text{iso}}$ .

<sup>f</sup> Calculated from Butler et al. 2007, 2010 fluence and assumed  $L_{\text{bol}}$ .

<sup>g</sup> Adopted from the calculations of Butler et al. 2007, 2010.

<sup>h</sup> Calculated from the fluence measured by *Swift*-BAT and assumed  $L_{\text{bol}}$ .

<sup>i</sup> GRBweb, <http://grbweb.icecube.wisc.edu>

## 10.2 GRB 090907A

GRB 090709A was discovered by the Burst Alert Telescope (BAT)<sup>1</sup> onboard *Swift* on 2009 July 9 at  $T_0 = 07:38:34$  UT in  $(\alpha, \delta)_{J2000} = (19^{\text{h}}19^{\text{m}}43^{\text{s}}, +60^{\circ}43'37.5'')$  (Morris et al., 2009). *Swift* immediately slewed to the GRB and start also observing the GRB with the X-Ray Telescope (XRT)<sup>2</sup> starting from  $T_0 + 67.8$  s. Several follow-up observations were made soon afterward, among others by the automated PAIRITEL Telescope<sup>3</sup> (Morgan, Bloom & Klein, 2009) in the infrared, the Palomar Observatory 60-inch (P60) telescope (Cenko et al., 2009), and by the Subaru telescope (Aoki et al., 2009).

The redshift of the GRB was not measured. PAIRITEL near-infrared observations and the P60 in the  $r'$  and  $z'$  band reveals an extremely red afterglow which suggest a very high redshift ( $z \sim 10$ ) GRB. However, spectroscopic analysis of X-ray from the data taken by XMM-Newton<sup>4</sup> and *Swift* data suggest a moderate redshift between 3.9 to 5.1 (de Luca et al., 2010).

The  $\gamma$ -ray fluence measured by *Swift* was found to be very bright, with measured bolometric fluences in the 1–10<sup>4</sup> keV band is  $120_{-30}^{+20} \times 10^{-6}$  erg cm<sup>-2</sup> (Butler, Bloom & Poznanski, 2010). This bright flux could also be a possible hint to a small redshift of the GRB. Butler (2009) analyzed the high-energy light curve of the GRB and suggests a low to moderate redshift,  $z \lesssim 2$ .

The power spectrum of the BAT light curve, shown in Figure 10.1, indicates a quasiperiodic signal with a period of 8 seconds (Markwardt et al., 2009). This is the first time such quasiperiodicity was observed in any GRB, which prompted Markwardt et al. (2009) to suggest that GRB 090709A could be of different origin than the standard scenario for a long GRB. The 8 seconds periodicity is typical for Galactic as well as extragalactic magnetars. This quasiperiodicity is however not observed in the power spectrum of the XRT and XMM light curve (Mirabal & Gotthelf, 2009; de Luca et al., 2010). From the BAT light curve it is found that the burst occurred between  $T_0 - 66.665$  s and  $T_0 + 509.035$  s, with  $T_{90} = 300 \pm 105$  s (Butler, Bloom & Poznanski, 2010).

At the ANTARES site which is located at geographical coordinates  $(\phi, \lambda) = (42^{\circ}47'56.1'' \text{ N}, 6^{\circ}9'56.5'' \text{ E})$ , the local coordinates of the GRB at  $T_0$  is  $(Az, Alt) = (331.62^{\circ}, 25.09^{\circ})$ . The GRB is lo-

<sup>1</sup> [http://heasarc.gsfc.nasa.gov/docs/swift/about\\_swift/bat\\_desc.html](http://heasarc.gsfc.nasa.gov/docs/swift/about_swift/bat_desc.html)

<sup>2</sup> <http://www.swift.psu.edu/xrt/>

<sup>3</sup> Peters Automated Infrared Imaging Telescope, <http://www.pairitel.org/>

<sup>4</sup> X-ray Multi-Mirror Mission, <http://xmm.esac.esa.int/>

The azimuth angle is measured from the celestial North towards the East.

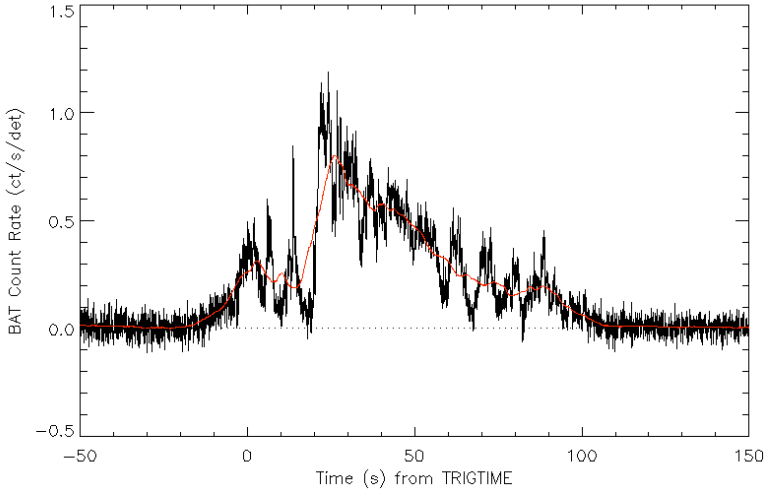


Figure 10.1: The BAT light curve of GRB 090709A, measured in the 15–350 keV band, with a smoothing curve in red performed by Markwardt et al. (2009).

cated rather close to the local horizon, which could result in a reduction of the number of expected muons due to the lengthening of the path traversed through the sea.

### 10.3 GRB 070220

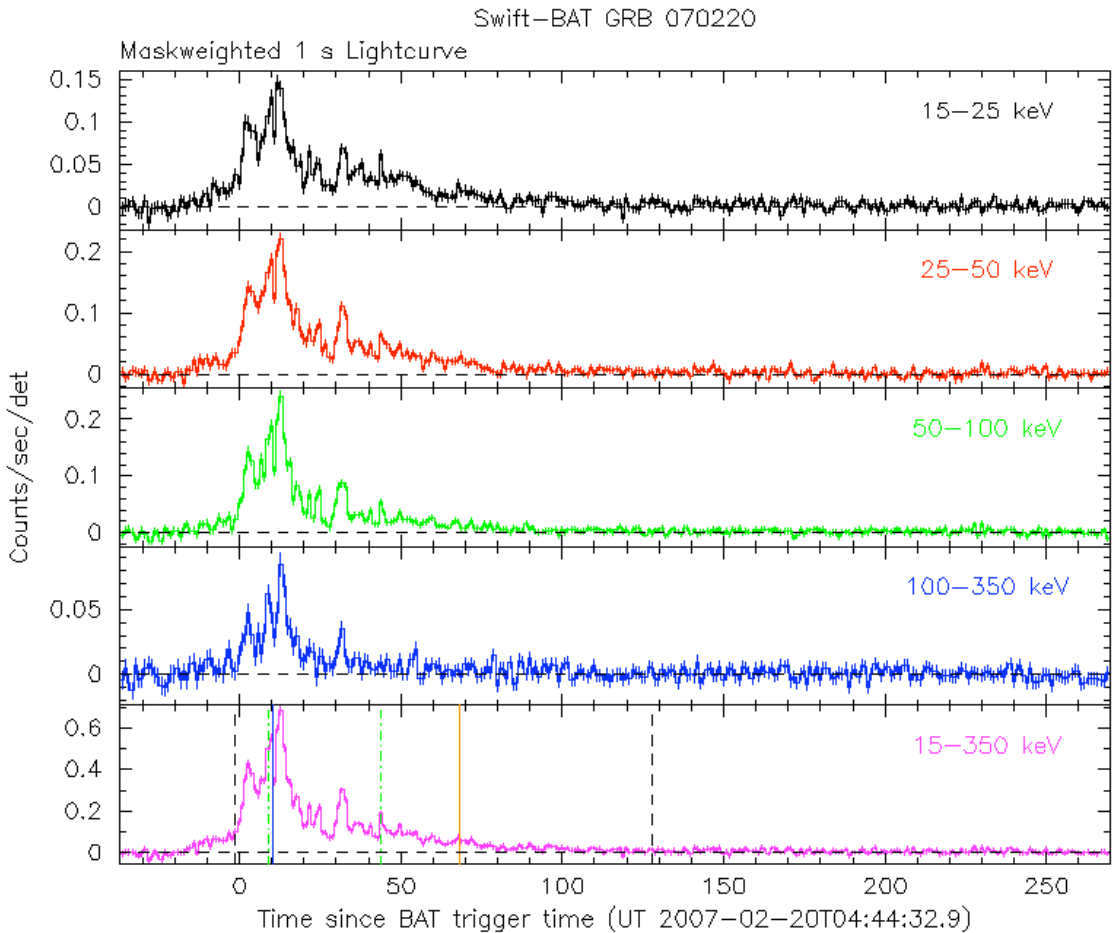
THIS GRB triggered BAT on 2007 February 20 at  $T_0 = 04:44:33$  UT. *Swift* immediately slewed towards the GRB and observed it with the XRT and the UVOT<sup>5</sup> starting respectively from  $T_0 + 79$  s and  $T_0 + 88$  s (Stamatikos et al., 2007a). The 90% confidence level of the GRB’s location is  $(\alpha, \delta)_{J2000} = (2^{\text{h}}19^{\text{m}}6.83^{\text{s}}, +68^{\circ}48'16.1'')$ , based on XRT observation of the afterglow (Beardmore et al., 2007).

The light curve of GRB 070220 (Figure 10.2) shows a multiple peaked structure with  $T_{90} = 129 \pm 6$  s (Parsons et al., 2007). The  $\gamma$ -ray bolometric fluence is measured to be  $E_{\text{bol}}^{\text{iso}} = 40_{10}^{30} \times 10^{-6}$  erg cm<sup>-2</sup> (Butler et al., 2007).

Follow-up observations of GRB 070220 were performed in the optical wavelength by the KANATA 1.5 m telescope in Hiroshima (Arai, Uemura & Uehara, 2007) and by the robotic Faulkes North Telescope (Melandri et al., 2007), in the near-infrared by the ART-3 Telescope (Torii, Tanaka & Tsunemi, 2007), and in the radio band

<sup>5</sup>Ultraviolet and Optical Telescope, <http://www.swift.psu.edu/uvot/>





at 8.46 GHz by the Very Large Array (VLA) (Chandra & Frail, 2007). All observations did not find any counterpart to the GRB in the bands observed.

The GRB is also observed by the *Konus* detector (Aptekar et al., 1995) onboard the *Wind* satellite<sup>6</sup>. *Konus* is sensitive to  $\gamma$ -rays in 20 keV–2 MeV, which allows for the high-energy spectral index  $\beta$  to be measured. By fitting the time-integrated energy spectrum of the GRB,  $\beta = -2.02^{+0.27}_{-0.44}$  is obtained (Golenetskii et al., 2007). This is very close to the most common value of  $\beta$ . Using this *Konus* spectral parameters, Pelangeon & Atteia (2007) obtained a

Figure 10.2: The BAT light curve of GRB 070220, measured in 4 different energy band and the total energy band in the 15–350 keV energy range (bottom plot). The green and black dotted lines bracket the  $T_{50}$  and  $T_{90}$  time intervals, respectively, while the blue and orange solid lines bracket the start and end of the slew, respectively. Figure reproduced from Stamatikos et al. (2007b).

<sup>6</sup> <http://wind.nasa.gov/>

pseudo-redshift of  $\hat{z} \sim 2.15 \pm 0.8$ . A pseudo-redshift is a redshift indicator proposed by Atteia (2003). The method works by using the observed spectral parameters and the burst duration as an input, and then the redshift is calculated by using the so-called Amati relation (Amati et al., 2002) that found a linear relation between the logarithm of  $\epsilon_{\text{pk}}$  and the logarithm of  $E_{\text{iso}}^{\text{bol}}$ .

The local coordinates of GRB 070220 at the ANTARES site at  $T_0$  is  $(Az, Alt) = (4.68^\circ, 22.05^\circ)$ . The GRB is at an altitude close to the local horizon, and given also the predicted redshift of the GRB, most probably there are not many TeV  $\gamma$ -rays that could reach Earth in the first place.

We will simulate the interaction of TeV  $\gamma$ -rays that reach Earth with particles in the atmosphere of the Earth. This will be discussed in the next Chapter.

# 11 *Analysis of ANTARES data coinciding with two GRB events*

IN ORDER to obtain an optimized quality cut for the selection of events, it is necessary to estimate first the number of expected signal. While analytical calculations such as performed in Chapters 2–3 can give this number, there are several limitations to it if we also want to include detector effects. The best way to estimate the number of signals that could be expected from a GRB with the given parameters is by performing a full Monte Carlo simulation from the top of the atmosphere to the bottom of the sea. A full treatment of Monte Carlo simulations allow us to include the effects due to muon multiplicity, the lateral distribution of the muons at sea level, and the stochastic effects of muon energy loss in water, and furthermore the effects of photon detection by the PMTs.

The discussion in this Chapter will be started with a description of the simulation chain employed for both target GRBs.

## 11.1 *Muon production*

SIMULATIONS of muon production from in the atmosphere are performed with CORSIKA (Heck et al., 1998) version 6990. Hadronic interactions in the atmosphere are simulated with the QGSJET model while the electromagnetic interactions are simulated with the EGS4 package. The photon sources are fixed to the sky, with an azimuth and zenith distance conformed to the actual direction of the GRB.

The horizontal axes of CORSIKA are aligned with the Earth's north magnetic field, in order to include its effects to the tracks of the simulated particles. As noted by Guillard (2010), the effects of the Earth's magnetic field are negligible at TeV energy which is the interest of this study. Since there is negligible deviation due to magnetic field—which we shall also see later at reconstruction level—it is then safe to just consider that CORSIKA axes are aligned with the celestial North pole.

The results of the simulation are shown in Table 11.1 and Figure

No.	Name	$\alpha$	$\delta$	Azimuth	Altitude	$N_\gamma$	$N_\mu$	$N_{s,HE\mu}$
1	090709A	289.94	60.73	331.62	25.09	$\sim 10^8$	11 706 524	24765
2	070220	34.80	68.80	4.68	22.05	$\sim 5 \times 10^7$	4 179 214	10638

11.1. The spectrum is calculated using an analytical formulation involving the attenuation of TeV photons by the cosmic infrared background (CIB). Because attenuation is involved, the shape of the photon is then no longer in the form of a simple power sample, i.e.  $dN_\gamma/d\epsilon_\gamma \propto \epsilon_\gamma^{-\beta}$ , where  $\beta$  is the spectral index of the photon spectrum's high-energy component. Instead, the shape of the photon spectrum will be in the form of

$$\frac{dN_\gamma}{d\epsilon_\gamma} \propto \epsilon_\gamma^{-\beta} e^{-\tau_{\gamma\gamma}(\epsilon_\gamma, z)}, \quad (11.1)$$

where  $\tau_{\gamma\gamma}(\epsilon_\gamma, z)$  is the optical depth of the universe along the line of sight to the GRB, as a function of the photon energy in the observer frame  $\epsilon_\gamma$  and the redshift  $z$  of the GRB. The optical depth  $\tau_{\gamma\gamma}$  increases with increasing photon energy and redshift. Attenuation then get more severe. This is discussed in more detail in Section 2.3.

Because CORSIKA can only generate photons according to simple power law, a certain trick has to be used so that it will generate photons from an attenuated spectrum. The trick invented for this purpose is to chop the attenuated spectrum into small bins and calculate the number of photons that should be generated in the bin. This is done first by normalizing the spectrum to the total number of photons  $N_\gamma$  we want to generate:

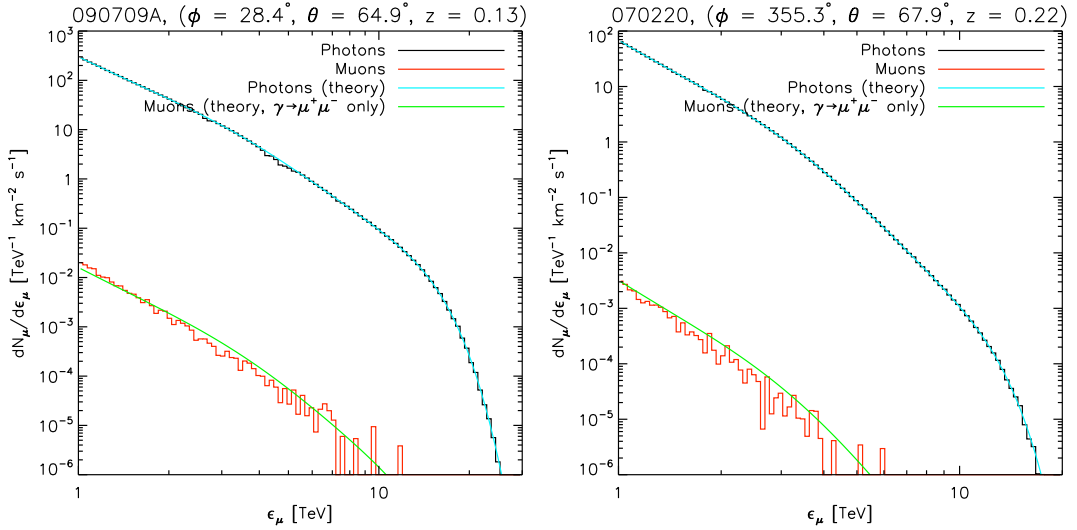
$$N_\gamma = f_\gamma \int_{\epsilon_{\gamma,\min}}^{\epsilon_{\gamma,\max}} d\epsilon_\gamma \epsilon_\gamma^{-\beta} e^{-\tau_{\gamma\gamma}(\epsilon_\gamma, z)}. \quad (11.2)$$

From this equation it is straightforward to calculate the normalization factor  $f_\gamma$ . The minimum energy  $\epsilon_{\gamma,\min}$  is set to 1 TeV and the maximum energy  $\epsilon_{\gamma,\max}$  is arbitrarily set to 300 TeV. We could then chop the spectrum into a number of  $n$  bins of equal bin width:

$$\Delta \log \epsilon_\gamma = \frac{1}{n} \log \left( \frac{\epsilon_{\gamma,\max}}{\epsilon_{\gamma,\min}} \right), \quad (11.3)$$

and calculate the number of photons that should be generated

Table 11.1: Summary of the CORSIKA simulation. All positional coordinates are in degrees. Azimuth is measured from the celestial North and is positive toward the East. Altitude is measured from the local horizon, positive towards the zenith and negative towards the nadir.  $N_\gamma$  is the total number of generated photons and  $N_\mu$  is the total number of muons generated in the atmosphere.  $N_{s,HE\mu}$  is the number of muon showers containing at least one muon with energy higher than 500 GeV. The photon and muon spectra are shown in Figure 11.1.



within the  $i$ -th bin:

$$N_{\gamma,i} = f_{\gamma} \epsilon_{\gamma,i} \ln(10) \Delta \log \epsilon_{\gamma} \frac{dN_{\gamma}}{d\epsilon_{\gamma}} e^{-\tau_{\gamma\gamma}(\epsilon_{\gamma,i}z)}. \quad (11.4)$$

The number of muons inside each bins as well as the minimum and maximum energy is then used as input to CORSIKA along with other required input. The resulting spectrum could then mimic the attenuated spectrum, as we can see in Figure 11.1.

Using this method, the calculation of the weights of the simulated events reduces to a single constant value and is invariable to energy.

## 11.2 Muon duplication

THE COLUMN with header  $N_{s,HE\mu}$  in Table 11.1 shows the number of muon showers that contain at least one muon with energy higher than 500 GeV. The content of the muon bundle generated in one photon shower can go up to hundreds of muons, although within this bundle of muons normally there would only be one or two very high energy muons. The number of showers containing high-energy muons are too low if we also think that they have to be propagated to the detector and then reconstructed, but increasing the number of photons to be simulated will increase the

Figure 11.1: The shape of the photon spectrum used to generate photons, and the resulting muon spectrum. The solid line on top of the photon histogram is the theoretical photon spectrum, while the solid line on top of the muon histogram is the theoretical calculation of the muon spectrum.

amount of computer time. It is faster to duplicate these showers and treat them as if they are different events.

It is also necessary to not only duplicate the muons but also to spread them into a more extended beam that covers all part of the detector. The generating area of the photons within CORSIKA is concentrated only to a beam with radius  $\sim 20$  m, which is too small compared to the size of the detector which radius is ten times the corsika beam radius. If we only propagate photons from a pencil beam, we would only simulate a small part of the detector which may introduce a bias in the result of the simulation.

The definition of the photon duplicating area at the surface must not be too large that muons at its edge would never be detected and thus waste computer time, but also must be large enough that it efficiently covers all part of the detector. One scheme that meets these requirements is shown in Figure 11.2. This scheme requires the dimension of the can that covers the instrumented volume, the vertical location of the detector's centre of gravity, the depth of the sea, and the direction of the GRB in local coordinates azimuth  $\phi$  and zenith distance  $\theta$ .

The basic idea is as follows: First we draw a circumscribing sphere around the can. It is straightforward to calculate the radius  $r_s$  of this sphere (Figure 11.3):

$$r_s = \left(\frac{1}{4}h_c^2 + r_s^2\right)^{1/2}, \quad (11.5)$$

where  $h_c$  is the height of the can which can be obtained if we know the vertical coordinates of the top and bottom and surface of the can:

$$h_c = z_{c,\max} - z_{c,\min}. \quad (11.6)$$

We can then draw a tube with radius  $r_s$  that points to the direction  $(\phi, \theta)$  of the GRB. This tube represents the beam of photon-induced muons. The muons inside this beam will hit all parts of the detector because the beam exactly covers the can. The cylindrical section of the tube that parallels the plane of the sea surface is then simply the muon duplication area, and is in the shape of an ellipse with semimajor axis

$$a = \frac{r_s}{\cos \theta'}, \quad (11.7)$$

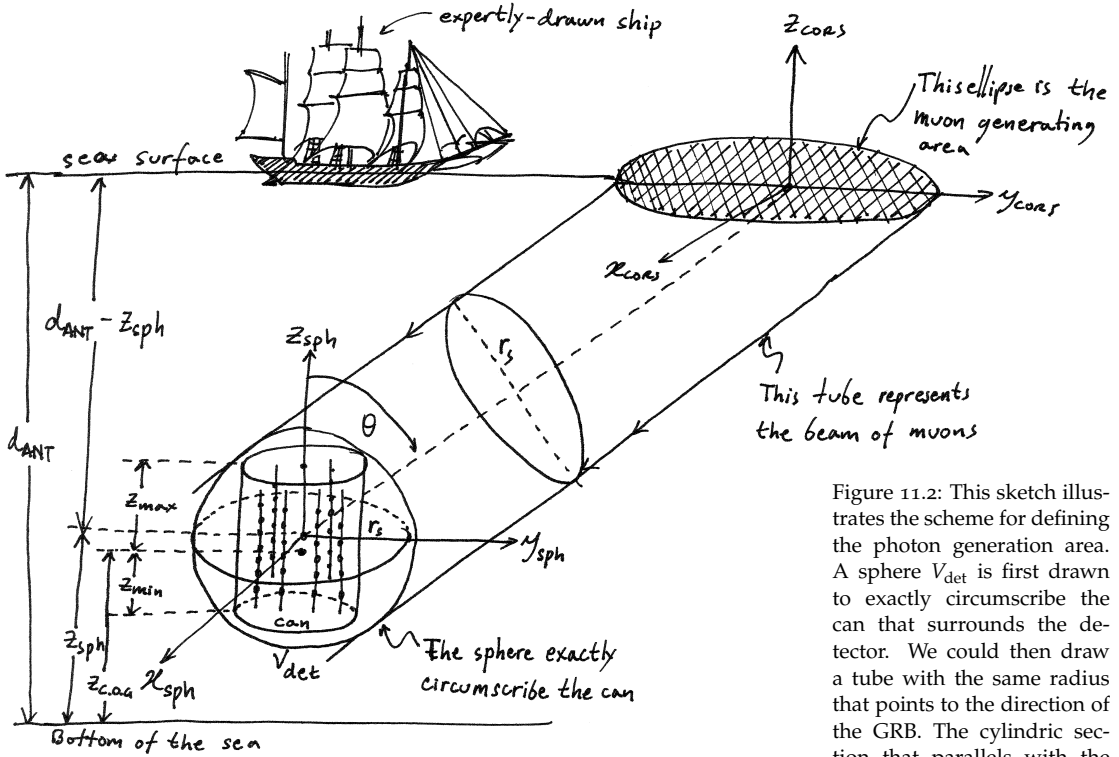


Figure 11.2: This sketch illustrates the scheme for defining the photon generation area. A sphere  $V_{det}$  is first drawn to exactly circumscribe the can that surrounds the detector. We could then draw a tube with the same radius that points to the direction of the GRB. The cylindrical section that parallels with the plane of the sea surface is then the photon generation area, which will be an ellipse. Illustration by the author.

and semiminor axis is  $b = r_s$ . Because the tube points to the direction of the GRB, the axes of the ellipse is inclined with angle  $\phi$  relative to the axes of the coordinate system. The area of the ellipse is  $A_{ellipse} = \pi ab$ .

The coordinates of the center of the ellipse relative to the center of gravity of the detector can be obtained if we know the depth of the sea  $d_{ANT}$  and the vertical coordinates of the detector's center of gravity  $z_{C.O.G.}$ . The coordinates for the center of gravity of the detector can be obtained from the km3 program. The vertical distance  $d_s$  of the circumscribing sphere to the surface is then

$$z_s = z_{C.O.G} + z_{c,max} - \frac{1}{2}h_c, \tag{11.8}$$

$$d_s = d_{ANT} - z_s. \tag{11.9}$$

Here  $z_s$  the vertical coordinates of the circumscribing sphere. The

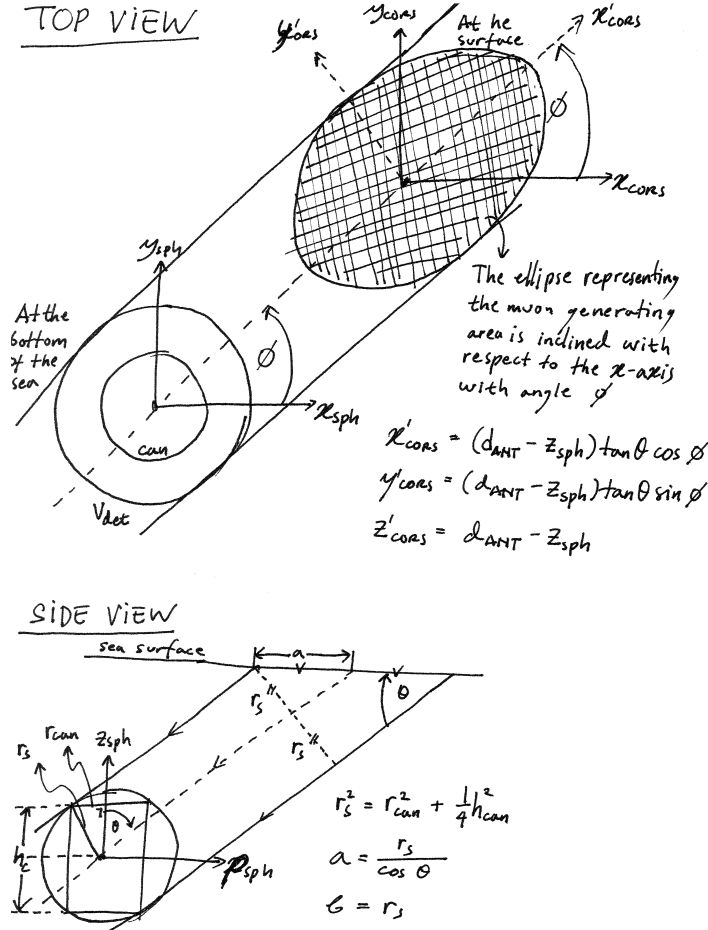


Figure 11.3: The top-view and side-view of the muon generating area and its orientation with respect to the can. Because the tube representing the beam of TeV photon-induced muons are directed toward the source, the ellipse representing the muon generating area is inclined with angle  $\phi = 360^\circ - \text{Azimuth}$  with respect to the  $x$ -axis. Calculating the size of the ellipse with respect to the can is straightforward if we consider a sphere exactly circumscribing the can. Illustration by the author.

coordinates of the center of the ellipse is then

$$\mathbf{r}_{\text{ellipse}} = \begin{bmatrix} x_{\text{ellipse}} \\ y_{\text{ellipse}} \\ z_{\text{ellipse}} \end{bmatrix} = \begin{bmatrix} d_s \tan \theta \cos \phi \\ d_s \tan \theta \sin \phi \\ d_s \end{bmatrix} \quad (11.10)$$

We could now generate random points within this ellipse that would be the new coordinates of the muons relative to the center of gravity of the detector. First we generate two random numbers  $\{R_1, R_2\} \in [0, 1]$ . Using these two random numbers we could then calculate the coordinates at the sea surface relative to the center of



No.	Name	$\phi$	$\theta$	$N_{s,HE\mu}$	Duplication	Run No.	$N_{rec}$	$\mu_s$
1	090709A	28.38	64.91	24 765	50 000	41812	27 221	$2.7 \times 10^{-4}$
2	070220	355.32	67.95	10 638	1 200 000	26128	912	$6.5 \times 10^{-8}$

the ellipse  $\mathbf{r}_{\text{ellipse}}$ :

$$\mathbf{r}'_{\text{surf}} = \begin{bmatrix} x'_{\text{surf}} \\ y'_{\text{surf}} \end{bmatrix} = \begin{bmatrix} -a + 2aR_1 \\ -b + 2bR_2 \end{bmatrix} \quad (11.11)$$

This generated coordinates will be accepted if the criterion

$$\left(\frac{x'_{\text{surf}}}{a}\right)^2 + \left(\frac{y'_{\text{surf}}}{b}\right)^2 < 1 \quad (11.12)$$

is satisfied. Next we rotate the coordinates by an angle  $\phi$ :

$$\mathbf{r}_{\text{surf}} = \begin{bmatrix} x_{\text{surf}} \\ y_{\text{surf}} \end{bmatrix} = \begin{bmatrix} \cos \phi & -\sin \phi \\ \sin \phi & \cos \phi \end{bmatrix} \begin{bmatrix} x'_{\text{surf}} \\ y'_{\text{surf}} \end{bmatrix} \quad (11.13)$$

The new coordinates for the muon will then be

$$\mathbf{r}_{\mu} = \mathbf{r}_{\text{ellipse}} + \mathbf{r}_{\text{surf}} + \mathbf{r}_{\mu,0}, \quad (11.14)$$

where  $\mathbf{r}_{\mu,0}$  are the original 2D coordinates of the muon at the sea surface, obtained from CORSIKA simulation. It is worthwhile to note here that  $\mathbf{r}_{\mu}$  are 3D coordinates with the same vertical components, i.e.  $z_{\text{ellipse}} = d_s$ .

This algorithm is repeated for all muons. The muons are also duplicated to increase the statistics at reconstruction level. The number of duplications are shown in Table 11.2.

The final position of the muons is shown in Figure 11.4. We can see that our calculations are correct since the size and orientation of the ellipse are correct and that the muons do point toward the detector.

### 11.3 Further simulation chains

MUON propagation from the sea surface towards the can is performed using the MUSIC code (Antonioli et al., 1997) that runs within the km3 software. Furthermore, km3 is also used to generate the Cherenkov photons and hits detected by the PMTs. The response of ANTARES to the photons is then simulated with TriggerEfficiency, and the tracks are reconstructed with the aafit v0r9 algorithm.

Table 11.2: Summary of the detector simulation. All positional coordinates are in degrees.  $\phi$  is measured from the celestial North and is positive toward the West, thus  $\phi = 360^\circ - \text{Azimuth}$ .  $\theta$  is measured from the zenith and is positive toward the nadir, and  $\theta = 90^\circ - \text{Altitude}$ .  $N_{s,HE\mu}$  is the number of photons that generate muon showers containing at least one muon with energy higher than 500 GeV. Duplication is the number of times  $N_{s,HE\mu}$  are duplicated. Run No. is the raw data file used for background simulation,  $N_{rec}$  is the final number of events at reconstruction level.  $\mu_s$  is the number of weighted signal events.

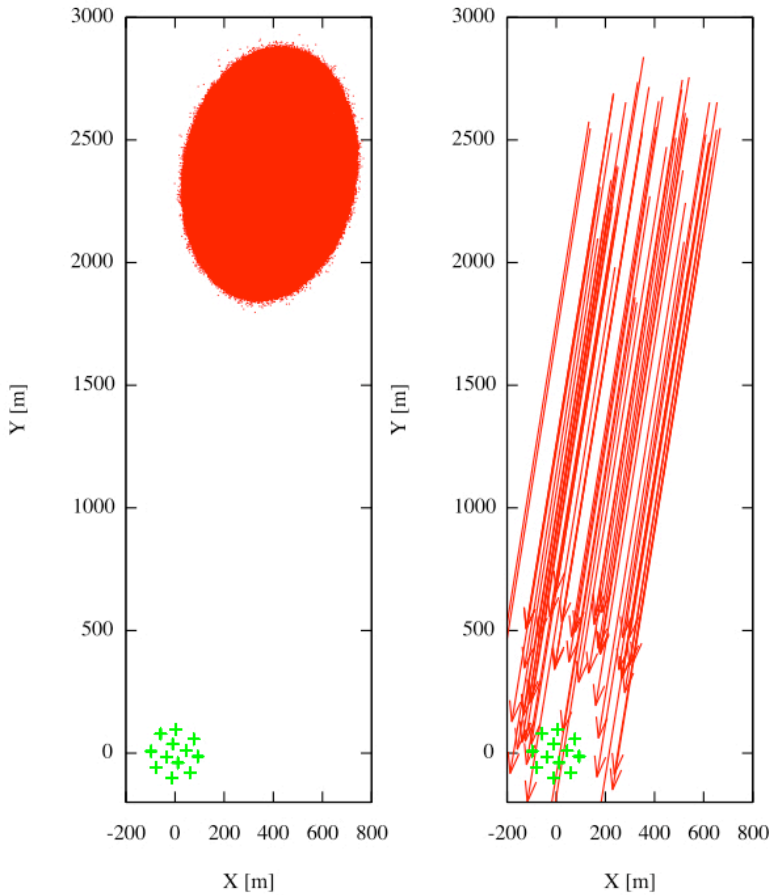


Figure 11.4: The initial positions (left) and momentum vectors (right) of the muons at the surface, relative to the center of gravity of the detector. The red dots in the left plot shows the final coordinates of the initial positions of the muons, after coordinate rotation has been performed. Green crosses show the positions of the detector strings. As we can see, the muons are distributed inside an ellipse with the prescribed size, as well as the inclination relative to the X-axis. In the right plot, the momentum vectors of several muons are shown, to make sure that they do point toward the detector.

To emulate environmental and detector conditions, the random background hits in `TriggerEfficiency` are generated by using input parameters obtained from the raw data file corresponding to the time when the GRBs took place. The quality of the data taken during the corresponding the run is shown Table 11.3.

#### 11.4 Results of the reconstruction

THE FINAL number of events at reconstruction level is shown in Table 11.2. This is the total number which already includes duplication. The expected number of signal  $\mu_s$  is shown in the last

Run No.	41812	26128
Baseline rate [kHz]	67.76	
Burst fraction	0.43	
Expected muon [minute <sup>-1</sup> ]	83.18	
Number of active lines	9	
Theoretical number of OMs	645	375
Number of active OMs	486	
Mean active OMs	509.91	
Mean rate [kHz]	96.45	118.91
Median trigger hits	12.19	
Number of muons [minute <sup>-1</sup> ]	84.90	
Data quality	1	
Run duration [s]	15704	

Table 11.3: Data quality of the runs containing the selected GRBs. These values are taken from the ANTARES database.

column, where

$$\mu_s = w_s N_{rec}, \quad (11.15)$$

here  $w_s$  is the weight of each individual signal event. Because of the way we generate the photons, the shape of the generated photon spectrum reproduces the expected photon spectrum. Consequently, the weight of each individual signal event  $w_s$  is invariant to the energy  $\epsilon_\gamma$  of the photons, and the value is the same for all signal events:

$$w_s = \frac{\left. \frac{dN_\gamma}{d\epsilon_\gamma} \right|_{\epsilon_\gamma}^{\text{th}} T_{90} A_{\text{ellipse}}}{\left. \frac{dN_\gamma}{d\epsilon_\gamma} \right|_{\epsilon_\gamma}^{\text{C}} N_{\text{duplication}}}. \quad (11.16)$$

Here  $\left. \frac{dN_\gamma}{d\epsilon_\gamma} \right|_{\epsilon_\gamma}^{\text{th}}$  is the theoretical photon spectrum at a certain energy  $\epsilon_\gamma$ ,  $\left. \frac{dN_\gamma}{d\epsilon_\gamma} \right|_{\epsilon_\gamma}^{\text{C}}$  is the CORSIKA photon spectrum at the same photon energy,  $T_{90}$  is the burst duration,  $A_{\text{ellipse}}$  is the size of the ellipse generating area, and  $N_{\text{duplication}}$  is the number of muon duplication performed.

#### 11.4.1 Detection efficiency

THE PLOTS that describe the detection efficiency  $\eta_\mu$  for each GRB is shown in Figure 11.5. For each GRB, the muon spectrum at

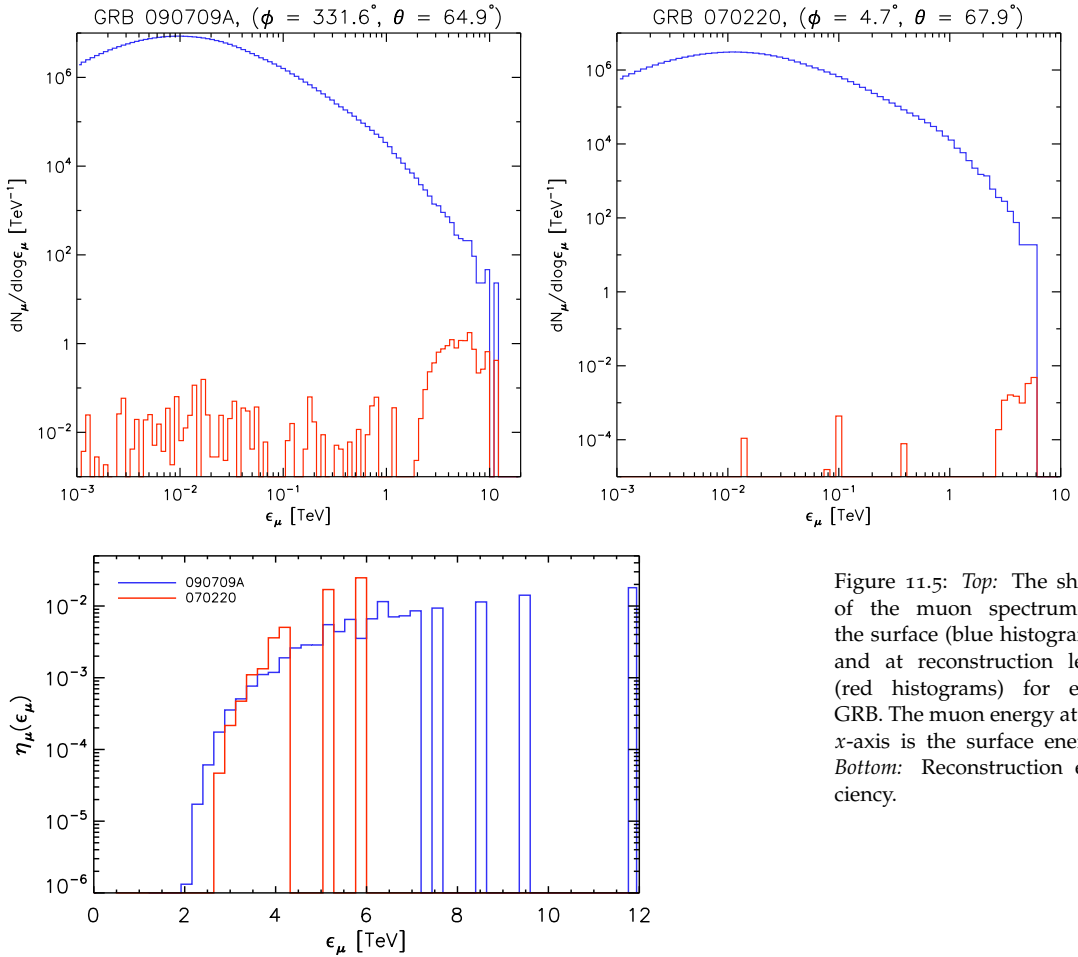


Figure 11.5: *Top*: The shape of the muon spectrum at the surface (blue histograms) and at reconstruction level (red histograms) for each GRB. The muon energy at the  $x$ -axis is the surface energy. *Bottom*: Reconstruction efficiency.

the sea surface is shown as the blue histogram, while the muon spectrum at reconstruction level is shown as the red histogram. The muon energy used at the  $x$ -axis is the muon energy at the sea surface. We can see that low-energy muons could penetrate the depth of the sea and be reconstructed, albeit with low efficiency. High-energy muons with  $\epsilon_\mu \geq 1$  TeV still comprise the majority of the reconstructed tracks. At the bottom plot of Figure 11.5, the detection efficiency  $\eta_\mu$  as a function of the muon energy is plotted for each GRB.

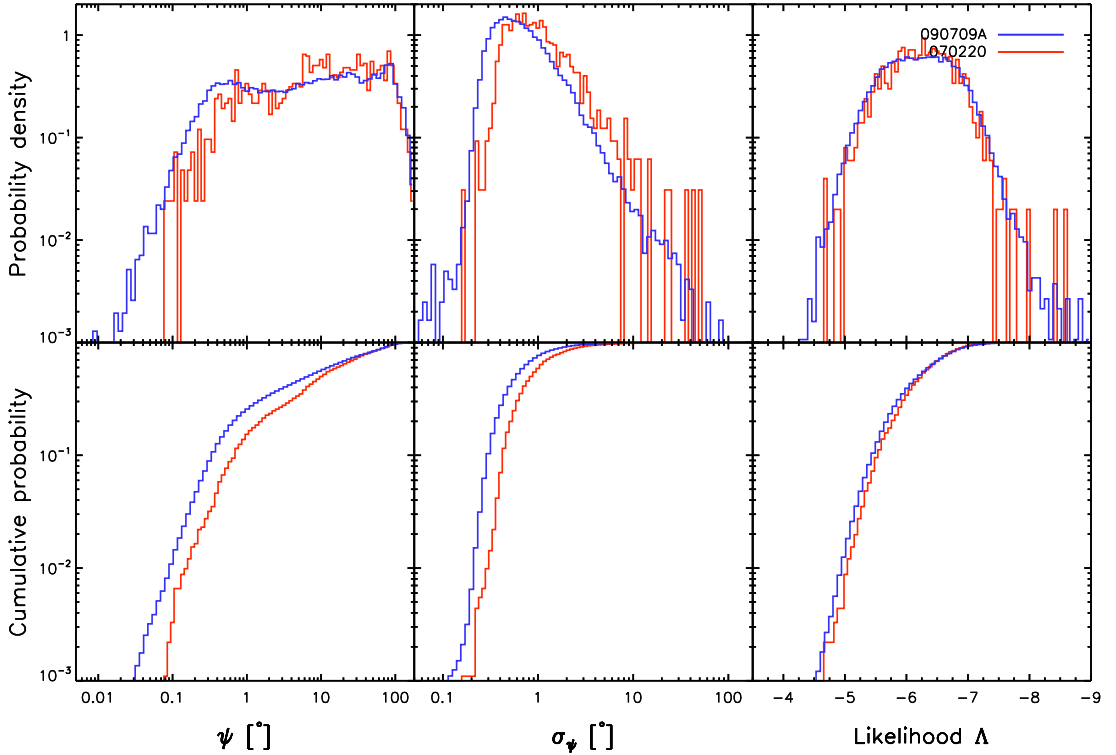
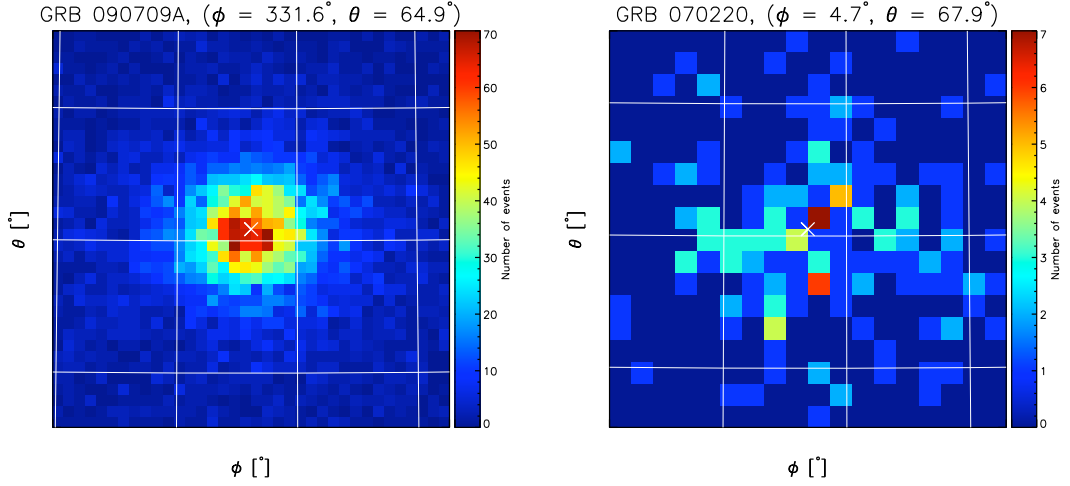


Figure 11.6: The probability distribution function (PDF) and cumulative distribution function (CDF) of the true angular resolution  $\psi$  (left), the angular uncertainty  $\sigma_\psi$  (center), and the fit likelihood  $\Lambda$  (right). Different color indicates different GRB, as indicated in the legend.

#### 11.4.2 Track reconstruction quality

THE DISTRIBUTION of the relevant parameters that define the quality of the reconstruction are shown in Figure 11.6. This Figure shows the distribution of the true angular resolution  $\psi$ , angular error estimate  $\sigma_\psi$ , and the goodness-of-fit  $\Lambda$  for both GRBs.

We can see that the distribution of  $\sigma_\psi$  and  $\Lambda$  is consistent with previous simulations shown in Chapter 7. The distribution of  $\psi$  however is different with what we would expect from a source at this zenith distance. This could arise from the fact that we are simulating the detector with realistic conditions, and that the detector conditions at the time the GRB took place was below the idealized optimum conditions. Table 11.3 shows the quality of the data taken in the run when the selected GRB events happened, as well as the detector condition at that moment. We can see that



when GRB 090709A (run number 41812) went off, only 9 lines out of the total 12 were active at that time. GRB 070220 (run number 26128) happened when the ANTARES detector consisted of only 5 lines. The quality of the data taken were category 1 for run number 41812. Quality 1 indicate that the data taken surpass the basic quality criteria and are suitable for physics analysis.

The point spread function of the reconstructed events for each GRB is shown in Figure 11.7. Here the weight of events are set to  $w_s = 1$  for illustration purpose. We can see that most of the interesting signal events are well-reconstructed, within a radius of the PSF is  $\sim 1^\circ$ .

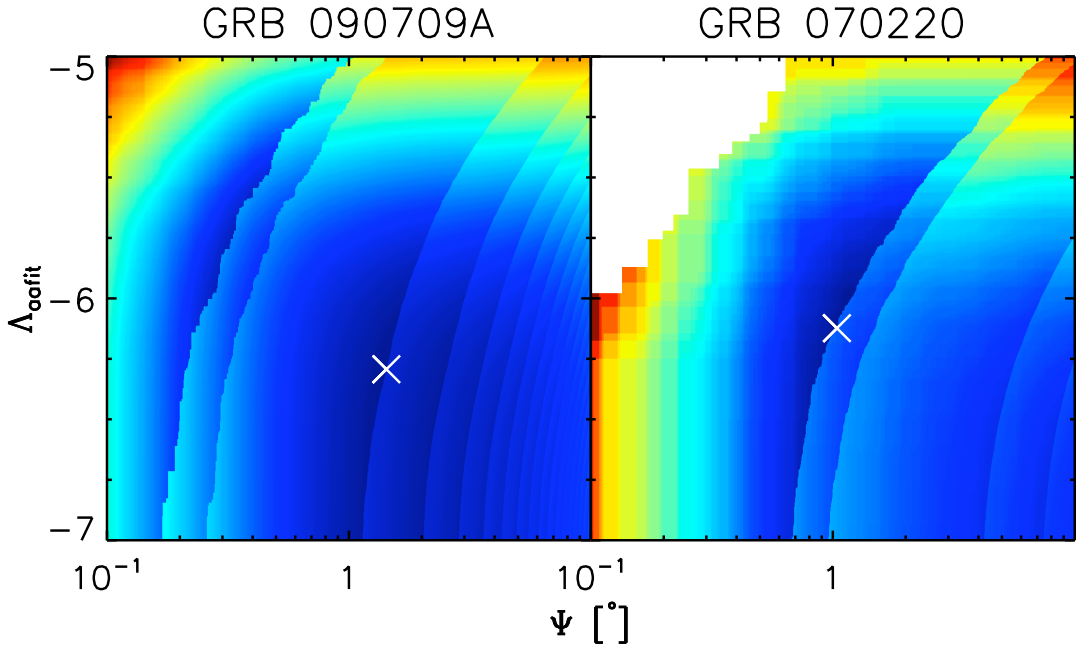
### 11.5 Optimization

THE OPTIMIZATION results for the model discovery potential (MDP) approach are shown in Figures 11.8–11.9 and Table 11.4, while the

GRB	MDP ( $3\sigma$ )		MDP ( $5\sigma$ )		MRF	
	$\Psi$ [ $^\circ$ ]	$\Lambda_{\text{aafit}}$	$\Psi$ [ $^\circ$ ]	$\Lambda_{\text{aafit}}$	$\Psi$ [ $^\circ$ ]	$\Lambda_{\text{aafit}}$
090709A	1.43	-6.29	1.24	-6.25	2.82	-6.55
070220	1.04	-6.12	7.29	-6.92	9.68	-7.00

Figure 11.7: The point spread function (PSF) of the muon events of the GRBs, drawn in Lambert azimuthal equal-area projection. The size of the box is  $3^\circ \times 3^\circ$  and the width between grid lines is  $1^\circ$ . The plot is centered on the supposed location of the GRB, marked by the white cross in the middle of each plot. For illustration purpose, the weight for each events is set to 1.

Table 11.4: The combination of cuts for each GRB that minimizes the MDP and MRF.



results for the model rejection factor (MRF) is shown in Figure 11.10 and Table 11.4. The optimization result is reasonable given that the expected number of signal events are very low.

### 11.5.1 Expected significance of the observation

WE COULD calculate the significance of the detection using the significance formula derived by Li & Ma (1983), which is based on the likelihood ratio method. For this calculation, an “ON” and “OFF” period must be defined: The “ON” time is the period in which we know there is a GRB event, while “OFF” is the period in which we know there is only background. For simplicity of the calculation we could define  $t_{\text{on}}$  as the  $T_{90}$  of the GRB, and  $t_{\text{off}}$  as the one hour period before the GRB in question took place. We

Figure 11.8: The model discovery potential (MDP) for a 50% probability of making a  $3\sigma$  discovery, as a function of opening radius  $\Psi$  and  $\Delta$ , for both GRBs. The cut in  $\Psi$  and  $\Delta$  that minimizes the MDP is shown as the white cross in the plot.

Table 11.5: Summary of the Li & Ma (1983) significance calculation. On-time  $t_{\text{on}}$  and off-time  $t_{\text{off}}$  are in seconds.  $n_{\text{on}}$  and  $n_{\text{off}}$  are the expected number of events during the respectively on and off period. The significance of the detection  $S$  is shown in the last column.

No.	Name	$t_{\text{on}}$	$t_{\text{off}}$	$n_{\text{on}}$	$n_{\text{off}}$	$S$
1	090709A	344.85	3600	0.07	0.76	$2.52 \times 10^{-4}$
3	070220	150.67	3600	0.32	7.60	$3.03 \times 10^{-8}$

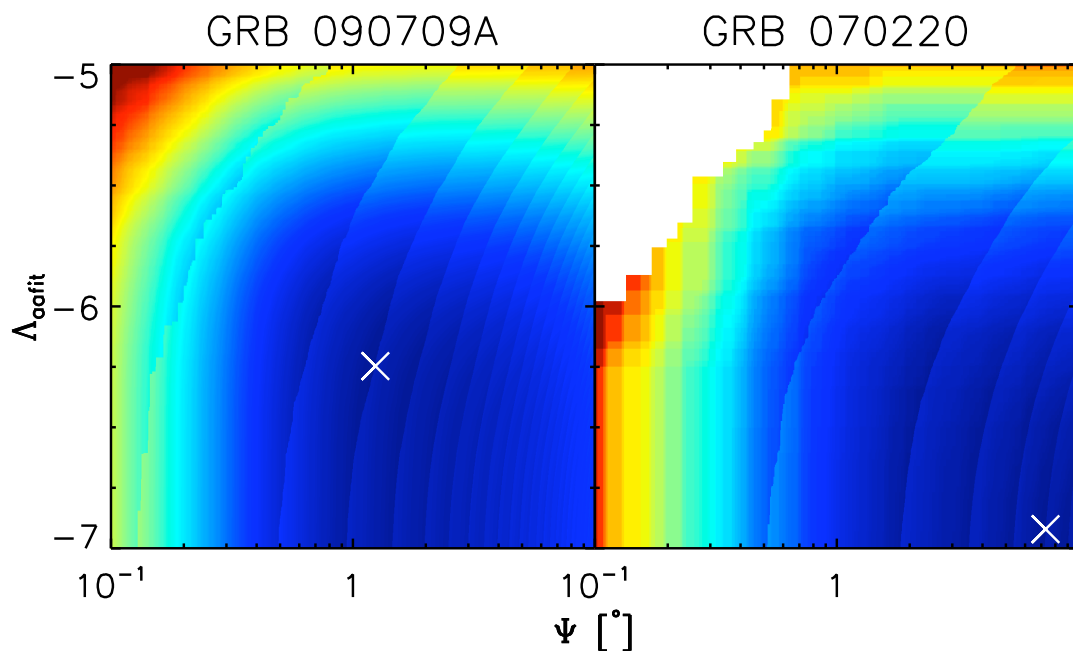


Figure 11.9: The same as in Figure 11.8, but for a 50% probability of making a  $5\sigma$  discovery.

measure the number of events during the “ON” period,  $n_{\text{on}}$ , as well as the number of events during the “OFF” period,  $n_{\text{off}}$ . From these four quantities, we can measure the significance  $S$  of the detection.

The results of these calculations are shown in Table 11.5. The expected significances for all GRBs are very low, despite the very low background rate. This is because the expected number of signal events itself is very low. Unless there is an enhancement of signal events at the source itself, this is the significance we could expect after unblinding of the data.

As the number of background events are very low, the observation time during the “off” period is taken to be 60 minutes.

### 11.5.2 Expected sensitivity

THE EXPECTED sensitivity plot for each individual GRBs is shown in Figure 11.11. This expected sensitivity is calculated by multiplying the theoretical photon spectrum by the value of the mini-



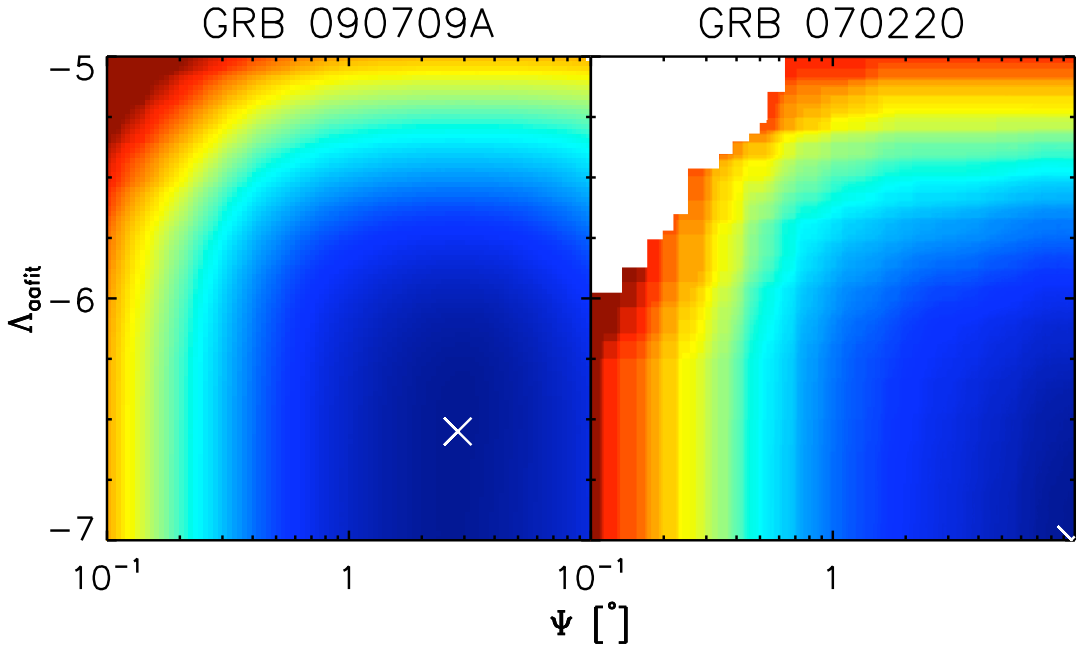


Figure 11.10: The plots for the 90% confidence limit model rejection factor (MRF), as a function of opening radius  $\Psi$  and  $\Delta$ , for the each proposed GRBs. The set of cuts that minimized the MDP and the MRF is shown as the white X in the each plot.

mum MRF:

$$\phi_{90}(\epsilon_\gamma) = \frac{\bar{\mu}_{90}(\mu_b)}{\mu_s} \phi(\epsilon_\gamma), \quad (11.17)$$

where  $\mu_s$  and  $\mu_b$  are respectively the expected values of the signal and background that pass the quality cuts that minimize the MRF, and  $\bar{\mu}_{90}(\mu_b)$  is the averaged upper limit at 90% confidence level. After the unblinding, this sensitivity will be recalculated by inserting the measured background and signal.

As we can see, ANTARES sensitivity is low for a GRB with a small flux. Unless there is an enhancement of TeV photon production at the source itself, we would not expect to see any event. However, since we are observing the GRB event from start to finish, this would be a very compelling limit in the TeV regime.

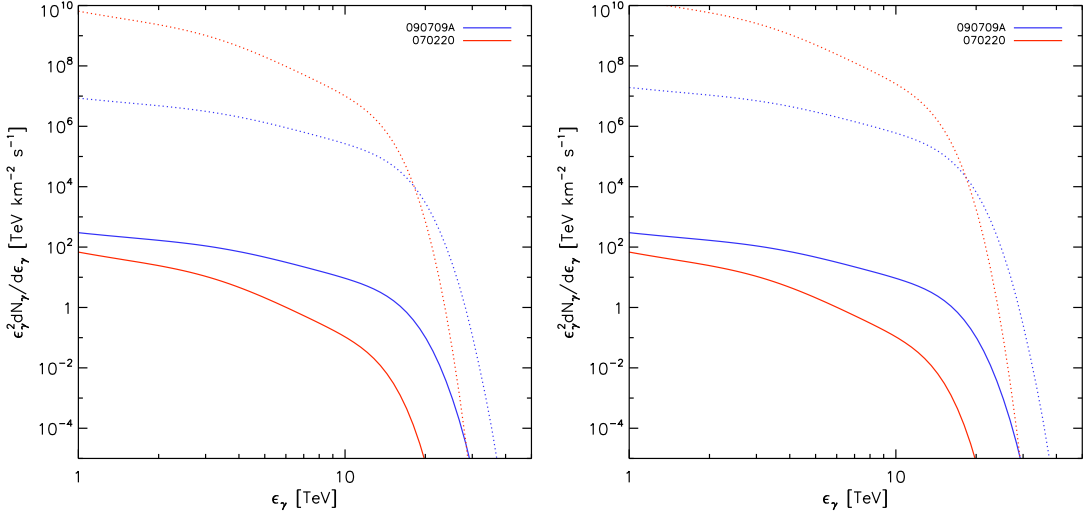


Figure 11.11: The expected sensitivity of ANTARES to each GRBs, shown here in dotted lines. The theoretical photon spectrum is shown in solid lines. The left plot shows the sensitivity if the MRF result approach is used, while the right plot shows the sensitivity if the MDP  $5\sigma$  approach is used. If the MDP values are used, the detector is slightly less sensitive than if the MRF results are used.

## 11.6 Summary

THE INDIVIDUAL optimization of the top two GRBs proposed to be unblinded has been performed. Using CORSIKA to simulate muon production in the atmosphere, the spatial distribution of high-energy muons at the surface has been obtained and has been put into good use.

A set of cuts that minimized the MDP and MRF has been obtained, and the expected detection significance and limit of the observation has been calculated. In principle all the necessary analysis for unblinding has been performed.

Due to the very low expectation to observe any signal event from GRB 070220 because of the small instrumented volume of the detector when the GRB happened, it was proposed that this GRB is dropped from the observation proposal. We will observe then only one GRB instead of two.

In summary, further analysis after unblinding will be:

1. We will observe for 60 minutes the area within the optimum radius  $\Psi$  (given the zenith distance  $\theta$  of the GRB) in the direction of the GRB before the time when the GRB is occurring. This way we could estimate the background rate  $\mu_b$  at that time.

2. The upper limit of signal event rate  $\mu_s$  will be determined by calculating the upper limit of the Feldman-Cousins confidence interval, given the estimated number of background  $\mu_b$ , the number of observed events  $n_{\text{obs}}$  and the required confidence limit  $\alpha = 90\%$ .
3. The compatibility of the observed events with the background-only hypothesis will be calculated by the likelihood ratio method.

The simulation suggests that no event will be observed during the ON period and at most a couple background events during the OFF period. This should also be the case when we unblind the data and look at it, unless there is an enhancement of TeV  $\gamma$ -rays production at the source itself. Such an enhancement could occur when a more efficient channel of TeV  $\gamma$ -ray production takes place in the GRB, for example the decay of secondary pions in the GRB fireball into neutrinos and high-energy  $\gamma$ -rays (Waxman & Bahcall, 1997; Fragile et al., 2004).

Should such enhancement do occur, the number of signal events would increase dramatically and it is not impossible that they are detectable even by ANTARES.

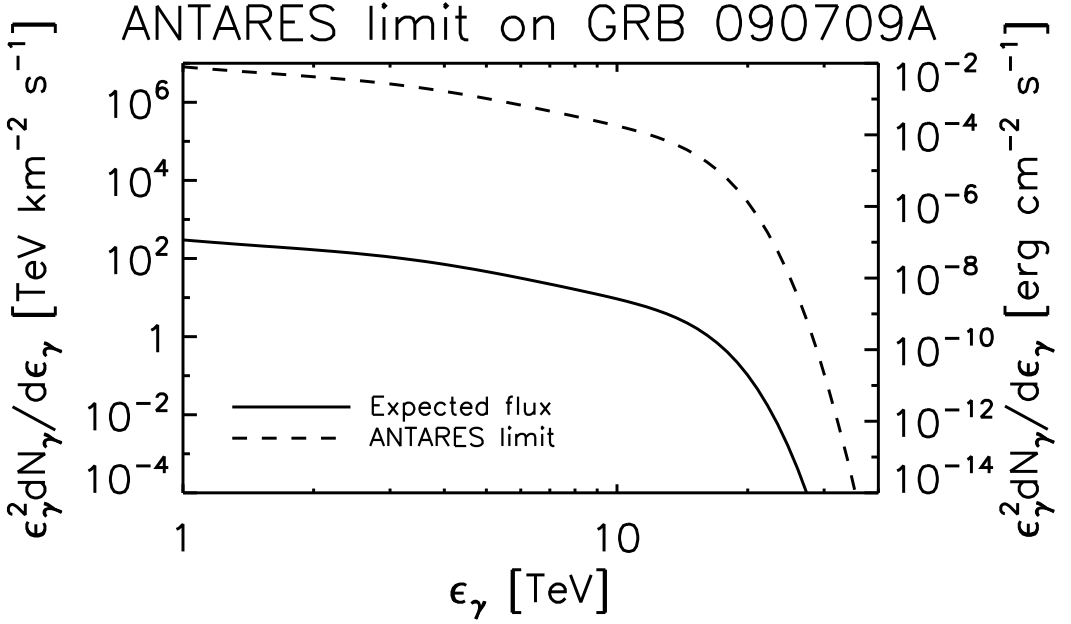
### 11.7 *The result of data unblinding*

THE UNBLINDING proposal has been granted on July 25 2012, and the analysis was performed according to the proposal.

The data from run number 41812 were reconstructed with the `aafit v0r9` algorithm. The Julian Date in the data is used to determine the time of arrival relative to  $T_0$  of the GRB, and local coordinates are used to determine the direction.

For GRB 090709A, the beginning of the on-time is taken to be -66.665 s with respect to the trigger time, and the end of it is taken to be 509.035 s after the alert time. Both values as well as the trigger time are taken from Butler, Bloom & Poznanski (2010).

The off-time is defined to be 1 hour before the on-time. Applying the cuts and knowing the local direction of the GRB at the time it happened, no event were observed during the on-time for both the MDP and MRF cuts. During the off-time, one event was observed for the MDP cut, while 2 events for the MRF cut were



observed. The observation of the 2 events after the MRF cuts were administered implies that the number of background is  $n_{\text{bg}} = 0.32$  during the on-time.

The sensitivity plot is shown in Figure 11.12. At 10 TeV, the photon is  $\phi(10 \text{ TeV}) = 9.25 \times 10^{-2} \text{ TeV}^{-1} \text{ km}^{-2} \text{ s}^{-1}$ . By means of Equation 11.17, the ANTARES upper limit is then

$$\phi_{90}(10 \text{ TeV}) = 2.5 \times 10^3 \text{ TeV}^{-1} \text{ km}^{-2} \text{ s}^{-1}. \quad (11.18)$$

Compared to the expected sensitivity shown in Figure 11.11, the unblinding result is consistent with the expected sensitivity.

Figure 11.12: The 90% confidence level of the sensitivity of the ANTARES Telescope to GRB 090709A, shown here in dotted lines. The theoretical photon spectrum is shown in solid lines.



PART IV

*Epilogue*



## 12 Conclusions and outlook

THE AUTHOR is of the opinion that the attempt to detect very-high energy (VHE)  $\gamma$ -rays from GRBs is a most difficult venture. Some of these difficulties will be discussed in the following.

It is possible that VHE  $\gamma$ -rays are not always produced in a GRB, as the production of VHE  $\gamma$ -rays in GRBs is determined largely by the bulk Lorentz factor  $\Gamma$ . As discussed in Chapter 2, the compactness of the GRB fireball is highly-dependent on  $\Gamma$  and will introduce a cutoff in the emitted  $\gamma$ -ray spectrum. The high-energy cutoff  $\epsilon_{\text{cut}}$  of the energy spectrum is approximated by Asano & Inoue (2007) as

$$\epsilon_{\text{cut}} \simeq \Gamma_{100}^4 L_{\text{iso},51}^{-1/2} \left( \frac{\delta t}{1 \text{ s}} \right)^{1.3} \text{ GeV}, \quad (12.1)$$

where  $\Gamma_{100} = 10^{-2}\Gamma$  is the Lorentz factor of the GRB fireball,  $L_{\text{iso},51} = L_{\text{iso}}/(10^{51} \text{ erg s}^{-1})$  is the isotropic luminosity of the GRB, and  $\delta t$  is the time variability of the GRB in the source frame. From this Equation we can see that  $\Gamma$  must be  $\sim 1000$  to allow for  $\gamma$ -rays of energies  $\epsilon_\gamma \lesssim 10 \text{ TeV}$  to escape from the fireball, assuming a variability timescale  $\delta t = 1 \text{ s}$ . This value of  $\Gamma$  is well above that constrained by Lithwick & Sari (2001), which is generally between 100 and 400. While GRB 090510 has been observed to have  $\Gamma \gtrsim 1200$  (Ackermann et al., 2010), this GRB might represent the higher end of a wide distribution in the bulk Lorentz factor  $\Gamma$ , and a typical GRB will have  $\Gamma \sim 200\text{--}720$  (Ackermann et al., 2012).

Even if VHE  $\gamma$ -rays can escape the fireball, they will interact with the cosmic infrared background radiation. The  $\gamma$ -rays are annihilated, producing electron–positron pairs in its place. The optical depth  $\tau_{\gamma\gamma}$  is a function of  $\gamma$ -ray energy and of the distance to the GRB. As we have seen in Section 2.3, the attenuation limits our observation only to the nearest GRBs. As can be seen from Figure 2.3, the cutoff in the observed photon spectrum is already severe for redshift  $z \sim 0.2$ . This effectively limits our observation only to the nearest GRB with redshift  $z \lesssim 0.2$ , which according to Le & Dermer (2007) has only a probability of  $P(z \leq 0.2) \sim 6.5 \times 10^{-3}$  of occurring. Despite this low probability predicted by



theoretical analyses, in the last 14 years alone we have observed at least 6 GRBs with  $z \leq 0.1$  and 12 GRBs with  $z \leq 0.2$ . This means that nearby GRBs could occur with higher frequency than what was predicted by theory.

The depth of the detector provides excellent shielding against muon background events. However, if the detector is too deep then even muon signal events can not penetrate to that depth. Consequently, the neutrino telescope can not play its role as a  $\gamma$ -ray observatory. The depth of the ANTARES neutrino telescope already provides sufficient shielding while still allowing energetic muons to reach the detector. To operate an underwater neutrino telescope as a  $\gamma$ -ray telescope, it is better if the detector is not deployed to a depth of more than  $\sim 2500$  m.

From the analysis of the expected muon rate from a single GRB event, we found out that the muon rate is largely dependent on three quantities: The distance to the GRB, the hardness of the GRB energy spectrum, and the size of the detector. The distance of the GRB, represented by its redshift  $z$ , determines the number of  $\gamma$ -rays that survive to reach Earth. The hardness of the energy spectrum, represented by its high-energy spectral index  $\beta$ , determines the growth or dissipation of the electromagnetic shower in the atmosphere. Finally, the size of the detector determines the number of detectable muons. An ANTARES-sized telescope however requires a typical GRB with spectral index  $\beta = -2$  to be at a redshift  $z \lesssim 0.05$ . This puts a heavy constraint on the discovery potential as a GRB event that occurs at so small a redshift is very rare. A  $\text{km}^3$ -sized neutrino telescope will have a horizon up to  $z \lesssim 0.1$ .

It is also possible to observe all detected GRBs that occur above the local horizon of the detector and stack them as if they are one single source. In order to understand this method, GRB events are simulated using distribution functions that reflect the properties of a GRB. From this simulation we learned that the effective area of the detector must be at least of the order of  $A_{\mu}^{\text{eff}} = 1 \text{ km}^2$  to obtain at least 50% probability of making a discovery with  $3\sigma$  significance or better in 5 years.

Simulations of the ANTARES Neutrino Telescope's response to downgoing muons show that the detector is capable of recon-

structuring downgoing muon tracks with reasonable efficiency. The muon detection efficiency is approximately  $\sim 20\%$  at a muon energy  $\epsilon_\mu = 10$  TeV. This corresponds to a muon effective area of approximately  $A_\mu^{\text{eff}} \sim 0.05$  km<sup>2</sup>. This relatively small size decreases the redshift threshold even further. GRBs must then occur at redshift  $z \lesssim 0.01$  in order to be detected by ANTARES.

It is to be understood that ANTARES is built more as a proof of principle for an undersea neutrino telescope—a continuation of the legacy left by its predecessors such as DUMAND and the still-active Baikal—than as an instrument of discovery. What has been shown in this dissertation is that the detector is capable to detect downgoing muon events with relatively good accuracy and that a physics analysis can be applied to these data. We have also seen that a statistical analysis can be applied to the data in order to impose a limit on the TeV flux of a selected GRB target.

The sensitivity plot shown in Figure 11.12 implies that the 90% confidence level of ANTARES sensitivity at 10 TeV is

$$\nu f_{\nu,90}(10 \text{ TeV}) = 4 \times 10^{-4} \text{ erg cm}^{-2} \text{ s}^{-1}. \quad (12.2)$$

This result shows that ANTARES is much less sensitive than other ground-based  $\gamma$ -ray observatories such as *Milagro*, MAGIC, or HESS. *Milagro* observed 28 GRBs between 2000–2008 and the best upper limit they obtained at 99% confidence level is  $\nu f_{\nu,99}(> 100 \text{ GeV}) \sim 10^{-6} \text{ erg cm}^{-2} \text{ s}^{-1}$  (Aune, 2009). Between 2005–2006, the MAGIC telescope observed 9 GRBs during their afterglow phase and obtained average upper limits in the order of  $\langle \nu f_\nu \rangle \sim 10^{-8} \text{ erg cm}^{-2} \text{ s}^{-1}$  (Albert et al., 2007). HESS observed GRB 060602B during its prompt and afterglow phases, and obtain an upper limit for  $\epsilon_\gamma > 1$  TeV at 99% confidence level of  $\nu f_{\nu,99}(> 1 \text{ TeV}) = 2.9 \times 10^{-9} \text{ erg cm}^{-2} \text{ s}^{-1}$  (Aharonian et al., 2009). Even though MAGIC and HESS have better sensitivities than *Milagro*, their low duty cycle and slow slew rate make it difficult for them to observe GRBs in the prompt phase.

The currently largest neutrino telescope in the world, IceCube, might be able to play a role as a  $\gamma$ -ray observatory. Two southern GRBs were recently detected by *Swift* and should be within the field of view of IceCube (Table 12.1). The host galaxy of GRB 100316D was identified to be at redshift  $z = 0.059$  (Vergani et al.,

Name	$T_0$ [UT]	$\alpha_{J2000}$ [h:m:s]	$\delta_{J2000}$ [° ' "]	$T_{90}$ [s]	$z$	References
100316D	12:44:50	07 <sup>h</sup> 10 <sup>m</sup> 30.63 <sup>s</sup>	-56°15'19.7"	240	0.059	Vergani et al. (2010)
111005A	08:05:14	14 <sup>h</sup> 53 <sup>m</sup> 15.6 <sup>s</sup>	-19°43'19.1"	26	0.01326?	Levan et al. (2011)

2010) and an associated supernova, SN 2010bh was detected by Wiersema et al. (2010). The host of GRB 111005A was not identified as the GRB occurred at  $\sim 35^\circ$  from the Sun. However, Levan et al. (2011) noticed that the BAT error circle contains a bright, nearby galaxy at redshift  $z = 0.01326$ . If GRB 111005A is indeed associated with this galaxy, then it would be the closest GRB identified since GRB 980425/SN 1998bw. Observing these two GRBs with IceCube could provide us with interesting results given the capabilities of IceCube.

Future neutrino telescopes such as the Gigaton Volume Detector (GVD) in Lake Baikal and KM<sub>3</sub>NeT in the Mediterranean Sea will have a more serious chance to impose a stricter limit or making a discovery. As mentioned in Chapter 1, KM<sub>3</sub>NeT is expected to be completed in 2020 and is expected to cover an instrumented volume of 5–8 km<sup>3</sup>. The site for KM<sub>3</sub>NeT has not yet been determined at this time, however the design for the spherical casing that will house the PMTs has been defined.

The digital optical module (DOM) of KM<sub>3</sub>NeT (Figure 12.1) will be a 17-inch glass sphere equipped with 31 3-inch PMTs. The PMTs are oriented towards various directions, from straight down to about 45° upwards. The advantages of this design among others are that the overall photocathode area exceeds that of a 10-inch PMTs by more than a factor of three, and that it provides more directional sensitivity (Katz & Spiering, 2012). With this design and its large volume, the sensitivity of KM<sub>3</sub>NeT to VHE  $\gamma$ -rays could be increased to as much as a factor of 15 as compared to ANTARES. Combine this large volume with a reconstruction algorithm that can accurately reconstruct the direction of muons of lower energies and better background rejection method, the sensitivity of KM<sub>3</sub>NeT could be increased to as much as 100 times that of ANTARES.

HAWC might be the detector with the best chance to observe TeV  $\gamma$ -rays from GRBs. It has not only a wide field-of-view with

Table 12.1: The parameters of two nearby southern GRBs whose TeV  $\gamma$ -ray emission could possibly be observed by IceCube.



Figure 12.1: The prototype of the KM<sub>3</sub>NeT digital optical module (DOM). Credit: Proprietary KM<sub>3</sub>NeT Consortium, <http://km3net.org>

near 100% duty cycle, but also a large photon collecting area with  $A_{\gamma}^{\text{eff}} \sim 10^5 \text{ m}^2$  at  $\epsilon_{\gamma} = 10 \text{ TeV}$  (Abeysekara et al., 2012). HAWC is expected to have a sensitivity of  $\nu f_{\nu} \sim 10^{-7} \text{ erg cm}^{-2} \text{ s}^{-1}$  for GRBs at a zenith distance of approximately  $30^{\circ}$  (Abeysekara et al., 2012). This is still  $\sim 10$  times less sensitive than MAGIC and  $\sim 100$  times less than HESS, but the clear advantages of HAWC over both instruments are its aforementioned field-of-view and duty cycle.

The first confirmed discovery of TeV  $\gamma$ -rays from GRBs might be performed by HAWC several years after it is completed in 2014, however as we have seen in Chapter 5 it is possible that a detection of at least  $3\sigma$  significance could be achieved by KM<sub>3</sub>NeT within 5 years after it has been completed.

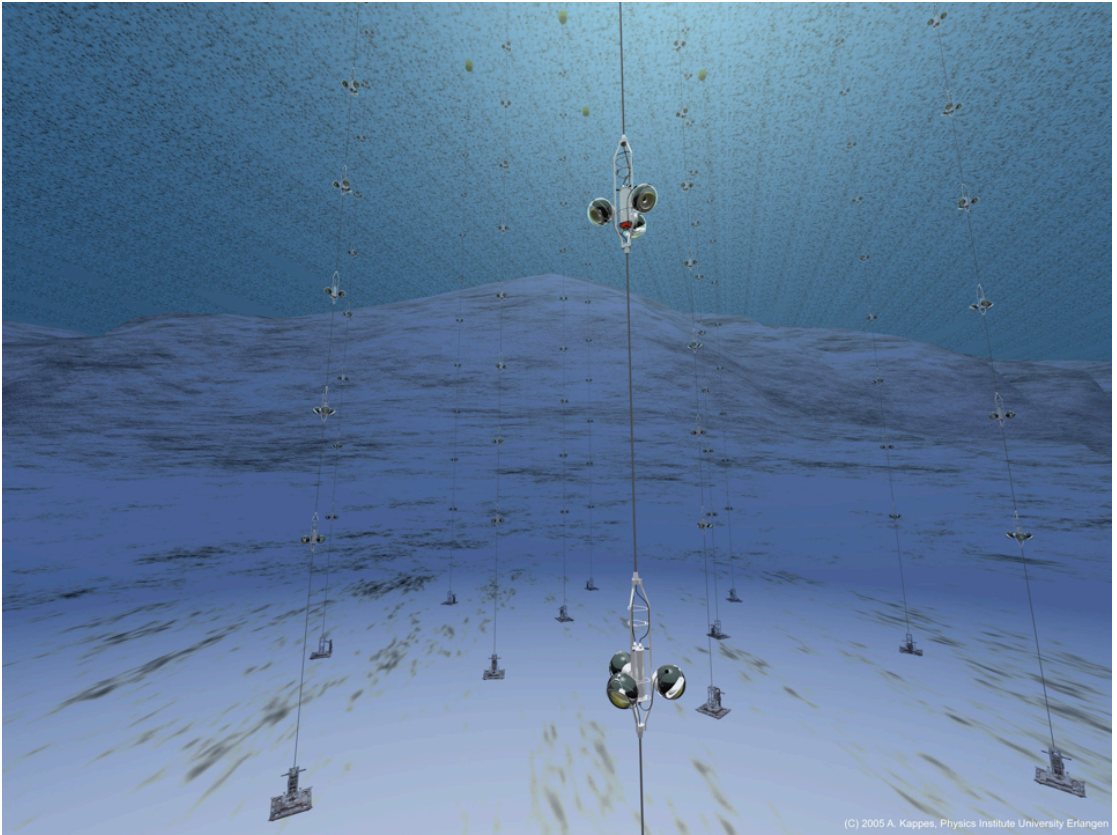
# Summary

AT THE bottom of the Mediterranean Sea, at a depth of 2500 meter and approximately 40 km off Toulon in south of France, lies the ANTARES Neutrino Telescope. It is an array of light-sensitive detectors pointed towards the ground to detect neutrinos that come from the other side of Earth and have passed through it.

Neutrinos are particles that interact very weakly with matter and thus are very difficult to detect. In fact, high-energy neutrinos must pass through the Earth before they have a good chance to interact with the Earth and produce muons, which will travel in the same directions as the neutrinos. When the muons come out of the seabed, they travel with velocities exceeding the velocity of light in water. An electromagnetic shock wave will be generated along the path of the muon, which will be in the form of coherent radiation of photons emitted at a characteristic angle relative to the trajectory of the muon. This coherent photon radiation is called Čerenkov photons. The light-sensitive detectors that comprise ANTARES can detect these photons and reconstruct the tracks of the muons. Detecting upward-going tracks will confirm the neutrino origin of the muons as no other known particle can traverse the entire Earth.

One of the scientific goals to build undersea and under-ice high-energy neutrino telescopes is to search for the acceleration site of cosmic rays at the highest-energy. Cosmic rays are fully ionized atomic nuclei accelerated to relativistic velocities. They constantly shower the Earth at all times and from all directions. The energy of cosmic rays ranged from below  $10^8$  eV up to  $10^{20}$  eV. This extremely-high energy exceeds anything that could be performed in the currently largest manmade particle accelerators on Earth, which is of the order of  $10^{12}$  eV. How these particles can be accelerated to such extreme energy and where are the sources, is still a matter of debate. Pinpointing the source of these natural accelerators could greatly help in understanding the mechanisms of the acceleration.

The search for the acceleration sites of cosmic rays is particularly difficult because they are charged particles and thus can be



(C) 2005 A. Kappes, Physics Institute University Erlangen

deflected to another random direction by ambient magnetic fields. Thus the observed directions of cosmic rays do not point back to the sources. On the other hand, cosmic rays of extremely-high energies are minimally deflected by magnetic fields. Their numbers are however are very low and their detection would require detectors of extreme size in order to detect them within reasonable time.

This is how neutrino telescopes come into the picture. Ultra-high energy neutrinos are expected as a by-product of cosmic ray interactions with the ambient matter of the acceleration site. Relativistically expanding matter will interact with its surrounding environment and create a shock wave. Shock-accelerated protons can escape to be observed on Earth as cosmic rays, but some

Figure 12.2: An artist impression of the ANTARES Neutrino Telescope. A discussion on the ANTARES Neutrino Telescope can be found on Chapter 6. Credit: Alexander Kappes (Physics Institute, University of Erlangen).



will interact with the ambient matter to produce ultra-high energy neutrinos.

Since neutrinos are electrically neutral they are not deflected by magnetic fields. They are also not absorbed by matter because they interact only weakly with it. Thus they point back straight to their production site.

GAMMA-RAY Bursts (GRBs) are attractive candidates for cosmic-ray acceleration sites. They are brief flashes of  $\gamma$ -rays occurring approximately once per day at random time and direction in space and is found to be nonrepeating. During this brief moment the  $\gamma$ -radiation lits up the otherwise dark  $\gamma$ -ray sky, outshining other  $\gamma$ -ray sources. GRBs have been understood to be the death throes of massive stars or the outcome of merger events between compact objects such as black holes or neutron stars. Whatever the progenitor was, the end result is an ultrarelativistic fireball expanding into the interstellar matter. In this environment, protons can be accelerated to reach extremely high energies and escape the fire-

Figure 12.3: An artist impression of a Gamma-Ray Burst. A description of observational and theoretical aspects of GRBs can be found in Chapter 1.2, while the mechanisms of VHE photon productions in GRBs is discussed in Chapter 2.1. Credit: ESO/A. Roquette.

ball as cosmic rays, and can also produce ultra-high energy neutrinos which can be detected by large-scale neutrino telescopes. Finding these ultra-high energy neutrino sources is the main goal of neutrino astrophysics.

Cosmic rays can also interact with the fireball to produce very-high energy (VHE) photons. These photons, of energies in the order of  $10^{12}$  eV and above, can also be detected by neutrino telescopes by the same principle of detection. As the photons reach Earth, they will interact with the atmosphere to produce muons, which can travel downward through the depth of the sea. They will lose their energy during their passage through the sea, but if they are energetic enough they can still invoke electromagnetic shockwaves which will generate Čerenkov photons. From these photons the telescope can then reconstruct the downward-going track of the muons. Thus by looking up like a photon astronomer would traditionally do, instead of looking down like a neutrino astronomer, a neutrino telescope could have a secondary function as a  $\gamma$ -ray telescope.

Neutrino telescopes have a very wide field-of-view and a very high duty cycle. Their coverage above the horizon is approximately  $\pi$  sr and they constantly take data 24 hours per day, 7 days per week, barring maintenance. Taking these two capabilities into account, GRBs are then suitable targets to be observed because of their transient and nonrepeating nature.

This idea of operating a neutrino telescope as a  $\gamma$ -ray telescope is an old one, but can only become a reality with the recent advent of very large volume neutrino telescopes such as ANTARES in the Mediterranean Sea, IceCube at the South Pole, and the future KM<sub>3</sub>NeT. A very large detection volume is required not only because in photon showers muons are produced only in small numbers, but also because VHE photons are absorbed by ambient infrared photons on their way from the source to the Earth.

THE FIRST step in exploring the prospect of this idea is by estimating the number of detectable muons at the detector. A number of factors must be taken into account in this calculation: The intrinsic number of VHE photons produced in the GRB itself, the number of photons absorbed by ambient infrared photons during their



propagation from the source to the Earth, the number of muons produced in the Earth's atmosphere, and the muon energy loss in the sea given the depth of the detector.

Part I of this dissertation is focused on answering this first step. The intrinsic number of VHE photons can be calculated by assuming a certain distance to the GRB, indicated by its redshift  $z$ , and that the photons are emitted with an energy spectrum in the shape of a power-law function. The severity of photon absorptions by infrared ambient matters can be estimated by using currently-available absorption models to calculate the optical depth  $\tau(\epsilon_\gamma, z)$  of the universe to VHE photons as a function of energy and distance to the source.

The calculation of photon-induced muons is performed first by identifying the two most probable channels. The first one is from the decay of pions. High-energy photons interact with the nuclei in the atmosphere to produce pions through the reaction  $\gamma + N \rightarrow \pi + X$ , followed by leptonic decay of pions into a positive muon and a muon neutrino, or a negative muon and a muon antineutrino:  $\pi^\pm \rightarrow \mu^\pm + \nu_\mu(\bar{\nu}_\mu)$ . The energy spectrum of the muons resulting from this channel has been calculated for a specific photon energy spectrum obeying the  $\epsilon_\gamma^{-2}$  function by Drees, Halzen & Hikasa (1989), and has been generalised to an arbitrary spectral index by Halzen, Kappes & Ó Murchadha (2009).

The second channel is the direct muon-pair production from the interaction of high-energy photons with atmospheric nuclei,  $\gamma + X \rightarrow \mu^+ + \mu^-$ . For this to occur, the photon energy must be higher than  $\sim 43.9$  GeV. The cross section for direct lepton-pair productions has been calculated by Bethe & Heitler (1934) for electrons, but the equation can be generalised to any type of lepton by integrating the atomic form factor over the transferred momentum with the mass of the lepton involved as the upper limit (Halzen, Kappes & Ó Murchadha, 2009).

The resulting muon spectrum from these two channels can then be calculated. At low energies, the dominant channel is the pion decay; however, the number of high-energy muons that can be produced from this channel goes down rapidly with increasing energy. At energies higher than 1 TeV, the dominant channel of muon production is pair production, because the total cross sec-

tion increases with photon energy before reaching a saturation point at  $\epsilon_\gamma \gtrsim 10$  TeV.

As the muons traverse the sea, they will lose their energy through ionization and radiative processes. This is a stochastic process which can be evaluated by means of Monte Carlo simulations, but the average energy loss can be calculated by taking the standard muon energy loss formula (Barrett et al., 1952). Using this formula, the relation between the muon energy at the sea surface and the energy at a certain depth can be calculated. It is now also possible to calculate the muon spectrum at the depth of the detector.

From these theoretical calculations, the three most important factors in detecting VHE photons from GRBs has been identified. The redshift  $z$  of the GRB determines the number of VHE photons that survives the journey to the Earth, the hardness of the energy spectrum determines whether the electromagnetic spectrum grows or dissipate in the atmosphere, and finally the size of the detector determines the number of muons that can be detected. Assuming a GRB with an average physical parameters, it is found that an ANTARES-sized neutrino telescope can detect VHE photons provided that the GRBs are located at redshift  $z \lesssim 0.05$ . A larger telescope with a muon effective area of  $A_\mu^{\text{eff}} = 1 \text{ km}^2$  can see up to  $z \sim 0.1$ .

TO UNDERSTAND the response of ANTARES to downgoing muon signals, Monte Carlo simulations are required. This is the main subject of Part II. The simulations are performed in the environment around the detector. The volume is defined to be a cylinder, called the *can*, with the detector placed at the centre. The size of the can covers the detector with a margin equal to a few times the attenuation of light. With this definition, the Čerenkov photons produced outside the can do not reach the detector and thus do not need to be simulated. This can significantly increase the speed of the simulation.

In the atmosphere, several muons can be produced at once in a bundle. These muon bundles travel next to each other and can be inaccurately reconstructed. Monte Carlo simulations of muon production in the atmosphere, performed with the CORSIKA pack-

age, indicate that very high energy muon bundles that can penetrate the depth of the detector are very rare. Most of the muons that reach the detector are single muons. It is thus appropriate to generate only single muon tracks to study the detector response.

The results of the simulations indicate that the detector can accurately reconstruct downgoing muon tracks, albeit with reduced efficiency compared to upgoing tracks. This is because the light-detectors are pointed downwards to maximize light collecting from upgoing tracks. The photon effective area of ANTARES is found to be approximately  $1 \text{ m}^2$  at 5 TeV. Taking into account these detector effects, the sensitivity of ANTARES to an average GRB is only up to redshift  $z \sim 0.01$ .

From the simulation we can also use the angular distribution of reconstructed events to model a point spread function (PSF). The PSF for the signal events can be approximated as a bivariate normal distribution. The background events, which are muons produced from the interaction of cosmic rays with atmospheric nuclei, can be studied using actual data taken by ANTARES. Using a data set taken in 2008, in which ANTARES is running with full capabilities, it is found that the angular distribution of the background events can be approximated by a constant function, assuming that only small opening angles are considered. Using these two ingredients, toy Monte Carlo simulations can be performed to generate background and signal events. These simulations can be used for hypothesis testing to evaluate the compatibility of the data with the background-only hypothesis or the signal plus background hypothesis. From this analysis it is found that detecting only 5 signal events already gives a 90% probability of making a discovery with  $3\sigma$  significance.

THE FIRST attempt to find VHE photons from GRBs using a neutrino telescope is performed in this dissertation. This is described in Part III. We first compile a list of detected GRB from various sources; then the number of detectable muons from these GRBs is calculated. The most prospective GRBs are then the ones that have the highest emitted signal events.

To obtain an optimum quality cut that can maximize the discovery potential, we need to estimate the number of expected signal

and background events. The former is estimated by performing a full Monte Carlo simulation from the top of the atmosphere to the detector volume, while the latter is estimated by analysing the data taken by ANTARES during the period when the GRB took place. After an optimum quality cut has been obtained, the data coinciding with the GRB is then observed.

From the two GRBs to be observed, no event was observed during the time period when the GRB took place. Limits however have been set at 90% confidence level, which is found to be  $\nu f_{\nu,90\%}(10 \text{ TeV}) = 4 \times 10^{-4} \text{ erg cm}^{-2} \text{ s}^{-1}$ . This result shows that ANTARES is much less sensitive than other ground-based  $\gamma$ -ray observatories such as HESS, *Milagro*, or MAGIC.

Two very nearby GRBs took place within the field-of-view of IceCube. As the largest neutrino telescope in the world, IceCube should observe these two GRBs. They should obtain interesting limits given their capabilities.

Future neutrino telescopes such as the Gigaton Volume Detector (GVD) in Lake Baikal and KM<sub>3</sub>NeT in the Mediterranean sea will have a more serious chance to impose a stricter limit or even making a discovery. KM<sub>3</sub>NeT is expected to be completed in 2020 and is expected to cover a volume of 5–8 km<sup>3</sup>. Another instrument that has possibly the best chance to observe VHE photons from GRBs is HAWC, which has a photon effective area of  $A_{\gamma}^{\text{eff}} \sim 10^5 \text{ m}^2$  at  $\epsilon_{\gamma} = 10 \text{ TeV}$  (Abeysekera et al., 2012), and an expected sensitivity of  $\nu f_{\nu} \sim 10^{-7} \text{ erg cm}^{-2} \text{ s}^{-1}$ . This is still  $\sim 10$  times less sensitive than MAGIC and  $\sim 100$  times less sensitive than HESS, but HAWC has a very wide field-of-view and high duty cycle. It is possible that HAWC will make the first confirmed discovery of VHE photons from GRBs after it is completed in 2014.

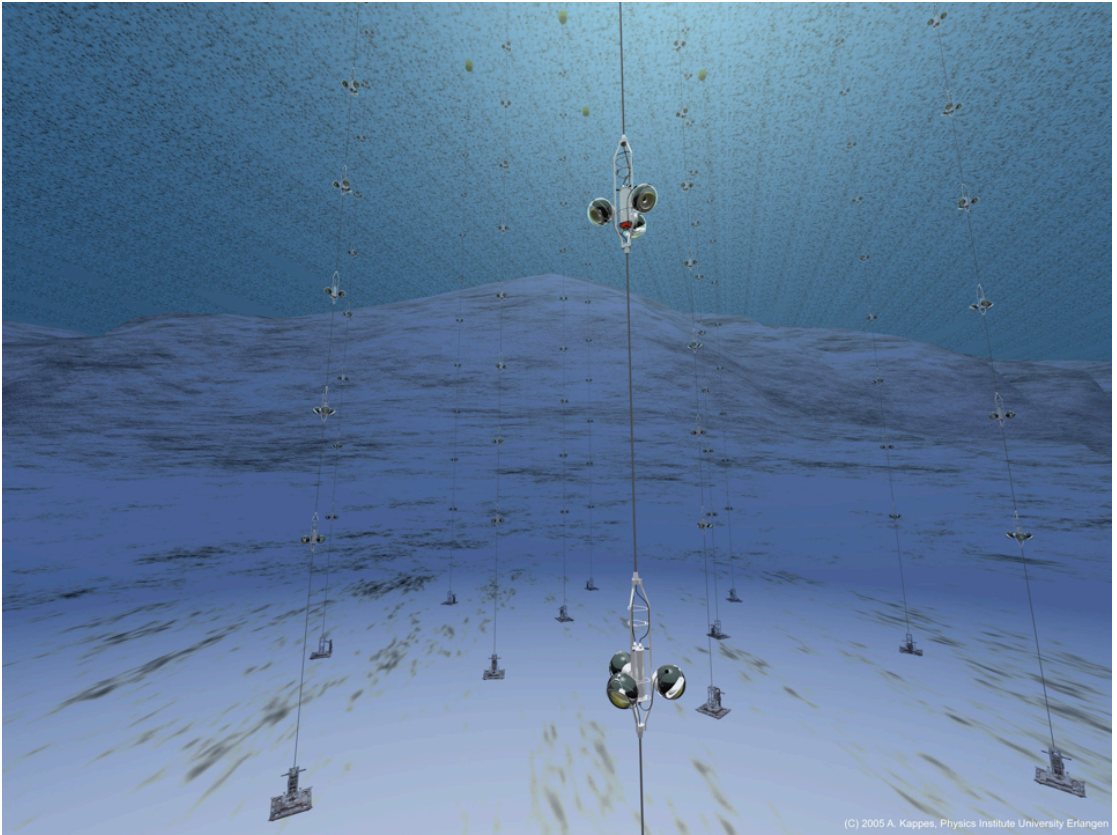
# Samenvatting

OP DE BODEM van Middellandse Zee, op een diepte van 2500 meter en ongeveer 40 km van Toulon in Zuid-Frankrijk, staat de ANTARES neutrino-telescoop. Deze telescoop bestaat uit een verzameling lichtgevoelige sensoren. Neutrino's zijn deeltjes die heel zwak wisselwerken met materie en daarom erg moeilijk zijn waar te nemen.

Neutrino's met een hoge energie kunnen bij een interactie met het zeewater een muon produceren. Dit muon reist in nagenoeg dezelfde richting als het neutrino, en met een snelheid die de snelheid van licht in water overtreft. Hierdoor wordt een elektromagnetische schokgolf teweeggebracht. Deze schokgolf maakt een karakteristieke hoek ten opzichte van het muonspoor en wordt ook wel Čerenkov licht genoemd. Met de lichtgevoelige sensoren van de ANTARES telescoop kan het Čerenkov licht worden gedetecteerd. Uit de plaats en tijd van het gedetecteerde licht kan het muonspoor gereconstrueerd worden. Uit de richtingen van de muonen kan de herkomst van de neutrino's bepaald worden. Het bijzondere is dat neutrino's dwars door de aarde kunnen reizen. Geen enkel ander deeltje kan dat. Dus als een naar boven gaand muon wordt gedetecteerd dan zal dat door een neutrino gemaakt zijn.

Een van de doelen van een neutrino-telescoop is het vinden van de oorsprong van kosmische stralen. Kosmische straling bestaat uit volledig geïoniseerde atoomkernen. De aarde wordt continu en uit alle richtingen bestookt met kosmische stralen. De energie van de kosmische stralen varieert van  $10^8$  eV tot aan  $10^{20}$  eV. De hoogste energie overtreft de energie die ooit bereikt zou kunnen worden met deeltjesversnellers op aarde. Hoe deze deeltjes kunnen worden versneld tot zulke extreem hoge energieën en waar de astrofysische deeltjesversnellers zijn, is nog steeds een vraag die de wetenschap bezig houdt. Het opsporen van de bron zou kunnen leiden naar het antwoord op de vraag hoe deze deeltjesversnellers werken.

De zoektocht naar de bron van kosmische stralen wordt echter bemoeilijkt omdat de kosmische stralen ten gevolge van hun elek-



trische lading worden afgebogen door (inter-)galactische magnetische velden. Hierdoor kan men uit de waargenomen richtingen niet direct de bron achterhalen. Alleen het traject van kosmische stralen met extreem hoge energieën blijft voldoende recht. Hun aantallen zijn echter te gering om binnen een redelijke termijn voldoende statistiek te kunnen verzamelen. Dit is het punt waar neutrino telescopen een bijdrage kunnen leveren.

Neutrino's kunnen ontstaan bij botsingen tussen de kosmische stralen en materie (of zelfs licht). Sommige atoomkernen kunnen ontsnappen uit hun versneller en zo waargenomen worden als kosmische straling op aarde. Andere atoomkernen kunnen botsen met de omringende materie en zo neutrino's produceren. Daar neutrino's elektrisch neutraal zijn worden ze niet afgebogen door

Figuur 12.4: Een schets van de ANTARES neutrino telescoop. Een beschrijving van de ANTARES neutrino telescoop is te vinden in Hoofdstuk 6. Met dank aan Alexander Kappes (Universiteit Erlangen).



magnetische velden. Ze worden slechts sporadisch geabsorbeerd in materie omdat ze zo zwak wisselwerken met materie. Dus wijzen neutrino's direct terug naar hun bron.

**GAMMAFLITSEN** (*Gamma-Ray Burst*, GRB's) kunnen mogelijk dienst doen als kosmische deeltjesversneller. Deze korte  $\gamma$ -flitsen worden ongeveer eens per dag waargenomen worden. Deze  $\gamma$ -flitsen geschieden op willekeurige tijden en plaatsen in de ruimte. Tot nu toe lijken GRB's zich niet te herhalen. Een GRB verschijnt gedurende korte tijd aan de gewoonlijk donkere hemel en overtreft dan alle andere astrofysische bronnen van  $\gamma$ -straling in helderheid. Over het algemeen wordt aangenomen dat een GRB ontstaat tijdens de laatste fase van de implosie van een zeer zware ster is, of bij een fusie tussen twee astrofysische objecten zoals zwarte gaten of neutronensterren. In beide gevallen bestaat het eindresultaat uit een ultrarelativistische vuurbal die zich uitbreidt door de interstellaire materie. In zo'n omgeving kunnen atoomkernen heel effectief versneld worden. Met het bereiken van voldoende

Figuur 12.5: Een schets van een Gammaflits (*Gamma-Ray Burst*, GRB). Een beschrijving van de theoretische en praktische aspecten van GRB's zijn te vinden in Hoofdstuk 1.2. De onderliggende mechanismen worden in Hoofdstuk 2.1 besproken. Met dank aan ESO/A. Roquette.

hoge energieën kunnen zij ontsnappen uit de vuurbal. Men heeft echter nog geen verband kunnen leggen tussen GRB's en de kosmische stralen. Veel modellen van GRB's voorspellen de productie van neutrino's die waargenomen kunnen worden met neutrinotelescopen. Het waarnemen van deze neutrino's zou dit verband onomstotelijk kunnen vastleggen.

Bij de botsingen van de atoomkernen kan ook licht geproduceerd worden. De golflengte van dit licht is zeer klein en komt overeen met een energie van  $10^{12}$  eV of hoger. Bij deze energieën gedraagt het licht zich als een deeltje en wordt daarom ook wel  $\gamma$ -straal genoemd. Bereiken deze  $\gamma$ -stralen de aarde, dan zullen ze botsen met atoomkernen in de atmosfeer boven de ANTARES detector. Hierbij kunnen muonen geproduceerd worden. De muonen zullen een gedeelte van hun energie verliezen tijdens hun reis door de zee. Maar als ze genoeg energie bezitten kunnen ze de detector bereiken en kan de elektromagnetische schokgolf van Čerenkov licht gedetecteerd worden. Dus door omhoog te kijken, in plaats van omlaag, zou een neutrinotelescoop een tweede toepassing kunnen krijgen, namelijk als een  $\gamma$ -straal telescoop. Neutrino telescopen hebben een groot blikveld en zijn 24 uur per dag en 7 dagen per week operationeel. Deze eigenschappen maken een neutrinotelescoop zeer geschikt om GRB's waar te nemen.

Het idee om een neutrinotelescoop als een  $\gamma$ -straal telescoop te gebruiken is oud, maar is voor het eerst toegepast met ANTARES. Met de veel grotere IceCube neutrino telescoop op de Zuidpool en de toekomstige KM<sub>3</sub>NeT neutrino telescoop in de Middellandse Zee wordt de toepassing van dit idee relevanter. Een uiterst grote detector is vereist omdat de kans dat een detecteerbaar muon geproduceerd wordt klein is, en omdat de  $\gamma$ -stralen geabsorbeerd kunnen worden op hun reis van de bron naar de aarde.

DE EERSTE stap in het bepalen van het vooruitzicht van deze detectiemethode is een schatting van het aantal waarneembare muonen. Hierbij moet rekening gehouden worden met een aantal factoren, namelijk: (I) het aantal  $\gamma$ -stralen dat geproduceerd wordt in een GRB, (II) het aantal  $\gamma$ -stralen dat geabsorbeerd wordt door (infrarood) licht tijdens de reis van de bron naar de aarde, (III) het aantal muonen dat in de atmosfeer geproduceerd wordt en



(iv) het aantal muonen dat de detector bereikt.

In Deel I van deze dissertatie wordt uitgelegd hoe het aantal  $\gamma$ -stralen dat geproduceerd wordt in een GRB kan worden berekend voor een bepaalde afstand van de GRB (aangeduid door een roodverschuiving) en hoe het energiespectrum eruit ziet. Op basis van modellen kan de optische diepte van het heelal als functie van de energie van de  $\gamma$ -stralen en de afstand tot de bron berekend worden.

Voor de productie van muonen in de atmosfeer zijn twee dominante kanalen te identificeren. Het eerste kanaal verloopt via productie en verval van kortlevende pionen. Het energiespectrum van de muonen voortvloeiend uit dit kanaal is berekend voor een specifiek energiespectrum van  $\gamma$ -stralen door Drees, Halzen & Hikasa (1989) en later voor een algemener energiespectrum door Halzen, Kappes & Ó Murchadha (2009).

Het tweede kanaal verloopt via de directe productie van muonparen. De werkzame doorsnede voor de productie van elektronparen werd lange tijd geleden berekend door Bethe & Heitler (1934). Deze berekening is aangepast voor paren van muonen (Halzen, Kappes & Ó Murchadha, 2009).

Het energiespectrum van beide kanalen kan dus worden berekend. Bij lage energieën is het pionkanaal dominant. Echter, het aantal muonen dat geproduceerd kan worden via dit kanaal neemt af met toenemende energie terwijl de productie van muonparen juist toeneemt. Hierdoor is bij energieën hoger dan  $10^{12}$  eV het paarproductiekanaal dominant.

Als het muon door het water reist, verliest het energie door ionisatie van het water en door uitstraling van  $\gamma$ -stralen en paren van elektronen. De laatste twee processen gedragen zich als een stochastisch proces en kunnen met Monte Carlo simulaties geëvalueerd worden. Het gemiddelde energieverlies kan simpelweg berekend worden door de standaard formule voor het energieverlies te nemen (Barrett et al., 1952). Door deze formule te gebruiken kan snel het verband tussen de muonenergie aan het zeeoppervlak en de energie op een bepaalde diepte worden berekend. Het is ook mogelijk om het energiespectrum te berekenen op de plek van de detector.

Met deze informatie kan, op basis van de roodverschuiving van

de GRB, het aantal muonen dat de detector bereikt bepaald worden. Uiteindelijk bepaalt de (effectieve) grootte van de detector het aantal muonen dat gedetecteerd wordt. Uitgaande van een gemiddelde GRB blijkt dat men met de ANTARES neutrino-telescoop energetische  $\gamma$ -stralen kan detecteren, mits de GRB relatief dichtbij heeft plaatsgevonden (roodverschuiving  $z < 0.05$ ). Met de IceCube en KM<sub>3</sub>NeT telescopen kan men verder kijken ( $z < 0.1$ ).

OM DE RESPONS van de ANTARES neutrino-telescoop op muonen te begrijpen, wordt gebruik gemaakt van Monte Carlo simulatie software. Dit wordt beschreven in Deel II. Om de snelheid van de berekening te verhogen, wordt alleen het Čerenkov licht in de omgeving van de detector gesimuleerd. Dit volume wordt gedefinieerd door een cilinder rondom de detector. Er moet dan voldoende ruimte zijn tussen de wand van de cilinder en de detector, zodat het Čerenkov licht dat buiten de cilinder wordt geproduceerd geen detecteerbaar signaal kan opleveren.

In de atmosfeer kunnen meerdere muonen tegelijkertijd geproduceerd worden. Zo'n bundel muonen kan minder nauwkeurig worden gereconstrueerd dan een enkel muonspoor. Gebruikmakend van het CORSIKA software programma is aangetoond dat verreweg de meeste bundels die de detector bereiken uit een enkel muon bestaan. Daarom wordt een enkel spoor van een muon gesimuleerd om de respons van de detector te bestuderen.

Met deze simulaties is aangetoond dat de sporen van neerwaartse muonen nauwkeurig gereconstrueerd kunnen worden met de ANTARES neutrino-telescoop, maar dat de efficiëntie vergeleken met die van de opwaartse muonen relatief laag is. Dit komt doordat de lichtgevoelige sensoren naar beneden zijn gericht om zodoende de detectie-efficiëntie van neutrino's te maximaliseren. Het effectieve oppervlak van de ANTARES detector voor energetische  $\gamma$ -stralen is ongeveer  $1 \text{ m}^2$  bij  $5 \times 10^{12} \text{ eV}$ . Als men de respons van de detector in rekening neemt komt de reikwijdte van de ANTARES detector voor GRB's overeen met een roodverschuiving van  $z \sim 0.01$ .

De simulaties kunnen ook gebruikt worden om de resolutie van de detector te bepalen. De resolutie kan worden bepaald op basis van de hoekverdeling van gereconstrueerde sporen ten opzichte

van de positie van de GRB. De achtergrond bestaat voornamelijk uit muonen die worden geproduceerd in de interacties van kosmische stralen met de atmosfeer. De achtergrond kan worden bestudeerd door de meetgegevens te gebruiken die met de ANTARES detector zijn verzameld. Uit de meetgegevens van 2008, het jaar waarin ANTARES gereed kwam, is de hoekverdeling van de achtergrond bepaald. Op basis van de twee hoekverdelingen, één van het veronderstelde signaal en één van de gemeten achtergrond, kan een hypothesetest worden opgezet. De ene hypothese is dat er alleen achtergrond aanwezig is ( $H_0$ ) en de andere hypothese is dat er een verondersteld signaal van een GRB is met daarbij achtergrond ( $H_1$ ). De compatibiliteit van de meetgegevens met de twee hypothesen kan dan getest worden. Uit mijn analyse blijkt dat het detecteren van slechts 5 muonen al 90% waarschijnlijkheid biedt om een ontdekking te doen met een significantie die overeenkomt met  $3\sigma$ .

IN DEEL III wordt de eerste poging beschreven om met de ANTARES neutrino telescoop energetische  $\gamma$ -stralen te detecteren die afkomstig zijn uit een GRB. Hiertoe is allereerst een lijst van GRB's samengesteld en het aantal detecteerbare muonen uit iedere GRB berekend. De meest kansrijke GRB's zijn die GRB's die het grootste aantal detecteerbare muonen opleveren. Echter, voor een optimale selectie moet naast het verwachte aantal muonen van een GRB ook de achtergrond worden bepaald. Na een evaluatie op basis van de hypothesetest met gesimuleerde experimenten wordt de uiteindelijke selectie bepaald. Tijdens de twee GRB's die zijn geselecteerd, werd er geen enkel muon in de ANTARES neutrino telescoop waargenomen. Daarom zijn er limieten bepaald op de intensiteit van hoogenergetische  $\gamma$ -stralen uit de GRB's. Deze limieten kunnen geformuleerd worden als  $\nu f_{\nu,90\%}(10 \text{ TeV}) = 4 \times 10^{-4} \text{ erg cm}^{-2} \text{ s}^{-1}$ .

Hoewel de ANTARES detector veel minder gevoelig is dan daarvoor ingerichte observatoria zoals HESS, Milagro, of MAGIC, biedt deze een breed en continu zicht op het heelal. Dat maakt het toch interessant om met ANTARES naar GRB's te kijken. Twee intense GRB's vonden kort na elkaar plaats in het blikveld van IceCube. Gezien de grootte van IceCube is het zinvol om dezelfde

analyse toe te passen.

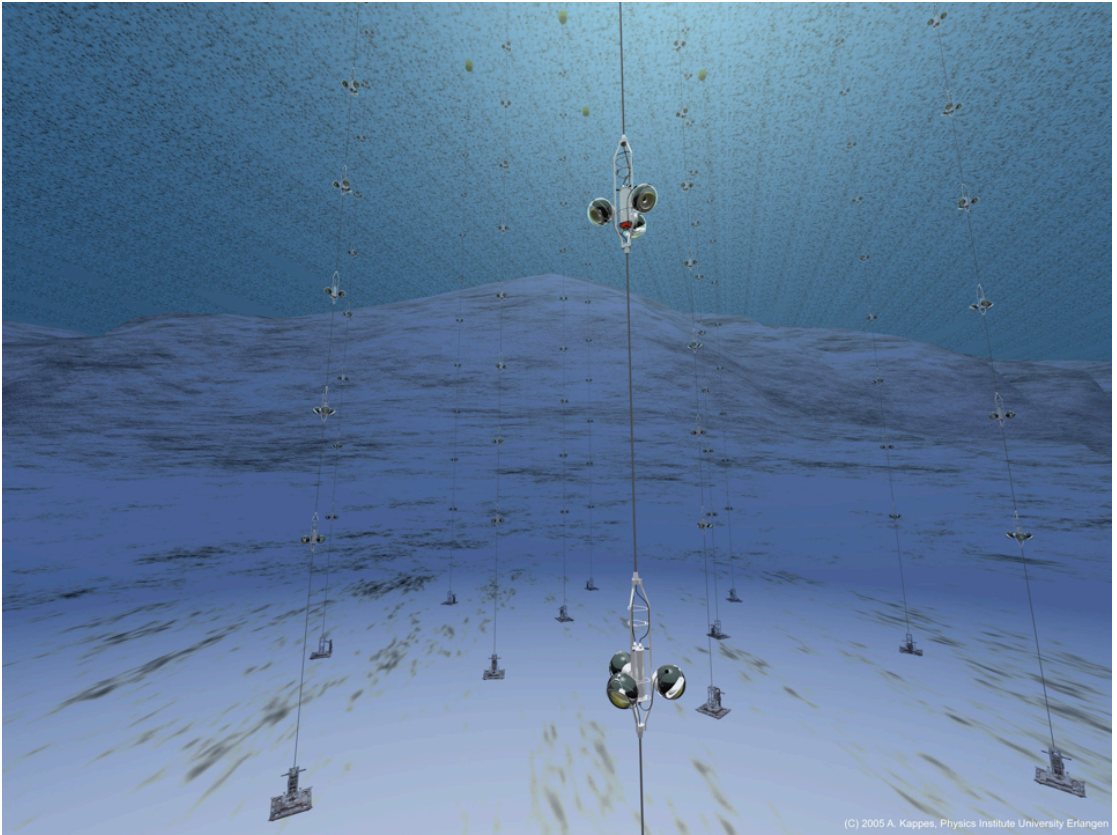
Met toekomstige neutrino telescopen zoals de Gigaton Volume Detector (GVD) in het Baikal-meer en KM<sub>3</sub>NeT in de Middellandse Zee zullen nog betere limieten bepaald kunnen worden of kan er zelfs een ontdekking worden gedaan. KM<sub>3</sub>NeT komt naar verwachting in 2020 gereed. Een ander instrument dat mogelijk de beste kansen heeft om energetische  $\gamma$ -stralen uit GRB's te kunnen waarnemen is HAWC, dat een effectief oppervlak heeft van  $10^5 \text{ m}^2$  bij  $\epsilon_\gamma = 10^{13} \text{ eV}$  (Abeysekara et al., 2012) en een verwachte gevoeligheid van  $\nu f_\nu \sim 10^{-7} \text{ erg cm}^{-2} \text{ s}^{-1}$ . Dit is nog altijd  $\sim 10$  keer minder gevoelig dan MAGIC en  $\sim 100$  keer minder gevoelig dan HESS, maar HAWC heeft een zeer breed blikveld en is continu operationeel. Het is dus goed mogelijk dat met HAWC de eerste ontdekking van energetische  $\gamma$ -stralen uit GRB's zal worden gedaan zodra het gereed komt in 2014.

# Ringkasan

DI DASAR Laut Tengah, pada kedalaman 2500 meter dari permukaan laut dan sekitar 40 km dari kota Toulon di Perancis Selatan, dapat ditemukan Teleskop Neutrino ANTARES. ANTARES adalah rangkaian detektor peka-cahaya yang diarahkan ke dasar laut untuk mendeteksi neutrino energi tinggi.

Neutrino adalah partikel yang berinteraksi sangat lemah dengan materi dan dengan demikian sangatlah sulit dideteksi. Neutrino energi-tinggi yang menembus seluruh Bumi dapat menghasilkan muon, yang akan bergerak dalam arah yang sama dengan neutrino asalnya. Muon tersebut akan bergerak lebih cepat dari kecepatan cahaya di air laut. Akibatnya, gelombang kejut elektromagnetik akan dihasilkan sepanjang jejak muon tersebut. Wujud gelombang kejut ini adalah pancaran radiasi koheren foton yang akan dipancarkan dalam sebuah sudut karakteristik relatif terhadap jejak muon tersebut. Radiasi koheren foton ini dinamakan foton Čerenkov. Detektor peka cahaya yang menyusun ANTARES dapat mendeteksi foton-foton ini. Dari posisi dan waktu saat foton-foton tersebut dideteksi, dapat direkonstruksi jejak muon yang menyebabkan gelombang kejut tersebut. Arah dari mana datangnya neutrino yang menghasilkan muon tersebut kemudian dapat ditentukan. Mendeteksi jejak yang bergerak naik menjauhi dasar laut akan memastikan bahwa partikel tersebut berasal dari neutrino, karena tidak ada partikel lain yang diketahui dapat menembus perut Bumi.

Salah satu tujuan pembangunan teleskop neutrino adalah untuk mencari sumber sinar kosmik berenergi tertinggi. Sinar kosmik adalah inti atomik yang telah terionisasi sepenuhnya. Setiap saat sinar kosmik menghujani Bumi dari segala arah, dengan energi merentang dari  $10^8$  eV hingga  $10^{20}$  eV. Energi yang sangat ekstrim ini melebihi kemampuan akselerator partikel terbesar yang pernah dibuat manusia. Bagaimana partikel-partikel ini dapat dipercepat hingga mencapai energi yang begitu ekstrim dan dimanakah lokasi akselerator alami ini, hingga kini masih diperdebatkan. Menemukan lokasi akselerator alami ini akan dapat membantu kita memahami mekanisme pemercepatannya.



(C) 2005 A. Kappes, Physics Institute University Erlangen

Mencari lokasi dipercepatnya sinar kosmik dipersulit oleh kenyataan bahwa sinar kosmik memiliki muatan listrik dan oleh karena itu dapat dibelokkan oleh medan magnet (antar-)galaksi. Dengan demikian arah datangnya sinar kosmik tidak menunjuk balik ke sumbernya. Di lain sisi, sinar kosmik berenergi ekstrim tidak banyak terbelokkan dan akan menunjuk balik ke sumber asalnya. Persoalannya adalah jumlah mereka sangat kecil dan dibutuhkan waktu lama untuk dapat mendeteksinya dalam kurun waktu yang masuk akal.

Di sinilah bagaimana teleskop neutrino akan dapat membantu. Neutrino berenergi ultra-tinggi dapat muncul dari tumbukan sinar kosmik dengan materi di sekitar lokasi akselerasi. Proton yang dipercepat pada sumbernya dapat melesat dari gumpalan

Gambar 12.6: Sebuah gambaran pelukis mengenai Teleskop Neutrino ANTARES. Diskusi teknis mengenai ANTARES ditulis di Bab 6. Sumber: Alexander Kappes (Institut Fisika, Universitas Erlangen).



materi ini dan akan diamati di Bumi sebagai sinar kosmik, namun sebagian akan berinteraksi dengan gumpalan materi tersebut dan menghasilkan neutrino berenergi ultra-tinggi. Neutrino tidak bermuatan listrik dan oleh karena itu tidak terbelokkan oleh medan magnet. Mereka juga tidak diserap oleh materi karena berinteraksi sangat lemah. Oleh karena itu neutrino yang diamati di Bumi akan menunjuk balik ke lokasi di mana mereka dihasilkan.

KANDIDAT lokasi percepatan sinar kosmik yang paling menarik adalah Semburan Sinar Gamma (GRB). GRB adalah kilatan singkat sinar- $\gamma$ , terjadi sekitar 1 kali sehari pada waktu dan lokasi di langit yang tak bisa diramalkan dan juga tak berulang kembali di lokasi yang sama. Di saat yang singkat ini radiasi sinar- $\gamma$  dari GRB tersebut lebih terang dari sumber-sumber sinar- $\gamma$  lainnya. Asal muasal GRB telah dipahami sebagai hasil dari kematian bintang masif atau bisa juga hasil penggabungan objek-objek kompak seperti lubang hitam atau bintang neutron. Apapun progenitor GRB, hasil akhirnya tetap sama yaitu sebuah bola api relativistik

Gambar 12.7: Sebuah gambaran pelukis mengenai Semburan Sinar-Gamma (GRB). Deskripsi aspek-aspek pengamatan dan teoritis GRB dapat ditemukan di Bab 1.2, sementara mekanisme produksi foton berenergi tinggi dari GRB didiskusikan di Bab 2.1. Sumber: ESO/A. Roquette.

yang mengembang di dalam materi antar bintang. Di dalam bola api ini, proton dipercepat hingga mencapai kecepatan relativistik dan melesat dari bola api tersebut sebagai sinar kosmik. Kaitan antara sinar kosmik dengan GRB hingga kini masih belum dapat dibuktikan. Banyak model GRB meramalkan penciptaan neutrino energi-tinggi yang dapat dideteksi oleh teleskop neutrino skala besar. Menemukan sumber-sumber yang memancarkan neutrino berenergi tinggi dapat memastikan sumber pemercepatan sinar kosmik.

Sinar kosmik juga dapat berinteraksi dengan bola api tersebut dan menghasilkan foton berenergi sangat tinggi. Foton ini, yang berenergi  $10^{12}$  eV ke atas, juga dapat dideteksi oleh teleskop neutrino. Saat mencapai Bumi, foton-foton ini akan berinteraksi dengan atmosfer dan menghasilkan muon, yang akan bergerak menembus kedalaman laut. Mereka akan kehilangan energinya saat menembus laut, namun apabila cukup enerjik mereka masih akan dapat menimbulkan gelombang kejut elektromagnetik. Dengan demikian, dengan melihat ke langit sebagaimana biasa dilakukan astronom foton dan bukan ke tanah seperti yang dilakukan astronom neutrino, sebuah teleskop neutrino memiliki fungsi sekunder sebagai teleskop sinar- $\gamma$ . Teleskop neutrino memiliki medan pandang yang sangat luas dan beroperasi terus-menerus mengambil data 24 jam sehari, 7 hari seminggu. Dua kemampuan ini menjadikan mereka instrumen yang cocok untuk mengamati GRB.

Ide untuk mengoperasikan sebuah teleskop neutrino sebagai teleskop sinar- $\gamma$  sudah dicetuskan semenjak lama, namun baru pertama kalinya diterapkan untuk ANTARES. Dengan adanya teleskop neutrino bervolume sangat besar seperti IceCube di Kutub Selatan dan pembangunan teleskop neutrino KM<sub>3</sub>NeT di masa depan, maka penerapan ide ini menjadi lebih relevan. Detektor berukuran besar dibutuhkan tidak hanya karena di dalam hujan partikel di atmosfer yang diakibatkan oleh foton, muon yang dihasilkan sangat kecil jumlahnya, namun juga karena foton-foton berenergi tinggi diserap oleh foton inframerah dalam perjalanannya ke Bumi.

LANGKAH pertama dalam menjelajahi prospek penggunaan teleskop neutrino sebagai teleskop sinar- $\gamma$  adalah dengan memperki-



rakan jumlah muon yang dapat dideteksi detektor. Sejumlah faktor harus diperhitungkan: Jumlah intrinsik foton berenergi tinggi yang dihasilkan oleh GRB itu sendiri, jumlah foton yang diserap oleh foton inframerah sekitar dalam perjalanan dari sumber ke Bumi, jumlah muon dihasilkan dalam interaksi foton tersebut dengan nukleus di atmosfer Bumi, dan hilangnya energi muon dalam penjalanan di laut.

Bagian Pertama disertai ini difokuskan untuk menjawab langkah pertama ini. Jumlah intrinsik foton energi tinggi yang dihasilkan dari sebuah GRB bergantung dari jaraknya, dinyatakan dengan pergeseran merah (*redshift*)  $z$ , dan bagaimana wujud spektrum energi foton GRB tersebut. Dari model dapat diperkirakan pula kekedapan alam semesta terhadap foton berenergi tinggi sebagai fungsi energi dan jarak sumber.

Produksi muon dalam hujan partikel yang diakibatkan oleh foton dihitung dengan mengidentifikasi dua saluran yang paling dominan. Saluran pertama adalah melalui produksi dan peluruhan pion. Spektrum energi muon yang berasal dari saluran ini telah dihitung oleh Drees, Halzen & Hikasa (1989) untuk spektrum energi foton yang menaati fungsi  $\epsilon_\gamma^{-2}$ , dan telah digeneralisir untuk sembarang indeks spektrum oleh Halzen, Kappes & Ó Murchadha (2009).

Saluran kedua adalah produksi langsung pasangan muon dari interaksi foton energi tinggi dengan nuklei atmosfer. Penampang silang untuk produksi pasangan lepton telah dihitung oleh Bethe & Heitler (1934) untuk kasus elektron. Perhitungan ini telah diterapkan untuk kasus muon oleh Halzen, Kappes & Ó Murchadha (2009).

Spektrum energi muon yang diproduksi dari kedua saluran ini dapat dihitung. Untuk muon berenergi rendah, saluran yang dominan adalah peluruhan pion, namun jumlah muon energi tinggi yang dapat dihasilkan melalui saluran ini menurun drastis seiring meningkatnya energi. Untuk energi lebih tinggi dari 1 TeV, saluran produksi muon yang dominan adalah produksi pasangan karena penampang silang reaksi ini meningkat seiring dengan meningkatnya energi foton, sebelum dicapai titik saturasi pada  $\epsilon_\gamma \gtrsim 10$  TeV.

Ketika muon merambat di kedalaman laut, mereka akan kehi-

langan energi melalui proses ionisasi dan radiatif. Ini adalah proses stokastik yang dapat dievaluasi dengan simulasi Monte Carlo, namun laju rata-rata hilangnya energi dapat dihitung dengan menggunakan persamaan standar hilangnya energi muon (Barrett et al., 1952). Dengan formula ini, hubungan antara energi muon di permukaan laut dan energi pada kedalaman tertentu dapat dihitung. Dengan demikian kita dapat menghitung spektrum energi muon pada kedalaman detektor.

Dari hitungan teoritis ini, tiga faktor terpenting dalam mendeteksi foton berenergi tinggi dari GRB telah diidentifikasi. Pergeseran merah  $z$  GRB menentukan jumlah foton berenergi tinggi yang masih tersisa dan tiba di Bumi, kerasnya spektrum energi foton menentukan apakah hujan partikel yang ditimbulkan akan berkembang atau menyusut, dan akhirnya ukuran detektor menentukan jumlah muon yang dapat dideteksi. Apabila kita menggunakan GRB dengan parameter fisis rata-rata, ditemukan bahwa teleskop neutrino berukuran ANTARES dapat mendeteksi foton berenergi tinggi apabila GRB tersebut terletak pada  $z \lesssim 0.05$ . Teleskop yang berukuran lebih besar, dengan permukaan efektif muon  $A_{\mu}^{\text{eff}} = 1 \text{ km}^2$  dapat mengamati hingga  $z \sim 0.1$ .

UNTUK memahami bagaimana respons ANTARES terhadap sinyal muon yang bergerak ke bawah, dibutuhkan simulasi Monte Carlo. Ini adalah pembahasan utama Bagian Kedua. Untuk meningkatkan waktu komputasi, simulasi dilakukan hanya di lingkungan sekitar detektor. Volume ini didefinisikan sebagai sebuah silinder yang berpusat pada detektor. Ukuran silinder ini mencakup seluruh detektor dengan batas beberapa kali panjang penyerapan cahaya. Dengan definisi ini, foton Čerenkov yang berada di luar silinder tidak dapat mencapai detektor dan demikian tidak perlu disimulasikan.

Di atmosfer, beberapa muon dapat diproduksi sekaligus dalam bundel. Bundel muon ini bergerak bersanding dan direkonstruksi dengan kualitas yang lebih rendah dari jejak muon tunggal. Seberapa sering bundel muon berenergi tinggi ini muncul, dapat ditentukan dengan menggunakan paket simulasi produksi muon di atmosfer, misalnya paket CORSIKA. Simulasi CORSIKA menunjukkan bahwa kemunculan bundel muon yang dapat menembus

kedalaman detektor sangatlah jarang. Sebagian besar muon yang mencapai detektor adalah muon tunggal. Oleh karena itu studi respons detektor dilakukan dengan menggunakan muon tunggal.

Hasil simulasi menunjukkan bahwa ANTARES dapat dengan akurat merekonstruksi jejak muon yang bergerak ke bawah, meskipun dengan efisiensi yang lebih rendah apabila dibandingkan dengan rekonstruksi jejak muon yang bergerak ke atas. Ini karena detektor peka cahaya yang menyusun ANTARES diarahkan ke bawah untuk memaksimalkan pendeteksian cahaya dari jejak yang bergerak ke atas. Luas permukaan efektif foton ANTARES ditemukan sekitar  $1 \text{ m}^2$  pada energi 5 TeV. Apabila efek detektor diikutkan, kepekaan ANTARES terhadap GRB rata-rata hanya sampai  $z \sim 0.01$ .

Dari simulasi ini kita juga dapat menentukan resolusi detektor. Resolusi detektor dapat ditentukan dengan cara menghitung sudut ruang antara jejak sinyal muon yang direkonstruksi dengan posisi GRB. Derau, yaitu muon yang diproduksi dari interaksi sinar kosmik dengan nuklei atmosfer, dapat dipelajari dengan menggunakan data yang telah diambil ANTARES. Dengan menggunakan set data yang diambil pada tahun 2008, ketika ANTARES mengambil data dengan kemampuan maksimal, ditemukan bahwa distribusi anguler dari kejadian-kejadian derau dapat didekati dengan fungsi konstan, dengan asumsi hanya bukaan sudut yang kecil yang dipertimbangkan. Dengan menggunakan dua bahan ini, dapat dilakukan pengujian hipotesis untuk menguji kesesuaian data dengan hipotesis hanya-derau atau hipotesis sinyal-tambah-derau. Dari analisis ini ditemukan bahwa hanya dengan mendeteksi 5 kejadian sinyal, maka sudah diperoleh 90% kebolehjadian untuk membuat penemuan dengan signifikansi  $3\sigma$ .

USAHA pertama untuk menemukan foton berenergi tinggi dari GRB dengan menggunakan teleskop neutrino dijabarkan dalam Bagian Ketiga. Pertama-pertama dari berbagai sumber dikumpulkan daftar GRB yang selama ini telah dideteksi semenjak pendirian ANTARES. Selanjutnya jumlah muon yang dapat dideteksi dari GRB-GRB ini kemudian dihitung. GRB yang paling prospektif adalah mereka yang diharapkan memancarkan sinyal dalam jumlah terbesar.

Untuk memperoleh seleksi kualitas optimum yang dapat memaksimalkan potensi deteksi, kita harus memperkirakan jumlah kejadian sinyal dan derau. Jumlah kejadian sinyal dapat diperkirakan dengan melakukan simulasi Monte Carlo penuh dari atas atmosfer hingga volume detektor di bawah laut, sementara jumlah kejadian derau diperkirakan dengan menganalisis data yang diambil ANTARES pada saat terjadinya GRB yang dianalisis. Setelah seleksi kualitas optimum telah ditemukan, data yang beririsan dengan terjadinya GRB kemudian diamati.

Dari dua GRB yang diamati, tidak ada kejadian apapun diamati pada saat GRB terjadi. Sebuah limit dengan tingkat keyakinan 90% telah diberikan, yaitu  $\nu f_{\nu,90\%}(10 \text{ TeV}) = 4 \times 10^{-4} \text{ erg cm}^{-2} \text{ s}^{-1}$ . Hasil ini menunjukkan bahwa ANTARES masih jauh kurang sensitif dibandingkan observatorium sinar- $\gamma$  landas-Bumi lainnya seperti HESS, *Milagro*, atau MAGIC.

Dua GRB yang sangat dekat terjadi dalam medan pandang IceCube. Sebagai teleskop neutrino terbesar di dunia, IceCube harus mengamati kedua GRB ini. Dengan kapabilitas IceCube, mereka akan memperoleh limit yang menarik.

Teleskop-teleskop neutrino di masa depan, seperti *Gigaton Volume Detector* (GVD) di Danau Baikal dan  $\text{KM}_3\text{NeT}$  di Laut Tengah akan memiliki kesempatan yang lebih serius untuk menaruh limit yang lebih ketat terhadap pancaran foton berenergi tinggi dari GRB, atau bahkan membuat sebuah penemuan.  $\text{KM}_3\text{NeT}$  diharapkan akan selesai dibangun pada tahun 2020 dan diperkirakan akan mencakup volume sekitar  $5\text{--}8 \text{ km}^3$ . Instrumen lain yang kemungkinan memiliki kesempatan lebih baik untuk mengamati foton berenergi tinggi dari GRB adalah HAWC, yang memiliki luas permukaan efektif foton  $A_{\gamma}^{\text{eff}} \sim 10^5 \text{ m}^2$  pada  $\epsilon_{\gamma} = 10 \text{ TeV}$  (Abeysekera et al., 2012), dan kepekaannya diharapkan mencapai  $\nu f_{\nu} \sim 10^{-7} \text{ erg cm}^{-2} \text{ s}^{-1}$ . Ini masih  $\sim 10$  kali lebih lemah daripada MAGIC dan  $\sim 100$  kali lebih lemah daripada HESS, namun HAWC memiliki medan pandang yang sangat luas dan siklus kerja yang sangat tinggi. Boleh jadi HAWC akan membuat penemuan pertama foton berenergi tinggi dari GRB setelah penyelesaian pembangunannya pada tahun 2014.

# Bibliography

- Abdo A. A. et al. 2010. *Fermi Large Area Telescope Constraints on the Gamma-ray Opacity of the Universe*. **ApJ**, **723**: 1082–1096
- Abdo A. A. et al. 2009. *Fermi Observations of High-Energy Gamma-Ray Emission from GRB 080916C*. **Science**, **323**: 1688–1693
- Abdo A. A. et al. 2008. *A Measurement of the Spatial Distribution of Diffuse TeV Gamma-Ray Emission from the Galactic Plane with Milagro*. **ApJ**, **688**: 1078–1083
- Abdo A. A. et al. 2007. *TeV Gamma-Ray Sources from a Survey of the Galactic Plane with Milagro*. **ApJ**, **664**: L91–L94
- Abeyssekara A. U. et al. 2012. *On the sensitivity of the HAWC observatory to gamma-ray bursts*. **Astroparticle Physics**, **35**: 641–650
- Abraham J. et al. 2004. *Properties and performance of the prototype instrument for the Pierre Auger Observatory*. **NIMPA**, **523**: 50–95
- Abramowitz M., Stegun I. A. 1964. *Handbook of mathematical functions with formulas, graphs, and mathematical tables*. New York, NY: Dover
- Ackermann M. et al. 2012. *Constraining the High-energy Emission from Gamma-Ray Bursts with Fermi*. **ApJ**, **754**: 121
- Ackermann M. et al. 2010. *Fermi Observations of GRB 090510: A Short-Hard Gamma-ray Burst with an Additional, Hard Power-law Component from 10 keV TO GeV Energies*. **ApJ**, **716**: 1178–1190
- Actis M. et al. 2011. *Design concepts for the Cherenkov Telescope Array CTA: an advanced facility for ground-based high-energy gamma-ray astronomy*. **Experimental Astronomy**, **32**: 193–316
- Ageron M. et al. 2011. *ANTARES: The first undersea neutrino telescope*. **NIMPA**, **656**: 11–38
- Ageron M. et al. 2007. *The ANTARES optical beacon system*. **NIMPA**, **578**: 498–509
- Aguilar J. A. 2011. *Online Gamma-Ray Burst catalog for neutrino telescopes*. **ArXiv e-prints**
- Aguilar J. A. et al. 2011a. *Time calibration of the ANTARES neutrino telescope*. **Astroparticle Physics**, **34**: 539–549
- Aguilar J. A. et al. 2011b. *AMADEUS—The acoustic neutrino detection test system of the ANTARES deep-sea neutrino telescope*. **NIMPA**, **626**: 128–143
- Aguilar J. A. et al. 2010. *Performance of the front-end electronics of the ANTARES neutrino telescope*. **NIMPA**, **622**: 59–73
- Aguilar J. A. et al. 2005a. *Study of large hemispherical photomultiplier tubes for the ANTARES neutrino telescope*. **NIMPA**, **555**: 132–141
- Aguilar J. A. et al. 2007. *The data acquisition system for the ANTARES neutrino telescope*. **NIMPA**, **570**: 107–116
- Aguilar J. A. et al. 2005b. *Transmission of light in deep sea water at the site of the ANTARES neutrino telescope*. **Astroparticle Physics**, **23**: 131–155
- Aharonian F. et al. 2009. *H.E.S.S. Observations of the Prompt and Afterglow Phases of GRB 060602B*. **ApJ**, **690**: 1068–1073
- Aharonian F. A. 2004. *Very high energy cosmic gamma radiation: a crucial window on the extreme Universe*. River Edge, NJ: World Scientific Publishing
- Ahrens J. et al. 2004. *Muon track reconstruction and data selection techniques in AMANDA*. **NIMPA**, **524**: 169–194
- Albert J. et al. 2008. *Very-High-Energy gamma rays from a Distant Quasar: How Transparent Is the Universe?* **Science**, **320**: 1752–1754
- Albert J. et al. 2007. *MAGIC Upper Limits on the Very High Energy Emission from Gamma-Ray Bursts*. **ApJ**, **667**: 358–366
- Amati L. et al. 2002. *Intrinsic spectra and energetics of BeppoSAX Gamma-Ray Bursts with known redshifts*. **A&A**, **390**: 81–89
- Amenomori M. et al. 1999. *Observation of Multi-TeV Gamma Rays from the Crab Nebula using the Tibet Air Shower Array*. **ApJ**, **525**: L93–L96
- Amenomori M. et al. 2000. *Detection of Multi-TeV Gamma Rays from Markarian 501 during an Unforeseen Flaring State in 1997 with the Tibet Air Shower Array*. **ApJ**, **532**: 302–307
- Amenomori M. et al. 2003. *Multi-TeV Gamma-Ray Flares from Markarian 421 in 2000 and 2001 Observed with the Tibet Air Shower Array*. **ApJ**, **598**: 242–249
- Amenomori M. et al. 2001. *Search for gamma-ray bursts with the Tibet air shower array*. In F. A. Aharonian & H. J. Völk, ed., *American Institute of Physics Conference Series*, volume 558 of *American Institute of Physics Conference Series*, pp. 844–849
- Amenomori M. et al. 2010. *Observation of TeV Gamma Rays from the Fermi Bright Galactic Sources with the Tibet Air Shower Array*. **ApJ**, **709**: L6–L10
- Amram P. et al. 2002. *The ANTARES optical module*. **NIMPA**, **484**: 369–383

- Amram P. et al. 2000. *Background light in potential sites for the ANTARES undersea neutrino telescope*. **Astroparticle Physics**, **13**: 127–136
- Andrés E. et al. 2001. *Observation of high-energy neutrinos using Čerenkov detectors embedded deep in Antarctic ice*. **Nature**, **410**: 441–443
- ANTARES collaboration 1997. *ANTARES proposal: Towards a large scale high energy cosmic neutrino undersea detector*. **ArXiv Astrophysics e-prints**
- Antonoli P., Ghetti C., Korolkova E. V., Kudryavtsev V. A., Sartorelli G. 1997. *A three-dimensional code for muon propagation through the rock: MUSIC*. **Astroparticle Physics**, **7**: 357–368
- Aoki K., Ishii M., Kuzuhara M., Takahashi Y., Kawai N. 2009. *GRB 090709A: Subaru NIR observation*. **GRB Coordinates Network**, **9634**: 1
- Aptekar R. L. et al. 1995. *Konus-W Gamma-Ray Burst Experiment for the GGS Wind Spacecraft*. **Space Sci. Rev.**, **71**: 265–272
- Arai A., Uemura M., Uehara T. 2007. *GRB 070220: observation with the KANATA 1.5m telescope*. **GRB Coordinates Network**, **6117**: 1
- Ardid M. 2009. *Positioning system of the ANTARES neutrino telescope*. **NIMPA**, **602**: 174–176
- Asano K., Inoue S. 2007. *Prompt GeV-TeV Emission of Gamma-Ray Bursts Due to High-Energy Protons, Muons, and Electron-Positron Pairs*. **ApJ**, **671**: 645–655
- Askebjerg P. et al. 1995. *Optical Properties of the South Pole Ice at Depths Between 0.8 and 1 Kilometer*. **Science**, **267**: 1147–1150
- Astraatmadja T. L. 2011. *On the detection of TeV  $\gamma$ -rays from GRB with  $\text{km}^3$  neutrino telescopes — I. Muon event rate from single GRBs*. **MNRAS**, **418**: 1774–1786
- Astraatmadja T. L., 2012a, *On the detection of TeV  $\gamma$ -rays from GRB with  $\text{km}^3$  neutrino telescopes: ANTARES's responses to downgoing muons*. Technical Report ANTARES-PHYS-2012-005
- Astraatmadja T. L., 2012b, *On the detection of TeV  $\gamma$ -rays from GRB with  $\text{km}^3$  neutrino telescopes: Simulation and optimization of three selected GRBs*. Technical Report ANTARES-PHYS-2012-006
- Atkins R. et al. 2005. *Constraints on Very High Energy Gamma-Ray Emission from Gamma-Ray Bursts*. **ApJ**, **630**: 996–1002
- Atkins R. et al. 2000a. *Milagro, a TeV air-shower array*. **NIMPA**, **449**: 478–499
- Atkins R. et al. 2003. *The High-Energy Gamma-Ray Fluence and Energy Spectrum of GRB 970417a from Observations with Milagro*. **ApJ**, **583**: 824–832
- Atkins R. et al. 2000b. *Evidence for TeV Emission from GRB 970417A*. **ApJ**, **533**: L119–L122
- Atteia J.-L. 2003. *A simple empirical redshift indicator for gamma-ray bursts*. **A&A**, **407**: L1–L4
- Atwood W. B. et al. 2009. *The Large Area Telescope on the Fermi Gamma-Ray Space Telescope Mission*. **ApJ**, **697**: 1071–1102
- Aune T. 2009. *A Search for GeV-TeV Emission from GRBs Using the Milagro Detector*. In Meegan C., Kouveliotou C., Gehrels N., eds., *American Institute of Physics Conference Series*, volume 1133 of *American Institute of Physics Conference Series*, pp. 385–387
- Avrorin A. et al. 2011. *The Gigaton Volume Detector in Lake Baikal*. **NIMPA**, **639**: 30–32
- Aynutdinov V. et al. 2006. *The BAIKAL neutrino experiment: From NT200 to NT200+*. **NIMPA**, **567**: 433–437
- Bailey D. J. L., 2002, *Genhen v5r1 : Software Documentation*. Technical Report ANTARES-SOFT-2002-004
- Balkanov V. A. et al. 1997. *Reconstruction of Atmospheric Neutrinos with the Baikal Neutrino Telescope NT-96*. In *International Cosmic Ray Conference*, volume 7 of *International Cosmic Ray Conference*, p. 25
- Band D. et al. 1993. *BATSE observations of gamma-ray burst spectra. I - Spectral diversity*. **ApJ**, **413**: 281–292
- Barat C., Dezalay J. P., Talon R., Syunyaev R., Kuznetsov A., Terekhov O. 1992. *Observation of gamma-ray burst spectra at high energy by the PHEBUS experiment*. In Paciesas W. S., Fishman G. J., eds., *American Institute of Physics Conference Series*, volume 265 of *American Institute of Physics Conference Series*, pp. 43–47
- Baring M. G., Harding A. K. 1997. *The Escape of High-Energy Photons from Gamma-Ray Bursts*. **ApJ**, **491**: 663
- Barrett P. H., Bollinger L. M., Cocconi G., Eisenberg Y., Greisen K. 1952. *Interpretation of Cosmic-Ray Measurements Far Underground*. **Rev. Mod. Phys.**, **24**(3): 133–178
- Barthelmy S. D., Cline T. L., Butterworth P., Kippen R. M., Briggs M. S., Connaughton V., Pendleton G. N. 2000. *GRB Coordinates Network (GCN): A status report*. In R. M. Kippen, R. S. Mallozzi, & G. J. Fishman, ed., *Gamma-ray Bursts, 5th Huntsville Symposium*, volume 526 of *American Institute of Physics Conference Series*, pp. 731–735

- Beardmore A. P. et al. 2007. *GRB 070220: Swift-XRT refined analysis*. **GRB Coordinates Network**, **6118**: 1
- Bethe H., Heitler W. 1934. *On the Stopping of Fast Particles and on the Creation of Positive Electrons*. **Royal Society of London Proceedings Series A**, **146**: 83–112
- Bezrukov L. B. et al. 1984. *Progress report on Lake Baikal neutrino experiment: site studies and stationary string*. In Kleinknecht K., Paschos E. A., eds., *Neutrino Physics and Astrophysics*, pp. 550–555
- Bhattacharjee P., Gupta N. 2003. *The proton synchrotron model of TeV gamma ray bursts and their detectability by AMANDA/ICECUBE type detectors*. **Astroparticle Physics**, **20**: 169–187
- Bionta R. M., Blewitt G., Bratton C. B., Casper D., Ciocio A. 1987. *Observation of a neutrino burst in coincidence with supernova 1987A in the Large Magellanic Cloud*. **Physical Review Letters**, **58**: 1494–1496
- Blandford R., Eichler D. 1987. *Particle acceleration at astrophysical shocks: A theory of cosmic ray origin*. **Phys. Rep.**, **154**: 1–75
- Blumenthal G. R., Gould R. J. 1970. *Bremsstrahlung, Synchrotron Radiation, and Compton Scattering of High-Energy Electrons Traversing Dilute Gases*. **Reviews of Modern Physics**, **42**: 237–271
- Bouwhuis M. 2005. *Detection of Neutrinos from Gamma-Ray Bursts*. PhD thesis, Universiteit van Amsterdam
- Breit G., Wheeler J. A. 1934. *Collision of Two Light Quanta*. **Physical Review**, **46**: 1087–1091
- Briggs M. S. et al. 1996. *BATSE Observations of the Large-Scale Isotropy of Gamma-Ray Bursts*. **ApJ**, **459**: 40
- Brunner J. 2011. *The ANTARES neutrino telescope—Status and first results*. **NIMPA**, **626**: 19
- Butler N. 2009. *GRB090709A: high energy BAT/XRT analysis suggests low to moderate redshift*. **GRB Coordinates Network**, **9639**: 1
- Butler N. R., Bloom J. S., Poznanski D. 2010. *The Cosmic Rate, Luminosity Function, and Intrinsic Correlations of Long Gamma-Ray Bursts*. **ApJ**, **711**: 495–516
- Butler N. R., Kocevski D., Bloom J. S., Curtis J. L. 2007. *A Complete Catalog of Swift Gamma-Ray Burst Spectra and Durations: Demise of a Physical Origin for Pre-Swift High-Energy Correlations*. **ApJ**, **671**: 656–677
- Castro-Tirado A. J. et al. 1999. *Decay of the GRB 990123 Optical Afterglow: Implications for the Fireball Model*. **Science**, **283**: 2069
- Centko S. B., Bloom J. S., Morgan A. N., Perley D. A. 2009. *GRB 090709A: P60 observations*. **GRB Coordinates Network**, **9646**: 1
- Chandra P., Frail D. A. 2007. *VLA observation of GRB 070220*. **GRB Coordinates Network**, **6149**: 1
- Chudakov A. E., Dadykin V. L., Zatsepin V. I., Nesterova N. M. 1967. *A Search for High-Energy Photons from Discrete Sources of Cosmic Radio Emission*. In Shafer Y. G., ed., *Cosmic Rays and Problems of Space Physics*, p. 45
- Cline T. L. et al. 1981. *High-precision source location of the 1978 November 19 gamma-ray burst*. **ApJ**, **246**: L133–L136
- Cocco V. et al. 2002. *The science of AGILE: part I*. **Nuclear Physics B Proceedings Supplements**, **113**: 231–238
- Cocconi G. 1960. *An air shower telescope and the detection of  $10^{12}$  eV photon sources*. In Khrenov V. I. Z. . V. A., ed., *International Cosmic Ray Conference*, volume 2 of *International Cosmic Ray Conference*, p. 309
- Cockcroft J. D., Walton E. T. S. 1932. *Experiments with High Velocity Positive Ions. II. The Disintegration of Elements by High Velocity Protons*. **Royal Society of London Proceedings Series A**, **137**: 229–242
- Colgate S. A. 1968. *Prompt gamma rays and X-rays from supernovae*. **Canadian Journal of Physics**, **46**: 476
- Colgate S. A. 1974. *Early Gamma Rays from Supernovae*. **ApJ**, **187**: 333–336
- Connaughton V. et al. 1997. *A Search for TeV Counterparts to BATSE Gamma-Ray Bursts*. **ApJ**, **479**: 859–+
- Costa E. et al. 1997. *Discovery of an X-ray afterglow associated with the  $\gamma$ -ray burst of 28 February 1997*. **Nature**, **387**: 783–785
- Cowan, Jr. C. L., Reines F., Harrison F. B., Kruse H. W., McGuire A. D. 1956. *Detection of the Free Neutrino: A Confirmation*. **Science**, **124**: 103–104
- Cutler C., Thorne K. S. 2002. *An Overview of Gravitational-Wave Sources*. In Bishop N. T., Maharaj S. D., eds., *General Relativity and Gravitation*, pp. 72–111
- Davis R., Harmer D. S., Hoffman K. C. 1968. *Search for Neutrinos from the Sun*. **Physical Review Letters**, **20**: 1205–1209
- De Bernardis F., Pagano L., Serra P., Melchiorri A., Cooray A. 2008. *Anisotropies in the cosmic neutrino background after Wilkinson Microwave Anisotropy Probe five-year data*. **J. Cosmology Astropart. Phys.**, **6**: 13
- de Jong M., 2005, *The ANTARES Trigger Software*. Technical Report ANTARES-SOFT-2005-005
- de Jong M., 2009, *The TriggerEfficiency program*. Technical Report ANTARES-SOFT-2009-001

- de Luca A., Esposito P., Israel G. L., Götz D., Novara G., Tiengo A., Mereghetti S. 2010. *XMM-Newton and Swift observations prove GRB090709A to be a distant, standard, long GRB*. **MNRAS**, **402**: 1870–1876
- de Vaucouleurs G. 1961. *Astronomical photography: From the daguerrotype to the electron camera*. London: Faber & Faber
- Diehl R. 1988. *The COMPTEL experiment on the NASA Gamma-ray Observatory*. **Space Sci. Rev.**, **49**: 85–106
- Dingus B. L. 1995. *EGRET Observations of > 30 MeV Emission from the Brightest Bursts Detected by BATSE*. **Ap&SS**, **231**: 187–190
- Drees M., Halzen F., Hikasa K. 1989. *Muons in gamma showers*. **Phys. Rev. D**, **39**(5): 1310–1317
- Dzikowski T., Gawin J., Grochalska B., Korejwo J., Wdowczyk J. 1983. *The Existence of a Shower Excess from the Direction of the Crab Nebula*. In *International Cosmic Ray Conference*, volume 2 of *International Cosmic Ray Conference*, p. 132
- Fazio G. G., Stecker F. W. 1970. *Predicted High Energy Break in the Isotropic Gamma Ray Spectrum: a Test of Cosmological Origin*. **Nature**, **226**: 135–136
- Feldman G. J., Cousins R. D. 1998. *Unified approach to the classical statistical analysis of small signals*. **Phys. Rev. D**, **57**: 3873–3889
- Finke J. D., Razzaque S. 2009. *Constraints on the Extragalactic Background Light from very High Energy Gamma-Ray Observations of Blazars*. **ApJ**, **698**: 1761–1766
- Finke J. D., Razzaque S., Dermer C. D. 2010. *Modeling the Extragalactic Background Light from Stars and Dust*. **ApJ**, **712**: 238–249
- Fishman G. J., Meegan C. A. 1995. *Gamma-Ray Bursts*. **ARA&A**, **33**: 415–458
- Fishman G. J. et al. 1994. *The first BATSE gamma-ray burst catalog*. **ApJS**, **92**: 229–283
- Fowler W. A. 1958. *Completion of the Proton-Proton Reaction Chain and the Possibility of Energetic Neutrino Emission by Hot Stars*. **ApJ**, **127**: 551
- Fragile P. C., Mathews G. J., Poirier J., Totani T. 2004. *Constraints on models for TeV gamma rays from gamma-ray bursts*. **Astroparticle Physics**, **20**: 591–607
- Frail D. A., Kulkarni S. R., Nicastro L., Feroci M., Taylor G. B. 1997. *The radio afterglow from the  $\gamma$ -ray burst of 8 May 1997*. **Nature**, **389**: 261–263
- Franceschini A., Rodighiero G., Vaccari M. 2008. *Extragalactic optical-infrared background radiation, its time evolution and the cosmic photon-photon opacity*. **A&A**, **487**: 837–852
- Fritsch U. 2010. *Calibration of the ANTARES neutrino telescope*. In Leroy C., Rancoita P.-G., Barone M., Gaddi A., Price L., Ruchti R., eds., *Astroparticle, Particle and Space Physics, Detectors and Medical Physics Applications*, pp. 195–199
- Gaisser T. K. 1990. *Cosmic rays and particle physics*. Cambridge, UK: Cambridge University Press
- Gaisser T. K. 1997. *Neutrino Astronomy: Physics Goals, Detector Parameters*. **ArXiv Astrophysics e-prints**
- Gaisser T. K. 2011. *Atmospheric Neutrinos*. **Nuclear Physics B Proceedings Supplements**, **221**: 85–89
- Galama T. J. et al. 1998. *An unusual supernova in the error box of the  $\gamma$ -ray burst of 25 April 1998*. **Nature**, **395**: 670–672
- Gallant Y. A., Achterberg A. 1999. *Ultra-high-energy cosmic ray acceleration by relativistic blast waves*. **MNRAS**, **305**: L6–L10
- Gehrels N. et al. 2004. *The Swift Gamma-Ray Burst Mission*. **ApJ**, **611**: 1005–1020
- Gehrels N., Piro L., Leonard P. J. T. 2002. *The brightest explosions in the Universe*. **Scientific American**, **287**(6): 060000–59
- Gehrels N., Ramirez-Ruiz E., Fox D. B. 2009. *Gamma-Ray Bursts in the Swift Era*. **ARA&A**, **47**: 567–617
- Ghirlanda G., Nava L., Ghisellini G., Firmani C. 2007. *Confirming the  $\gamma$ -ray burst spectral-energy correlations in the era of multiple time breaks*. **A&A**, **466**: 127–136
- Gilmore R. C., Madau P., Primack J. R., Somerville R. S., Haardt F. 2009. *GeV gamma-ray attenuation and the high-redshift UV background*. **MNRAS**, **399**: 1694–1708
- Golenetskii S., Aptekar R., Mazets E., Pal’Shin V., Frederiks D., Cline T. 2007. *Konus-wind and konus-a observations of GRB 070220*. **GRB Coordinates Network**, **6124**: 1
- González M. M., Dingus B. L., Kaneko Y., Preece R. D., Dermer C. D., Briggs M. S. 2003. *A  $\gamma$ -ray burst with a high-energy spectral component inconsistent with the synchrotron shock model*. **Nature**, **424**: 749–751
- Górski K. M., Hivon E., Banday A. J., Wandelt B. D., Hansen F. K., Reinecke M., Bartelmann M. 2005. *HEALPix: A Framework for High-Resolution Discretization and Fast Analysis of Data Distributed on the Sphere*. **ApJ**, **622**: 759–771
- Gould R. J., Schröder G. P. 1967. *Pair Production in Photon-Photon Collisions*. **Phys. Rev.**, **155**(5): 1404–1407
- Greisen K. 1960. *Cosmic Ray Showers*. **Annual Review of Nuclear and Particle Science**, **10**: 63–108



- Grieder P. K. F. 1995. *Dumand II: String 1 deployment, initial operation, results and system retrieval*. **Nuclear Physics B Proceedings Supplements**, **43**: 145–148
- Grindlay J. E., Fazio G. G. 1974. *Cosmic Gamma-Ray Bursts from Relativistic Dust Grains*. **ApJ**, **187**: L93
- Guillard G. 2010. *Étude de la sensibilité du télescope à neutrinos Antares aux photons de très haute énergie — Contribution à l'étalonnage en temps du détecteur*. PhD thesis, Université de Strasbourg
- Guillard G. 2011. *ANTARES sensitivity to steady cosmic gamma-ray sources*. In *International Cosmic Ray Conference*, volume 8 of *International Cosmic Ray Conference*, p. 74
- Gupta N., Zhang B. 2007. *Prompt emission of high-energy photons from gamma ray bursts*. **MNRAS**, **380**: 78–92
- Halzen F. 2007. *Cosmic Neutrinos and the Energy Budget of Galactic and Extragalactic Cosmic Rays*. In Sato K., Hisano J., eds., *Energy Budget in the High Energy Universe*, pp. 71–83
- Halzen F., Kappes A., Ó Murchadha A. 2009. *Gamma-ray astronomy with muons: Sensitivity of IceCube to PeVatrons in the Southern sky*. **Phys. Rev. D**, **80**(8): 083009
- Halzen F., Klein S. R. 2010. *Invited Review Article: IceCube: An instrument for neutrino astronomy*. **Review of Scientific Instruments**, **81**(8): 081101
- Hanlon L. O. et al. 1994. *Observations of gamma-ray bursts by COMPTEL*. **A&A**, **285**: 161–178
- Hauser M. G., Dwek E. 2001. *The Cosmic Infrared Background: Measurements and Implications*. **ARA&A**, **39**: 249–307
- Heck D., Knapp J., Capdevielle J. N., Schatz G., Thouw T. 1998. *CORSIKA: a Monte Carlo code to simulate extensive air showers*. TIB Hannover, Germany
- Heijboer A. 2004. *Track Reconstruction and Point Source Searches with ANTARES*. PhD thesis, Universiteit van Amsterdam
- Hess V. F. 1912. *Über Beobachtungen der durchdringenden Strahlung bei sieben Freiballonfahrten*. **Physikalische Zeitschrift**, **13**: 1084–1091
- Hill G. C., Rawlins K. 2003. *Unbiased cut selection for optimal upper limits in neutrino detectors: the model rejection potential technique*. **Astroparticle Physics**, **19**: 393–402
- Hillas A. M. 1996. *Differences between Gamma-Ray and Hadronic Showers*. **Space Sci. Rev.**, **75**: 17–30
- Hinton J. A., Hofmann W. 2009. *Teraelectronvolt Astronomy*. **ARA&A**, **47**: 523–565
- Hirata K., Kajita T., Koshiba M., Nakahata M., Oyama Y. 1987. *Observation of a neutrino burst from the supernova SN1987A*. **Physical Review Letters**, **58**: 1490–1493
- Hjorth J. et al. 2003. *A very energetic supernova associated with the  $\gamma$ -ray burst of 29 March 2003*. **Nature**, **423**: 847–850
- Hopkins A. M., Beacom J. F. 2006. *On the Normalization of the Cosmic Star Formation History*. **ApJ**, **651**: 142–154
- Horan D. et al. 2007. *Very High Energy Observations of Gamma-Ray Burst Locations with the Whipple Telescope*. **ApJ**, **655**: 396–405
- Hörandel J. R. 2010. *Cosmic rays at the highest energies*. **Progress in Particle and Nuclear Physics**, **64**: 351–359
- Horváth I. 1998. *A Third Class of Gamma-Ray Bursts?* **ApJ**, **508**: 757–759
- Horváth I. 2009. *Classification of BeppoSAX's gamma-ray bursts*. **Ap&SS**, **323**: 83–86
- Horváth I., Balázs L. G., Bagoly Z., Ryde F., Mészáros A. 2006. *A new definition of the intermediate group of gamma-ray bursts*. **A&A**, **447**: 23–30
- Horváth I., Balázs L. G., Bagoly Z., Veres P. 2008. *Classification of Swift's gamma-ray bursts*. **A&A**, **489**: L1–L4
- Hubaut F. 1999. *Optimisation et caractérisation des performances d'un télescope sous-marin à neutrinos pour le projet ANTARES*. PhD thesis, Université de la Méditerranée Aix-Marseille II
- Hurley K. et al. 1994. *Detection of a  $\gamma$ -ray burst of very long duration and very high energy*. **Nature**, **372**: 652–654
- Jakobsson P. et al. 2006. *A mean redshift of 2.8 for Swift gamma-ray bursts*. **A&A**, **447**: 897–903
- Jelley J. V. 1958. *Čerenkov radiation and its application*. Oxford, UK: Pergamon Press
- Kakuwa J., Murase K., Toma K., Inoue S., Yamazaki R., Ioka K. 2011. *Prospects for Detecting Gamma-Ray Bursts at Very High Energies with the Cherenkov Telescope Array*. **ArXiv e-prints**
- Kanbach G. et al. 1988. *The project EGRET (Energetic Gamma-Ray Experiment Telescope) on NASA's Gamma-Ray Observatory (GRO)*. **Space Sci. Rev.**, **49**: 69–84
- Kaneko Y., González M. M., Preece R. D., Dingus B. L., Briggs M. S. 2008. *Broadband Spectral Properties of Bright High-Energy Gamma-Ray Bursts Observed with BATSE and EGRET*. **ApJ**, **677**: 1168–1183
- Katz U. F., Spiering C. 2012. *High-energy neutrino astrophysics: Status and perspectives*. **Progress in Particle and Nuclear Physics**, **67**: 651–704

- Kelner S. R., Kokoulin R. P., Petrukhin A. A., 1995, *About cross section for high-energy muon bremsstrahlung*. Technical Report MEPHI-95-24, Moscow State Engineering Physics Institute
- Kippen R. M. et al. 1998. *Characteristics of gamma-ray bursts at MeV energies measured by COMPTEL*. **Advances in Space Research**, **22**: 1097–1100
- Klebesadel R. W., Strong I. B., Olson R. A. 1973. *Observations of Gamma-Ray Bursts of Cosmic Origin*. **ApJ**, **182**: L85
- Klimushin S. I., Bugaev E. V., Sokalski I. A. 2001. *Parametrization of atmospheric muon angular flux underwater*. **Phys. Rev. D**, **64**(1): 014016–+
- Kneiske T. M., Bretz T., Mannheim K., Hartmann D. H. 2004. *Implications of cosmological gamma-ray absorption. II. Modification of gamma-ray spectra*. **A&A**, **413**: 807–815
- Konopelko A. et al. 1999. *Performance of the stereoscopic system of the HEGRA imaging air Čerenkov telescopes: Monte Carlo simulations and observations*. **Astroparticle Physics**, **10**: 275–289
- Kouveliotou C., Koshut T., Briggs M. S., Pendleton G. N., Meegan C. A., Fishman G. J., Lestrade J. P. 1996. *Correlations between duration, hardness and intensity in GRBs*. In C. Kouveliotou, M. F. Briggs, & G. J. Fishman, ed., *American Institute of Physics Conference Series*, volume 384 of *American Institute of Physics Conference Series*, pp. 42–46
- Kouveliotou C., Meegan C. A., Fishman G. J., Bhat N. P., Briggs M. S., Koshut T. M., Paciesas W. S., Pendleton G. N. 1993. *Identification of two classes of gamma-ray bursts*. **ApJ**, **413**: L101–L104
- Kouveliotou C. et al. 2004. *Chandra Observations of the X-Ray Environs of SN 1998bw/GRB 980425*. **ApJ**, **608**: 872–882
- Krupp E. C. 1994. *Echoes of the ancient skies. The astronomy of lost civilizations*. New York, NY: Oxford University Press
- Kulkarni S. R. et al. 1999. *The afterglow, redshift and extreme energetics of the  $\gamma$ -ray burst of 23 January 1999*. **Nature**, **398**: 389–394
- Kwok P. W. et al. 1993. *EGRET observations of gamma-ray bursts on June 1, 1991 and August 14, 1991*. In Friedlander M., Gehrels N., Macomb D. J., eds., *American Institute of Physics Conference Series*, volume 280 of *American Institute of Physics Conference Series*, pp. 855–859
- Le T., Dermer C. D. 2007. *On the Redshift Distribution of Gamma-Ray Bursts in the Swift Era*. **ApJ**, **661**: 394–415
- Le T., Dermer C. D. 2009. *Gamma-ray Burst Predictions for the Fermi Gamma Ray Space Telescope*. **ApJ**, **700**: 1026–1033
- Levan A. J., Tanvir N. R., Wiersema K., O’Brien P. T. 2011. *GRB 111005A: bright galaxy in error circle*. **GRB Coordinates Network**, **12414**: 1
- Li T., Ma Y. 1983. *Analysis methods for results in gamma-ray astronomy*. **ApJ**, **272**: 317–324
- Lim G. M. A. 2011. *Searching for Dark Matter with the Antares Neutrino Telescope*. PhD thesis, Universiteit van Amsterdam
- Lithwick Y., Sari R. 2001. *Lower Limits on Lorentz Factors in Gamma-Ray Bursts*. **ApJ**, **555**: 540–545
- Lytikov M., Blandford R. 2003. *Gamma Ray Bursts as Electromagnetic Outflows*. **ArXiv Astrophysics e-prints**
- MacFadyen A. I., Woosley S. E. 1999. *Collapsars: Gamma-Ray Bursts and Explosions in “Failed Supernovae”*. **ApJ**, **524**: 262–289
- Markov M. 1960. *On high energy neutrino physics*. In Sudarshan E. C. G., Tinlot J. H., Melissinos A. C., eds., *Proceedings of International Conference on High Energy Physics*, p. 578. New York, NY: Rochester University Department of Physics, Interscience
- Markov M. 1961. *On high energy neutrino physics in cosmic rays*. **Nucl. Phys. A**, **27**: 385–394
- Markwardt C. B., Gavriil F. P., Palmer D. M., Baumgartner W. H., Barthelmy S. D. 2009. *GRB 090709A: quasiperiodic variations in the BAT light curve*. **GRB Coordinates Network**, **9645**: 1
- Marshak M. L. et al. 1985. *Evidence for muon production by particles from Cygnus X-3*. **Physical Review Letters**, **54**: 2079–2082
- Matz S. M., Forrest D. J., Vestrand W. T., Chupp E. L., Share G. H., Rieger E. 1985. *High-energy emission in gamma-ray bursts*. **ApJ**, **288**: L37–L40
- Mazets E. P., Golenetskij S. V., Il’Inskij V. N. 1974. *Burst of cosmic gamma -emission from observations on Cosmos 461*. **Pis ma Zhurnal Eksperimental noi i Teoreticheskoi Fiziki**, **19**: 126–128
- Meegan C. A., Fishman G. J., Wilson R. B., Horack J. M., Brock M. N., Paciesas W. S., Pendleton G. N., Kouveliotou C. 1992. *Spatial distribution of gamma-ray bursts observed by BATSE*. **Nature**, **355**: 143–145
- Meegan C. A. et al. 1996. *The Third BATSE Gamma-Ray Burst Catalog*. **ApJS**, **106**: 65–110
- Melandri A. et al. 2007. *GRB 070220 : faulkes telescope north optical limit*. **GRB Coordinates Network**, **6115**: 1
- Mészáros P. 2006. *Gamma-ray bursts*. **Reports on Progress in Physics**, **69**: 2259–2321

- Mészáros P., Rees M. J. 1997. *Optical and Long-Wavelength Afterglow from Gamma-Ray Bursts*. **ApJ**, **476**: 232
- Mészáros P., Rees M. J. 2001. *Collapsar Jets, Bubbles, and Fe Lines*. **ApJ**, **556**: L37–L40
- Metzger M. R., Djorgovski S. G., Kulkarni S. R., Steidel C. C., Adelberger K. L., Frail D. A., Costa E., Frontera F. 1997. *Spectral constraints on the redshift of the optical counterpart to the  $\gamma$ -ray burst of 8 May 1997*. **Nature**, **387**: 878–880
- Mirabal N., Gotthelf E. V. 2009. *GRB 090709A: Swift XRT timing analysis*. **GRB Coordinates Network**, **9696**: 1
- Mirabal N., Halpern J. P., An D., Thorstensen J. R., Terndrup D. M. 2006. *GRB 060218/SN 2006aj: A Gamma-Ray Burst and Prompt Supernova at  $z = 0.0335$* . **ApJ**, **643**: L99–L102
- Moiseev A. A. 2008. *Gamma-ray Large Area Space Telescope: Mission overview*. **NIMPA**, **588**: 41–47
- Morgan A. N., Bloom J. S., Klein C. R. 2009. *GRB 090709A - PAIRITEL discovery of a red afterglow*. **GRB Coordinates Network**, **9635**: 1
- Morris D. C. et al. 2009. *GRB 090709: Swift detection of a bright burst*. **GRB Coordinates Network**, **9625**: 1
- Morrison P. 1958. *On gamma-ray astronomy*. **II Nuovo Cimento**, **7**: 858–865
- Nakamura K., Particle Data Group 2010. *Review of Particle Physics*. **Journal of Physics G Nuclear Physics**, **37(7)**: 075021–+
- Natarajan P., Albanna B., Hjorth J., Ramirez-Ruiz E., Tanvir N., Wijers R. 2005. *The redshift distribution of gamma-ray bursts revisited*. **MNRAS**, **364**: L8–L12
- Navas S., Thompson L., 1999, *KM3 User Guide and Reference Manual*. Technical Report ANTARES-SOFT-1999-011
- Nemiroff R. J. 1994. *A Century of Gamma Ray Burst Models*. **Comments on Astrophysics**, **17**: 189
- Paciesas W. S. et al. 1999. *The Fourth BATSE Gamma-Ray Burst Catalog (Revised)*. **ApJS**, **122**: 465–495
- Paczynski B. 1986. *Gamma-ray bursters at cosmological distances*. **ApJ**, **308**: L43–L46
- Paczynski B. 1988. *Gamma-ray bursts from cusps on superconducting cosmic strings at large redshifts*. **ApJ**, **335**: 525–531
- Paczynski B. 1990. *Super-Eddington winds from neutron stars*. **ApJ**, **363**: 218–226
- Padilla L. et al. 1998. *Search for gamma-ray bursts above 20 TeV with the HEGRA AIROBICC Cherenkov array*. **A&A**, **337**: 43–50
- Panaitescu A., Meszaros P. 1998. *Simulations of Gamma-Ray Bursts from External Shocks: Time Variability and Spectral Correlations*. **ApJ**, **492**: 683
- Parsons A. et al. 2007. *GRB 070220 Swift-BAT refined analysis*. **GRB Coordinates Network**, **6121**: 1
- Pe'er A., Waxman E. 2004. *Prompt Gamma-Ray Burst Spectra: Detailed Calculations and the Effect of Pair Production*. **ApJ**, **613**: 448–459
- Pe'er A., Waxman E. 2005. *High-Energy Photon Emission in the Early Afterglow of GRBs*. **ApJ**, **633**: 1018–1026
- Pelangeon A., Atteia J.-L. 2007. *GRB 070220: pseudo- $z \sim 2.15$  from spectral parameters of the prompt*. **GRB Coordinates Network**, **6129**: 1
- Pian E. et al. 2000. *BEPOSAX Observations of GRB 980425: Detection of the Prompt Event and Monitoring of the Error Box*. **ApJ**, **536**: 778–787
- Piran T. 1999. *Gamma-ray bursts and the fireball model*. **Phys. Rep.**, **314**: 575–667
- Podsiadlowski P., Rees M. J., Ruderman M. 1995. *Gamma-ray bursts and the structure of the Galactic halo*. **MNRAS**, **273**: 755–771
- Poirier J., D'Andrea C., Fragile P. C., Gress J., Mathews G. J., Race D. 2003. *Search for sub-TeV gamma rays in coincidence with gamma ray bursts*. **Phys. Rev. D**, **67(4)**: 042001–+
- Popham R., Woosley S. E., Fryer C. 1999. *Hyperaccreting Black Holes and Gamma-Ray Bursts*. **ApJ**, **518**: 356–374
- Preece R. D., Briggs M. S., Mallozzi R. S., Pendleton G. N., Paciasas W. S., Band D. L. 2000. *The BATSE Gamma-Ray Burst Spectral Catalog. I. High Time Resolution Spectroscopy of Bright Bursts Using High Energy Resolution Data*. **ApJS**, **126**: 19–36
- Primack J. R., Bullock J. S., Somerville R. S. 2005. *Observational Gamma-ray Cosmology*. In F. A. Aharonian, H. J. Völk, & D. Horns, ed., *High Energy Gamma-Ray Astronomy*, volume 745 of *American Institute of Physics Conference Series*, pp. 23–33
- Rees M. J., Mészáros P. 1992. *Relativistic fireballs - Energy conversion and time-scales*. **MNRAS**, **258**: 41P–43P
- Rees M. J., Mészáros P. 1994. *Unsteady outflow models for cosmological gamma-ray bursts*. **ApJ**, **430**: L93–L96
- Reines F. 1960. *Neutrino Interactions*. **Annual Review of Nuclear and Particle Science**, **10**: 1–26

- Ricker G. R. et al. 2003. *The High Energy Transient Explorer (HETE): Mission and Science Overview*. In G. R. Ricker & R. K. Vanderspek, ed., *Gamma-Ray Burst and Afterglow Astronomy 2001: A Workshop Celebrating the First Year of the HETE Mission*, volume 662 of *American Institute of Physics Conference Series*, pp. 3–16
- Roberts A. 1992. *The birth of high-energy neutrino astronomy: A personal history of the DUMAND project*. **Reviews of Modern Physics**, **64**: 259–312
- Rossi B. 1952. *High-Energy Particles*. New York, NY: Prentice-Hall
- Rossi B., Greisen K. 1941. *Cosmic-Ray Theory*. **Reviews of Modern Physics**, **13**: 240–309
- Rosswog S., Ramirez-Ruiz E., Davies M. B. 2003. *High-resolution calculations of merging neutron stars - III. Gamma-ray bursts*. **MNRAS**, **345**: 1077–1090
- Rybicki G. B., Lightman A. P. 1979. *Radiative processes in astrophysics*. New York, NY: Wiley-Interscience
- Sadler E. M., Stathakis R. A., Boyle B. J., Ekers R. D. 1998. *Supernova 1998bw in ESO 184-G82*. **IAU Circ.**, **6901**: 1
- Samorski M., Stamm W. 1983. *Detection of  $2 \times 10^{15}$  to  $2 \times 10^{16}$  eV gamma-rays from Cygnus X-3*. **ApJ**, **268**: L17–L21
- Sari R., Esin A. A. 2001. *On the Synchrotron Self-Compton Emission from Relativistic Shocks and Its Implications for Gamma-Ray Burst Afterglows*. **ApJ**, **548**: 787–799
- Sari R., Piran T., Narayan R. 1998. *Spectra and Light Curves of Gamma-Ray Burst Afterglows*. **ApJ**, **497**: L17
- Schneid E. J. et al. 1992. *EGRET detection of high energy gamma rays from the gamma-ray burst of 3 May 1991*. **A&A**, **255**: L13–L16
- Soffitta P. et al. 1998. *GRB 980425*. **IAU Circ.**, **6884**: 1
- Sommer M. et al. 1994. *High-energy gamma rays from the intense 1993 January 31 gamma-ray burst*. **ApJ**, **422**: L63–L66
- Stamatikos M. et al. 2007a. *GRB 070220: Swift detection of a burst*. **GRB Coordinates Network**, **6114**: 1
- Stamatikos M., Barthelmy S. D., Beardmore A. P., de Pasquale M., Burrows D. N., Roming P., Gehrels N. 2007b. *Swift observations on GRB 070220*. **GCN Report**, **34**: 1
- Stanev T., Gaisser T. K., Halzen F. 1985. *Muons in gamma showers from Cygnus X-3?* **Phys. Rev. D**, **32**(5): 1244–1247
- Stanev T., Vankov C. P., Halzen F. 1985. *Muons in gamma showers*. In Jones F. C., ed., *International Cosmic Ray Conference*, volume 7 of *International Cosmic Ray Conference*, pp. 219–222
- Starling R. L. C. et al. 2011. *Discovery of the nearby long, soft GRB 100316D with an associated supernova*. **MNRAS**, **411**: 2792–2803
- Stecker F. W., Malkan M. A., Scully S. T. 2006. *Intergalactic Photon Spectra from the Far-IR to the UV Lyman Limit for  $0 < z < 6$  and the Optical Depth of the Universe to High-Energy Gamma Rays*. **ApJ**, **648**: 774–783
- Tinney C. et al. 1998. *GRB 980425*. **IAU Circ.**, **6896**: 3
- Torii K., Tanaka S., Tsunemi H. 2007. *GRB 070220: ART-3 optical and NIR limits*. **GRB Coordinates Network**, **6122**: 1
- Totani T. 1998a. *TeV Burst of Gamma-Ray Bursts and Ultra-High-Energy Cosmic Rays*. **ApJ**, **509**: L81–L84
- Totani T. 1998b. *Very Strong TeV Emission as Gamma-Ray Burst Afterglows*. **ApJ**, **502**: L13
- Totani T. 1999. *Pair creation by very high-energy photons in gamma-ray bursts: a unified picture for the energetics of GRBs*. **MNRAS**, **307**: L41–L45
- Totani T. 2000. *An Interpretation of the Evidence for TeV Emission from GRB 970417A*. **ApJ**, **536**: L23–L26
- Tremaine S., Żytkow A. N. 1986. *Can comet clouds around neutron stars explain gamma-ray bursts?* **ApJ**, **301**: 155–163
- Tsai Y. 1974. *Pair production and bremsstrahlung of charged leptons*. **Reviews of Modern Physics**, **46**: 815–851
- Čerenkov P. A. 1934. *Visible luminescence of pure fluids induced by gamma rays*. **Dokl.Akad.Nauk Ser.Fiz.**, **2**: 451–454
- Čerenkov P. A. 1937. *Visible Radiation Produced by Electrons Moving in a Medium with Velocities Exceeding that of Light*. **Physical Review**, **52**: 378–379
- van Helden A. 1977. *The invention of the telescope*. **Trans. Am. Philos. Soc. Vol. 67, Part 4**
- van Paradijs J. et al. 1997. *Transient optical emission from the error box of the  $\gamma$ -ray burst of 28 February 1997*. **Nature**, **386**: 686–689
- van Paradijs J., Kouveliotou C., Wijers R. A. M. J. 2000. *Gamma-Ray Burst Afterglows*. **ARA&A**, **38**: 379–425
- Vedrenne G. 1981. *Cosmic gamma-ray bursts*. **Royal Society of London Philosophical Transactions Series A**, **301**: 645–658
- Vergani S. D., Levan A. J., D'Avanzo P., Covino S., Malesani D., Hjorth J., Tanvir N. R., Antonelli L. A. 2010. *GRB 100316D: Gemini/GMOS and VLT/X-shooter observations*. **GRB Coordinates Network**, **10513**: 1

- Vietri M. 1997. *GeV Photons from Ultrahigh Energy Cosmic Rays Accelerated in Gamma Ray Bursts*. **Physical Review Letters**, **78**: 4328–4331
- Wang X. Y., Dai Z. G., Lu T. 2001a. *Prompt High-Energy Gamma-Ray Emission from the Synchrotron Self-Compton Process in the Reverse Shocks of Gamma-Ray Bursts*. **ApJ**, **546**: L33–L37
- Wang X. Y., Dai Z. G., Lu T. 2001b. *The Inverse Compton Emission Spectra in the Very Early Afterglows of Gamma-Ray Bursts*. **ApJ**, **556**: 1010–1016
- Waxman E., Bahcall J. 1997. *High Energy Neutrinos from Cosmological Gamma-Ray Burst Fireballs*. **Physical Review Letters**, **78**: 2292–2295
- Weekes T. C. 2003. *Very high energy gamma-ray astronomy*. Bristol, UK: Institute of Physics Publishing
- Weekes T. C. et al. 1989. *Observation of TeV gamma rays from the Crab nebula using the atmospheric Cerenkov imaging technique*. **ApJ**, **342**: 379–395
- Wiersema K., D'Avanzo P., Levan A. J., Tanvir N. R., Malesani D., Covino S. 2010. *GRB 100316D: possible supernova*. **GRB Coordinates Network**, **10525**: 1
- Winkler C. et al. 2003. *The INTEGRAL mission*. **A&A**, **411**: L1–L6
- Winkler C. et al. 1995. *COMPTEL observations of the strong gamma-ray burst GRB 940217*. **A&A**, **302**: 765
- Woosley S. E. 1993. *Gamma-ray bursts from stellar mass accretion disks around black holes*. **ApJ**, **405**: 273–277
- Woosley S. E., Bloom J. S. 2006. *The Supernova Gamma-Ray Burst Connection*. **ARA&A**, **44**: 507–556
- Zhang B., Mészáros P. 2001. *High-Energy Spectral Components in Gamma-Ray Burst Afterglows*. **ApJ**, **559**: 110–122
- Zhang B., Mészáros P. 2004. *Gamma-Ray Bursts: progress, problems & prospects*. **International Journal of Modern Physics A**, **19**: 2385–2472
- Zhang B.-B. et al. 2011. *A Comprehensive Analysis of Fermi Gamma-ray Burst Data. I. Spectral Components and the Possible Physical Origins of LAT/GBM GRBs*. **ApJ**, **730**: 141–+

# *Curriculum vitae*

IT WAS not really clear in the beginning that I was going to become an astronomer. In 1983, when I was 2 year old, a total solar eclipse passed through Java. My family, against the dictatorial New Order regime's warning to remain at home and not observe the eclipse, went to the countryside and observed the eclipse. My two-year-old self was unable to appreciate the significance of this event, and later on photos of a whining and crying two-year-old me adorned the family album along with the neatly taken photos of the eclipse.

My family's second attempt to fascinate me with the universe also failed spectacularly. During a trip to the Jakarta Planetarium, my fear of darkness overcame me and I cried so hard that the show narrator had no other choice but to politely ask my parents to take me out of the show. My father took me out and I can still remember my father comforting me at the steps of the Planetarium, possibly whispering to me that darkness is not something to be feared, but something to be understood.

It was years later, at age 14, after reading so many books on the solar system, the night sky, and the universe, that my fascination with astronomy grew. I did manage to overcome my fear of darkness and to go back to the Planetarium and watched all 16 episodes, which changed weekly. In my high-school years, Carl Sagan's inspirational TV series *Cosmos* and novel *Contact* gave me the final push towards my decision to pursue a career in astronomy.

I WAS admitted in 1999 to the Department of Astronomy of the Bandung Institute of Technology (ITB), the only place in Indonesia to pursue a higher education in Astronomy. I graduated in 2006 after writing a Bachelor thesis on the kinematics of the solar neighborhood, under the supervision of Moedji Raharto. In the same year I was admitted to the two-year Master program of Leiden Observatory. The Leids Universiteits Fonds provided me with a scholarship for the first year of my study.

The international environment of the Observatory and the high-traffic of astronomers passing through to give colloquia and lec-

tures provided me with an excellent opportunity to experience state-of-the-art astronomical research, on top of the courses given by the excellent faculty members. In Leiden I performed two research projects. The first one involved a search for hypervelocity stars using astrometric catalogues, supervised by Anthony G.A. Brown and Yuri Levin. In the second project I performed a kinematic study of stars in the Galactic bulge, supervised by Koen Kuijken.

IN 2008, a newly-appointed Leiden professor, Maarten de Jong, offered me to become his PhD student and work with the data from the then nearly-completed ANTARES neutrino telescope. I accepted his offer and started to investigate the prospect and possibility of operating ANTARES as a  $\gamma$ -ray observatory, which has now become this dissertation. I was attached to the Department of Physics of Leiden University as well as the National Institute for Subatomic Physics (Nikhef) in Amsterdam.

Working within the ANTARES Collaboration allowed me to work together with other European scientists and to report my results within the Collaboration in several European cities. As a member of the Collaboration I was also required to do shift duty, which involved managing the data taking of ANTARES for a full week. I did this duty numerous times, both remotely and on-site. I was also given the chance to participate in schools such as the Nijmegen Astroparticle Physics School in 2009 and the 40th Saas-Fee Advanced Course in 2010 on astrophysics at very-high energies. I also presented my research in two international symposia, the TeV Particle Astrophysics (TeVPA) 2011 in Stockholm, Sweden, and the International Astronomical Union (IAU) Symposium No. 279 in Nekkō, Japan.

WHEN my PhD research was nearly concluded, I was happy to accept the offer made by Coryn Bailer-Jones from the Max Planck Institute for Astronomy (MPIA) in Heidelberg, Germany, to become his postdoctoral researcher and work with him to develop machine-learning algorithms for automatic classification of objects to be observed by the *Gaia* satellite. From September 2012 onward I am involved in this exciting research project.